Linking Adhesive Properties and Pore Organisation of Silicone Emulsions Obtained by Reactive Blending

Anaïs Giustiniani

NNT : 2017SACLS379

Thèse de doctorat de l'Université Paris-Saclay préparée à l'Université Paris-Sud

Ecole doctorale n°564
Ecole doctorale Physique en Ile de France
Spécialité de doctorat : Physique
par

Anaïs Giustiniani

Linking Adhesive Properties and Pore Organisation of Silicone Emulsions Obtained by Reactive Blending

Thèse présentée et soutenue à Orsay, le 11 décembre 2017.

Composition du Jury :

Mme. Brigitte Pansu	Professeure, Univ. Paris-Saclay	Présidente
M. Christophe Derail	Professeur, Univ. de Pau	Rapporteur
Mme. Joelle Frechette	Professeure, Univ. John Hopkins	Rapportrice
M. Reinhard Höhler	Professeur, Univ. Paris-Est-Marne-la-Vallée	Rapporteur
Mme. Wiebke Drenckhan	Chargée de recherche, Univ. Strasbourg	Directrice
M. Christophe Poulard	Maitre de conférences, Univ. Paris-Sud	Co-directeur

Remerciements / Acknowledgements

After these three years, there are many people that I have (or should I say need) to thank.

First of all, I would like to thank my reviewers, Joelle Frechette, Christophe Derail and Reinhard Höhler, for the time they took to read and judge my work. Je souhaite également remercier chaleureusement Brigitte Pansu d'avoir présidé mon jury lors de la soutenance, et d'avoir pris le temps de lire mon manuscrit quand de nombreux autres se sont empilés sur son bureau.

Je me dois aussi bien sûr de remercier ma directrice, Wiebke Drenckhan, ainsi que mon co-directeur Christophe Poulard, même si quelques mots n'arriveront certainement pas à montrer toute ma gratitude. Wiebke, au delà de ta bonne humeur à toute épreuve, qui a manqué à tout le LPS à ton départ, j'ai pour ma part surtout apprécié ton honnêteté, qui m'a permis je pense (j'espère) de m'améliorer aussi bien sur le plan scientifique que sur le plan humain. Elle fait de toi une personne avec qui j'ai aimé travailler autant que boire un verre de vin en parlant de ce vaste sujet qu'est la vie. Christophe, je ne vais bien sûr pas parler de ton enthousiasme légendaire à la vue des résultats que je t'amenais, mais tu as su te montrer très disponible pour moi pendant ces trois années, ce qui est même probablement plus expressif que l'enthousiasme au final, et je te remercie de cet investissement. A vous deux, vous avez formé une équipe de directeurs efficaces et complémentaires. Cette opportunité de pouvoir travailler de près avec des personnes de domaines différents a je pense été une vraie chance (et un sacré exercice) pour moi.

Je remercie également Philippe Guégan de nous avoir beaucoup aidé à connaitre et comprendre les réactions chimiques dans notre mélange. Cette information a été la clef de la partie A de ce manuscrit, et montre que les physiciens ne devraient pas faire de chimie tout seuls. David Mariot nous a aussi aidé sur la chimie, et je l'en remercie.

I had the chance to work with several researchers in Germany, here in the order of their appearance. First, thanks to Francisco García-Moreno to have opened his tomography lab to me to image my emulsions, and to have invested time in this project. I also thank Paul Kamm who showed me how to do the tomographies, and more generally for welcoming me in the lab. A big thank you also to Matthias Schröter for taking an interest in this "weird system" and working so much on its understanding along with Simon Weis who took time away from his own PhD thesis to do this. These collaborations allowed me to take the turn towards the structure part of this thesis, (and to spend some time in Germany, which is also very cool), and for this I am very grateful to you all and hope I'll have the chance to work with you (or at least see you in conferences) in the future.

Je voudrais également mentionner le travail conséquent réalisé par les stagiaires qui se sont succédés sur ce projet: Manon Marchand, Vincent Morales et Nicolas Paupy. Je les en remercie grandement.

A l'Institut Charles Sadron de Strasbourg, je souhaite remercier Patrick Kékicheff pour les images qu'il a réalisées pour nous au synchrotron Soleil, ainsi que Thierry Roland, Gaetan Dalongeville et Mouhamadou Dabo pour leur travail sur la simulation des propriétés mécaniques des émulsions solides. A l'ESPCI de Paris, je voudrais remercier Costantino Creton pour son aide précieuse sur les propriétés adhésives des émulsions solides.

En dehors des collaborateurs directs de ce travail, j'ai également reçu beaucoup d'aide de la part des services techniques et administratif du laboratoire. Je tiens donc à remercier Mélanie Decraene, Véronique Thieulart, Sabine Hoarau ainsi que Sophie Tourlet de l'administration pour leur aide et leur disponibilité au quotidien, ainsi que leur gentillesse (et surtout patience) à mon égard pendant ces trois années. Merci à l'équipe Elinstru, et en particulier à Vincent Klein et Jérémie Sanchez pour les impressions 3D des supports et le logiciel de pilotage de la manip de traction. Merci également à Ilan Settouraman et Loan Co du service informatique pour leur grande disponibilité.

Chaque thésard du labo devait choisir un parrain de thèse, et pour ma part j'ai eu la bonne idée de choisir Julien Bobroff, qui s'est montré exemplaire dans cette tache. J'ai pris un grand plaisir à discuter

de tes projets de vulgarisation, et tu as été très efficace quand il a fallu rappeler les échéances de la rédaction. Un grand merci à toi. Ludovic Pauchard du FAST a également accepté de participé à mon comité de thèse et je le remercie du temps qu'il y a accordé.

Enfin, et heureusement, une thèse ne se résume pas qu'à du travail. Je vais commencer par remercier les membres de l'équipe MMOI (oui, c'est vraiment comme ça que l'équipe s'appelle) pour les repas + café où on parlait de tout mais pas souvent de physique, et ça faisait du bien ! Mais également pour l'agréable ambiance qui y règne, et la disponibilité de tout le monde quand une personne cherche quelque chose désespérément ou a un problème. Sandrine tu es la plus cool des mamans que j'ai pu rencontrer, ne change rien, et donne moi des nouvelles (promis j'en donnerai aussi !). Je voudrais aussi mentionner la coolitude des thésards/postdocs du labo, depuis ceux qui m'ont "abandonnée" en cours de route me laissant là le coeur brisé (ma vieille chinoise, Thibaut qui a été un excellent co-bureau, Sébastien à qui j'ai servi de co-bureau de remplacement quand il était seul et qu'il avait peur, et bien d'autres qui ont contribué à des soirées inoubliables), jusqu'à ceux qui seront encore là après moi (Marceau et Alexis, merci de m'avoir incitée à faire de l'escalade avec vous, et d'être toujours chauds pour une bière, Marion qui s'est avérée être une partenaire de pétanque au top, Pan who was an excellent office mate after Thibaut, et encore bien d'autres qui ont participé à mes dernières soirées au LPS). Merci à toutes ces personnes pour les week ends, et les soirées que je ne suis pas prête d'oublier.

A mon arrivée dans cette belle ville qu'est Orsay il y a maintenant 6 ans, j'ai eu la chance de tomber d'abord sur Nadia et Aurélien qui m'ont acceptée malgré mes manières "de bourge", suivis de près par Mauvais, Guillaume, BAUUUUUR, Macé, Nicolas, Gabi et Seb, qui ont constitué mon "noyau dur" d'amis pendant toutes ces années. On a beaucoup fait la fête ensemble, mais surtout on a muri ensemble, et vous êtes fantastiques, et vous allez énormément me manquer, et j'espère qu'on se "collera" suffisamment longtemps pour réaliser notre idée de maison du bonheur quand on sera à la retraite. Quoiqu'il arrive, mes souvenirs avec vous sont impérissables. De la fac, mais d'autres promos, merci à Marianne et Clément (ça me fait toujours bizarre de t'appeler comme ça...) d'avoir aussi été d'excellents éléments de ma vie ici. Merci également à ma binôme de M2, Hélène, pour ces bons moments passés en cours et à Bordeaux. Et avant d'être à Orsay, j'avais aussi des amis (oui vraiment), et certains le sont encore. Joy et Lucie, mes copines de prépa, ainsi que Kévin et Thomas d'encore avant, les moments passés avec chacun de vous, bien que peu fréquents, sont d'une grande qualité et je vous en remercie. Ce sont des amis différents mais des amis quand même : merci à Atos, Nouchemi, Leo et Marcel d'être fluffy et cools.

Bien sûr, je souhaite remercier mes frères, ma soeur, ma mémé, ainsi que mes parents, de m'avoir soutenue moralement et financièrement tout au long de mes études. Il est indéniable que ma réussite est fortement liée à ma qualité de vie pendant mes études.

Et je finirai simplement par ces mots sages: România este cea mai bună țară din lume!

Contents

General introduction

Macro-cellular polymers are highly searched-for materials thanks to their rich physical properties. These arise from the internal structure of the material, in which discrete cells of gas or liquid are tightly packed within a continuous polymeric solid. The size, shape, organisation and relative volume of these cells have an important influence on the overall material properties. Commonly, the cellular organisation is the signature of an initially liquid state, in which gas bubbles (foam) or liquid droplets (emulsion) are compacted within a continuous liquid monomer/polymer matrix which is solidified to obtain the final material. Understanding and controlling the cellular organisation of the initially liquid template is therefore of utmost interest in order to control the properties of the cellular solid. This requires the control over the size, organisation and relative volume of the cells, and also over the stability of the liquid template with respect to ageing effects like cell coalescence (Figure 1).

Cellular materials with different polymers have been developed for various industrial applications. For example, mattresses are usually made using polyurethane or polyether, and surfboards using polystyrene. However, most polymers cause problems in terms of resistance to ageing, consistent material properties over a wide range of temperatures, biocompatibility, production, or production of a foam out of them, implying harmful reactions, etc. The use of the polydimethylsiloxane (PDMS), also called silicone, allows to overcome some of these issues. Indeed, silicone is low cost, thermally stable over a wide range of temperature, is permeable to gas, transparent in the visible spectrum, etc., which makes silicone elastomers good candidates for a large panel of applications from biomedical to electronics.

However, the stabilisation of an emulsion (or a foam) with silicone as the continuous phase still suffers from a lack of efficient stabilising agents against ageing processes such as coalescence and coarsening. This thesis is therefore concerned with establishing a new and efficient approach to stabilise such liquid materials. We thus developed a polyHIPE (High Internal Phase Emulsion) approach via reactive blending, which consists in stabilising the emulsions by provoking chemical reactions at the interface. In Part A, we present the stabilisation process of polyethyleneglycol (PEG) drops in silicone, and we establish the link between the onset of the stability of the emulsions and the evolution of the interfacial tension between the two immiscible phases, by associating both to the formation of a solid-like skin at the drop surface.

In Part B, we first show that we are able to use the reactive emulsions to generate various types of materials (liquid emulsion, solid foams and solid emulsions) with controllable cell sizes and of infinite stability. We then characterise the overall organisation of the drops in the liquid emulsion template using X-ray tomography, and show that it differs greatly from classic surfactant-stabilised emulsions. By analysing the interactions between two drops, we highlight the fact that this peculiar organisation

of the drops is a direct consequence of the presence of both frictional and adhesive forces between the emulsion drops thanks to the solid-like skin produced by the reactive stabilisation process. In this part, we thus answer the question: **how does the reactive stabilisation process impact the organisation of the drops in the PEG-in-silicone emulsion?** Indeed, the structure of a packing of surfactant-stabilised emulsion droplets has been the object of many investigations [1–3], while the study of the structure of packings of drops presenting friction and/or attractive normal forces is only at its infancy. We show here that the packings of our emulsion drops share many structural properties with the packings of hard, frictional, adhesive spheres, while they display certain surprising features due to the deformability of the drops. Systems like the one we developed may therefore help in understanding better how the structural properties of athermal sphere packings depend on their complex interactions (deformability, friction, adhesion).

After solidification of the continuous silicone phase, we obtain "solid emulsions" whose mechanical properties we study in Part C of this manuscript, paying particular attention to their adhesive properties. While the mechanics of solid foams has received its share of the scientific literature and for the entire range of void density [4–8], the mechanical properties of liquid inclusions in a solid have only been studied for low liquid inclusions densities [9]. Also, the impact of a substructure in a material on its adhesive properties was until now only studied for 2D systems [10, 11]. The properties of the solid emulsions have never been investigated before. In Part C, we therefore tackle the question: **how does the presence of the drops in the substructure of the silicone elastomer impact its mechanical and adhesive properties?** Using rheology and contact mechanics experiments, we investigate both the mechanical and the adhesive properties of the solid emulsions with respect to their structural properties, studied in Part B. We show that the presence of the drops changes the elastic modulus and that it enhances greatly their adhesive properties through the increase of viscous energy dissipations.

Globally we will show in this thesis that the use of reactive emulsion stabilisation opens new pathways to the investigation of sphere packings with complex sphere interactions; and to the fabrication of new types of cellular materials with intriguing mechanical properties. While our investigations present only first steps in this vast field, they point towards a set of interesting and important scientific questions which will be worthy of deeper and more systematic investigation in the future.

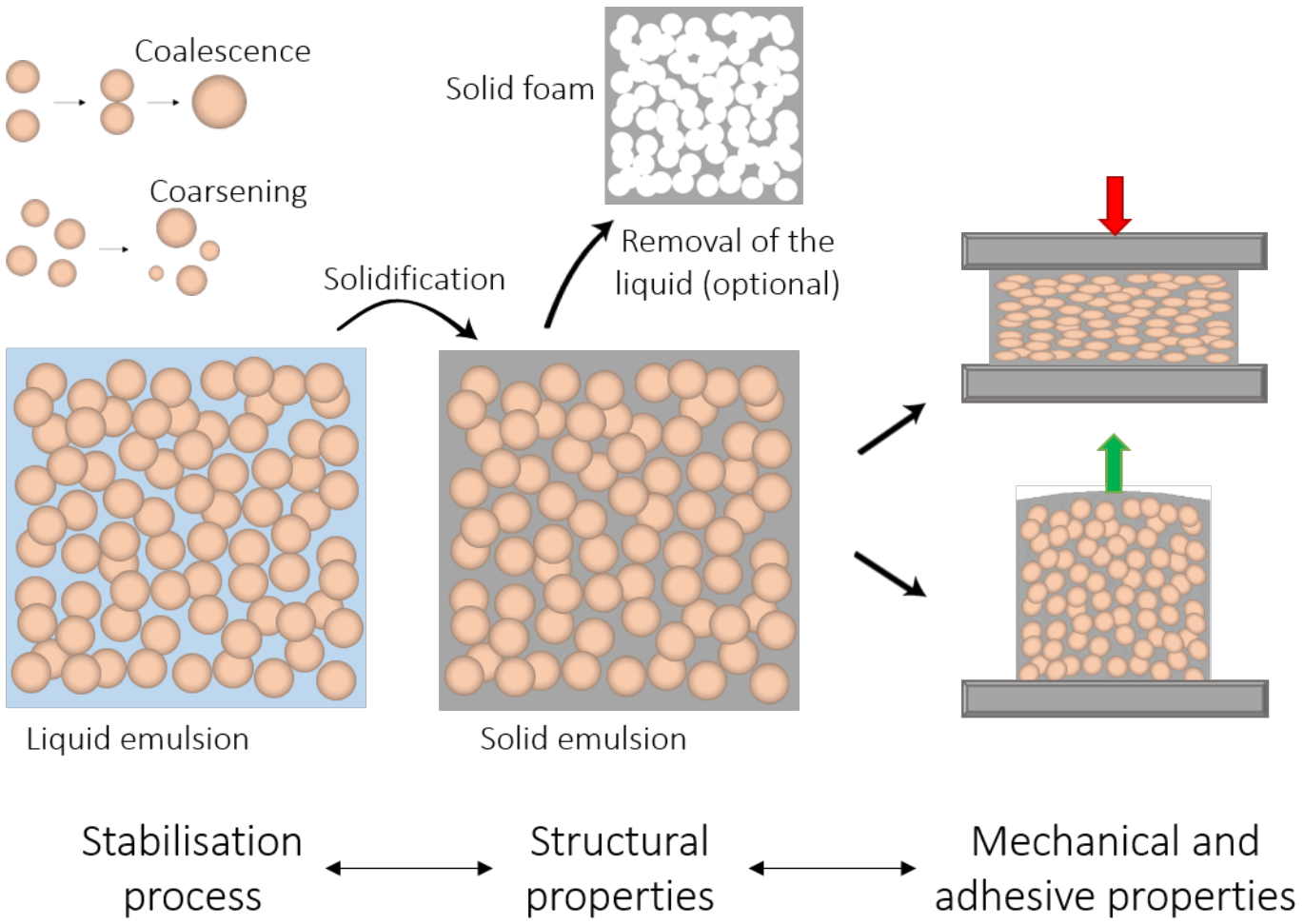

Figure 1: Context of this thesis

Chapter 1

Materials and methods

This manuscript is divided into three parts which address different physical phenomena: the emulsion stabilisation via a reactive blending approach (Part A), the structural properties of the emulsions (Part B), and their mechanical and adhesive properties (Part C). For all these three parts, the same materials were used to generate the emulsions, and we present them in Section 1.1. In Section 1.2 we detail how the different sample were generated, from the generation of different drop sizes to the solidification of the emulsions. Finally, in Sections 1.3, 1.4 and 1.5, we describe the different experiments that were carried out in the different parts of this work, in the order of their appearance in the manuscript.

1.1 Materials

1.1.1 Raw materials used

The different molecules used in this study are summarised Table 1.1 with their principal characteristics. The structures of some of them are given in Figure 1.1.

The MethylHydrosiloxane - Dimethylsiloxane Copolymers, Trimethylsiloxy terminated (MHDS) (Figure 1.1a) was used as received from GELEST or PETRARCH systems (CAS number: 68037-59-2). It has a PDMS backbone (dimethylsiloxane chain trimethyl terminated) where some Si-CH_3 groups are replaced by reactive Si-H groups. The percentage of Si-H groups in a chain[1] is given by the percentage Mole%(MeHSiO) in Table 1.1. The MHDS are statistical copolymers, meaning that this percentage is a mean on the entire melt and that there is no order in the position of the reactive Si-H groups. We characterise more accurately the structural properties of these molecules in Section 1.1.2.

The polyethylene glycol (PEG) with molecular weight M_w=200 and 400 g/mol (Figure 1.1b) are used as received from SIGMA-ALDRICH (CAS number: 25322-68-3).

The crosslinker/catalyst (Figure 1.1c), and the solidifier (Figure 1.1d) were used as received from SIGMA-ALDRICH and GELEST (CAS numbers: 68478-92-2 and 68585-32-0 respectively). They are composed of silicone molecules among which a certain percentage is complexed with a platinum Pt atom, which serves as a catalyser of the different reactions. The concentration of catalyst Pt in

[1] given by the number of Si-H groups divided by the total number of Si-H and Si-CH_3 groups

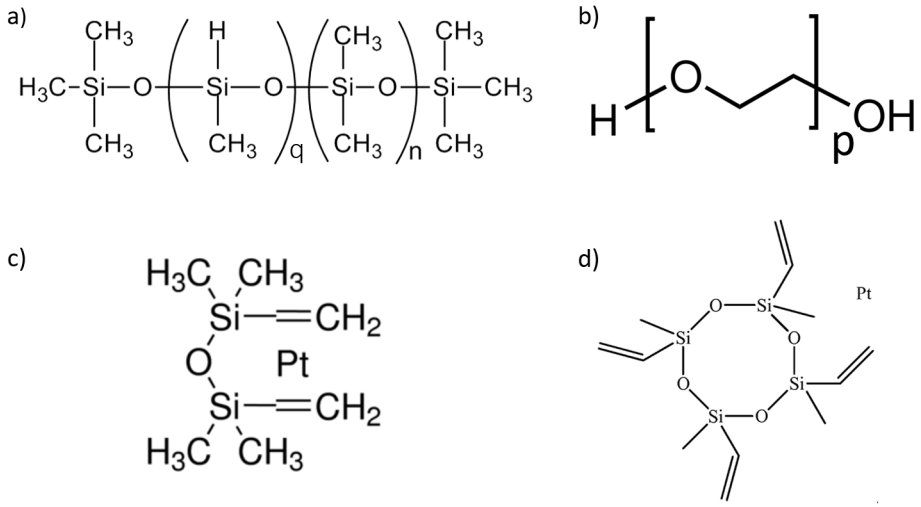

Figure 1.1: Structure of the molecules used for this study, called by their name given Table 1.1: a) MHDS, b) PEG, c) crosslinker/catalyst and d) solidifier. n, q and p are integers.

the crosslinker/catalyst mixture, $F(Pt)$ (in mol%) is originally 0.02, and can be reduced by diluting the original mixture with the same siloxane molecule (pure crosslinker, purchased from SIGMA-ALDRICH). The percentage of platinum complexed crosslinker in the solidifier is under 10% according to the supplier[2].

The Sylgard 184® is a commercial polymer supplied by DOW CORNING as a two-parts kit: a base composed in majority of vinyl terminated silicone chains and silica particles, and a curing agent containing the solidifier and MHDS chains amongst other molecules [12]. Upon mixing of the base and the curing agent with a 10:1 ratio, and helped with a platinum catalyser present in the solidifier, the hydrosilylation reaction between the Si-H groups and the vinyl groups starts and solidifies the PDMS. The silica nanoparticles present in both phases reinforce the final solid material. The rate of the reaction is dependent on temperature. At moderate temperatures ($\approx$ 50 to 70°C), it takes approximately 3 hours to crosslink the material, while it takes approximately 48 hours at ambient temperature. This allows to manipulate the uncrosslinked Sylgard 184® at ambient temperature during the time needed to generate the emulsions.

In Part B of the manuscript, octamethylcyclotetrasiloxane (also called D_4) was used to replace the Sylgard 184® curing agent (CAS number: 556-67-2). It was used as received from SIGMA-ALDRICH, with the same proportions: ratio 10:1 between the base and the D_4.

In Part B, we added dodecane in the continuous phase to change the drop-drop interactions (CAS number: 112-40-3), at a percentage $\%Dod$ (in weight) of the Sylgard 184® base and D_4 total weight.

[2]http://www.gelest.com/wp-content/uploads/product_msds/SIP6832.2-msds.pdf

Molecule	Name used	M_w (g/mol)	Density at 25°C [a] (g/mL)	Viscosity at 25°C [b] (mPa.s)	Characteristics	Supplier
MethylHydrosiloxane - Dimethylsiloxane Copolymers, Trimethylsiloxy terminated (MHDS)	MHDS 2000-6.5	2000	0.97	18	Mole%(MeHSiO) = 6.5%	Gelest
	MHDS 2000-25	2000	0.98	18	Mole%(MeHSiO) = 25%	Gelest
	MHDS 13000-3.5	13000	0.97	209	Mole%(MeHSiO) = 3.5%	Petrarch Systems
Polyethylene glycol (PEG)	PEG-200	200	1.124	49		Sigma-Aldrich
	PEG-400	400	1.128	96		Sigma-Aldrich
Platinum(0)-1,3-divinyl-1,1,3,3-tetramethyldisiloxane complex solution 0.1 M in poly(dimethylsiloxane), vinyl terminated	Crosslinker/catalyst	381.48	0.98		Active at ambient temp.	Gelest
Platinum-cyclovinylmethyl-siloxane complex	Solidifier	539.74	0.98		Active at moderate temp.	Gelest
	Sylgard 184® base	$\sim$ 50000	1.11	5000 (base alone) 3100 (10:1 mix)		Dow Corning
	Sylgard 184® crosslinker		1.03	100	Active at moderate temp.	Dow Corning
Octamethyl-cyclotetrasiloxane	D_4		0.956			Sigma-Aldrich
Dodecane		170	0.75		Solvent of PDMS	Sigma-Aldrich

Table 1.1: Molecules used for this study and their relevant properties. [a] as given by the supplier. [b] measured with a bulk rheometer (cf Section 1.1.2).

1.1.2 Characterisation of the polymers used

The different MHDS and the Sylgard 184® base are statistical copolymer melts. Here, we show how we characterised these molecules with different techniques allowing us to obtain informations about their structure. Indeed, the properties given by the suppliers are often mean values (such as the molecular weight of polymers which is usually a more or less polydisperse distribution[3]), or have changed due to ageing of the melt after opening the bottle. To better characterise the polymers used in this study, we measured the molecular weight distribution by gel permeation chromatography, the number of Si-H groups along the backbone of the MHDS molecules by nuclear magnetic resonance spectroscopy and the number of Si-OH groups in the Sylgard 184® base using Infra-red Spectroscopy. We also measured the viscosity of the MHDS and PEG melts.

Gel Permeation Chromatography

The polydispersity of the molecular weight of the polymers can be measured by Gel Permeation Chromatography (GPC), which separates species in a solvent on the basis of their size (or their hydrodynamic volume), contrarily to other chromatographic techniques which separate the analytes based on their interactions with the solvent and the substrate of the chromatography column.

The basis of the technique is the following: the chromatography column is filled with a porous polymer gel in which the macromolecules in a good solvent can penetrate more or less according to their size. The smaller molecules penetrate deeper into the pores, therefore are retained longer, and are then the last to emerge from the chromatography column. To know absolutely the size of the molecules that are characterized, it is necessary to have previously calibrated the column with a macromolecule of known polydispersity. The output signal S_i at a time t is proportional to the number of monomers n_i of weight M_i contained in the cell at this instant $S_i \sim n_i M_i$.

It is then possible to determine the number average molecular weight M_n and the weight average molecular weight M_w, as well as the polydispersity index PDI,

$$M_n = \frac{\sum_i n_i M_i}{\sum_i n_i}, \tag{1.1}$$

$$M_w = \frac{\sum_i n_i M_i^2}{\sum_i n_i M_i}, \tag{1.2}$$

$$PDI = \frac{M_w}{M_n}. \tag{1.3}$$

Our GPC was calibrated with polydimethylsiloxane (PDMS), and gave the non-corrected results given in Table 1.2. Since the calibration was made with PDMS chains with only Si-CH_3 groups along the backbone, we need to correct the values of M_n and M_w, taking into account that some of the Si-CH_3 groups are replaced by Si-H groups. The molecular mass of a monomer with two Si-CH_3 groups (indexed by n) is 74 g/mol and the molecular mass of a monomer with one Si-CH_3 and one Si-H groups (indexed by q) is 60 g/mol. In that case, we can correct the data in Table 1.2 using

$$M_w = M_w^* \cdot (1 - 14 \cdot N_{Si-H}), \tag{1.4}$$

[3]The polymerization reaction allowing to obtain polymers from their monomers often results in chains with different sizes.

MHDS	M_n^* (kg/mol)	M_w^* (kg/mol)	N_{Si-H}	M_n (kg/mol)	M_w (kg/mol)	M_w(supplier) (kg/mol)	PDI
2000-25	5.5	7.9	0.401	1.6	2.3	1.9-2.0	1.43
13000-3.5	17.5	21.6	0.028	16.4	20.2	13.0	1.24

Table 1.2: Non-corrected values M_n^*, M_w^*, M_n and M_w, and PDI found by GPC for the MHDS 2000-25 and the MHDS 13000-3.5.

where M_w^* is the value given by the GPC software and given in Table 1.2, M_w is the corrected value of M_w^* and N_{Si-H} is the ratio of Si-H groups relative to Si-CH_3 groups in the molecule[4]. N_{Si-H} is measured using ^{1}H NMR spectroscopy (see paragraph below). From this analysis we get the corrected values[5] M_w and M_n.

The value of M_w for the MHDS 2000-25 is very close to the one given by the supplier (∼2000 g/mol), while the value for the MHDS 13000-3.5 is higher than the one provided by the supplier (∼ 13000 g/mol). This can be due to the fact that the samples used for this GPC study came from a newly opened bottle in the case of the MHDS 2000-25, and from a bottle opened few months prior the measure in the case of the MHDS 13000-3.5. Indeed, Si-H groups are not stable against air for long exposure times, because of the reaction with the water contained in the air [13], and they might have caused the MHDS 13000-3.5 to crosslink. This causes a change of the chains sizes, i.e. an increased value of the PDI. A perfectly monodisperse polymer has a PDI=1. Here, both the MHDS 2000-25 and the MHDS 13000-3.5 have rather large PDI values i.e. large distributions of sizes. This might be due to the ageing of the reactive groups as just discussed, or to the difficulty to obtain monodisperse polymers with a polymerisation reaction.

GPC was also used by Laetitia Dies-Diverchy [14] to measure the size distribution of the vinyl terminated PDMS chains in the Sylgard 184®. Figure 1.2 shows a large polydispersity of the chains with the polydispersity index PDI = 1.98, with M_n = 27.5 kg/mol and M_w = 54.6 kg/mol. The other components of the base, the silica nanoparticles and the small tetra(trimethylsiloxy)silane molecules (M_w = 384.84 g/mol) are sufficiently small for them to be excluded from the signal.

Nuclear Magnetic Resonance

Nuclear Magnetic Resonance (NMR) spectroscopy is a widely used technique in chemistry to obtain or confirm the structure of organic molecules. The nuclear magnetic resonance is a property of the nucleus of an atom which possesses a spin I which depends on the number of protons p and neutrons n inside the nucleus: $I = 0$ if $p = n$, I =1/2, 3/2 or 5/2 and if $p + n$ is an odd number or I =1, 2 or 3 if p and n are both odd numbers. The nucleus spin has, according to quantum mechanics, $I + 1$ possible orientations. In many atoms, ^{12}C for example, $p = n$ meaning $I = 0$ and the nucleus spin has only 1 possible orientation. But in the case of ^{1}H and ^{13}C atoms, $I = 1/2$ and the nucleus spin has 2 possibles orientations. In the absence of an external magnetic field ($B = 0$ T), these two orientations have the same energy. However, if $B \neq 0$ the energy levels split into two levels with a magnetic quantum number $m = -1/2$ or $+1/2$, respectively with and against the applied magnetic field (Figure 1.3). The initial population of these levels follow a Boltzmann distribution, i.e. the lower energy level is slightly more

[4]Note that N_{Si-H} is different than the percentage $Mole\%(MeSiHSiO)$.
[5]This correction does not change the PDI values.

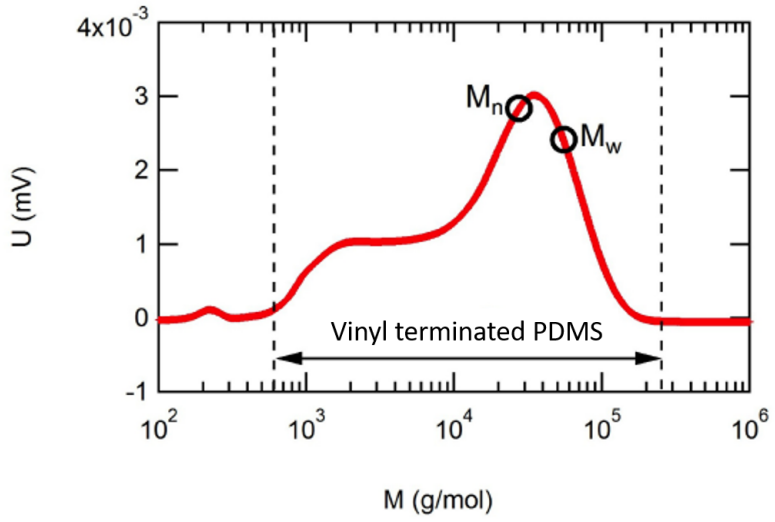

Figure 1.2: Molecular size distribution of the vinyl terminated PDMS chains in the base of the Sylgard 184® obtained by GPC. From [14].

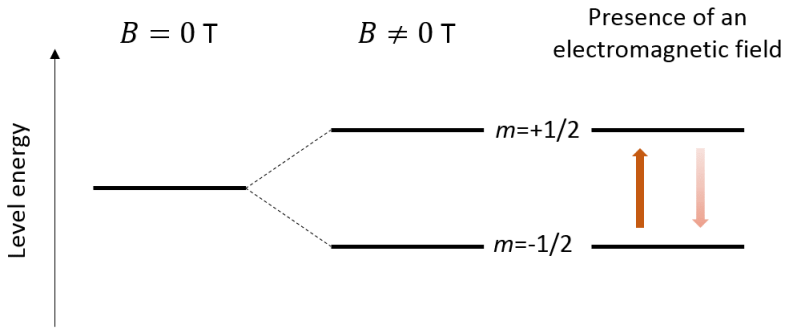

Figure 1.3: Energy levels for a nucleus with spin quantum number $I = 1/2$

populated that the higher energy level. Electromagnetic radiations can excite the nuclei in the lower energy level to the higher energy level, which then relax back to the lower energy level while emitting a radiation wave. The measure of the frequency of radiation absorbed (or emitted) depends on the energy difference between the two levels and is characteristic of the nature of the nucleus.

In the case of a molecule, the effective magnetic field "felt" by a particular nucleus does not depend only on the applied magnetic field because of the "nuclear shielding" caused by the surrounding electrons and nuclei. The signal then absorbs at a different frequency than for the single nucleus. This shift from a reference value (usually tetramethylsilane, defined at δ =0) is called the chemical shift δ, in ppm (parts per million). The values of δ are tabulated for every nucleus with any possible environment, which allows to obtain the structure of a molecule from its NMR spectrum. It is possible to use NMR with respect to the resonance of any of the nuclei that have a spin $I = 1/2$, in our case, we used the proton NMR (^{1}H NMR) which uses the resonance of hydrogen nuclei in the molecules.

Figure 1.4 shows the spectra for two different MHDS molecules used in this study, dissolved in deuterated chloroform ($CDCl_3$) (solvent of MHDS): the MHDS 2000-25 and the MHDS 13000-3.5. In the MHDS spectra, we can distinguish the peaks of the proton resonance of the Si-CH_3 at $0 < \delta < 0.2$ ppm, and the reactive Si-H groups at $\delta \approx 4.7$ ppm. The presence of multiple resonance peaks for Si-CH_3 is due to the fact that all of these protons do not have exactly the same environment. The

same goes for the Si-H peaks, with the hydrogen atoms at different location along the backbone of the polymer.

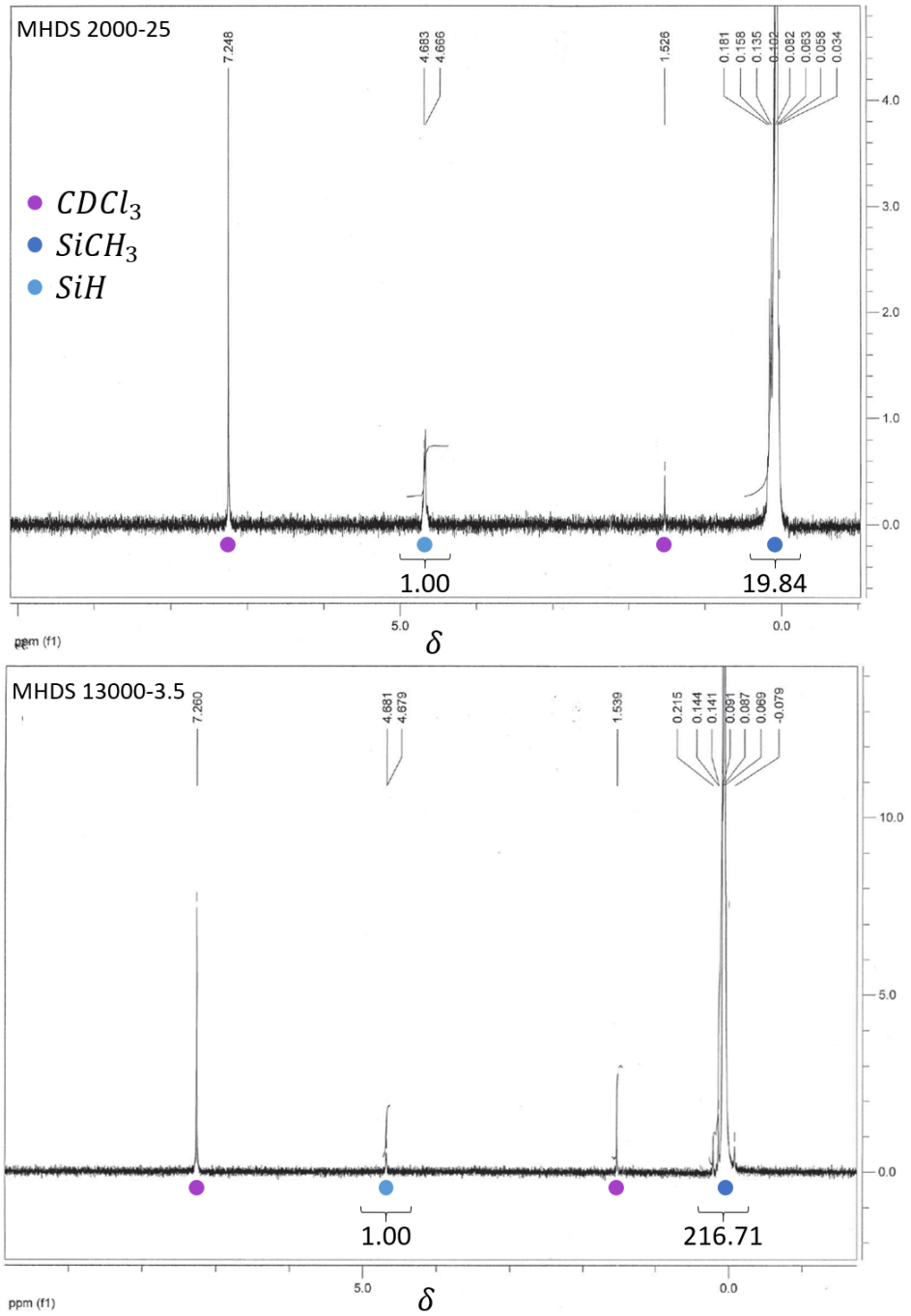

Figure 1.4: ^{1}H NMR spectra of MHDS 2000-25 in deuterated chloroform ($CDCl_3$) and MHDS 13000-3.5 in $CDCl_3$. The purple dots are peaks associated with the proton (^{1}H) resonance in the $CDCl_3$, the dark and light blue dots are associated with the ^{1}H resonance of respectively the Si-CH_3 groups and the reactive Si-H groups of the MHDS molecule.

By integrating the signal of the spectrum for each peak, we can determine the percentage of Si-H against the Si-CH_3 groups (Mole%(MeHSiO) number Table 1.1), knowing the molecular weight M_w of the polymer (measured by GPC, see above paragraph). Indeed, with the notations of Figure 1.1, we

have for MHDS 2000-25 (left) and MHDS 13000-3.5 (right)

$$\begin{cases} 162 + 74n + 60q = 2300 \\ 18 + 6n + 3q = 19.84q \end{cases} \qquad \begin{cases} 162 + 74n + 60q = 20200 \\ 18 + 6n + 3q = 216.71q \end{cases}$$

where the first equation of each system relates to the molecular weight given by the GPC measurements and the second equation gives the number of Si-H groups on the molecule. The resolution of the systems gives

$$\begin{cases} n = 21.80 \approx 22 \\ q = 8.75 \approx 9 \\ \text{Mole\%(MeHSiO)} = 24.6\% \end{cases} \qquad \begin{cases} n = 264.70 \approx 265 \\ q = 7.51 \approx 8 \\ \text{Mole\%(MeHSiO)} = 2.25\% \end{cases}$$

where Mole%(MeHSiO)=$\frac{60q}{74n+60q}$.

As for the GPC study, the value of Mole%(MeHSiO)=24.6% for the MHDS 2000-15 is very close to the one given by the supplier (25%), while the value of 2.25% for the MHDS 13000-3.5 is lower than the one provided by the supplier (3.5%), confirming our hypothesis the sample MHDS 13000-3.5 might have aged before the study.

Infra-red spectroscopy

Infra-red spectroscopy uses the interactions between infra-red radiations and matter to obtain the structure of the molecules composing the sample, which can be a solid, a liquid or a gas. The principle of the technique is the following: liaisons between two atoms in a chemical group can vibrate at different resonant frequencies depending on the symmetry and the direction of the vibration (Figure 1.5). When an IR radiation is sent on the sample, some of the energy is absorbed by these liaisons, and the absorbed frequencies depend on the atoms composing the chemical group, and if the liaisons are simple, double or triple. From there, the IR spectrum, which are graphs of the absorbed infra-red radiation vs. the frequency or the wave number (in cm^{-1}), are calculated. The positions of the peaks characteristic of different liaisons are tabulated [15]. IR spectroscopy is used either to identify an unknown molecule or chemical group in a sample, or to quantify the amount of a particular liaison in a molecule, for example to quantify the Si-H liaisons in the MHDS as we did using RMN. In Appendix III, we use it to show the presence of a small amount of Si-OH groups in the Sylgard 184® base, though these are not listed in the composition given by the manufacturer.

We used an IR spectrometer Nicolet iS50 FT-IR from Thermo Scientific piloted by the software OMNIC Spectra, where FT-IR means Fourier Transform Infra Red spectroscopy. The use of the Fourier transform allows the improve the speed of the acquisition and the signal-to-noise ratio. In this apparatus, the incident beam of IR light is guided through a Michelson interferometer, and then through the sample. The spectra of the sample is systematically compared with the spectra of a reference. In our case, we used NaCl windows (20 mm of diameter and 2 mm of thickness, purchased from Edmund Optics) to sandwich the Sylgard 184® base or curing agent, because these windows to not absorb the IR light between 400 and 4000 cm^{-1} which is where are located the characteristic peaks of silicone

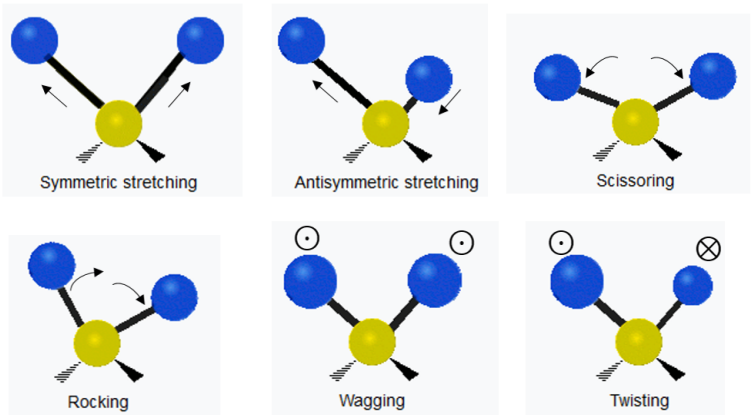

Figure 1.5: The different vibrational modes of a CH_2 group in an organic compound. Adapted from the Wikipedia page about Infra-red spectroscopy.

polymers. The reference for the characterisation of the Sylgard 184® base or curing agent was then the two NaCl windows without the sample in between, surrounded by air.

Viscosity measurement

We measured the viscosity of the polymers in Table 1.1 using a bulk rheometer (Anton Paar® MCR-302). For the viscosity measurements we used only the the rheometer in rotation mode with a cone-plane geometry (Figure 1.6a) with a 50 mm diameter and an angle between the plane and the cone $\alpha = 2.0\,°$. The plate is a peltier plate which allows to control the temperature at which the measurement is made. The liquid is placed between the cone and the plate, and the cone is rotated with an amplitude γ, also called the strain. The resistance to the rotation called the torque M is measured throughout the experiment, allowing to obtain the shear stress $\sigma = M/A$, A being the surface area of the geometry.

The dynamic viscosity η of the sample is measured using Newton's law

$$\eta = \frac{\sigma}{\dot{\gamma}}. \tag{1.5}$$

Figure 1.6b shows the viscosity η of the two PEGs of molecular sizes $M_w = 200$ and 400 g/mol, the MHDS 13000-3.5 and the MHDS 2000-25 and Figure 1.6c the viscosity of Sylgard 184® and Sylgard 184® base + D_4 with 0%, 5% and 10% of dodecane at 25°C used in this study and given in Table 1.1. These graphs show that η is constant with the shear rate $\dot{\gamma}$ over the range $1\ s^{-1} < \dot{\gamma} < 100\ s^{-1}$ for all these melts. This is characteristic of the so-called *Newtonian* fluids (cf Chapter 8 Section 8.2.1). Note here that the viscosity of the MHDS 2000-6.5 is expected to be the same as the viscosity of the MHDS 2000-25.

1.1.3 Preparation of the polymeric mixtures

To prepare the PEG-in-MHDS emulsions, we use the MHDS as received. We add to the PEG phase a crosslinker/catalyst molecule (Figure 1.1c) at different concentrations C. The crosslinker/catalyst is weighted using a precision balance (OHAUS Pioneer®) and mixed to the PEG by stirring for 10

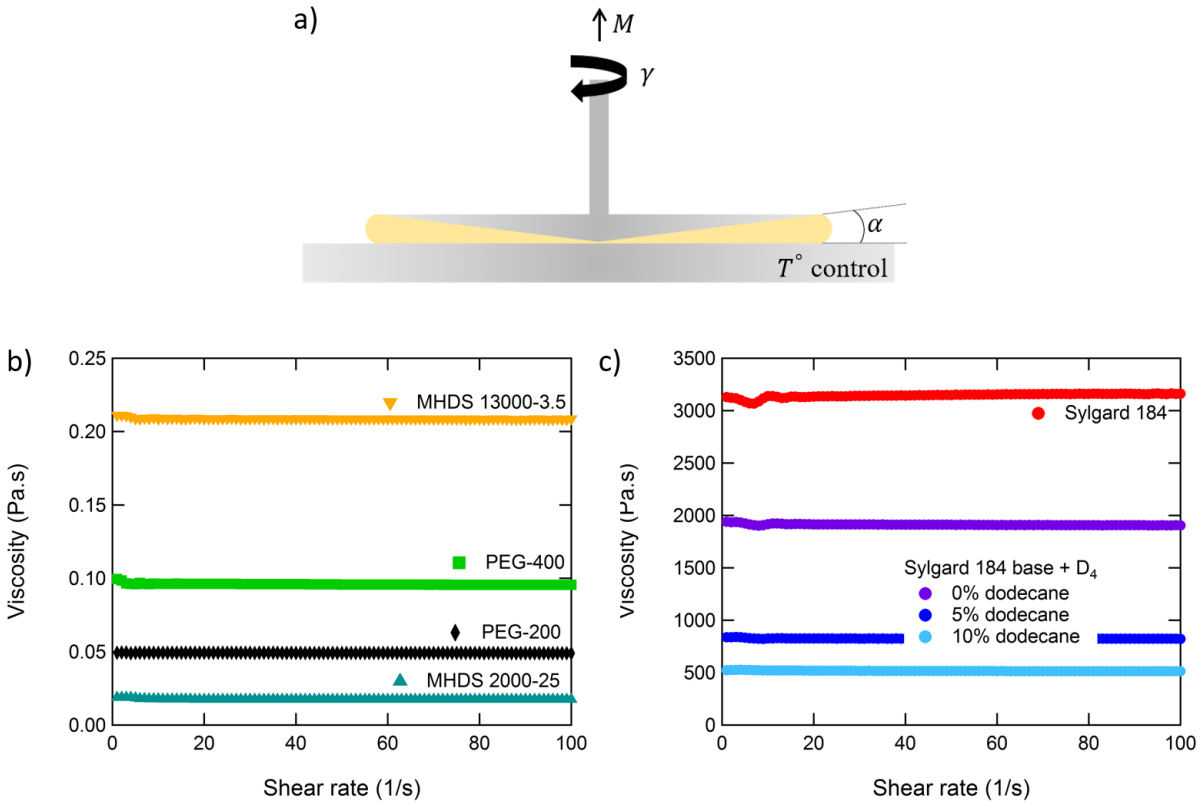

Figure 1.6: a) Scheme of the cone-plane geometry of the rheometer. b) Dynamic viscosity η for shear rates 1 $s^{-1} < \dot{\gamma} < 100$ s^{-1} for PEG-200, PEG-400, MHDS 2000-25 and MHDS 13000-3.5 at 25°C. c) Dynamic viscosity η for shear rates 1 $s^{-1} < \dot{\gamma} < 100$ s^{-1} for Sylgard 184® and Sylgard 184® base + D_4 with 0%, 5% and 10% of dodecane at 25°C.

min. The bottles used for the mix are previously cleaned using dishwashing liquid, then toluene, then ethanol and finally ultra-pure water. They are then dried in a 60°C oven. As the crosslinker is a siloxane molecule, its solubility in the PEG is low and the phases tend to separate with time. We therefore stir the solution for 10 min right before each use.

The concentration of catalyst Pt in the crosslinker/catalyst mixture, $F(Pt)$ (in mol%) is originally 0.02, and is reduced occasionally by diluting the original mixture with the same siloxane molecules (pure crosslinker without catalyst purchased from ABCR).

The two parts of the Sylgard 184® are mixed with a ratio of 10:1 of base:curing agent in a plastic cup, then degassed using a vacuum pump. The curing (solidification) of the Sylgard 184 is made in a 60-70°C oven for a few hours as the curing agent is active at moderate temperature.

1.2 Emulsion generation

Different techniques can be used to generate emulsions with variable drop sizes. We present here the ones we used for this study: breakup under shear, dripping and millifluidic techniques.

1.2.1 Generation by breakup under shear

The breakup under shear is a widely used technique in industry, because of its simplicity and its ability to produce materials at an industrial scale. This method is based on the ability of one of the phases

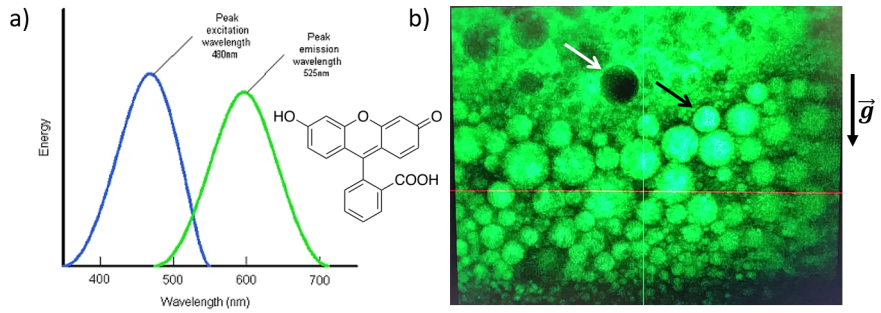

Figure 1.7: a) Excitation and emisson wavelenght of a fluorescein solution. Insert is the scheme of the fluorescein (http://www.opsweb.org/). b) Optical image obtained with a confocal microscope of an emulsion generated by breakup under shear of PEG and PDMS showing both PEG-in-PDMS (black arrow) and PDMS-in-PEG (white arrow) droplets. Fluorescein was added in the PEG phase. Image courtesy of Sandrine Mariot.

to deform under shear until breakup occurs to form droplets. The final drop size distribution depends in this case on both external parameters such as the temperature, the shear rate and the duration of mixing or extrusion time (though an equilibrium is rapidly achieved [16]), and on the fluid properties like the rheological properties of the two fluids, the interfacial tension between the two phases, and the compatibilising agent [17]. The impact of the stabilisation process on the diminution of the drop size under shear is discussed in Section 2.3 in Chapter 2.

We used here an Ultra-Turrax purchased from SIGMA-ALDRICH. Since in our system no surfactant was added initially to stabilize the emulsions (but surfactants were rather created *in-situ* directly at the interface), and as both phases have viscosities close to each other (η(PEG400)=0.1 Pa.s and η(MHDS 2000-25)=0.03 Pa.s for example), the formation of PEG-in-MHDS or of MHDS-in-PEG emulsion is *a priori* equally probable.

To show this, we added a hydrophilic fluorophore, fluorescein (Figure 1.7a) in the PEG phase. We generated an emulsion using the Ika Ultra-Turrax disperser tool, stainless steel dispersing element for T-18 basic disperser, 10 mm, 1/cs purchased from SIGMA-ALDRICH. The mix was composed of 1/3 of MHDS and 2/3 of PEG + 0.05 mol% of crosslinker/catalyst + fluorescein. The mixing was made at room temperature, for 2 to 3 min. We obtained emulsions with drop radii between 1 and 10 µm (Figure 1.7b). Using a confocal microscope and a UV (ultra-violet) excitation laser, we were able to observe whether the turbulent mixing produced PEG-in-MHDS or MHDS-in-PEG emulsions. Figure 1.7b clearly shows the presence of both fluorescent green drops in a dark background and dark drops in a fluorescent green background. This means that if both emulsion configurations are equally probable, then we obtain a mixte emulsion. In this image, we see that both configurations are separated from bottom to top. This is due to the density difference between the PEG and the MHDS and to the fact that the emulsion had time to sediment between generation and imaging.

Classical emulsification techniques such as breakup under shear then lack a selection mechanism which does not allow to fully control the structural properties of the emulsions. It is therefore not a suitable emulsion generation technique in our case.

1.2.2 Dripping

To generate large drops with millimetric dimensions, we use a simple technique: we dispense the PEG/crosslinker/catalyst mixture from a syringe at constant flow rate using a syringe pump (World

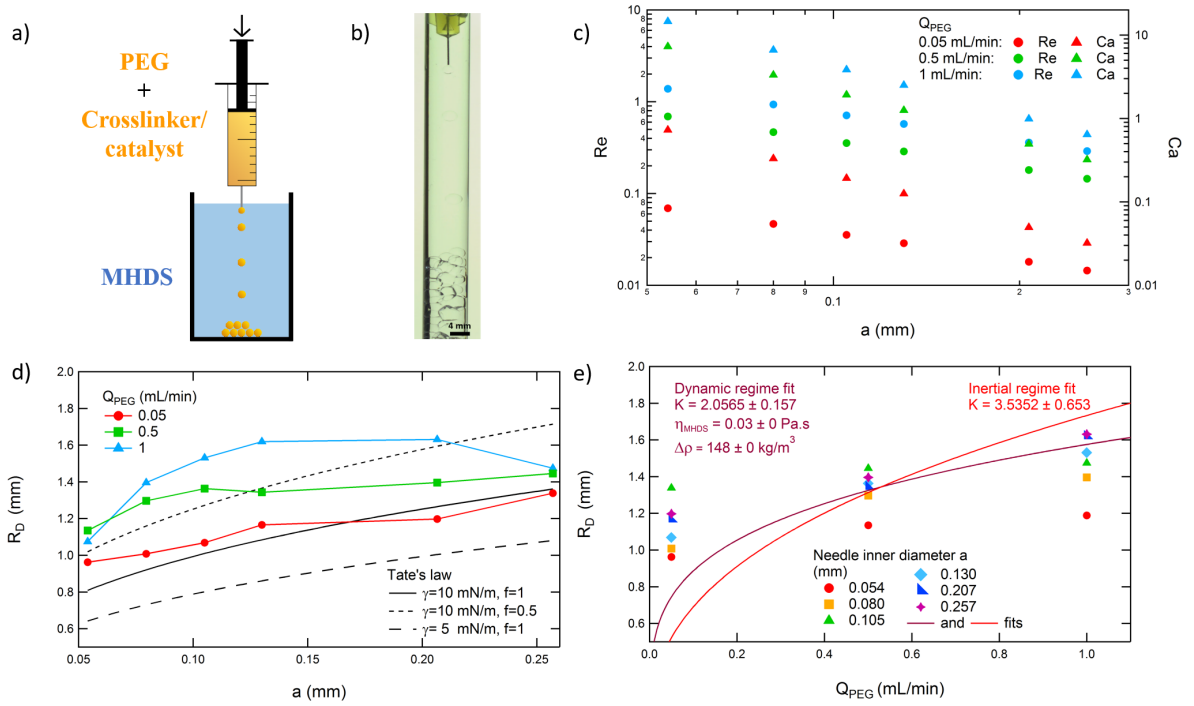

Figure 1.8: a) Scheme of the generation of millimetre-sized PEG/crosslinker/catalyser drops in MHDS by gravity-driven dripping from a needle using a syringe pump. b) Image of a PEG-in-MHDS emulsion during generation by dripping. c) Dependency of the dimensionless Reynold Re and capillary Ca numbers on the inner radius of the needle a, for flow rates Q_{PEG} = 0.05, 0.5 and 1 mL/min, for PEG400 created directly in contact with MHDS 2000-25 and C=0.1 mol%. d) Dependency of the experimental drop radius R_D on the inner radius of the needle a with the dripping technique, for flow rates Q_{PEG} = 0.05, 0.5 and 1 mL/min. The dashed and continuous black lines are points for equation 1.6 for different values of γ and f. e) Dependency of the experimental drop radius R_D on the flow rate Q_{PEG} for different inner radius of the needle a. The solid lines are fit for the scaling of R_D in the viscous-dominated (purple) and inertia-dominated (red) dymanic regimes.

Precision Instrument, AL-1000), creating drops that fall from the needle due to gravity. (Figure 1.8a and b). If the viscosity of the continuous phase is low, the drops can be created directly in contact with the MHDS, and in the case the viscosity is too high, they can be created in air.

Three parameters have an influence on the drop size R_D: the flow rate Q_{peg}, the viscosity η_{PEG} and the needle inner diameter a. Their influence can be separated in three regimes [2]: a quasi-static regime for very low Q_{peg} where only a influences R_D, a viscous-dominated dynamic regime and an inertia-dominated dynamic regime for which the flow rate plays a non-negligible role.

The maximum drop volume R_D accessible in quasi-static conditions with this method is given by Tate's law [18],

$$R_D = \left(\frac{3}{2f} \frac{\gamma}{\Delta\rho g} a \right)^{1/3}, \tag{1.6}$$

where γ is the interfacial tension between the liquids, $\Delta\rho$ the density difference between the liquids and g the gravitational acceleration. f is a tabulated parameter [19] which takes into account the fact that a fraction of liquid stays attached to the needle after the drop detachment $f = m/m^* = f(a/V^{1/3}) < 1$, where m^* is the mass of the total pendant drop and m and V respectively the mass and volume of the drop that fell from the needle. In this regime, only the interfacial forces and gravity are the driving forces of the detachment of the drop.

In the dynamic regime, the distinction is made between viscous-dominated and inertia-dominated. In

the viscous-dominated regime, the viscous drag exerted by the MHDS on the PEG adds a viscous stress which resists the detachment and therefore leads to larger drops. In that case, surface tension and inertial forces can be neglected, and the drop size can be estimated by

$$R_D = K \cdot \left(\frac{\eta_{peg} Q_{peg}}{\Delta \rho g} \right)^{1/4}, \tag{1.7}$$

where η_{peg} is the viscosity of the PEG and K is a proportionality constant of order 1 which depends on the diameter of the needle and the wetting conditions between the PEG and the needle.

In the inertia-dominated regime, the interfacial tension and the viscous forces are negligible compared to the inertial forces, which allows the formation of a jet which finally destabilises to form drops. The drop size then scales as [20]

$$R_D = K' \cdot \frac{Q_{peg}^{2/3}}{g^{1/3}}, \tag{1.8}$$

where K' is a proportionality constant of order 1. The polydispersity of the drops tends to increase in this regime.

The separation between these regimes can be understood in terms of the values of the Reynolds number Re and the Capillary number Ca, defined as

$$Re = \frac{\rho_{peg} Q_{peg}}{\pi \eta_{peg} L}, \tag{1.9}$$

and

$$Ca = \frac{\eta_{peg} Q_{peg}}{\pi \gamma L^2}, \tag{1.10}$$

where ρ_{peg} is the density of the PEG, and L is a characteristic length of the system which we take here equal to a. Here we take γ equal to 10 mN/m ($\gamma(t = 0$ s)). The Reynold number is a measure of the competition between the inertial and viscous forces, while the capillary number measures the competition between the viscous and the interfacial forces. For very low flow rates, $Re \ll 1$ and $Ca \ll 1$ and the drop size is controlled by the interfacial forces and given by the quasi-static regime model. For low flow rates but viscous forces higher than interfacial forces, $Re \ll 1$ and $Ca \approx 1$ and the system is in the viscous-dominated dynamic regime. Finally, for high flow rates, $Re \gg 1$ and $Ca \gg 1$ and the system is in the inertia-dominated regime, characterized by the creation of a jet at the nozzle of the needle. Figure 1.8c gives the Reynold and Capillary numbers of our system depending on a and Q_{peg}. From this we understand that, for this range of Q_{peg} and a, the system should never be in the inertia-dominated regime since the values of Ca and especially Re are not higher than 10-15.

Experimentally, we obtain drops of PEG in MHDS emulsions with drop radii ranging from 0.9 to 1.6 mm (Figure 1.8d and e). We see that both the needle inner diameter (also called needle gauge) and the flow rate have an impact on the drop size as expected. In Figure 1.8d we plotted the evolution of the drop size with a for the different flow rates. The theoretical curves for the Tate's law are given for different values of γ and f (black lines). From this figure, it seems that the quasi-static model fits well the evolution of R_D with a for the flow rate $Q_{peg} = 0.05$ mL/min, with $\gamma = \gamma_0$ the interfacial tension between the PEG and the MHDS for C=0 mol%. Since during the creation of the drop the interface is constantly increasing, the impact of the few surface active species at the interface during that time should indeed be negligible. The values of Re for this flow-rate are coherent with the use of this model

for the entire range of a. The values of Ca however are close to 1 for the smallest values of a, i.e. viscous forces start to play a role, which might explain the slight deviation from the model at these values. If we now look at the evolution of R_D with Q_{peg} (Figure 1.8e), we see that the viscous-dominated model seems to validate the values of $R_D = f(Q_{peg})$ for the flow rates $Q_{peg} = 0.5$ and 1 mL/min, while the inertia-dominated model does not capture the behaviour of R_D here. In regard to the values of Re and Ca that are only in the order of 1-10 at these flow rates, this behaviour seems understandable.

We thus create PEG drops in MHDS in either the quasi-static or the viscous-dominated regimes, and the polydispersity is kept to a minimum of 2 to 5%.

1.2.3 Millifluidic technique

In order to generate smaller emulsion drops, we used millifluidic techniques. At micro- and millimeter scales, the effect of surface tension and viscosity start to dominate the system over gravitational forces, which leads to interesting effects that can be used for various applications, one of them being droplet-based millifluidic. Contrary to the dripping technique (Section 1.2.2), in millifluidic geometries the two phases are flowing with flow rates Q_d and Q_c for the dispersed and continuous phase respectively. Three types of geometries are used in the litterature in order to create droplets using the millifluidic techniques: T-junction, flow-focusing and co-flowing. For this work, we used the flow-focusing (Figure 1.9) and T-junction (Figure 1.10) geometries only. The drop size obtained using these geometries obey the same scaling laws, and we describe them in this section.

Flow-focusing

Flow-focusing geometries are widely used in micro and millifluidic applications thanks to their ability to generate monodisperse bubbles and drops [2, 21–24]. Figure 1.9a and b show a scheme and a photograph of such a geometry. The dispersed phase (the PEG/crosslinker/catalyst mixture in our case) is injected with a flow rate Q_d inside a channel at the end of which there is a geometric constriction of characteristic width R_0. The continuous phase (the MHDS) is injected at a flow rate Q_c in two channels perpendicular[6] to the dispersed phase channel. This way, the continuous phase pinches periodically the dispersed phase in the constriction, leading to the formation of equal-volume drops.

Fabrication of the flow-focusing device and setup The flow-focusing geometries used for this work were fabricated in the lab using a micro-milling machine. The fabrication process is the following:

- drawing of the geometry (size of the channels and the restriction) using the software *Solidworks*[7],
- preparation to milling with the software *Esprit*[8],
- milling of the geometry using a micro-milling machine in PMMA (polymethyl methacrylate) (Figure 1.9 c),
- molding of the PMMA chip with Sylgard 184®, giving the "inverted" geometry,

[6] in some geometries, the channels are not perpendicular but form an angle $0° < \theta < 90°$.
[7] http://www.solidworks.fr/
[8] http://www.espritcam.fr/

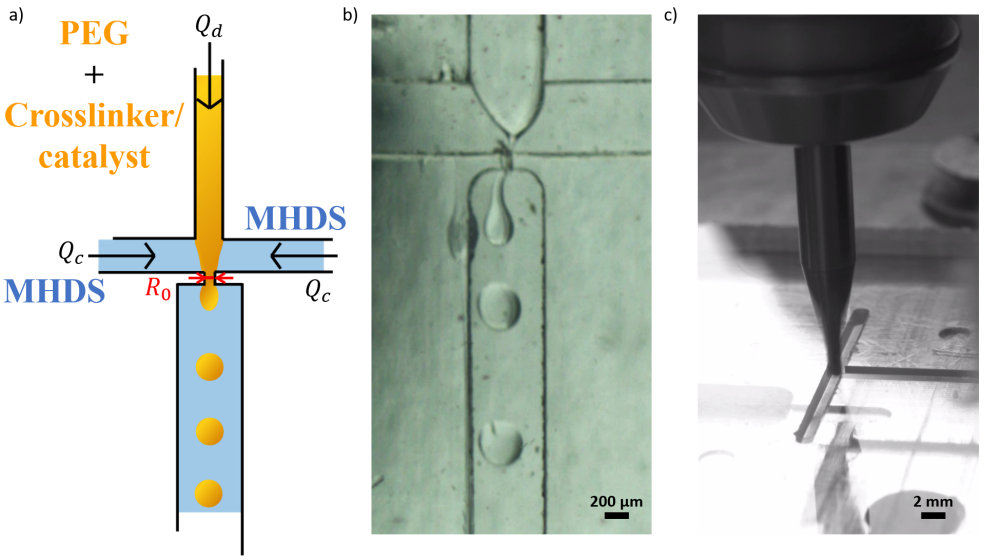

Figure 1.9: a) Scheme of the generation of micrometer-sized PEG/crosslinker/catalyser drops in MHDS using a flow-focusing geometry. b) Image of a PEG-in-MHDS emulsion during generation by flow-focusing. c) Image of a flow-focusing chip while being fabricated with the micro-milling machine. Image courtesy of Julien Bobroff.

- molding of the Sylgard 184® chip with COC (cyclo olefine copolymer), to obtain the desired geometry,
- milling of the continuous and dispersed phases entries in the COC chip,
- sealing of the chip by a Sylgard 184® sheet and a glass sheet by applying pressure on the COC/Sylgard/glass system.

The reason behind the molding of the PMMA chip is to be able to fabricate disposable COC chips without re-using the micro-milling machine each time. The flow rates of the continuous and dispersed phases flow-rates are controlled by syringe-pumps (World Precision Instrument, AL-1000).

T-junction

The T-junction geometry also allows to generated monodisperse drops, and was the most used during this work, because of the possibility to buy plastic T-junctions on a one-use only basis. Indeed, for some samples the MHDS phase needs to be solidified with a chemical reaction which needs to start directly in the geometry. The need to fabricate a new flow-focusing geometry for each sample drove us to use commercial T-junction geometries, purchased from Nordson Medical with $w = 1.13$ mm (ref T210-9).

Figure 1.10a represents a scheme of a T-junction geometry. There are only two fluid entries, one for the dispersed phase with the flow rate Q_d and one for the continuous phase with the flow rate Q_c, controlled by syringe pumps.

Scaling laws for millifluidic devices

As for the dripping technique (Section 1.2.2), the size of the drops in a millifluidic device is given by different scale laws depending on the values of the flow rates of both the continuous and the dispersed

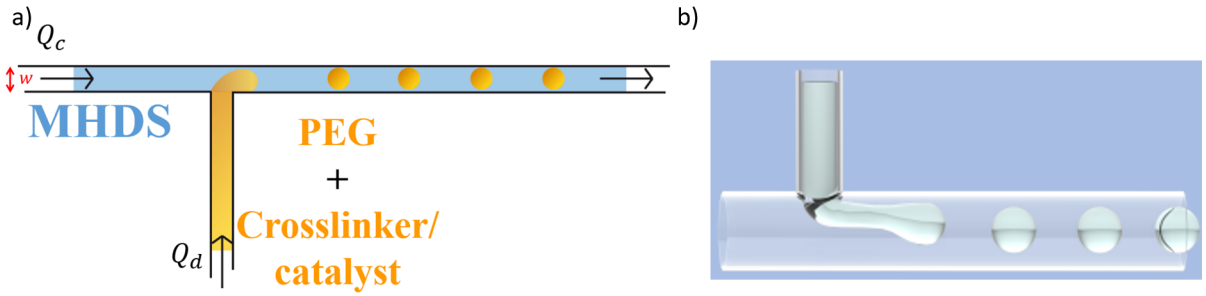

Figure 1.10: a) Scheme of the generation of micrometer-sized PEG/crosslinker/catalyser drops in MHDS using a T-junction geometry. b) Generation of drops using a T-junction geometry in the *jetting* regime. Image from http://www.elveflow.com.

phases. The behaviour of the drop size with the flow rate is separated in three regimes: quasi-static, dripping and jetting.

At low flow rates Q_c and Q_d (quasi-static regime, with $Ca \ll 1$ and $Re \ll 1$), the dispersed phase can fill the entire constriction, which causes the continuous phase to enter the constriction from the sides and pinch the dispersed phase to create a drop that flows away in the outlet of the chip. After the detachment of the drop, the cycle continues periodically. In this regime, the drop size scales as [21]

$$R_D^Q \sim \left(V_c \frac{Q_d}{Q_c}\right)^{1/3}, \tag{1.11}$$

where V_c is the volume of the constriction.

Upon increasing the flow rates, the system enters a dynamic regime where, for moderate flow rates the viscous drag of the continuous phase on the dispersed phase takes over the capillary forces that resist the detachment of the drop (higher Ca, $Re \ll 1$). By equating the capillary forces $2\pi\gamma R_0$ with R_0 a characteristic length of the constriction, and the viscous forces also called Stokes forces $6\pi R_D \eta_c u_c$ where η_c and u_c are the viscosity and the velocity of the continuous phase respectively, we obtain

$$R_D^V \sim \frac{\gamma R_0}{\eta_c u_c} = Ca^{-1} R_0. \tag{1.12}$$

Since both η_c and γ depend on the temperature, the drop radius is also here a function of the temperature. In order to change the drop diameter for a given pair of liquids, one can either change the flow rates or change the temperature [24].

For $Re \gg 1$ and $Ca \gg 1$, the system is dominated by inertia. A jet of the dispersed phase forms at the constriction, which destabilises to form droplets. In this regime, the drop size follows the behaviour [2, 23]

$$R_D^I \sim \left(\frac{Q_d}{Q_c}\right)^{2/5} \cdot R_0. \tag{1.13}$$

With the flow-focusing geometry, we were able to generate PEG drops with radii between 100 and 500 µm in MHDS 2000-25. Table 1.3 compares the experimental radii of the drops for two cases with the theoretical values using Equations 1.11 and 1.12. A better agreement is found with the model of the quasi-static regime, which is coherent with the low values of $Re \sim \{10^{-1}; 10^{-2}\}$ and $Ca \sim 10^{-2}$ for $\gamma \sim$ 10 mN/m. With the T-junctions, we were able to generate monodisperse droplets of PEG in Sylgard 184® in the quasi-static regime as the very low values of Re and Ca suggest in Table 1.3.

Geometry	$R_0(w)$ (µm)	Q_d (mL/min)	Q_c (mL/min)	Re	Ca	R_{exp} (µm)	R_D^Q (µm)	R_D^V (µm)	R_D^I (µm)
F-F	100	0.1	0.04	$6.9 \cdot 10^{-2}$	$6.4 \cdot 10^{-2}$	485 ± 11	135	1571	144
F-F	300	0.1	0.2	0.12	$3.5 \cdot 10^{-2}$	165 ± 3	188	8482	227
T-J	1130	$6.7 \cdot 10^{-3}$	$1.7 \cdot 10^{-3}$	$8.7 \cdot 10^{-4}$	$9.8 \cdot 10^{-7}$	311 ± 44	356	$1 \cdot 10^6$	1956

Table 1.3: Comparison of experimental values of the drop radius R_{exp} with theoretical values obtained from the quasi-static regime and the viscous-dominated dynamic regime for the MHDS 2000-25 / PEG-400, $F(Pt)$ = 0.02 system in flow-focusing (F-F) devices and the Sylgard 184® / PEG-400, $F(Pt)$ = 0.02 system in a T-junction (T-J), with the crosslinker/catalyst concentration C = 0.05 mol%.

In conclusion, using these techniques, we were able to generate drops with radius between 100 and 500 µm, by varying the flow rates and/or changing the size of the constrictions R_0 for the flow-focusing devices.

1.2.4 Emulsion solidification

For PEG-in-MHDS or PEG-in-Sylgard 184® emulsions, the solidification of the continuous phase after generation at ambient temperature of the emulsions is done by the addition of a platinum-based crosslinker (platinum cyclovinylmethylsiloxane complex Table 1.1) called the "solidifier" in the silicone phase prior to emulsification. The solidifier contains vinyl groups which react with the Si-H groups of the MHDS and crosslink the volume of the continuous phase. This crosslinker is active at moderate temperatures, which necessitates the solidification to be made at 50-60°C in an oven for 24 hours. For the PEG-in-Sylgard 184® emulsions, the moderate temperature active crosslinker is already in the continuous phase after mixing of the two elements of the kit. To achieve the complete solidification of the Sylgard 184®, the emulsions need to stay in the oven at 50-60°C for at least 3 hours.

We studied the solidification of the continuous phase using oscillating shear rheology with a cone-plane geometry, by measuring the storage $\mathcal{G}'$ and loss $\mathcal{G}''$ moduli every 30 s with oscillations of amplitude 0.5% and a frequency f = 1 Hz, at different temperatures. An example is shown for the solidification of the Sylgard 184® in (Figure 1.11). The gel point, which delimits the transition from liquid to solid of a solidifying material, is defined as the time needed for the curves of the storage and loss moduli to cross each other. We define in this study the solidification time as the time needed to reach the plateau values of the storage $\mathcal{G}'$ and loss $\mathcal{G}''$ moduli. After solidification, we obtain liquid PEG drops inside a solid silicone matrix.

1.3 Emulsion stabilisation

1.3.1 Emulsion stability experiments

In Section 2.5 in Chapter 2, we investigate the impact of the concentration of crosslinker/catalyst C in PEG on the emulsions stability. To do so, we generated the emulsions by dripping drops of the

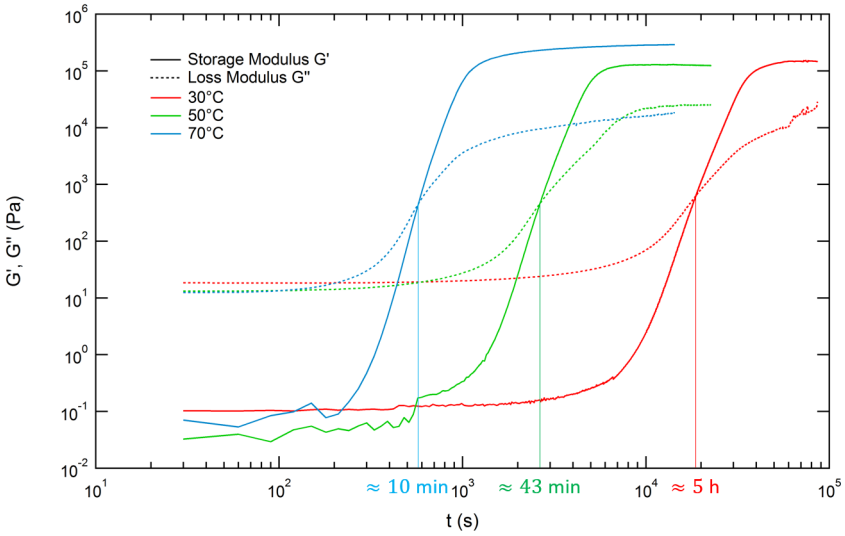

Figure 1.11: Evolution of the storage G' and loss G'' modulus of the Sylgard 184® with time at 30°C, 50°C and 70°C, measured with oscillating shear rheology at the frequency $f = 1$ Hz. The time at which $G' = G''$ (gel point) are indicated on the graph for each temperature.

mixture of PEG and crosslinker/catalyst at a constant rate using a syringe pump (World Precision Instrument, AL-1000) in silicone as explained in Section 1.2.2 and followed their evolution with time. The recipients used were disposable plastic cuvettes (polystyrene disposable cuvettes, inner dimensions 10x10x45 mm^3, purchased from Carl Roth). The evolution of the emulsion height was monitored by taking pictures at a given frame-rate using a digital camera (u-eye camera).

1.3.2 Interfacial tension measurements

In Chapter 3, we investigate the evolution of interfacial tension between the MHDS and the mixture of PEG and crosslinker/catalyst. The measurements were made using a pendant drop apparatus (Tracker from Teclis, Figure 1.12a), using the Laplacian profile method with a regulation of temperature [25]. In our study, the temperature is always fixed at 25°C.

The principle is the following: a drop of the PEG/crosslinker/catalyst mixture is generated in MHDS at a constant velocity ($\sim$ 0.5 µL/s) with a volume ranging between 2 and 10 µL. A camera takes images of the shape of the drop which are used to measure the volume of the drop and the interfacial tension γ between the two phases (Figure 1.12b).

The curvature of the drop creates a difference of pressure Δp between the two phases called the Laplace pressure (Figure 1.12c), given by the equation

$$\Delta p_{Laplace} = p_A - p_B = \gamma \cdot (\frac{1}{R_1} + \frac{1}{R_2}), \tag{1.14}$$

where R_1 and R_2 are the principal radii of curvature of the drop. This Laplace pressure alone causes the drop to minimize its surface and tend toward a sphere with R_1=R_2.

Under the effect of gravity, a hydrostatic pressure is produced inside the drop across the z axis, given by the Pascal's law

$$\Delta p_{Pascal} = \Delta p_0 - \Delta \rho g z, \tag{1.15}$$

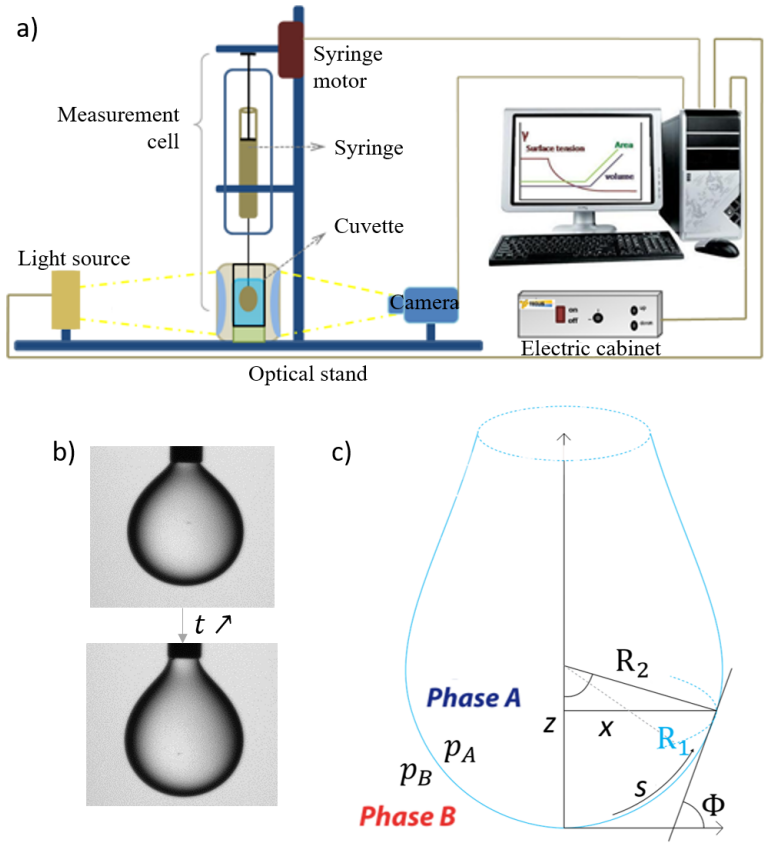

Figure 1.12: a) Scheme of the tensiometer used to measure γ in this study. Image from http://www.teclis-instruments.com/index.php/en/offer/products/tensiometer. b) Image of a PEG/crosslinker/catalyst drop in MHDS as time increases. c) Scheme of an interface between two phases A and B. Adapted from http://www.dataphysics.de.

where Δp_0 is the Laplace pressure at an arbitrary reference plane z=constant, $\Delta\rho$ is the density difference between the two phases and g is the gravitational acceleration. This pressure gradient affects the main radii of curvature R_1 and R_2 due to the weight and gives to the drop its pear-like shape.

At the apex of the drop (the lowest point) R_1=R_2=R. It is then convenient to place the reference plane at this point. Taking into account that at every other point of the interface $R_2 = \frac{x}{\sin\Phi}$, it follows

$$\frac{2}{R} - \frac{\Delta\rho g z}{\gamma} = \frac{1}{R_1} + \frac{\sin\Phi}{x}. \tag{1.16}$$

The introduction of a parametrisation using the arc length s of the drop shape results in a set of three first-order differential equations with three boundary values, solvable by numerical procedures. The measure of γ is finally given by the numerical fit of the drop shape recorded by the camera.

In order to be accurate, the drop has to have a sufficiently large volume to be measurably deformed by gravity. Also, as seen in Section 1.2.2, the drop has to be sufficiently small to avoid detachment from the needle. Therefore, an optimum drop size which balances the gravitational and interfacial forces needs to be found for each experiment.

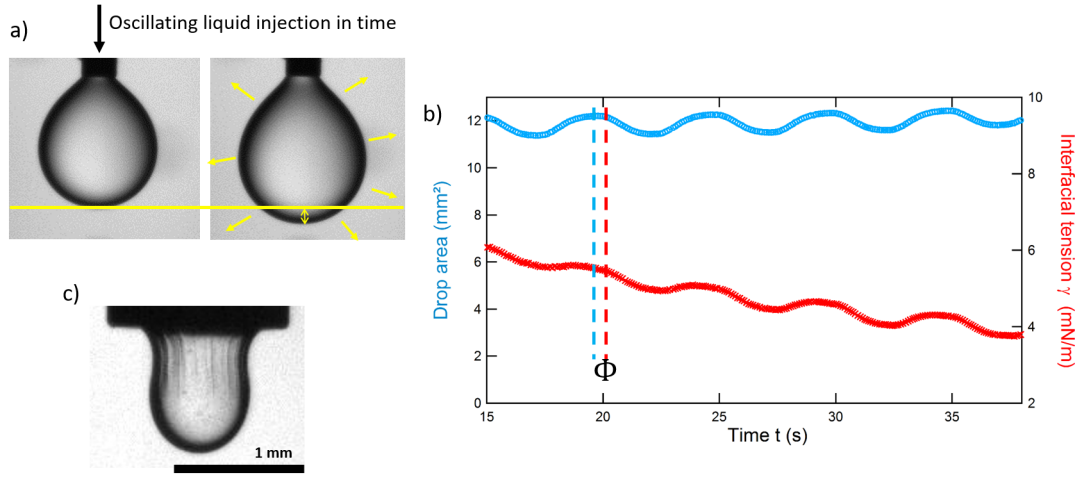

Figure 1.13: a) Images of a PEG and crosslinker/catalyst drop in MHDS during oscillation cycles. b) Evolution of the interfacial tension γ and the drop surface area A with the time t during oscillation cycles, with the definition of the phase shift Φ between S and γ. c) Image of a PEG and crosslinker/catalyst drop in MHDS presenting wrinkles at the interface during compression.

1.3.3 Interfacial elasticity measurements

The pendant drop apparatus also allows to measure the dilatational surface elasticity E_0 and dilatational surface viscosity η of the PEG/MHDS interface with time (Chapter 3). The general equation of the dilatational viscoelasticity of an interface undergoing cycles of expansion/contraction of its surface area S (Figure 1.13a) is

$$\Delta\gamma = \gamma(t) - \gamma_{ref} = E_0\alpha + \eta\frac{d\alpha}{dt}, \tag{1.17}$$

where $\alpha = (S(t) - S_{ref})/S_{ref}$ is the variation of the surface area, and γ_{ref} and S_{ref} are the reference values of γ and S respectively when the drop surface is not subject to any deformation [26].

Just as in Section 1.3.2, a drop of PEG and the crosslinker/catalyst mixture is created at a constant velocity in the MHDS, and a camera takes images of the shape of the drop used to measure γ with the Laplacian profile method described above and the drop area A. If a sinusoidal oscillation of the form $S = S_{ref} + \tilde{S}\exp(i2\pi\omega t)$ with $\tilde{S}$ the amplitude and ω the frequency of the oscillation (Figure 1.13b) is imposed on S, and if the amplitude is not too important (usually $< 10\%$), the response of γ gives

$$\gamma = \gamma_{ref} + \tilde{\gamma}\exp(i2\pi\omega t + \phi), \tag{1.18}$$

where $\tilde{\gamma}$ is the amplitude of the oscillations of γ and Φ is the phase shift between the area perturbation and the response of γ ((Figure 1.13b).

The complex viscoelastic modulus E is defined by

$$E = \frac{\Delta\gamma}{\Delta S}S_{ref} = E_0 + i2\pi\omega\eta, \tag{1.19}$$

which gives

$$E = \frac{\tilde{\gamma}}{\tilde{S}/S_{ref}}\exp(i\phi). \tag{1.20}$$

The real part and imaginary part of E respectively give the dilatational surface elasticity E_0 and

dilatational surface viscosity η of the interface (in N/m). They usually depend on the oscillations frequency ν.

The use of the drop shape analysis applied on oscillating pendant drops to measure the surface elasticity should however be subject to caution. Indeed, Stanimirova *et al.* [27] showed that out of three different ways of measuring E_0, this method gave a much lower value than the two others (Langmuir trough and capillary pressure tensiometry with spherical drops). They state that this is generalisable to all highly elastic interfaces and that it is due to the non-isotropic surface deformations during the dilatation/compression cycles. In this manuscript, we use those measurement to follow the evolution of the dilatational elasticity at the PEG/MHDS interface, but the absolute values are not taken as valid.

1.4 Characterisation of the structural properties of the emulsions

1.4.1 Scanning Electron Microscopy

Scanning Electron Microscopy (SEM) is a surface imaging technique with a resolution up to 1 nm. A source produces electrons at the top of a column which are passed through a combination of electromagnetic lenses and apertures to produce an electron beam focalised on the surface of the sample. The interaction between the electron beam and the sample generates signals from different parts of the interaction volume (tear drop shaped volume below the surface), detected by appropriate detectors, the most common being the secondary electron detector. Secondary electrons are in the conduction or valence band and do not need a lot of energy to be transferred in the vacuum. The measure of the number of secondary electrons ejected from the sample provides information about the morphology and the surface topography. The contrast is dominated by the edge effect: more secondary electron can leave the sample at edges rather than smooth surfaces, leading to increased brightness. The number of secondary electrons detected also depends on the atomic number of the atoms in the sample, which allows to separate different phases in a sample.

The SEM images in this manuscript were made at the Institut Charles Sadron (ICS) in Strasbourg, France, with the help of Prof. Thierry Roland.

1.4.2 Measurement of the angle of repose

In Chapter 6, we measure the angle of repose made by the pile of PEG/crosslinker/catalyst drops in silicone during the emulsion generation. To do this, we generated the drops using the dripping technique given in Section 1.8, pushing the PEG at a constant rate (0.05 mL/min) with a syringe pump. They pile at the bottom of a plastic container, and we record images periodically during the generation. The angle of repose, which is the angle between the pile of drops and an horizontal line passing by the top of the pile, is measured using Image J.

1.4.3 Double drops experiment

The double drop experiments were made at the Institut Charles Sadron (ICS) in Strasbourg, France, with an experimental setup developed by the service "Elinstru" (V. Klein and J. Sanchez) of the LPS in Orsay, France.

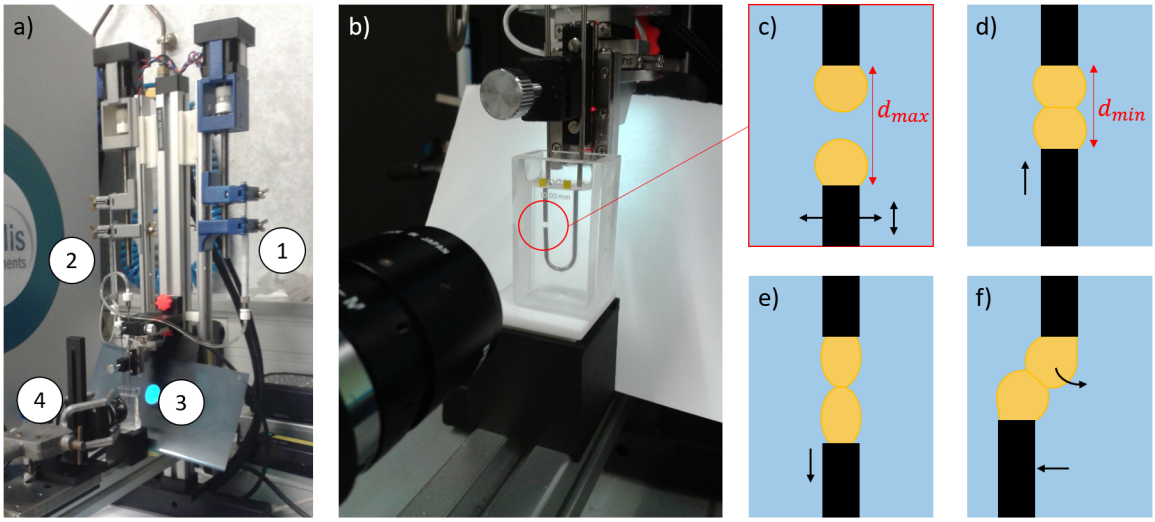

Figure 1.14: a) Photograph of the DDE: ① and ② syringe n°1 and 2 respectively mounted on their computer piloted motor to deliver precisely the drop volumes, ③ recipient filled with the PDMS phase in which the needles are immersed, ④ camera. b) Zoom on the recipient containing the PDMS phase and the needles holding the two drops. c) Scheme of the two drops while not in contact. Needle n°1 (bottom) can move vertically and horizontally. d) The two drops are put into contact. From this position, the drops can be separated to observe the drops adhesion (e), or slided over one another to observe friction at the interface (f).

The idea of the "double drops experiment" (DDE) is to be able to look at the interactions between two drops during the emulsion generation while avoiding the impact of the presence of other drops. To do so, two syringes (① and ②) are mounted on a holder and connected at the top to a motor which delivers or removes a controlled volume of the liquid (or air) in the syringe (Figure 1.14a). On the other side, the syringes are connected to two needles, one straight and one curved (Figure 1.14b). The syringe attached to the curved needle can move vertically and horizontally, which allows in a first step to fix its position exactly in line of the other syringe (Figure 1.14c). The experiment is piloted by a *Labview* software, which allows to fix the desired volume of each drop, the stabilisation time T_s during which the drops do not touch each other, the contact time T_c during which the drops are in contact, the positions d_{min} (Figure 1.14c) and d_{max} (Figure 1.14d) of the contact and stabilisation phases respectively, and the approach speed of the two needles v.

With this setup, we propose two experiments: a measure of the interfacial friction, and a measure of the adhesive properties of the interface. Note here that this setup can also be used to study the stability against coalescence of the drops. Both experiments start with a stabilisation phase of time T_s at a distance d_{max} during which the drops remain separated and the interfaces are undergoing a chemical reaction, followed by a contact phase of time T_c during which the drops are put in contact at a distance d_{min} (Figure 1.14c and d). Once the drops are in contact, we can investigate the adhesive properties at the interface by increasing the distance between the needles (Figure 1.14e). Resistance to the detachment and wrinkling of the interface are clues of the adhesion between the drops. To study the friction at the interface, we slide the needles horizontally against each other and look at the time needed by the drop on the top to relax to its initial vertical position (Figure 1.14f).

1.4.4 X-Ray tomography

X-Ray tomography, also known as CT scan, is an imaging technique which uses slices of the sample to reconstruct a 3D representation (tomograms) of the sample through the use of penetrating X-Rays. This technique allows to penetrate inside the sample, which makes it possible to image both the sample exterior and interior [28]. Here we give the principle of the technique, followed by the characteristic of the setup used during this thesis. We then detail the image treatment to obtain the 3D reconstruction of the sample.

Principle

The basic principle of the technique is the following: the sample is placed in between an X-Ray source and a detector (Figure 1.15a). Depending on the density of the sample, the X-Rays are more or less absorbed which results in spatial differences in the detected intensity, giving an image (called a projection) of the sample through its absorption for one angle (Figure 1.15b and c). The tomographic device gives radiographs of the sample for different rotation angles. These have to be treated in order to be analysed. Using the commercially available software Octopus, the background of the images is normalized (Figure 1.15d), and then reconstructed to obtain horizontal slices of the sample (Figure 1.15e). The data is then analysed using the software Avizo which provides access to informations on the objects inside the samples such as their volume, their diameter and their position (Figure 1.15f).

Lab setup

The X-Ray tomography experiments were performed at the Technische Üniversitat of Berlin, Germany, on the lab setup of Pr. Francisco García-Moreno.

The tomographic device was composed of a micro-focus 150 kV Hamamatsu X-ray source with tungsten target. The sample was mounted on a precision rotation stage from Huber Germany (one circle goniometer 408) synchronised with the recording software, providing a stack of images when rotating the sample by 360°. The geometrical magnification of the cone beam tomography setup is given by the ratio between the source-to-detector distance and the source-to-sample distance. The sample's radioscopic projections are recorded using a flat panel detector C7942 aldo from Hamamatsu (120 mm x 120 mm, 2240 x 2368 pixels, pixel size 50 µm). The spatial resolution in this configuration is therefore limited by the detector pixel size and a physical resolution of about 20 µm.

A 60 kV filament voltage and a 500 µA intensity were found to provide the best contrast and lowest noise in the reconstructed emulsions images at high spatial resolution for our experimental setup.

1.5 Mechanical and adhesive properties of the solid emulsions

In Part C of this manuscript, we study the mechanical and adhesive properties of solid emulsions. To do so, we used three different experiments: a probe-tack setup (Section 1.5.1), a JKR experiment (Section 1.5.2), and bulk rheology on solids (Section 1.5.3). Here, we detail the experimental protocols for each experiment.

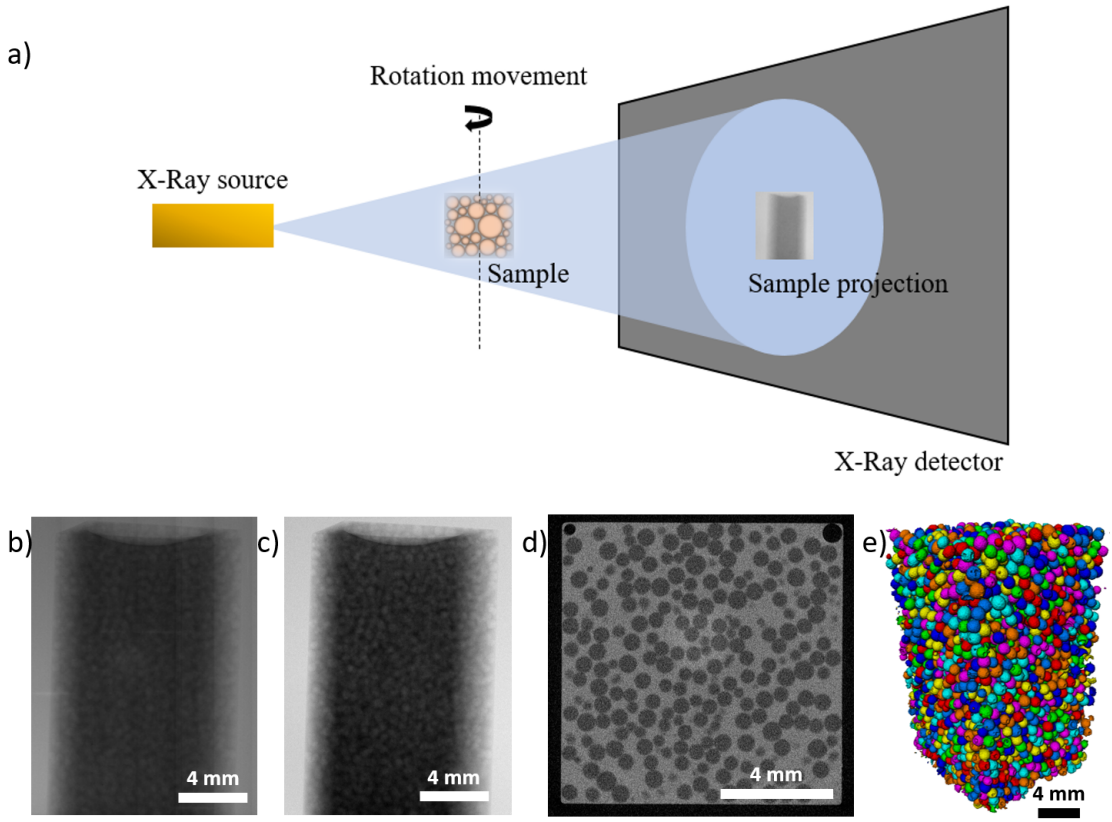

Figure 1.15: a) Scheme of an X-Ray tomography setup. b) Example of a radiograph of a solid PEG-in-Sylgard 184® sample for a 60 kV filament voltage and a 166 µA. c) Radiograph at the same rotation angle as in b) after background normalization using the software Octopus. d) Horizontal slice of the sample after sample reconstruction using the software Octopus. e) 3D rendering volume of the solid emulsion obtained by absorption contrast X-Ray tomography showing separated droplets marked by different colours after image processing.

1.5.1 The probe-tack test

To measure the adhesive properties of the solid emulsions, we measured the dissipated energy during a compression/decompression cycle in a probe-tack experiment. During a cycle, the sample (③) is approached towards a glass plate (④) with a constant speed v until the indentation d is achieved (Figure 1.16a). Then, the sample is retracted from the glass plate, still at the same speed v until the sample and the glass plate separate. We measure the force F with a force sensor (②) during the entire cycle. The traction machine used to measure the dissipated energy during a compression/decompression cycle between a glass plate and our samples is a Adamel-Lhomargy traction tester. It allows minimal displacement steps of 10 µm, with indenter speed from 0.01 mm/min up to 10 mm/min[9]. The machine is piloted via a *Labview* program made at the LPS by engineers in the instrumentation service. The cycles of compression/decompression were realised as shown in Figure 1.16b: the indenter approaches and retracts itself from the surface at a constant speed v. During the experiments, we investigated the impact of the indentation distance and the speed on the dissipated energy of each sample. We systematically indented the sample with values of $\delta = d - d_c$ (d_c being the distance of contact between the sample and the glass plate) allowing to stay in the linear regime of the mechanical response of the samples (cf Chapter 8 Section 8.1.1).

[9]the machine actually allows to move at higher speeds, but small experimental errors on the value of d were already observed at 10 mm/s.

In some cases, it is necessary to stop moving the indenter at the end of the compression phase, i.e. at the maximal deformation, to allow the system to relax. Figure 1.16c shows that in our case the force does not relax with time during this waiting phase for all the samples tested in this study. Taking this into account, we do not wait after the compression cycle in our experiments.

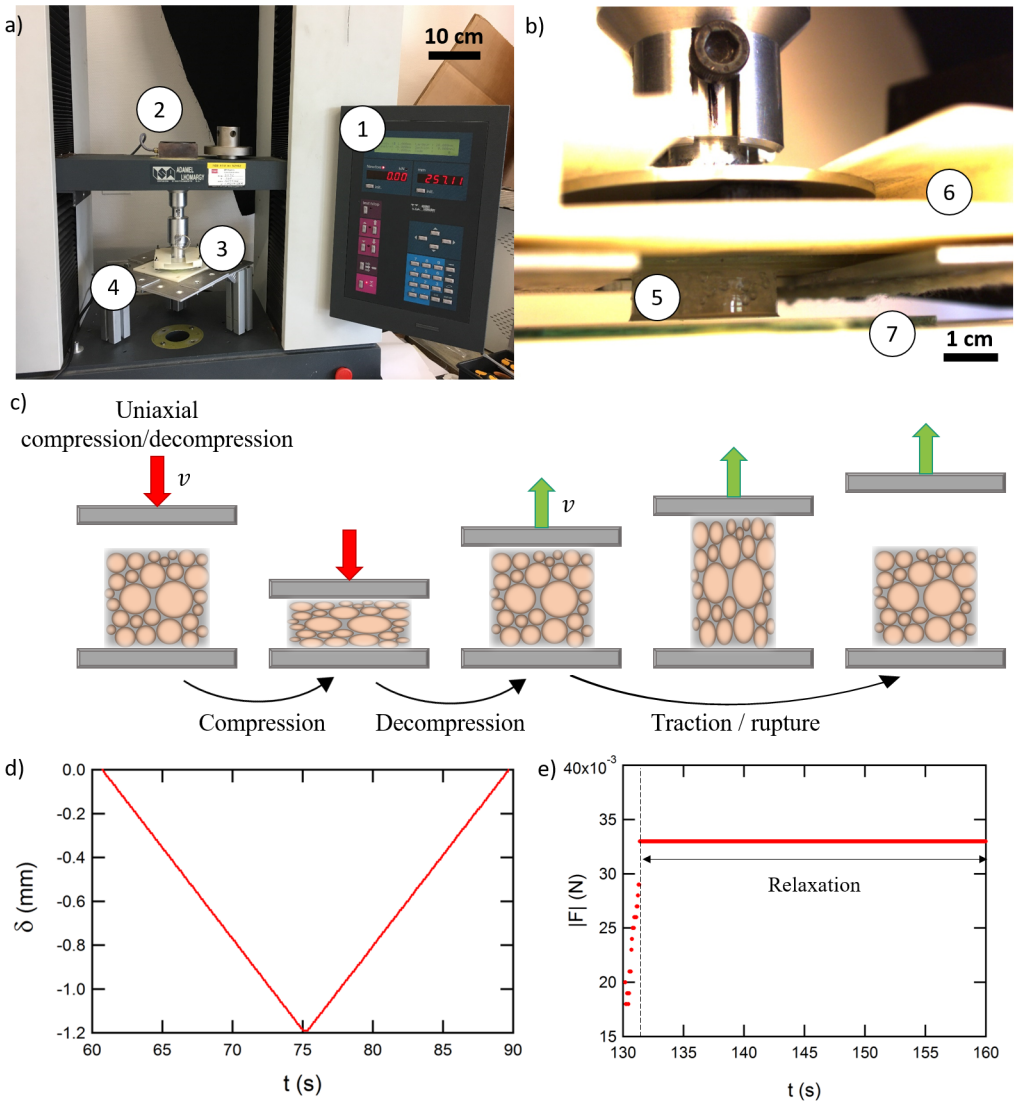

Figure 1.16: a) Photo of the probe-tack experiment: ① manual control of the Adamel machine, ② force sensor, ③ sample holder and ④ glass plate holder. b) Close-up photo of the sample in the probe-tack experiment: ⑤ sample (solid emulsion) glued to a microscope slide, ⑥ plastic sample holder closed with a metallic sheet and ⑦ glass plate attached to the glass plate holder. c) Scheme of a compression/decompression/traction cycle during a probe tack test on a solid emulsion. d) Evolution of the indentation δ with time during a compression/decompression/traction cycle. e) Relaxation of the force $|F|$ after compression of the sample by the indenter with time. (d) and e) are actual measures and the time is measured by the software, and serves here as an indication of the time-scales of the experiments, and do not relate with each other.)

The samples are glued to a glass microscope slide with Sylgard 184®, and inserted inside a plastic 3D printed home-made holder, himself made to be inserted on the machine holder. The glass plate is attached to a metallic support mounted on 3 screws to allow to adjust to parallelism between the glass plate and the surface of the sample.

Prior to any experiment, the surfaces of the solid emulsions were cleaned with isopropanol and then dried with argon to remove impurities. The glass plate was cleaned using toluene to remove any trace of

possible adsorbed PDMS chain, then dried with argon. All experiments are made at room temperature without control.

1.5.2 The JKR experiment

The JKR experiments are made on the same Adamel-Lhomargy traction tester, in which the sample is indented by a glass lens of radius of curvature $R_{lens} \ll R_{drops}$ (50.0 mm Dia.x 50.0 mm FL, Uncoated, Plano-Convex Lens purchased from Edmund Optics). The sample is approached towards the glass lens with a speed v while we measure the force F (with a 10 N force sensor) and the indentation d (Figure 1.17a). The cycles of compression/decompression were realised as shown in Figure 1.17b: 7 steps of indentation $d = 20$ µm at $v = 0.5$ mm/min followed by 15 s during which the system is allowed to relax, then 15 steps of indentation d = -10 µm at $v = 0.5$ mm/min followed by 180 s of relaxation. While the experiment is running, a camera takes images every 0.5 s which are used to measure the contact radius a (Figure 1.17a, and cf. Chapter 8 Section 8.1.3).

Prior to any experiment, the surfaces of the solid emulsions were cleaned with isopropanol and then dried with argon to remove impurities. The glass lens was cleaned using toluene to remove any trace of possible adsorbed PDMS chain, then dried with argon. All experiments are made at room temperature without control.

Image treatment

As detailed in Chapter 8 Section 8.1.3, the JKR experiments allows to obtain the values of the thermodynamical work of adhesion W and the energy release rate G out of $F = f(a)$ curves. It is then necessary to measure the contact radius a during the experiments and to associate it with its value of the force F. Figure 1.17c and d show photographs of a sample's surface before and after contact with the glass lens. As the contrast on these images is not optimal to measure the contact radius a, we substract c to d in order to obtain the image in Figure 1.17e. The contact radius a is then measured by fitting the surface of contact with an ellipse using *Image J*. Figure 1.17f shows the evolution of the force $F(t)$ with time during the relaxation phase of a step of the cycle (here a decompression step). We wait for the total relaxation, and extract the value of the force at equilibrium F_{eq}. The measure of F_{eq} and a are made at the exact same time during the experiment. This allows to obtain the curve $F = f(a)$ in Figure 1.17g, in this case for the bare Sylgard 184®.

1.5.3 Rheology of solids

To measure the storage $\mathcal{G}'$ and loss $\mathcal{G}''$ moduli of the solid emulsions, we use the MCR-302 rheometer commercialised by Anton-Paar in plane-plane configuration. To make sure that the samples do not move during the measurements, we start by applying uncrosslinked Sylgard 184® between the peltier plate and the bottom surface of the sample and the top surface of the surface and the geometry (Figure 1.18). The temperature is then increased to 70°C and kept at this value overnight thanks to the peltier plate to crosslink the small layer of Sylgard 184® in contact with the peltier plate and the geometry. Afterwards, the temperature is decreased to 25°C, the temperature at which all the experiments are made after waiting for the relaxation of the temperature for at least 2 hours.

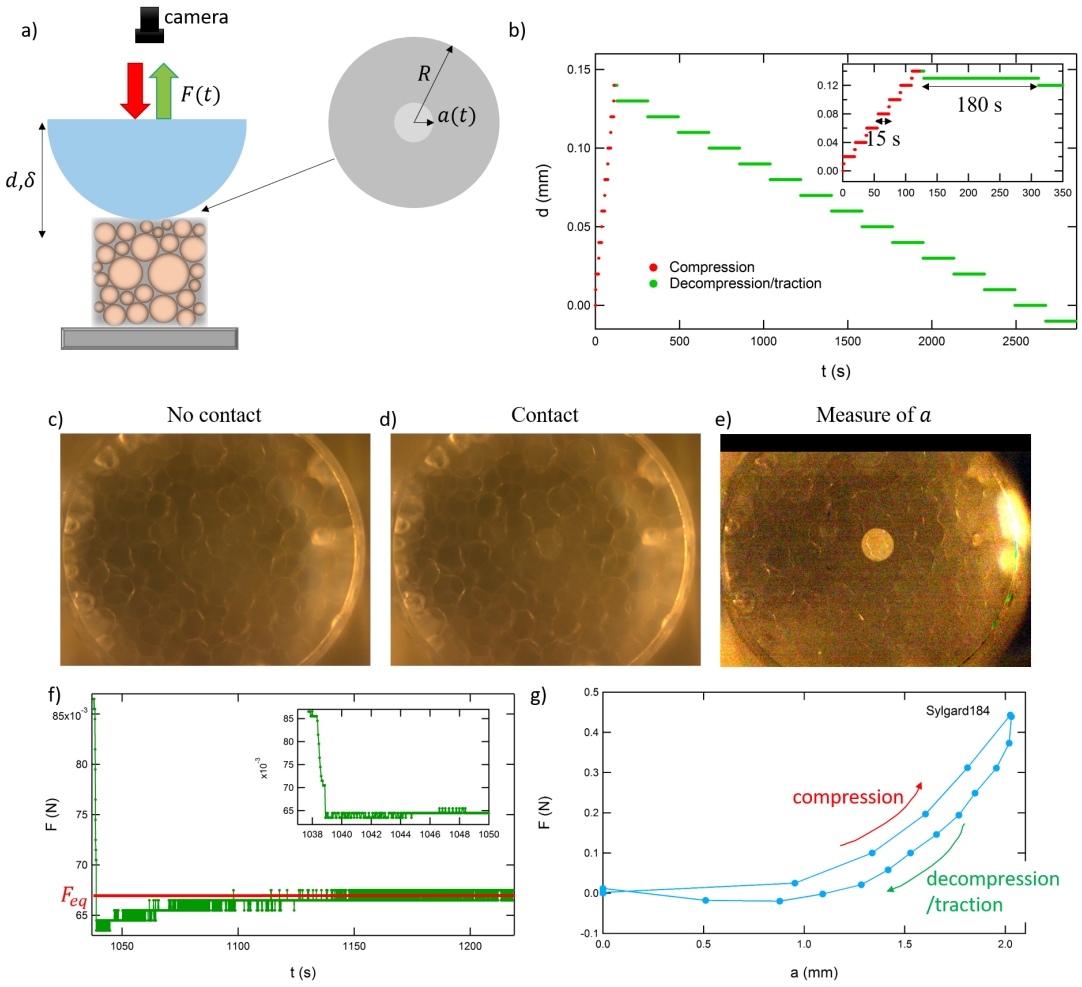

Figure 1.17: a) Scheme of the JKR experimental setup. b) Cycle of indentation d with time during the compression (red) and decompression/traction (green) cycle. The insert is a close-up on the compression phase. c) Photograph of the sample surface before contact with the glass lens. d) Photograph of the sample surface in contact with the glass lens after the system relaxation. e) Image obtained after substraction of a) from b) using *Image J* allowing to measure the contact radius a. f) Force F as a function of the time t during one step of the cycle in b which shows the relaxation of F over time and the value of F_{eq} used to construct the $F = f(a)$ curve in g).

G' and G'' are measured at frequencies w between 0.1 and 100 rad/s, and for different amplitudes γ (in %). The rheometer measures these parameters using the equations [29]:

$$\mathcal{G}' = \frac{2b}{\pi l^4 \Omega_0} \cdot C', \tag{1.21}$$

and

$$\mathcal{G}'' = \frac{2b}{\pi l^4 \Omega_0} \cdot C'', \tag{1.22}$$

where b is the distance between the peltier plate and the geometry, l the radius of the sample, Ω_0 is the angular speed, and C' and C'' the real and imaginary parts of the measured torque. In normal conditions of use of the rheometer, the sample radius and the geometry radius are equal (Figure 1.6a), therefore the rheometer is programmed to take l as the radius of the geometry. However, in our case, the radius of the samples is not equal to the diameter of the geometry (13 mm and 25 mm respectively),

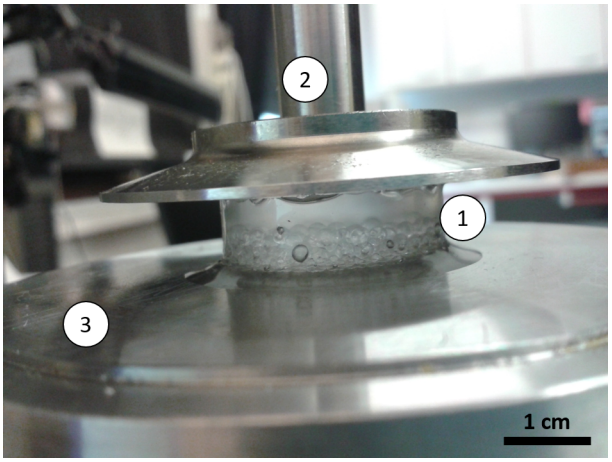

Figure 1.18: Photograph of a solid emulsion (①) attached with Sylgard 184® to the plane geometry (②) and the peltier plate of the rheometer (③).

so we need to adjust the measures of $\mathcal{G}'$ and $\mathcal{G}''$. To fix this issue, we apply systematically

$$\mathcal{G}'_{true} = \mathcal{G}'_{meas} \cdot \left(\frac{l_{geometry}}{l_{sample}}\right)^4, \tag{1.23}$$

and

$$\mathcal{G}''_{true} = \mathcal{G}''_{meas} \cdot \left(\frac{l_{geometry}}{l_{sample}}\right)^4. \tag{1.24}$$

Part A

Emulsion stabilisation: behaviour of reactive interfaces

Introduction of Part A

Emulsions are dispersions of two immiscible liquids, one being dispersed in the other. They are found daily in our environment: human-made such as the salad seasoning at our table or the moisturising cream in our bathroom, or even natural emulsions like the milk produced by mammals to feed their own infants. Applications can also include drugs encapsulations in the pharmaceutics industry, or the production of paints. The major problematic in all these cases is the emulsion stability. Indeed, most emulsions are naturally unstable and tend to separate into two phases through coalescence and coarsening phenomena, due to the energetic cost of the creation of an interface. The addition of surface active agents (surfactants) in the continuous phase was proven to be effective against destabilisation processes for emulsions composed of simple liquids such as water and oil [30–33].

Dispersions of polymers (called polymeric emulsions) also find a great deal of applications in the industry, and in this work, we are particularly interested in emulsions with silicone as the continuous phase. While questions on the emulsion stability have been investigated successfully for different types of polymers, only few advances have been made for materials with a silicone matrix such as PDMS (polydimethylsiloxane) [34–38]. This is due to the difficulty of finding sufficiently efficient stabilising agents for the liquid template which allow to obtain high volume fractions of the internal phase.

In order to tackle this problem, we combine a reactive blending [39–41] with a polyHIPE (High Internal Phase Emulsion) approach [42–47] using a model system which consists of two immiscible polymers: closely-packed PEG (polyethylene glycol) drops in a continuous phase of siloxane copolymer MHDS (MethylHydrosiloxane - Dimethylsiloxane Copolymers, Trimethylsiloxy terminated) with Si-H groups along the chain.

These drops are stabilised against coalescence thanks to a crosslinking reaction initiated by a mixture of a crosslinker and a catalyser which is initially dissolved in the PEG droplets. The diffusion of the crosslinker/catalyst molecules to the surface of the droplet creates a solid-like skin of silicone around the PEG drop when both liquids enter into contact. After proper optimisation of the formulation, the created PEG-in-MHDS emulsion is indefinitely stable and the size and organisation of the droplets can be adjusted at will before solidifying the continuous matrix by a second crosslinker/catalyser pair previously dissolved in the continuous phase.

In Chapter 1, we gave out necessary informations about the materials and methods used throughout the study. In this Part A, we first review in Chapter 2 the available literature on the interfacial properties of non-reactive and reactive interfaces, and the structure and stability of emulsions stabilized by a reactive approach. We then show the feasibility of the reactive approach to stabilise the silicone emulsions in Section 2.5 and we correlate the onset of the stability with the reactions occurring at the PEG/MHDS interface in Chapter 3.

Chapter 2

Interfacial tension of reactive, liquid interfaces and its consequences

Emulsions and polymer blends are dispersions of two immiscible liquids. In the case of emulsions, the liquids consist of low-molecular weight molecules, while in the case of a polymer blend, the two liquids are polymer melts which are often solidified after dispersion. Both, emulsions and polymer blends, find applications in number of industries in both liquid and solid state such as food, cosmetics, pharmaceutics, construction and plastics, thanks to their ability to combine the properties of both phases. In these biphasic systems, the morphology is a key parameter to understand and control the optical, rheological (in liquid/liquid state) and mechanical (in solid/liquid and solid/solid state) properties. However, the high interfacial tension between the liquids tends to separate the two phases, leading to coarse dispersions. This results in weak and anisotropic rheological and mechanical properties. Stabilisation of the emulsions or polymer blends is then of capital interest, and requires the addition of a third constituent in the dispersion, called compatibiliser or surface active agent (shortened as surfactant). This component, either a short molecule, a polymer, a protein, or a particle, is dispersed in one of the phases (usually the continuous one) and diffuses towards the interface. The stabilisation efficiency depends on the diffusion kinetics of the surfactant, on the visco-elastic properties of the surfactant monolayers created at the interface and on the interaction between the monolayers at the interface of two approaching dispersed drops.

There are two ways of adding surfactants to an emulsion or polymer blend. Either one can disperse the preformed surfactant in a separate step in one of the phases, or the surfactant can be created *in-situ* with a chemical reaction at the interface which starts as soon as the phases containing reactive molecules are in contact. Understanding and controlling the stabilisation mechanisms at the interface in both ways via analysis of the kinetics and equilibrium of adsorption/desorption/reaction processes is therefore of prime interest in order to control the properties of the dispersion.

A wide body of literature is available on the adsorption/desorption mechanisms and the stabilisation efficiency in blends and emulsions stabilised by pre-made surfactants [48–54], and on the applicability of the reactive compatibilisation [39,55–57]. However, even though reactive stabilisation is majoritarily used in industry for polymer blends for example, we could only find one review from 2002 dealing with the interfacial behaviour of reactive blends [58]. In that regard, this chapter is dedicated to provide new insights into the kinetics and equilibrium behaviour of interfacial tension at reactive interfaces, and to understand the implications on both the interface and the dispersion morphologies.

To do so, in Section 2.1 we first concentrate on the definition and behaviour of interfacial tension at non-reactive interfaces, in order to compare with its behaviour at interfaces where a chemical reaction occurs in Section 2.2. Finally, in Section 2.3 we review the impact of the reactive stabilisation by considering the stability of the dispersion, interfacial instabilities and drop size evolution.

2.1 Non-reactive interfaces

In order to be able to compare the non-reactive and reactive interfaces and to allow the reader to get a broad idea on both, we begin this chapter with a summary of the properties of the non-reactive interfaces. First, we briefly describe in Section 2.1.1 the interfacial tension, microscopically and thermodynamically, and the molecules used to stabilise interfaces called surfactants in Section 2.1.2. Then in Section 2.1.3 we will consider the effect of the surfactants on the interfacial tension both regarding kinetics and equilibrium. Finally, in Section 2.1.4, we discuss the stabilisation process of emulsions and polymer blends in light of these considerations.

2.1.1 Interfacial tension between fluids

Microscopic origin

In a liquid phase, molecules exert attractive forces on each other, such as Van der Walls forces or hydrogen bonding among others. These keep them close, in opposition to a gas phase. A molecule located in the bulk of an isotropic liquid interacts only with molecules that happen to be identical to it, meaning that the total force field exerted on each molecule is isotropic. In the case of a molecule at the interface with another liquid, a part of the attractive forces felt by the molecules are exerted by molecules of a different phase. Since interaction forces between molecules (Van der Walls forces, hydrogen bonding, polar interactions, etc.) are stronger between two identical molecules than between two different ones, the cohesive energy at the interface is weaker than in the bulk (Figure 2.1). The interfacial tension $\gamma_{A/B}$ at the interface between two phases A and B, equivalently expressed in mN/m or mJ/m^2, measures this energy shortfall per unit surface area. This implies that the stronger the interactions between two identical molecules, the higher the interfacial tension at the interface. For strongly cohesive liquids such as mercury, the interfacial tension against air is $\gamma_{mercury/air} \approx 500\,\text{mN/m}$ [59]. Low cohesive liquids like oils present interfacial tensions of $\gamma_{oil/air} \approx 20\,\text{mN/m}$. Water, because of hydrogen bonds between the molecules, has a higher interfacial tension against air $\gamma_{water/air} \approx 72\,\text{mN/m}$.

Thermodynamic definition

If it costs energy for a molecule to stay at the interface, it costs energy to create an interface. In a system composed of two phases α and β and an interface I, we can define the internal energy U as

$$U = U^\alpha + U^\beta + U^I, \tag{2.1}$$

where U^α and U^β are the internal energies of both homogeneous phases and U^I represents the excess internal energy arising from the presence of an interface, and can vary under transfer of mass in and

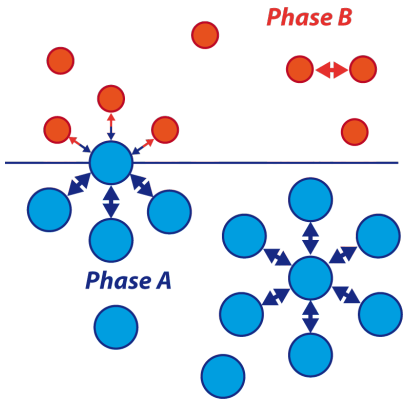

Figure 2.1: Scheme of an interface between two phases A and B showing the interactions between two A molecules, between two B molecules and between one A molecule and one B molecule.

out of the interface [60]. In this case, the change in internal energy is given by

$$dU = TdS - pdV + \gamma dA + \sum_i \mu_i dn_i, \tag{2.2}$$

where TdS is the heat transfer with T the temperature and S the entropy, PdV and γdA are the mechanical work which takes into account changes in the system volume V and the interfacial area A respectively, $\sum_i \mu_i dn_i$ is the chemical work with μ_i the chemical potential of the molecule i and n_i the number of moles of the species i. The chemical potential of the species i is defined as $\mu_i = kTln(a_i)$ with k the Boltzmann constant and a_i the activity of the molecule i.

From the internal energy we can define the Gibbs free energy $G = U + pV - TS + \sum_i \mu_i n_i$ which gives

$$dG = -SdT - Vdp - \gamma dA + \sum_i \mu_i dn_i. \tag{2.3}$$

At constant temperature T, pressure p and number of moles n_i, the interfacial tension γ is defined by

$$\gamma = \frac{\delta G}{\delta A}\Big|_{T,p,n_i} \tag{2.4}$$

and represents the increase of free energy δG that occurs when increasing the interface area by δA. In order to minimize its energy, the system will spontaneously minimize the interface area.

2.1.2 Surface active agents

When mixing two immiscible liquids, the energy required to create an interface is too high and the system spontaneously tends to a minimal area of contact i.e. demixing of the phases occurs. Surface active agents, usually called surfactants, present affinities for both phases in contact. They can be short molecules [32, 61, 62], usually hydrophobic carbon chains with a hydrophilic neutral or charged end, larger molecules such as proteins [33, 63] or copolymers where each polymer has a strong affinity for one of the phases [64–66]. Here, we will also take the particles into account in our definition of surfactants [67] due to the strong similarities of interfacial behaviour [68–71].

Their ambivalent affinities drive these agents towards the interface where they form an energy barrier against demixing of the two phases. This barrier is the result of interactions between two liquid

films in contact, also called disjoining pressure (steric and/or electrostatic repulsion) and the visco-elastic properties of the interface: when for example two oil drops in a solution of surfactants in water come close to one another, the presence of the surfactants at both interfaces in contact prevents coalescence [31, 72, 73].

2.1.3 Evolution of interfacial tension in the presence of surface active agents

Here, we will discuss only the case where the surfactants have a finite solubility in one of the two liquids only. As just mentioned, the primary role of surfactants is to stabilise an emulsion of two immiscible liquids. Their presence however also has an impact on the value of interfacial tension. Figure 2.2a shows a typical evolution of interfacial tension with time just after the creation of a fresh interface, in this example between heptane and an aqueous buffer solution for different bulk concentrations of ovalbumine [30]. The interfacial tension measured at $t = 0$ s is naturally the value measured between the two phases without any surfactants γ_0. It then decreases with different characteristic times τ depending on the type and concentration of the added surfactants, to finally reach an equilibrium value γ_{eq}. This overall relaxation behaviour is observed for all types of surfactants, and only the values of γ_0, τ and γ_{eq} vary between different systems. The shape of the relaxation curve depends on the type of surfactant and can be quite complex, for example, when energy barriers of adsorption are present or when the surfactant has a finite solubility in both phases.

Initially, when a fresh interface is created, the surface concentration Γ (in units/m^2) of surfactants is negligible. This creates a flux of surfactants from the bulk to first the subsurface and then the interface until an equilibrium between adsorption and desorption is reached (Figure 2.2). Depending on the surfactant used, two models are discussed in Section 2.1.3.

The first model is the so-called *diffusion controlled* model [74]. It makes the assumption that once the surfactant has diffused from the bulk to the subsurface it is directly adsorbed at the interface. The limiting time-scale is the diffusion time from the bulk to the subsurface.

The other model is the *mixed kinetic-diffusion* model. Here, an energetic barrier is assumed for the surfactant to go from the subsurface to the interface [75], which becomes the limiting phenomenon in the kinetics of absorption at the interface. It can be attributed to the fact that there are less and less vacant sites at the interface, making it more difficult for new surfactants to adsorb with time. This can also apply when dealing with large molecules that can cause steric repulsions or need to have the right orientation to absorb, and ionic surfactants that cause electrostatic repulsions.

The equilibrium value of interfacial tension, and the kinetic models both at the very beginning of the evolution of interfacial tension ($t \to 0$) and at the equilibrium phase ($t \to \infty$) can be analysed separately.

Equilibrium interfacial tension and CMC

At an interface composed of solvent molecules of both phases and a surfactant (assumed to have a high solubility in one phase and a low solubility in the other), the position of the interface is conveniently chosen so that $\Gamma_{solvent} = 0$. In the dilute solution approximation (when the activity a can be approximated by the bulk concentration of surfactant c, thus $d\mu$ can be approximated by $kTd\ln(c)$),

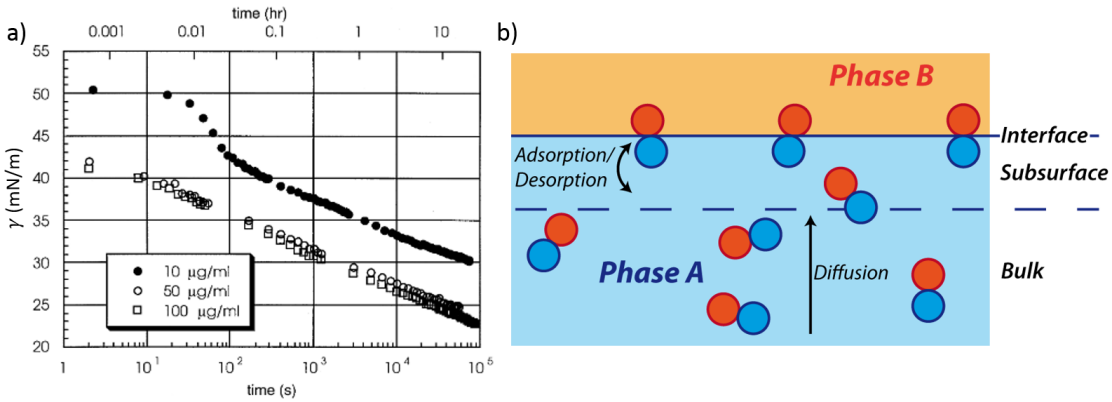

Figure 2.2: a) Dynamic interfacial tension of ovalbumin at the interface between heptane and an aqueous buffer (pH 7.1, 100 mM sodium phosphate) interface at different bulk concentration of ovalbumin (from [30]). b) Scheme of the differentiation between bulk, subsurface and interface.

the value of equilibrium interfacial tension γ is linked to the equilibrium surface excess of surfactants Γ by the Gibbs adsorption isotherm

$$\Gamma = -\frac{1}{mRT}\left(\frac{\delta\gamma}{\delta \ln c}\right)_{T,V,n_i}, \tag{2.5}$$

where R is the gas constant, and m depends on the nature of the surfactant. For non-ionic surfactants, $m = 1$ is in very good agreement with several experimental studies [76–81], as well as $m = 2$ for 1:1 ionic surfactants assuming electrical neutrality of the interface [82, 83]. For 2:1 surfactants[1], however, discrepancies in the experimental results motivated the use of an adjustable parameter α caused by ion impurities at the interface [83, 84], and led to $m = 2 - \alpha$.

Looking at the value of interfacial tension at equilibrium against the bulk concentration allows to obtain the *critical micellar concentration*, or CMC, which is the bulk concentration above which the surfactants start to create micelles in the bulk. For $c > CMC$, the equilibrium interfacial tension γ_{eq} will be independent of c. This is shown by $\gamma_{eq}(c)$ curves (Figure 2.3), where for $c < CMC$ the value of γ_{eq} decreases with c, and then reaches a plateau value. The CMC is defined by the crossover between the plateau and the decreasing curve.

The Gibbs isotherm is a way of measuring indirectly the equilibrium surface concentration of surfactants Γ_{eq} with varying c.

Kinetic description

Diffusion-controlled interfaces

A widely used mathematical model to describe the adsorption processes of surfactants at an interface where the limiting time-scale is controlled by diffusion is the model proposed by Ward and Tordai in 1946 [74]. This model takes into account the progressive filling of the interface by surfactants, meaning that it becomes more and more difficult for them to adsorb because of interactions with the already

[1] for 1:1 ionic surfactants, the charged group of the surfactant and the counterion have opposite charges (± 1), where for 2:1 ionic surfactants the hydrophilic group and the counterion have charges of ± 2 and ∓ 1, i.e. the global molecule is non neutral.

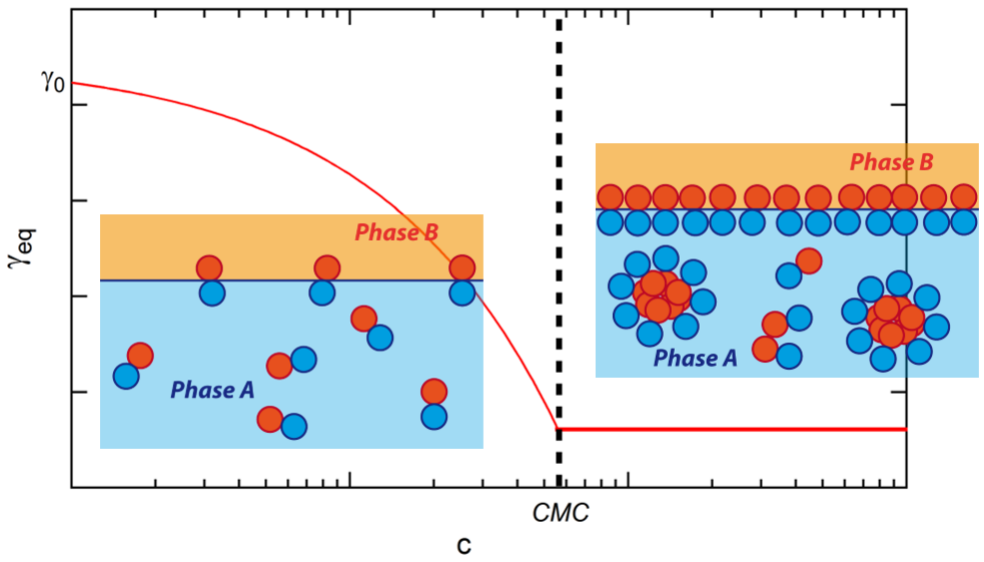

Figure 2.3: Scheme of a generic evolution of the equilibrium interfacial tension γ_{eq} against the bulk concentration of surfactants c.

adsorbed surfactants, and consequently allows back diffusion, i.e. desorption from the interface. This equation however cannot be solved analytically, which is why Miller, Fainerman and Makievski [85] derived asymptotic solutions to this equation to describe the kinetics of the interfacial tension decay. These solutions look at the behaviour of the interfacial tension at $t \to 0$ and $t \to \infty$. Here, we assume for simplicity that the surfactant is insoluble in one of the phases.

Initially, there are almost no surfactants at the interface (i.e. $\gamma \to \gamma_0$), so they will not desorb from the interface. This, in the case of an ideal surface layer, gives:

$$\gamma_{t\to 0} = \gamma_0 - 2nRTc\sqrt{\frac{Dt}{\pi}}, \tag{2.6}$$

where D is the diffusion coefficient of the surfactant in the phase it is dissolved in.

When $t \to \infty$, the subsurface concentration tends to the bulk concentration and allows, along with the Gibbs equation, to get:

$$\gamma_{t\to\infty} = \gamma_{eq} + nRTc\sqrt{\frac{\pi}{Dt}}. \tag{2.7}$$

This diffusion-controlled model generally works very well for $t \to 0$ and at low initial concentration c_0 as shown in Figure 2.4 for the surfactant $C_{10}E_4$ in water [50].

Mixed kinetic-diffusion controlled adsorption

Equation (2.7) on the other hand was shown to be ineffective to capture the behaviour of the interfacial tension at longer times by several experimental studies [80, 86–90]. The solution to this problem was theoretically implemented by Barret *et al.* [91] and Liggieri *et al.* [92, 93] and is called the mixed kinetic-diffusion controlled adsorption.

This model relies on the assumption that once a surfactant has diffused from the bulk to the subsurface, it may not instantly adsorb at the interface, for different possible reasons, mainly related to steric or

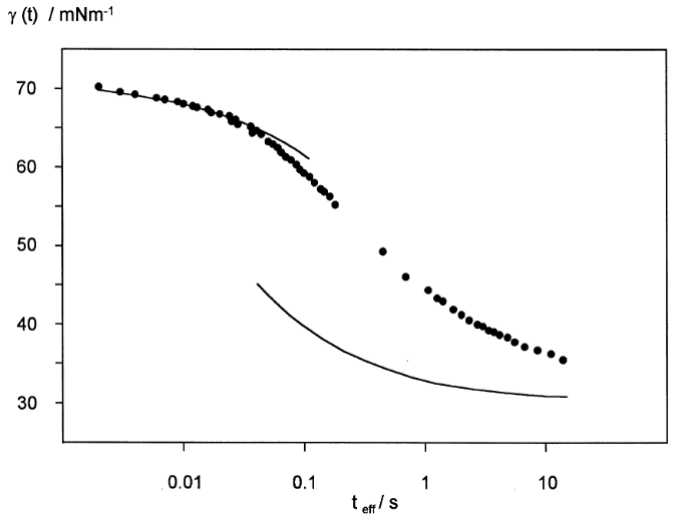

Figure 2.4: Lin-log representation of the interfacial tension γ as a function of time for the surfactant $C_{10}E_4$ in water. The solid lines are calculations using Equations (2.6) and (2.7) at long and short time respectively. From [50].

electrostatic repulsions and need of the right orientation (in the case of long chain molecules i.e. proteins and polymers) [94–98]. All of this can be understood as the existence of an activation energy ϵ_a that the surfactant has to overcome to itself go from the subsurface to the interface. It induces a renormalized diffusion coefficient

$$D^* = D\exp(-\epsilon_a/RT), \tag{2.8}$$

theoretically predicted [91–93], and confirmed experimentally [80, 86–90]. By using D^*, it is possible to consider this a diffusion problem again and to change the Ward and Tordai equation accordingly. Most systems are well described by the simple diffusion model at short times and switch to the mixed kinetic-diffusion model with increasing time, even for $c < CMC$.

2.1.4 Application to stabilisation processes

Surfactants are used in the making of emulsions and polymer blends to stabilise them against coalescence (rupture of the film between two drops) and Ostwald ripening (diffusion of molecules from small to large drops). The diffusion time τ from the bulk towards the interface and its dependence on the surfactant size, and desorption from the interface then have important consequences on the stability of the dispersion.

When dealing with phases with low viscosities and low molecular weight surfactants, this stabilisation process proves to be efficient [49,99–102], thanks to the fact that small surfactants can easily diffuse in a low-viscosity medium. In these conditions, the surfactant will rapidly go from the bulk to the interface to stabilise the emulsion. The life-time of the emulsions and blends depends on the surfactants ability to create repulsive interactions against one another upon the approach of two interfaces (disjoining pressure) [103], and on the visco-elastic properties which they confer to the interface [104].

Heterogeneous polymer blends, which are dispersions of two immiscible polymer melts [39], are more difficult to stabilise than the cases discussed above for several reasons. As mentioned before, surfactants come under different configurations, from small amphiphilic molecules (neutral or ionic), to large

molecules such as proteins and polymers. If emulsions of two simple liquids can be stabilised with any of those, in the case of complex liquids such as polymer-polymer interfaces, it is more efficient to use surfactants in the form of block or graft copolymers. These are composed of segments that present complementary affinities towards the two phases of the blend [105–111], to mimic the amphiphilic nature of low molecular weight surfactants. Of course these molecules are large, and as a result they diffuse slowly which causes slow adsorption kinetics at the interface. This, associated to the fact that the CMC is easily exceeded with large molecules, results in poor stabilisation of the polymer blend [16, 39].

Another drawback of the use of surfactants in the stabilisation process is the possible presence of micelles in the phase they were first added for any concentration c below or above the CMC, especially in the case of block-copolymers. If the lifetime of the micelle is longer than the time for the interface to reach equilibrium, i.e. if the thermodynamic barrier of breaking a micelle is high, then less molecules adsorb at the interface and participate to the stabilisation process [50].

To avoid the problems caused by the use of pre-made surfactants, reactive compatibilisation, which consists in provoking a chemical reaction at the interface only that creates a surfactant in-situ, has been largely used in immiscible polymer blending [55, 57, 112–122].

2.2 Evolution of interfacial tension at reactive interfaces

The stabilisation of immiscible liquid dispersions is a subject of great interest in commercial applications. The use of pre-made surfactants to stabilise the drops has proven not to be effective enough for viscous systems because of slow adsorption kinetics and poor adhesion at the interface. Indeed, in order to stabilise efficiently the drops in a dispersion and since the dynamics of adsorption are so slow and impaired by the creation of micelles, the block-copolymers need to be irreversibly adsorbed at the interface. This is possible only if they are insoluble in either phase, because of their size for example, which means that they cannot be initially dispersed in one of the phases. As, if they cannot be dispersed, they cannot adsorb to the interface, reactive compatibilisation of immiscible dispersions is used, i.e. the stabilising agent is created in-situ, at the interface. While this approach has mostly been developed for polymer blends, it is now increasingly used for emulsions.

Here, in Section 2.2.1 we summarize the principal methods of compatibilizing polymer blends and emulsions by a chemical reaction. Then we study in Section 2.2.2 the equilibrium of interfacial tension at reactive interfaces and try a comparison with the non-reactive case studied previously in Section 2.1.3. Finally, in Section 2.2.3 we focus on the kinetics of evolution of interfacial tension and surface concentration in reactive systems.

2.2.1 Methods of reactive compatibilisation

Compatibilisation of interfaces by a chemical reaction occurs by functionalizing the molecules of the different phases with complementary functional groups (Figure 2.5) [112–116, 119, 123], sometimes with the help of a precursor [117, 118, 120–122]. As soon as the two liquids are in contact, the chemical reaction starts and so does the stabilisation. As functionalised molecules are much more expensive

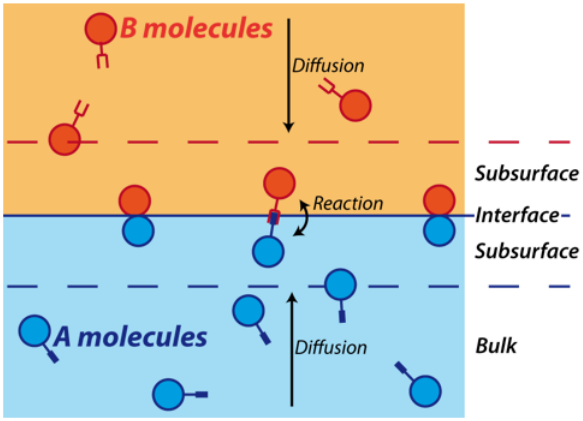

Figure 2.5: Scheme of a reactive interface between two phases A and B containing reactive molecules, with respective concentrations c_A and c_B.

than not functionalised one, usually only a certain percentage of reactive molecules is added in each phase. The percentage needed to stabilise the blends depends on the size of the molecules, and the reaction kinetics.

These methods of reactive compatibilisation are to be adapted to the two polymers used in the blends. If the methods of reaction differ, the result is the same for all of them once the protocol is optimized: the blend is stabilised against demixing.

Depending on the reaction occurring at the interface, different molecules can be created at the interface. In most cases [112–123], the reaction creates in-situ block or graft copolymers which act as surfactants at the interface.

2.2.2 Equilibrium interfacial tension

Experiments show that the relaxation of the interfacial tension of reactive interfaces exhibits a strikingly similar behaviour to that of non-reactive interfaces [122–127]. All curves start at a value γ_0, which is the value of interfacial tension between the two non-reactive phases with no added surfactants. The surface tension γ then decreases with a characteristic relaxation time that depends on the bulk concentration of reactive polymers until it reaches an equilibrium value γ_{eq}. Can we then compare the behaviour of reactive and non-reactive interfaces? To answer this question, we will look first at the effect of the copolymer configuration at the interface, and then try to determine if the Gibbs equation (Equation (2.5) Section 2.1.3), used for non-reactive systems, is also applicable in the case of in-situ formed surfactants.

Comparing the properties for different pairs of immiscible polymers stabilised by either pre-made copolymers or in-situ formed copolymers shows that the equilibrium interfacial values are identical with both stabilisation routes. For example, Wagner *et al.* [128] measured the interfacial tension between PDMS and PEG with pre-made PDMS-PEG-PDMS and found equilibrium values close to the ones which Giustiniani *et al.* [122] found for PDMS and PEG stabilised by in-situ compatibilisation (Figure 2.6). As the configuration of the copolymers, in addition to their chemical composition, has an impact on the equilibrium value of interfacial tension γ_{eq} [127, 129, 130], the comparisons between the reactive and non-reactive cases is not straightforward. Indeed, while in non-reactive systems,

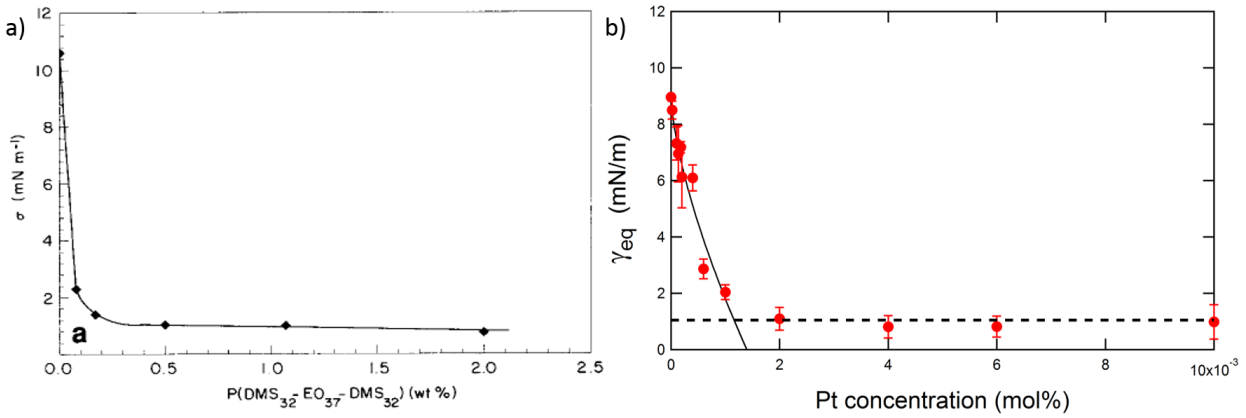

Figure 2.6: a) Interfacial tension (in mN/m) between PEO 35 (M_n = 32000 g/mol) and PDMS 100 (M_w = 177000 g/mol) for different concentrations of pre-made P(DMS$_3$2-EO$_3$7-DMS$_3$2) copolymers (in wt%) in the PEO phase (from [128]). b) Interfacial tension between PEG 400 (M_w = 400 g/mol) and reactive PDMS (M_w = 2000 g/mol) for different concentrations in platinum Pt (in mol%) in the PEG phase which allows the reaction between the PEG and the reactive PDMS (adapted from [122]).

the control over the chemical architecture of the surfactant is clear, in reactive systems the obtained molecules can have several reactive groups in their architecture which leads to more polydispersity in the surfactants at the interface. This also has consequences on the stabilisation efficiency and the adhesion between the phases after solidification [131, 132].

For non-reactive interfaces, the Gibbs adsorption isotherm (Equation (2.5) Section 2.1.3) links the interfacial tension to the surface coverage of surfactants. The principal hypothesis that allows to derive the Gibbs equation as it is given in Section 2.1 is the insignificance of the variation of the solvent's chemical potential. In the case of small surfactants in water for example, the Gibbs-Duhem equation gives $X_{water} d\mu_{water} = -X_{surf} d\mu_{surf}$ where X is the molar fraction and μ the chemical potential of the water and the surfactants. This implies that $d\mu_{water} \ll d\mu_{surf}$. Added to the fact that the solution has to be considered dilute, the Gibbs equation stands. To analyse their measures of surface tension relaxation at a reactive interface, Chi *et al.* also used the Gibbs equation [123]. They obtained access to the equilibrium surface concentration Γ^{∞} , and proved the Volmer model of adsorption kinetics[2] [133] to be effective in capturing the γ-Γ curve. They state that their analysis relies on the fact that less than 3% of the initially added reactants are used in the process, so the bulk concentration of reactant at equilibrium is approximately equal to its initial value.

In most cases, the surface concentration of copolymers Γ has been shown to be measurable directly and independently of the interfacial tension γ, either by XPS analysis of the interface [124, 134–138], gel permeation chromatography (GPC) [139] or dynamic secondary ion mass spectrometry (DSIMS) with a deuterium labelled reactant [140]. The interfacial tension is measured by the pendant drop method [122, 123] or the Neumann triangle method [126, 141].

The overall relaxation and equilibrium value of interfacial tension in reactive systems is comparable to non-reactive systems stabilised with pre-made surfactants. The same adsorption isotherms seem to be applicable to reactive systems only in specific conditions, namely large excess of reactants.

[2]The volmer model derives from the Gibbs equation and accounts for the non-ideal non-localised adsorption at the interface and the finite size of the surfactant molecules.

2.2.3 Kinetics of evolution of interfacial tension

In order to form in-situ surfactants at the interface, the reactive molecules in both phases in contact have the same kinetic limitations as pre-made surfactants, namely diffusion towards the interface, and existence of an energetic barrier due to steric or electrostatic repulsions. The latter can be reduced to a diffusion limited problem with an exponentially decreasing diffusion coefficient, as stated in Section 2.1.3. But in reactive systems, to these energy barriers has to be added the kinetic of the reaction itself, which requires of each reactive molecule to i) find a reaction partner and ii) react with it. In the presence of a reaction at the interface, the kinetics of the evolution of the surface concentration of surfactants Γ follows the rate equation [142]

$$\frac{d\Gamma}{dt} = k\rho_A(t)\rho_B(t), \tag{2.9}$$

where k is the reaction coefficient, and ρ_A and ρ_B the number density of reactive chains A and B in the vicinity of the interface. The densities ρ_A and ρ_B vary with time according to diffusion and reaction at the interface. We call τ_d and τ_r the characteristic diffusion and reaction times respectively. If $\tau_r \ll \tau_d$, i.e. the reaction takes place instantly, then the only limiting factor is the diffusion of the reactive molecules towards the interface linked with the probability of meeting a reaction partner. If, on the contrary, the reaction is slow compared to the diffusion, $\tau_r \gg \tau_d$, then the reaction is the limiting factor of the evolution of interfacial tension.

Diffusion-controlled interfaces

The simplest case here is when $\tau_r \ll \tau_d$ and the system is diffusion-limited. Assuming for simplicity that the initial concentrations of reactive chains A and B in each phase is low and equal for both A and B ($\rho_0 = \rho_A = \rho_B$), and that A and B have the same degree of polymerization($N = N_A = N_B$), Fredrickson and Milner [142] showed that the kinetics of the creation of copolymers at the interface exhibits three regimes, with different associated characteristic times (Figure 2.7). They define the times τ_ρ as the characteristic time for the number density of reactive ends ρ in the interfacial region to decay, and τ_Γ as the characteristic time of the evolution of copolymer coverage of the interface. They give the relations

$$\tau_\rho = \tau\frac{\ln^2 N}{(\rho_0 R^3)^2} \qquad \text{and} \qquad \tau_\Gamma = \frac{(\Gamma^*)^2}{D_0\rho_0^2}, \tag{2.10}$$

with τ the disentanglement time, also called the terminal relaxation time, Γ^* the copolymer coverage of the interface at which the chemical potential barrier is of order k_BT (with k_B the Boltzmann constant), and D_0 the center-of-mass diffusion coefficient of a reactive chain in the bulk. When $N < N_e$, N_e being the entanglement threshold, $\tau \sim N^2$ is the Rouse time. For entangled chains ($N > N_e$), $\tau \sim N^3$ is the reptation time.

In the short time regime ($0 < t < \tau_\rho$), there are already reactive chains at the interface, so the kinetic of evolution of Γ is determined by the reaction rate and the number densities ρ_A and ρ_B are approximately constants. Equation (2.9) becomes

$$\frac{d\Gamma}{dt} \approx k' \qquad \text{which gives} \qquad \Gamma \sim t \qquad \text{for} \quad t < \tau_\rho. \tag{2.11}$$

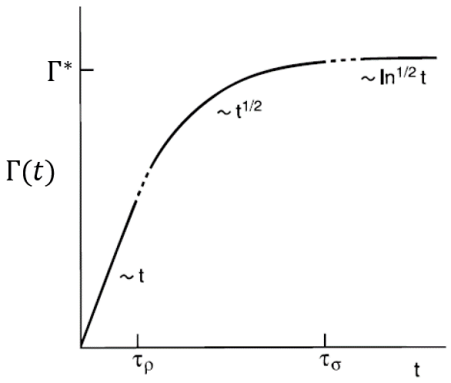

Figure 2.7: Qualitative summary of the time-dependent growth of copolymer coverage (number of di-blocks/area of interface) $\Gamma(t)$ for the case of an initially dilute concentration of reactive chains in the two bulk phases. From [142].

If the reaction is fast enough, the densities ρ_A and ρ_B start to dramatically decrease for $t \sim \tau_\rho$, and a depletion hole is created near the interface. The copolymer coverage of the interface is, in this intermediate regime ($\tau_\rho < t < \tau_\Gamma$), diffusion controlled, and the evolution of surface concentration is

$$\Gamma \sim t^{1/2} \qquad \text{for} \quad \tau_\rho < t < \tau_\Gamma. \tag{2.12}$$

When $t > \tau_\Gamma$, the copolymer coverage saturates starting from a value of the order $\Gamma^* \sim b^{-2}N^{-1/2}$ where b is the statistical segment length. Looking at the evolution of Γ during this final regime gives out

$$\Gamma \sim (\ln t)^{1/2} \qquad \text{for} \quad t > \tau_\Gamma. \tag{2.13}$$

It is worth paying special attention here to the different assumptions of this theory. First, the reactive polymers are assumed to have the same size. Yet, experimental studies often involve reactions between two polymers of different sizes, which implies different mobilities for each species and lead to qualitative changes in the results. Also, this study assumes very low initial concentrations of reactive species in both phases. Monte Carlo simulations carried out by Müller [143] showed that this theory for diffusion-controlled reactions at interfaces given by Fredrickson and Milner was indeed verified only for very low initial concentrations in reactive species. But most importantly, here it is assumed that the chemical reaction is fast. However, this is not the case in most reactive blending processes, as pointed out by O'Shaughnessy and Vavylonis [144]. This could explain why it is difficult to find experimental studies in agreement with the diffusion-controlled theory. Schulze *et al.* [145] compared their experimental results with the diffusion-limited theory of Fredrickson and Milner but found no agreement.

Reaction-limited systems

By comparing the estimated diffusion times of the reactive molecules in the bulk, from their size and the viscosity of the medium they are in, to the characteristic time of evolution of interfacial tension found experimentally, one can already have an idea of the kinetics of the reaction. For a system of PDMS-NH_2 in PDMS, with molecular weights ranging from M_n = 27000 to 62700 g/mol, and by considering that only the PDMS-NH_2 in a layer of thickness h actually play a role in the reactive

stabilisation, Chi *et al.* [123] found a range of diffusion times from 20 s for the lowest concentration of reactive PDMS to 1.6 s for the highest concentration. Since the characteristic time of evolution of interfacial tension for their system is at minimum of the order of 2-5 min, they concluded that the system was reaction-limited. In that case, $\tau_r \gg \tau_d$ and the evolution of interfacial tension cannot be described as a diffusion problem with a varying coefficient of diffusion as for non-reactive interfaces. The evolution of interfacial tension depends on the reaction kinetics, which depends on the rate of the reaction taking place at the interface i.e. on the reactivity of the functional groups [146].

Different approaches have emerged concerning the kinetics of evolution of interfacial tension of reaction-controlled systems. O'Shaughnessy and Vavylonis [144] state, using a mean-field theory approach, that for small reactivities between the functional molecules A and B, at short time scales and for a flat interface, the concentrations of reactive molecules close to the interface is constant, as in the short time scales regimes for diffusion-controlled reactions, meaning that equation (2.11) stands and $\Gamma \sim t$. They explain that if both initial concentrations $c_{A,0}$ and $c_{B,0}$ are approximately equal, this persists until the surface is crowded by A-B copolymers, but assuming that $c_{B,0} < c_{A,0}$, a depletion of B in the vicinity of the interfaces forces a crossover to a first-order diffusion-controlled kinetics. Berezkin *et al.* [147] used this theory at a flat interface to study the kinetic behaviour at a curved interface (drop) using dissipative particle dynamics modelisations, and showed that due to the curvature the size ratio between A and B played a crucial role in the surface coverage, though the same kinetic laws still applied.

Oyama *et al.* [134] applied a general treatment, commonly used in surface science for reactions at the gas/solid interface, to a liquid/liquid interface, and compared their finding with both their own experiments and experiments of other groups. The comparison with a gas/solid interface implies that the reaction rate is proportional to the number of vacant reactive sites at the interface. As both Fredrickson and Milner [142] and O'Shaughnessy and Vavylonis [144], they state that the limiting factor can either be the saturation of the interface (at a surface concentration Γ^*), or the depletion of either A or B. They take into account different considerations concerning the initial concentrations of A and B which lead to a change in the reaction kinetics. Assuming that there is no reverse reaction, that the formed interface is flat and two-dimensional between the polymers and that the copolymers formed at the interface cannot desorb, they give the rate equation for an interfacial reaction within a limited sub-surface

$$\frac{d\Gamma}{dt} = k(c_A - \Gamma)(c_B - \Gamma)(\Gamma^\infty - \Gamma), \tag{2.14}$$

where k is the reaction constant, c_A and c_B the number of molecules A and B respectively per area of sub-surface at time t (within the distances $\sqrt{2D_{A,B}t_\infty}$), and t_∞ is the reaction time needed to reach the final surfactant concentration at the interface Γ^∞. In this equation, $(\Gamma^\infty - \Gamma)$ represents the number of available reaction sites at time t. Two cases seem to be the most useful for interface stabilisation, and they assume in both that A is always in excess ($c_A \gg \Gamma$ at all t).

They show that, if B is also in excess, the reaction goes on until the interface is saturated and $\Gamma^\infty = \Gamma^*$, where Γ^* is the concentration of surfactants when the interface is saturated. In that case, $c_B \gg \Gamma$ at all t and the rate equation becomes

$$\frac{d\Gamma}{dt} = kc_{A,0}c_{B,0}(\Gamma^\infty - \Gamma(t)). \tag{2.15}$$

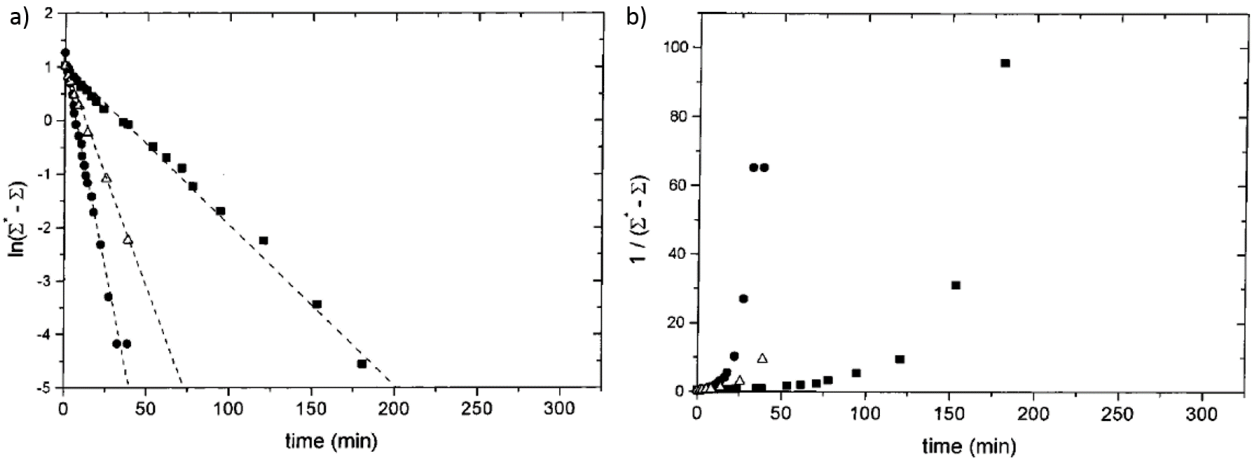

Figure 2.8: Reaction at the interface between SMA (styrene-maleic anhydride copolymer) and ATBA (amine terminated butadiene-acrylo-nitrile copolymer) (data from [148], analysis from [134]). a) First-order plot. b) Second-order plot. ■ reaction at 140 °C, △ reaction at 150 °C, • reaction at 160 °C.

The reaction is of order[3] 1 and its solutions are in the form of $\exp(-t)$. The addition of the term $-k_r\Gamma(t)$ in the equation allows to take into account the reverse reaction, k_r being its reaction constant [123]. The solutions in that case are in the same form but the pre-factors change.

If B is not in excess, then the reaction stops when there is a depletion of B in the vicinity of the interface, and $\Gamma^\infty < \Gamma^*$. In that case, the rate equation becomes:

$$\frac{d\Gamma}{dt} = kc_{A,0}(\Gamma^\infty - \Gamma(t)). \tag{2.16}$$

Here also, the reaction is of order 1, and the solutions are in the form of $\exp(-t)$.

Both these equations give access to the reaction constant k through the slope of the curve at short times $\frac{d\Gamma}{dt}(t \to 0) = kc_{A,0}c_{B_0}\Gamma_\infty$ or $\frac{d\Gamma}{dt}(t \to 0) = kc_{A,0}\Gamma_\infty$.

Experimentally, the first order dynamics has been confirmed for different systems. Oyama *et al.* [134] analysed the data of Scott *et al.* [148] trying both a first and second-order dynamics (where $1/(\Gamma_{eq} - \Gamma) \sim t$) which showed that only the first-order was in agreement with the experiments (Figure 2.8). They also confronted their theory to the one of Kramer [149] who assumed a reaction-controlled dynamics but with a reaction of order 2 and showed that the first-order dynamics fitted better the data. Kim *et al.* [150] compared their experimental data of the kinetics of evolution of the viscosity of the blend with fits of the first and second-order kinetics equations, and observed that both equations could fit their data in the initial stage, but only the first-order was capable of capturing the evolution throughout the entire data set. Chi *et al.* [123] observed a very good agreement of the first-order kinetic for small reactant concentrations at all times, but showed that for higher concentrations, the model of Oyama *et al.* [134] only captured the initial growth of the surface concentration. They attributed this to chain-chain interactions becoming progressively rate limiting as the interface approaches saturation. Jiao *et al.* [151] were able to fit the curve of surface copolymer coverage against time between functionalised polystyrene and poly(styrene-r-maleic anhydride) by a function of the form $\Gamma \sim (1 - \exp(-t/\tau))$ for the entire time-scale of the experiment, in agreement with the theory developed above.

[3]The order of a reaction is defined as the exponent to which its concentration term in the rate equation is raised.

Jeon *et al.* [139] showed that the functional group location along a polymer chain has a strong impact on the coupling reaction. Due to steric effects, a bulk reaction with end-functionalised polymers is sensibly faster than with mid-functionalised polymers. This effect is enhanced at the interface.

The kinetic behaviour of reactive liquid/liquid interfaces seems more complicated to analyse than their equilibrium behaviour. Indeed, the balance between the reaction time between the pair of functionalised molecules, and their diffusion time is a key parameter in order to know whether to apply the diffusion-limited or the reaction-limited model. This ratio depends on the reactivity of the pair, their respective sizes, but also on their concentrations in each phase. Despite the apparent complexity of the matter, theoretical approaches on both regimes, using simplistic approximations such as flat and two-dimensional interfaces, prove to be efficient for a large number of experimental studies using different reactive pairs. However, these theories are always treated for interfaces under quiescent conditions, which is not the case during emulsion or blend generation by turbulent mixing. Zhang *et al.* [152] showed experimentally that the presence of an external flow accelerates interfacial reactions. Song *et al.* [153] also showed an acceleration of the reaction under a compressive flow, and state that this explains the remarkable ability of co-extrusive processes to build multilayer products with little residence times. These more realistic experimental conditions are still missing in the theories of kinetic evolution of copolymer coverage of the interface.

2.3 Consequences of the reactive stabilisation

Reactive compatibilisation of liquid dispersions is mostly used industrially because of its ability to stabilise efficiently liquid dispersions and because of the cost reduction it implies compared to the stabilisation route with pre-made surfactants, since the production of tailor-made copolymers for a particular dispersion can be very expensive. However it is also worth taking an interest in the impact of the reactive stabilisation route on several parameters such as the stability and the morphology of the dispersion, and the shape of the interface through the apparition of instabilities. In this section, we review these different repercussions.

2.3.1 Dispersion morphology: influence on the drop sizes

There are several ways to mix the phases in an emulsion or a polymer blend. In order to be selective on the drop size and the role of each phase (either dispersed or continuous), one can generate the drops using microfluidic techniques or simple dripping of the dispersed phase in the continuous phase. For industrial processes however, these techniques do not allow a rapid and quantitative production, and it is then preferred to use turbulent mixing and twin-screw extrusion. These methods are based on the ability of one of the phases to deform under shear until breakup occurs to form droplets. The final drop size distribution depends in this case on both external parameters such as the temperature, the shear rate and the duration of mixing or extrusion time (though an equilibrium is rapidly achieved [65]), and on the fluids properties like the rheological properties of the two fluids, the interfacial tension between the two phases, and the compatibilizing agent [17]. In this section, we focus only on the influence of the compatibilisation process on the final drop size distribution of the polymer blend or emulsion, which is also influenced by the interfacial tension.

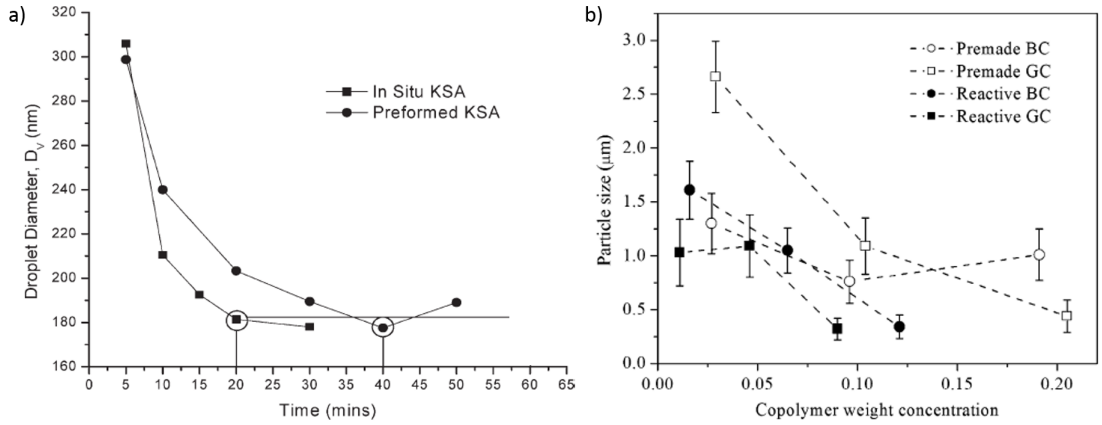

Figure 2.9: a) Droplet size evolutions for methyl methacrylate (non organic phase) droplets in an aqueous solution of butyl acrylate prepared with a rotor/stator (3 000 rpm) using equal amounts (9.0 mmol) of preformed potassium stearate (KSA) or in situ KSA (◯ minimum droplet size) (adapted from [154]). b) Particle size changes with copolymer concentration for all the compatibilised PMMA/PS blends. The terms BC and GC refer to respectively block and graft copolymers. The error bars are one standard deviations (from [155]).

During mixing, breakup of the dispersed phase occurs to form drops, which subsequently deform to allow the formation of smaller and smaller drops until an equilibrium size is achieved. This equilibrium size is the result of the breakup and coalescence rates becoming equals. The deformation of the drop towards breakup is subject to the tangential stress tending to elongate the drop being greater than the interfacial capillary pressure [156, 157] which tends to minimize the surface of the drop. This means that the lower the surface tension between the phases, the easier it is to deform the interface and we could expect smaller drop sizes. In that regard, the use of compatibilisers (preformed or in-situ generated) is relevant in order to decrease the mean drop size of the emulsion or polymer blend. But as suggested by Milner *et al.* [158], the sole influence of the diminution of surface tension on the size distribution of the drops cannot account for the role of the addition of a compatibiliser, but prevention of coalescence by steric effects could. Indeed, they theoretically showed that even a low content of compatibiliser is enough to prevent coalescence of submicron-sized droplets while having only a negligible impact on the surface tension. This dual effect is shown by several studies for various systems [159], for example nylon and ethylene-propylene rubber [157, 160, 161], nylon and polystyrene [162], nylon and polysulfone [163], nylon and poly(methyl metracrylate) [164], polystyrene and poly(methyl methacrylate) [165], polycarbonate and styrene–acrylonitrile copolymer [166] or oil and water [154, 167].

However, the question remains whether the in-situ generation of the compatibilisers is more efficient than the addition of pre-formed surfactants to reduce the mean drop size. Assuming the exact same molecular structure of the compatibiliser, the equilibrium value of interfacial tension does not change between in-situ generated and pre-formed surfactants, but the kinetics of the surface coverage by the compatibiliser does. In practice, it is difficult to control the final structure of the compatibiliser during reactive compatibilisation. Only few studies involve the direct comparison of the influence of either preformed or in-situ generated compatibilisers. Jeon *et al.* [155] noted that polymethyl methacrylate and polystyrene blends stabilised by pre-made surfactants showed the possibility to decrease the drop size down to ~ 1 μm, but the reactive blending allowed to go to even lower sizes (~ 0.3 μm) (Figure 2.9b). This could be attributed to the dispersion of the pre-made surfactants in the form of micelles in the bulk which reduces the number of molecules adsorbed at the interface [39]. Sundarajaj *et al.* [16]

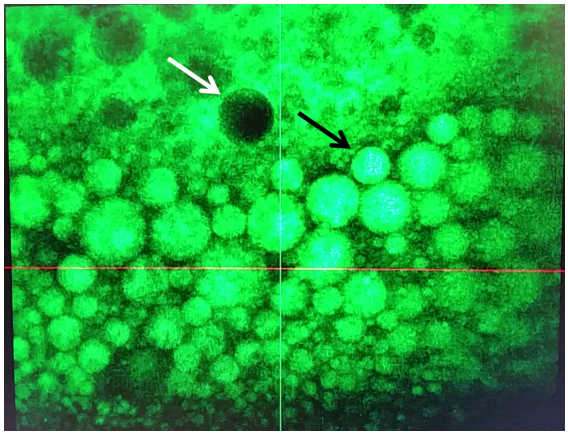

Figure 2.10: Optical image obtained with a confocal microscope of an emulsion generated by turbulent mixing of PEG and PDMS showing both PEG-in-PDMS (black arrow) and PDMS-in-PEG (white arrow) droplets. Fluorescein was added in the PEG phase. [122]

showed that the drop size depended on the volume fraction of dispersed phase with uncompatibilised blends and blends stabilised using diblock or triblock copolymers, but not for the reactive system. They attributed this result to the complete inhibition of coalescence with the reactive stabilisation. On the contrary, El-Jaby *et al.* [154] showed that in an oil-in-water emulsion, the same final drop size was obtained for both pre-formed and in-situ generated surfactants, and did not notice any influence of the amount of generated or added surfactants between the two systems on the final drop size. They showed however that the mixing time needed to reach the minimum drop size was two times longer with the pre-formed surfactant at a given shear rate (Figure 2.9a). On the other hand, Ballard *et al.* [167] showed that, for another oil-in-water system (the oil being styrene), the drop sizes were smaller for the in-situ compatibilised system than for the system with pre-made surfactants.

One drawback of the reactive stabilisation is the lack of selectivity of turbulent mixing in terms of which phase will be dispersed in the other. Since no surfactants are added initially in one of the phases as it is the case for non-reactive systems, the Bancroft rule, which states that the phase in which an emulsifier is more soluble constitutes the continuous phase, does not apply. This means that if the phases also have viscosities close to each other, both phases can *a priori* equally become the dispersed phase. This was observed by Giustiniani *et al.* [122] for a PDMS/PEG emulsion where they found both PEG droplets in PDMS and PDMS droplets in PEG when preparing the emulsion by turbulent mixing (Figure 2.10).

2.3.2 Dispersion stability

As mentioned in 2.1.4, the use of pre-made surfactants, especially in the case of polymer blending, can lack ability in stabilizing the system. This is attributed to different reasons. Short molecules can diffuse easily towards the interface, but are not large enough to stay anchored at the interface [165]. Large molecules, on the contrary, are entangled enough to be anchored at the interface, but present a slower kinetic of adsorption, in particular in viscous media [16]. Moreover their ability to stabilise the blend is impaired by their lower miscibility in the bulk and their higher tendency to form micelles which reduces the number of molecules participating in the adsorption processes at the interface [39].

In order to fix these issues, reactive stabilisation seems to be an appropriate candidate. Indeed, it generates the surfactant at the interface, where it is needed. This makes sure that, even though

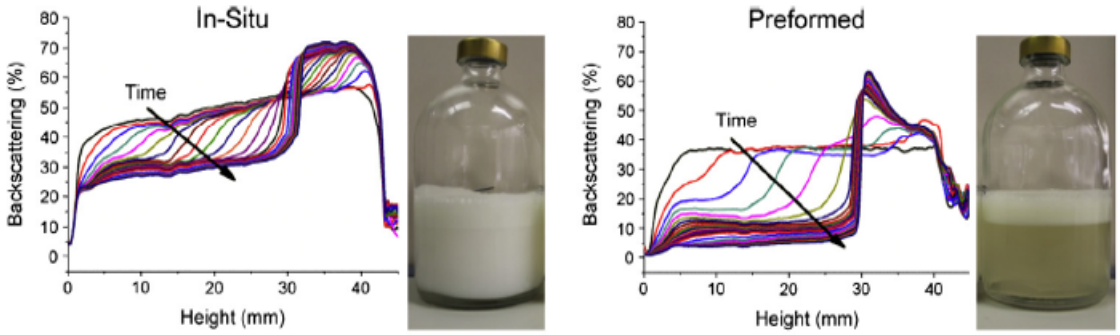

Figure 2.11: Backscattered light intensity variation with height over time of styrene in water emulsions with identical recipes formed by either in-situ technique (left) or preformed technique (right) after leaving to cream for 1 h. The spectra are shown at 1 min intervals for the first 15 min and subsequently every 15 min until 1 h. The photographs correspond to the identical systems after allowing to cream for 1 h (from [167].

desorption of the surfactant from the interface can occur under certain conditions, there will be less micelles in the bulk, and the copolymer surface coverage at comparable amount of added pre-made surfactants and reactive molecules is higher in the reactive stabilisation case [168]. Ballard *et al.* [167] showed that styrene-in-water emulsions were more stable using in-situ potassium oleate than preformed ones by measuring the backscattered light variation with height over time of the reactive and non-reactive emulsions (Figure 2.11).

Depending on the functionality of the reactive polymers in a reactive compatibilisation, one can obtain several surfactant architecture, such as block copolymers, Y shaped copolymers and graft copolymers. The size of this copolymer influences its ability to stay at the interface: the larger the molecule, the less desorption from the interface occurs. By increasing the amount of reactive polymers in the bulk, Giustiniani *et al.* [122] increased the reaction rate, and were able to form larger and larger molecules until a continuous network of cross-linked polymers was created at the interface. This allowed the complete inhibition of coalescence and Ostwald ripening between the drops and led to ultra-stable emulsions.

The reactive stabilisation approach has also been used to stabilise non-polymeric emulsion. Indeed, by using surfactants (phosphatidyl cholines bearing one or two methacrylate groups) polymerizable under irradiation, Regen *et al.* [169] were able to stabilise vesicles and showed that these were actually more stable than liposomes which are vesicles derived from naturally occurring phospholipids. Polymerized vesicles were also generated by Fendler *et al.* [170] using photo-excitation to cross-link the surfactants. Eaton *et al.* [171] also reported the generation of polymerized vesicles via a chemical reaction catalysed by heat. More recently, Summers and Eastoe [172] published a review dedicated to the possible applications of polymerizable surfactants, including the formation of micelles, vesicles, bilayers and emulsions.

2.3.3 Interfacial instabilities

Instabilities at the interface have been observed experimentally under different conditions for non-reactive [173, 174] and reactive systems [44, 126, 140, 151, 175–177]. These emerge as strong deformations of the interface (also called fingering of the interface), sometimes leading to a mechanism called spontaneous emulsification. Kim *et al.* [126, 140] and Jiao *et al.* [176] showed that the root mean square

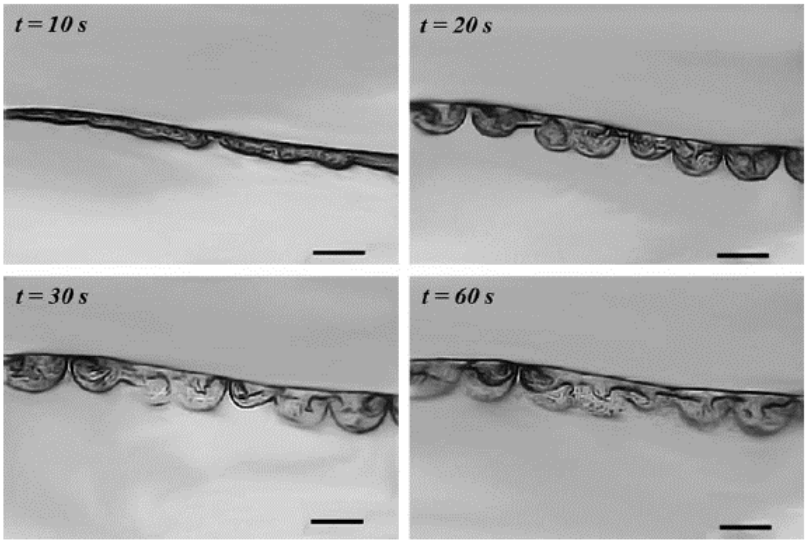

Figure 2.12: Interfacial polymerization at 25°C: top phase, 50% BDO + 50% PPO; bottom phase, diisocyanate. Time: a) 10 s; b) 20 s; c) 30 s; d) 60 s (from [178], adapted from [179]).

(rms) roughening of the interface between polystyrene and polystyrene maleic anhydride increases violently for a value of copolymer coverage of the interface corresponding to the interfacial tension turning negative. Lyu *et al.* [177] proposed a mechanism in which the strong decrease in interfacial tension between polystyrene and poly(methyl methacrylate), without turning negative, allows thermal fluctuations (i.e. capillary waves) to deform the interface, making it possible for other functionalised polymers to react at the interface and oversaturate it, inducing strong interfacial deformations by steric effects. Zhang *et al.* [44] also observed a strong increase in rms roughening of the interface once the copolymer surface coverage exceeds its equilibrium maximum value. These enhanced roughenings of interfaces were in every case associated with an emulsification of the interface (without stirring of the system), meaning that very small droplets or even micelles detached from the interface to the bulk phase. These instabilities typically arise when the different time scales of the system are such that the population of the interface is faster than its relaxation, leading to an overpopulation of the interface and hence to what some call an effective negative interfacial tension.

The formation of small droplets and micelles through interfacial instabilities induced by a negative surface tension was studied theoretically by Granek *et al.* [180] for a non-reactive compatibilisation. More recently, the case of a reactive coupling at the interface was studied theoretically by Patashinski *et al.* [178] and via modelisation by Berezkin and Kudryavtsev [147]. Patashinski *et al.* studied the effect of an negative surface tension on a flat interface caused by overpopulation of surfactants, and successfully predicted the surface roughening observed experimentally by Fields *et al.* [179] (Figure 2.12). Berezkin and Kudryavtsev studied both flat and curved interfaces and showed the influence of the size of each of the reactive species on the final morphology of the blend.

Reactive stabilisation offers many advantages compared to the use of pre-made surfactants: faster kinetics of surface coverage leads to a faster reduction of interfacial tension and inhibition of coalescence, both having an impact on the final drop size under mixing. Moreover it allows to create insoluble surfactants at the interface, which could not be used in pre-made form, and can lead to super-stable systems. However, the apparition of interfacial instabilities which roughen the interface between the two phases is very often observed, but can be used as a way to produce micelles in a controlled way [181].

2.4 Discussion

The stabilisation of emulsions and polymer blends is made possible by the presence of surfactants (both pre-made or created in situ) at the interface. Their kinetics of adsorption/creation and desorption play an important role in the stabilisation process and can be accessed by measuring the evolution of interfacial tension or surfactant surface coverage between the phases in contact. Our knowledge on these for non-reactive interfaces is now fairly advanced, thanks to theoretical models and numerous experimental studies in the literature. However, because of the difficulty for large molecules to diffuse, non-reactive stabilisation often results in poor stabilisation when dealing with viscous phases.

To deal with these issues, a number of studies used a reactive stabilisation, which forms the surfactant directly at the interface, where it is needed. It avoids the solubility issues of the large molecules in the bulk which prevents the addition of enough surfactants for the stabilisation. Depending on the structure of the reactive molecules, it can also, under certain conditions, block the desorption of the surfactants. The size of the reactive molecules is also necessarily smaller than the pre-made molecule it replaces, meaning lower diffusion times and therefore faster kinetics of surface coverage by surfactants.

For reactive interfaces, the values of interfacial tension (or equivalently surfactant surface coverage) at long times ("equilibrium" values) seem to follow the same behaviour as for their non-reactive counterparts, although systematic comparisons between the two are to this day limited in number. Most of the studies involving reactive stabilisations take the uncompatibilised blend or emulsion as reference, and make no mention of the non-reactive stabilisation process.

The kinetics of evolution of surface tension at reactive interfaces, however, has received a lot of attention these past two decades. Various theories have emerged, differentiating two regimes: reaction-controlled when the reactivity of the functionalised molecules and/or the concentration of functionalised groups are low, and diffusion-controlled when the reaction is fast and the only process limiting the kinetics of evolution is the diffusion of the reactive molecules. Numerous experimental studies report either the former or the latter, but the conclusions are sometimes a matter of debate [134]. Also, these theories are intentionally simplistic (flat, two-dimensional and quiescent interfaces, no surfactant desorption, etc.). Yet, even if they seem to be able to capture the general behaviour of the evolution of interfacial tension, reactive stabilisations are mostly used in industrial processes implying either co-extrusion or turbulent mixing, so they could be improved to match the experimental conditions.

Another important aspect to understand would be the apparition of instabilities at reactive interfaces. Only a few studies are tackling this phenomenon, though it could have a great impact in industrial processes where roughening of interfaces is to be avoided, or inversely provide new ways of making both micro and nanoemulsions.

Finally, it seems adequate to emphasize that emulsions and polymer blends are usually treated separately, when they are physically the same class of materials, the only difference being the size of the bulk molecules. Here for example, we handled them both equally regarding interfacial tension, and surely other aspects might be treated with the same approach. We certainly expect both fields to benefit from a closer collaboration.

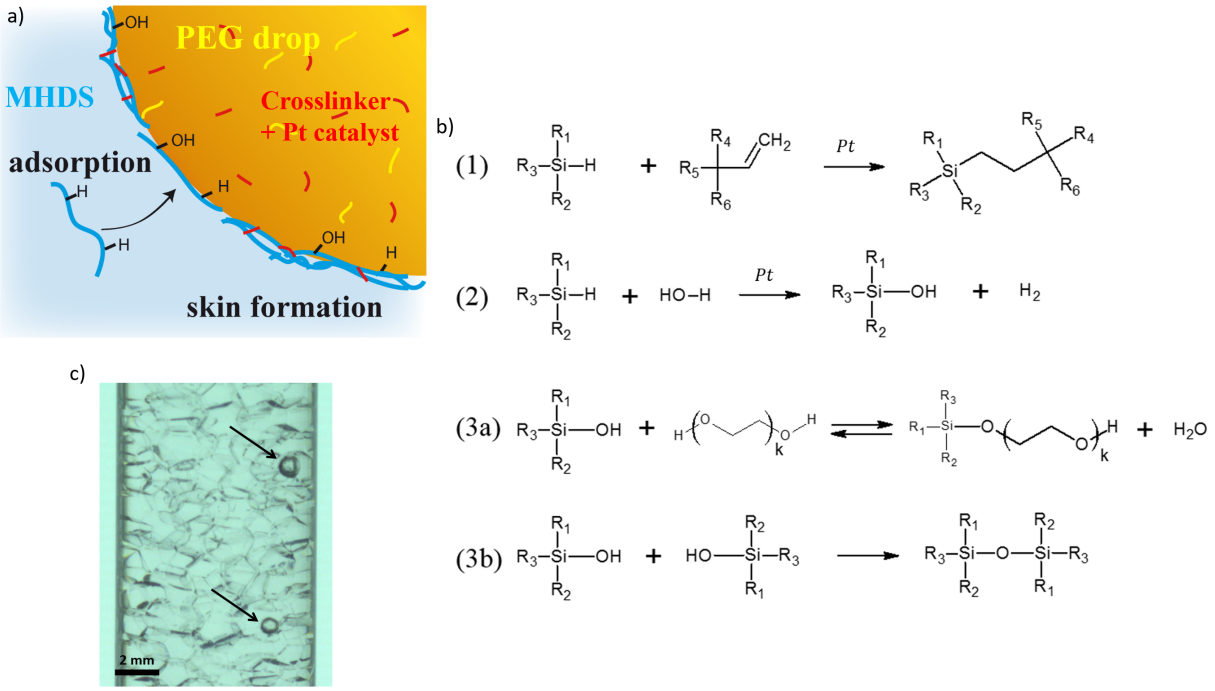

Figure 2.13: a) Scheme of the composition of the PEG-in-MHDS emulsions stabilised by a reactive stabilisation approach. b) Reaction mechanisms occurring at the interface between MHDS and PEG in presence of the crosslinker with its platinum counterpart and traces of water. c) Photograph of a PEG-in-MHDS emulsion with H_2 bubbles indicated by arrows.

2.5 Impact of the reactive stabilisation on PEG-in-MHDS emulsions

Here we study the impact of a reactive stabilisation of a PEG-in-MHDS emulsion. To stabilise the PEG-in-MHDS emulsion, a vinyl-terminated siloxane crosslinker containing a platinum (Pt) catalyst which is active at room temperature, is added in the PEG phase at a concentration C (in mol%) (Figure 2.13a). The idea behind this addition was to crosslink the interface, i.e. to increase the molecular size of the MHDS at the interface, in order to inhibit the ageing of the emulsion through coalescence and Ostwald ripening. However, during the course of this study we realised that other reactions were occuring. In Section 2.5.1 we therefore detail the different chemical reactions occurring at the PEG/MHDS interface due to the addition of the crosslinker/catalyst mixture. Then in Section 2.5.2 we show the impact of the addition of the crosslinker/catalyst in the PEG phase on the stability of the emulsion.

2.5.1 Reactions at the interface

The PEG and the MHDS do not react with each other without the addition of a third component, which means that for a crosslinker/catalyst concentration $C = 0$ mol%, the PEG/MHDS interface is chemically inert. The addition of the crosslinker/catalyst in the PEG phase has several effects on the reactivity at the interface, which are summarised and briefly explained in the following.

- First, the platinum atom Pt catalyses the cross-linking reaction between the Si-H groups on the MHDS chains with the vinyl ends of the crosslinker (hydrosilylation reaction)(Figure 2.13b, reaction (1)) which diffuses from the PEG drop into the MHDS phase, thus increasing the molec-

ular mass and finally creating a continuous network of the MHDS chains in the vicinity of the PEG/MHDS interface.

- However, the Pt also catalyses the oxidation of the MHDS via its Si-H bonds in contact with the PEG phase by the traces of water contained in the PEG, transforming the Si-H in Si-OH bonds while releasing dihydrogen bubbles (Figure 2.13b, reaction (2)), and preventing the hydrosilylation reaction from happening [182,183]. The observation of bubbles during the emulsion generation at high C is a hint that this reaction effectively happens (Figure 2.13c).

The created Si-OH bonds are unstable, and can be transformed in two ways:

- They have the possibility to react with the C-OH bonds of the PEG to create PDMS-b-PEG copolymers while releasing water (Figure 2.13b, reaction (3a)) [184–186]. These copolymers are also known to be unstable and the inverse reaction eventually happens.
- The Si-OH bonds can also react with each other, leading to a second crosslinking reaction of the MHDS (Figure 2.13b, reaction (3b)) [187].

We rely on these interfacial reactions to inhibit the coalescence of the drops and the Ostwald ripening in the emulsions. The impact of the concentration C of crosslinker/catalyst in the PEG phase is studied in Section 2.5.2. Out of these four reactions, two of them (reactions (1) and (3b) Figure 2.13b) contribute effectively to the crosslinking of the interface as wanted. However, the other two, reactions (2) and (3a), play a different role. They are involved in the creation of amphiphilic molecules with affinities for both the MHDS (through the PDMS backbone) and the PEG (through the -OH bond or the grafted PEG molecules) phases (surface active molecules or "surfactants"). These reactions are "parasite" reactions in the sense that they are directly in competition with reactions (1) and (3b). However, since they create surface active agents at the interface, they probably also have a role in the stabilisation of the emulsions, and they can be used to probe the effect of the reactions at the MHDS/PEG interface by measuring the evolution of the interfacial tension with time. This will be studied in Chapter 3.

2.5.2 Stabilisation of PEG-in-MHDS emulsions

To study the emulsion stability, we use a simple protocol: in a cuvette filled with the MHDS, millimetric drops of PEG containing the crosslinker/catalyst mixture (PEG/crosslinker/catalyst mixture) are generated one by one at a 0.1 mL.min^{-1} rate with a syringe pump (cf Section 1.3.1). Being heavier than the MHDS, they pile at the bottom of the cuvette, and the emulsion stability is monitored for different crosslinker/catalyst concentrations C by taking one image every 45 s at the beginning of the experiment when the emulsion is evolving rapidly, and one every hour after, using a digital camera (u-eye camera). An example of a sequence of photographs for some of the tested concentrations for the system MHDS 2000-25 / PEG400, $F(Pt)$=0.02 is shown in Figure 2.14a, where the emulsion height is defined as the height of remaining drops between the PEG and MHDS phases. The emulsion generation is prior to the beginning of the imaging at time t=0 s, so the h_0 is different for every concentration since the emulsion has already started evolving. From these images, we see that there is a critical concentration C^*, here between 0.02 and 0.05 mol%, beyond which the emulsions are indefinitely stable.

A brown colouration appears after a few days on the emulsions for high crosslinker/catalyst concentrations ($C \geq$ 0.1mol%), and its intensity increases with C. This is probably due to the presence of

Pt nanoparticles forming after consumption of the crosslinkers [188], and can be avoided by choosing C=0.05 mol% for the final material.

Figure 2.14b shows the evolution of the normalised emulsion height $h(t)/h_0$ obtained from the images shown in Figure 2.14a with time more precisely and for different concentrations C. It clearly shows the separation between two regimes: $C < C^*$ and $C > C^*$ with $C^* \approx 0.03$ mol%. We can see that even for $C > C^*$ the normalized emulsion height decreases slightly with time, even though we see no coalescence in those cases. This is due to the slow drainage of the MHDS out of the emulsion.

In order to understand the transition between the two regimes, we need to study in detail the PEG/MHDS interface while the reaction is taking place. This is done in Chapter 3.

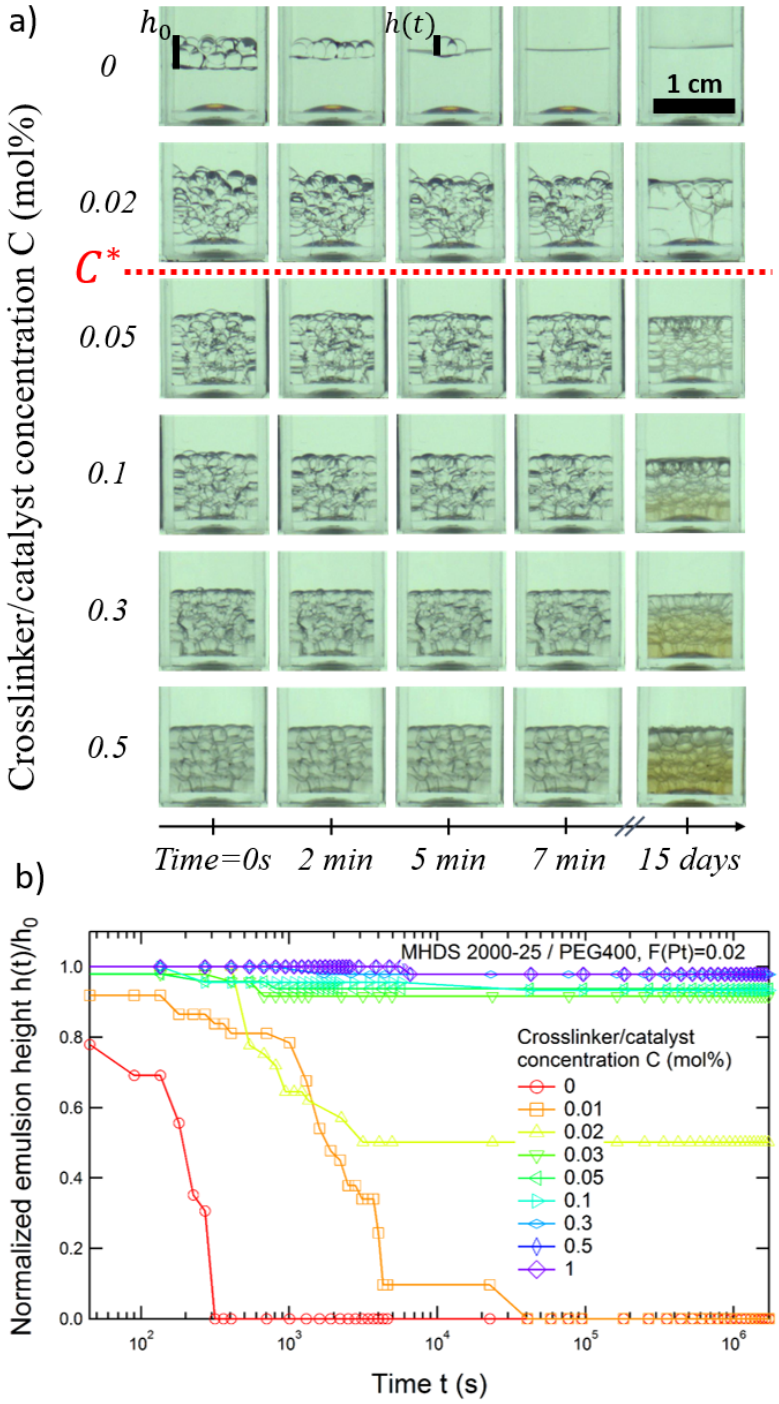

Figure 2.14: a) Evolution of emulsion stability with time for different concentrations C for the MHDS 2000-25 / PEG400, $F(Pt)$=0.02 system. b) Graphical expression of the stability experiment of a) with $h(t)$ and h_0 defined as the emulsion height at time t and $t = 0$ s respectively.

Chapter 3

Study of the PEG/PDMS interface: evolution of the interfacial properties

In Section 2.5 in Chapter 2, we saw that the PEG-in-MHDS emulsions were stable only for concentrations of crosslinker/catalyst above a critical concentration that we called C^*. We have now to understand the role of the chemical reactions at the interface, triggered by the addition of the crosslinker/catalyst.

As presented in Chapter 2, to follow the progress of the chemical reaction at the interface, it is possible to study the evolution of either the interfacial tension (if the created molecules are surface active) or the surfactant surface coverage with time, the two being interdependent. However our system is not as simple as a single reaction occurring at the interface (Figure 2.13). Reactions contributing to the crosslinking of the interface, i.e. the augmentation of the molecular weight of the PDMS at the interface, are competing with the reaction creating *in-situ* the PDMS-b-PEG surfactants at the interface. The behaviour of the interfacial tension between PEG and MHDS while these reactions are occurring, i.e. the equilibrium and kinetic behaviours, should depend on which reaction is preponderant, one creating surface active agent at the interface or one which does not change the interfacial tension. More precisely, we need to know how the kinetics of the different reactions influence the value of C^*.

In this chapter, we study the behaviour of the interfacial tension at long times (equilibrium of γ, Section 3.1) and during the evolution (Section 3.2) for different initial concentrations C. In Section 3.3, we study the relaxation of interfacial tension both in static and dynamic conditions. Using these results, we discuss in Section 3.4 that the two regimes of stabilization $C < C^*$ and $C > C^*$ reported in Section 2.5 in Chapter 2 can be interpreted as being the result of a competition between the different reactions kinetics.

3.1 Equilibrium of the interfacial tension

We probe the effect of the reactions at the MHDS/PEG interface by measuring the evolution of the interfacial tension with time at a constant temperature of 25°C using a pendant drop apparatus (cf Section 1.3.2 in Chapter 1). The crosslinker/catalyst concentration is ranging from 0 to 1 mol% in the PEG.

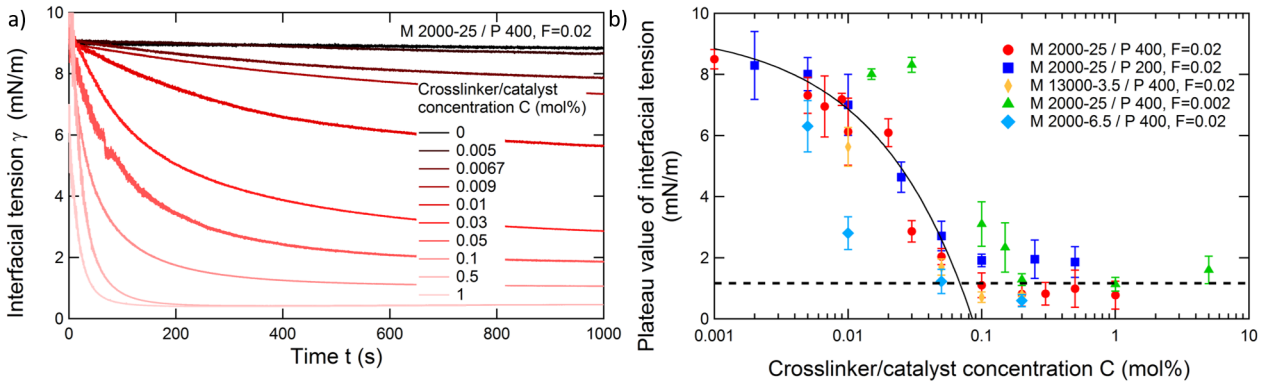

Figure 3.1: a) Time evolution of the interfacial tension between MHDS 2000-25 and PEG-400 with F(Pt)=0.02 for different concentrations of crosslinker/catalyst C in the PEG phase. b) Plateau value of the interfacial tension between MHDS and PEG as a function of the crosslinker/catalyst concentration C in the PEG phase. The different colors and markers correspond to different systems with different molecular weights M_w, $F(Pt)$, or number of reactive sites along the MHDS backbone, which are summarized in Table 1.1 in Chapter 1. The solid line is a guide to the eye.

The PEG drops containing the concentration C of crosslinker/catalyst are generated in MHDS at a constant velocity and their volume V ranges between 1 and 10 µL depending on the concentration C.

We look at the evolution of the interfacial tension with time for different crosslinker/catalyst concentrations. For non-zero values of C, a decrease in γ with time is observed in Figure 3.1a until a plateau is reached. Both the characteristic relaxation time of the $\gamma(C)$ curves and the plateau value decrease as C increases. We interpret this decrease of interfacial tension as a result of both the reactions (2) and (3a) shown in Figure 2.13 a. Indeed, reaction (2) creates Si-OH bonds at the interface between the MHDS and the PEG, which have a greater affinity with the PEG than the Si-H bonds. But we believe reaction (3a) to be preponderant in this process, especially since the interfacial tension reaches values which are close to those found in the literature when adding already prepared PDMS-b-PEG copolymers at a PDMS/PEG interface (Figure 2.6 in Chapter 2) [128].

We therefore have one set of reactions which is essentially responsible for the reduction in interfacial tension (reactions 2 and 3a) and one which essentially crosslinks the interface without changing the interfacial tension (reactions 1 and 3b). However, both phenomena are coupled. In order to better characterise this coupling, the experiment is repeated with PEG and MHDS chains of different molecular weight M_w, different numbers of reactive sites Mole%(MeHSiO) (Table 1.1 in Chapter 1) and/or using a different platinum ratio $F(Pt)$ (Table 3.1). We analyse both the equilibrium and kinetic behaviour of the interfacial tension.

We analyse the interfacial tension data at equilibrium, i.e. when the value of γ is no longer dependent on t. As seen in Chapter 2, for non-reactive interfaces, the equilibrium value of interfacial tension is generally plotted as a function of the surfactant concentration. This is then used for the interfacial analysis with the Gibbs equation.

Figure 3.1b shows the plateau values of the interfacial tension for all experiments (including the experiment of Figure 3.1a) as a function of the crosslinker/catalyst concentration C. This curve is very similar to a CMC curve for interfaces with pre-made surfactants (Chapter 2 Section 2.1.3). It highlights the existence of two regimes: one for low C where the plateau values of the interfacial tension

Name used	MHDS	PEG	$F(Pt)$
M2000-25/P400, F=0.02	2000-25	400	0.02
M2000-25/P200, F=0.02	2000-25	200	0.02
M13000-3.5/P400, F=0.02	13000-3.5	400	0.02
M2000-25/P400, F=0.002	2000-25	400	0.002
M2000-6.5/P400, F=0.02	2000-6.5	400	0.02

Table 3.1: Systems studied in this chapter. The characteristic of the molecules used are given in Table 1.1 in Chapter 1.

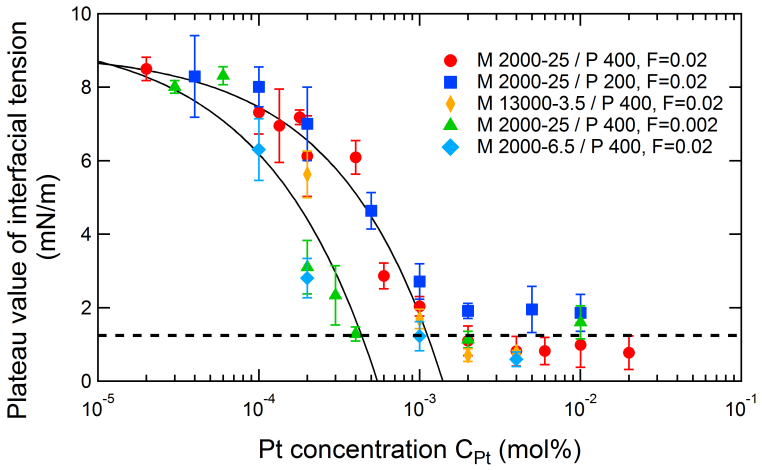

Figure 3.2: Plateau value of the interfacial tension between MHDS and PEG as a function of catalyst concentration in the PEG phase C_{Pt}. The different colors and markers correspond to different systems (Table 3.1) with different molecular weights M_w, $F(Pt)$, or number of reactive sites along the MHDS backbone, which are summarized in Table 1.1 in Chapter 1. The solid lines are a guide to the eye.

decreases with C, and another for high C where the plateau values of the interfacial tension is independent of the concentration C. However the different experiments do not all follow a single master curve: the experiments with the systems M2000-6.5/P400, F=0.02 and M2000-25/P400, $F = 0.002$ are out of the master curve (solid line) followed by the other systems. To overcome this problem, we plotted the plateau values of the interfacial tension against the platinum concentration C_{Pt} instead of C (Figure 3.2). Here the Pt concentration C_{Pt} in the PEG/crosslinker/catalyst mixture depends on the crosslinker/catalyst concentration C in the PEG by the relation: $C_{Pt} = C \cdot F(Pt)$. This allows to compare the different systems with the same platinum concentration rather than crosslinker concentration, since the crosslinker is not involved in the reactions responsible for the diminution of surface tension as seen in Section 2.5.1 in Section 2.5, but the platinum catalyses the reactions that are. Changing the abscissa does not change the general shape of the curve, i.e. we still observe a non-linear decrease of the equilibrium value of the interfacial tension with C_{Pt} down to about 1 mN/m at a critical concentration beyond which the interfacial tension is independent of C_{Pt} at long times. However, it allows to compare properly every experiment with a common parameter, since the system M2000-25/P400, F=0.002 has a different platinum concentration.

We observe that the concentration which separates the two regimes is, for the M2000-25/P400, F=0.02

system, the same as the critical concentration C^* found in the stability experiment in Section 2.5. The value of C^* is however not a constant in all the systems. It seems to be independent of the molecular weight of the PEG and the MHDS. But it also seems to be dependent on the number of reactive sites along the MHDS chain[1] and on the platinum ratio $F(Pt)$, which are both parameters which influence directly the reaction kinetics. We will interprete this behaviour in Section 3.4.

3.2 Kinetics of evolution of interfacial tension

We now look at the kinetic of the relaxation of interfacial tension seen in Figure 3.1a. We define the characteristic time τ of that relaxation as the intersection between the slope of the interfacial tension curve at short times and the t axis, here shown for $C = 0.03$ mol% as an example in Figure 3.3a. Figure 3.3b shows the evolution of τ with the platinum concentration C_{Pt}, for the same systems as in Figure 3.1b. We can see that it shows a rather complex behaviour for which we cannot find a single master curve. If we concentrate on the systems M2000-25/P400, $F = 0.02$, M2000-25/P200, F=0.02 and M 2000-6.5/P 400, F=0.02 (red, dark blue and light blue markers) for which the only common point is the molecular weight of the MHDS, we can distinguish a region for $C_{Pt} > 0.001$ mol% where τ seems to follow a power law $\tau \sim C_{Pt}^{-2/3}$ (dashed line), though we do not have an interpretation for this result at this stage. For $C_{Pt} < 0.001$ mol%, the curves separate from the -2/3 power law. This transition appears for the same concentration C^* as in Figure 3.2 and Figure 2.14. Let us now look at the system M13000-3.5/P400, $F = 0.02$, which we plotted separately in Figure 3.3c, for which we increased the MHDS molecular weight. The values of τ have been shifted towards higher values compared to the systems just discussed. However, we do not observe a clear transition for this system. Finally, the evolution of τ with C_{Pt} for the system M2000-25/P400, $F = 0.002$ (Figure 3.3d) shows a clear transition at the same concentration C^* as in Figure 3.2, but the saturation of τ appears for lower platinum concentrations.

From this we can deduct that the concentration of crosslinker/catalyst along with the value of $F(Pt)$ does not have a linear impact on the kinetic of the overall evolution of interfacial tension.

3.3 Relaxation of the interfacial tension under compression

Relaxation processes of the interfacial tension can give several informations about the surfactants at the interface, depending on the conditions of the compression of the interface, static (only one compression) or dynamic (oscillations). Indeed, during a dilatation of the interface, the creation of fresh interface allows the surfactants to diffuse from the bulk to the interface in the case of pre-made surfactants, or to be created at the interface in the case of reactive stabilisation. During a compression of the interface on the other hand, the surfactants rearrange by diffusing out of the interface into the bulk because of steric effects. These rearrangements are dependent on the diffusion coefficient D of the surfactants which depends on their molecular size M_w, and as a result are time dependent. In Section 3.3.1, we first look at the relaxation of the interfacial tension under dynamic compression/decompression cycles, i.e. we look at the kinetic of growth of the surfactants at the PEG/MHDS interface in the presence of crosslinker/catalyst molecules. Then, in Section 3.3.2, we look at the static relaxation after compression of a PEG/MHDS interface at equilibrium.

[1] Note here that there is the same number of reactive Si-H sites on the MHDS 2000-25 and MHDS 13000-2.5.

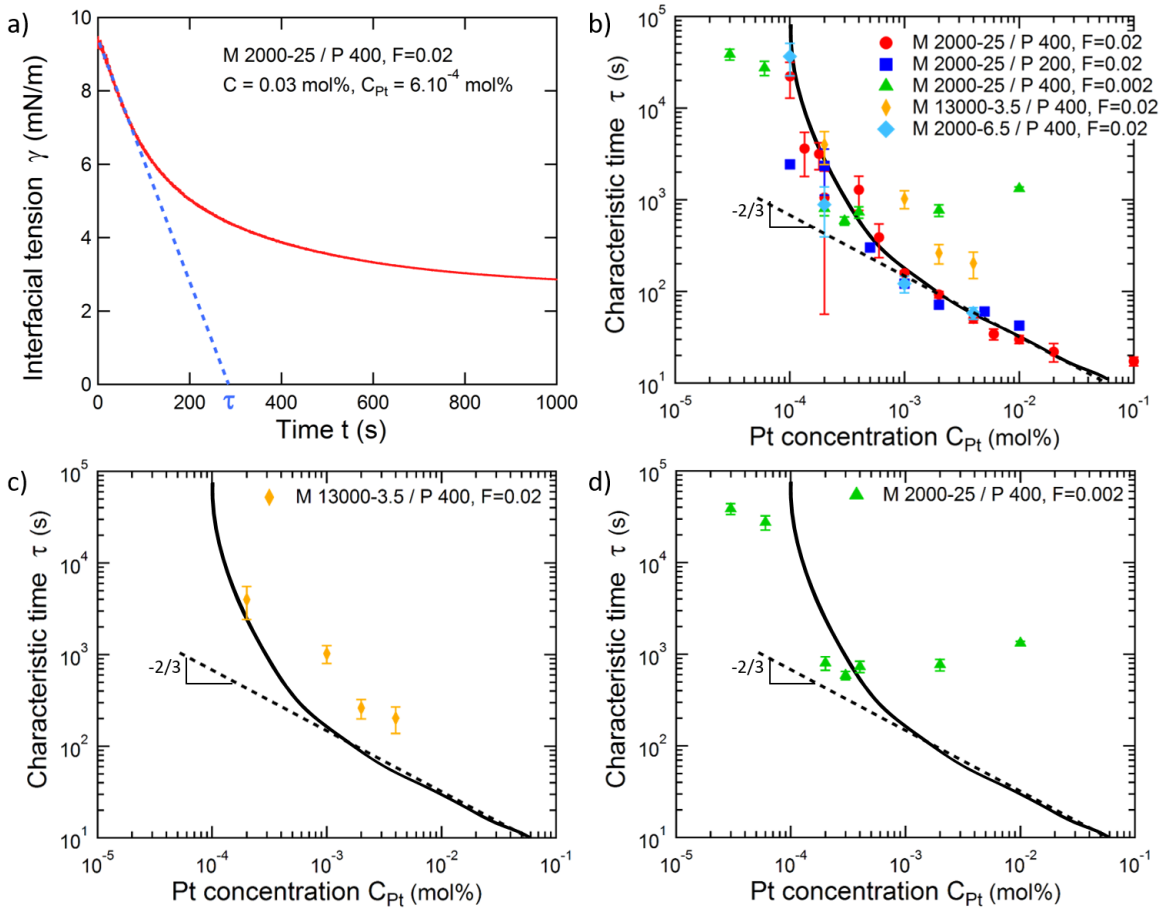

Figure 3.3: a) Definition of the characteristic time τ of the relaxation of interfacial tension with time. b) Log-log plot of the evolution of τ with the platinum concentration C_{Pt}. The different colors and markers correspond to different systems (Table 3.1) with different molecular weights M_w, $F(Pt)$, or number of reactive sites along the MHDS backbone, which are summarized in Table 1.1 in Chapter 1. The solid line is a guide for the eye. c) Log-log plot of the evolution of τ with the platinum concentration C_{Pt} for the M13000-3.5/P400, F = 0.02 only. d) Log-log plot of the evolution of τ with the platinum concentration C_{Pt} for the M2000-25/P400, F = 0.002 only.

3.3.1 Dynamic compression/decompression cycles

The dilatational surface elasticity measures the resistance to deformation of a surfactant populated interface [189–191]. This resistance is the result of transport processes between the bulk and the interface, i.e. absorption and desorption of the surfactants in and out of the interface [192]. In the general case of pre-made surfactants at the interface, these processes all depend on the molecular weight of the surfactants and the bulk concentration. In our case, since the surfactants are created directly at the interface by a chemical reaction, these parameters are coupled through the kinetics of the reaction. In order to probe the kinetics of creation of the surfactants at the interface, we measure the dilatational surface elasticity E_0 of the reactive PEG/MHDS interface thanks to a tensiometer (cf Chapter 1 Section 1.3.3).

Figure 3.4 shows the evolution of $E_0(t)$ for the two systems M2000-25/P200, F=0.02 and MHDS 2000-25/PEG-400, F(Pt)=0.02, with increasing crosslinker/catalyst concentration C for a particular oscillation period of 2.5 s. The amplitude of the oscillations was kept between 3 and 6%. For both systems, the dilatational surface elasticity increases with time for a given crosslinker/catalyst concen-

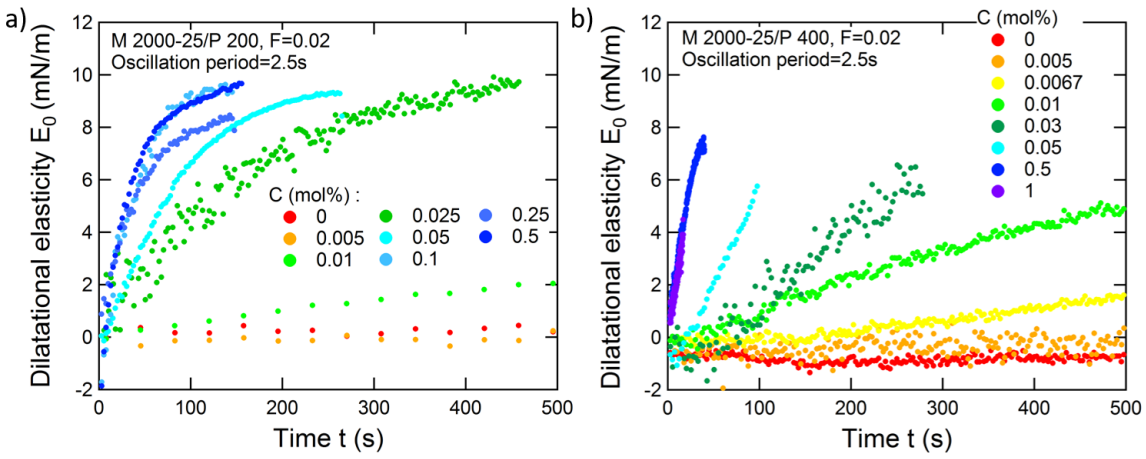

Figure 3.4: Dilatational surface elasticity E_0 (real part of E) (oscillation period 2.5 s) with time for different crosslinker/catalyst concentrations C for the systems: a) M2000-25/P200, F=0.02 and b) M2000-25/P400, F=0.02.

tration. We can also see that for a given time, E_0 increases with C until it saturates for the highest concentrations. This means that the resistance to deformation of the PEG/MHDS interface increases with the crosslinker/catalyst concentration, which implies that the surfactants have more and more difficulties to diffuse out of the interface. An increase of the molecular weight of the surfactants at the interface with C could explain this effect. Indeed, the reactions (1) and (3b) are responsible for the crosslinking of the interface which, if they are promoted, should increase the molecular weight of the molecules at the interface and diminish their ability to desorb.

Particular attention should here be given to the absolute values of E_0, which appear to be very low ($E_{0,max} \sim 10$ mN/m). As stated in Section 1.3.3, the drop shape analysis of oscillating pendant drops tends to greatly underestimate the values of E_0 and should therefore be used only to comment on the evolution of E_0 with respect to a reference value (in our case C=0 mol%). The "true" values of dilatational elasticity could be measured with a Langmuir trough for example[2].

The measures of E_0 here are made by oscillations of the drop volume, which means that we do not allow a complete relaxation of the interface after each compression. We study the complete relaxation after compression in Section 3.3.2.

3.3.2 Complete relaxation of the interfacial tension after compression

We now look at the complete relaxation of the PEG/MHDS interface under compression for the system M2000-25/P400, $F = 0.02$. To do so, we create a drop of the PEG/crosslinker/catalyst mixture in the MHDS in the pendant drop device Tracker, and leave it at rest for a sufficiently long time for the interfacial tension to reach its plateau value for different crosslinker/catalyst concentrations C (Figure 3.5a). The volume of the drop is then abruptly reduced of 50% by aspiration of liquid and

[2]We tried however to measure the shear elasticity using a surface rheometer, in which a bicone geometry is placed at the interface between the two phases and the response to oscillations is measured. These measures would probe the increase of the molecular weight of the molecules at the interface, but not the surface elasticity due to in and out bulk diffusion. However, if these type of measurements are easily done for liquid/air interfaces, placing the bicone exactly at the interface between two liquids appeared to be a rather tricky task to do and after unsuccessful tries lead us to prefer the measurements with the tensiometer.

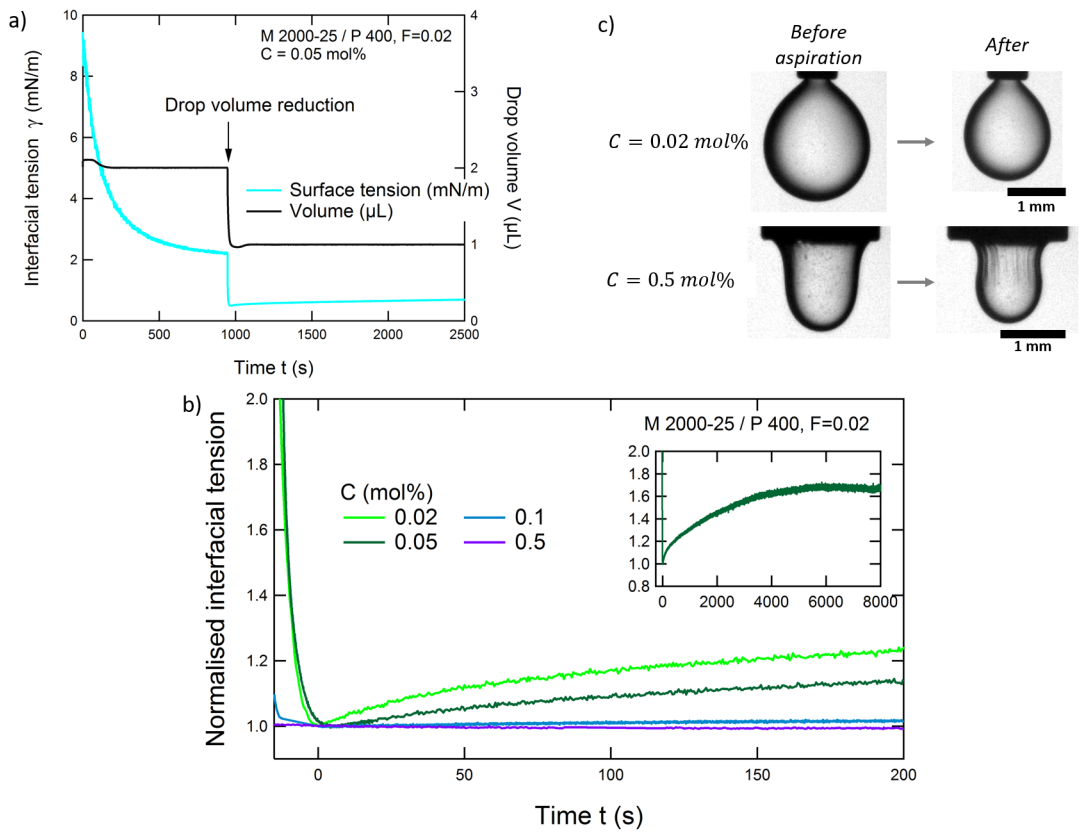

Figure 3.5: a) Interfacial tension (blue curve) and drop volume (black curve) with time during the desorption experiment. b) Time evolution of the normalized interfacial tension after a rapid volume reduction of the drop at t=0 s, for the M2000-25/P400, F=0.02 system. The insert is the long-time evolution for C=0.05 mol%. c) Pictures of the experiment Figure 3.5 b before and after volume reduction of the drop for two crosslinker/catalyst concentrations in the two different regimes identified Figure 3.2.

the evolution of the interfacial tension is followed while the drop volume is kept constant at its new value [193]. Upon rapid volume reduction, the interfacial tension also decreases since the hydrophilic groups on the MHDS surface created via the chemical reactions (2) and (3a) (respectively Si-OH groups and PDMS-b-PEG copolymers which act as surfactants) are compacted.

We then normalise the interfacial tension for each crosslinker/catalyst concentration C with its value right after the volume reduction (Figure 3.5b). For low crosslinker/catalyst concentrations ($C < C^*$), the surface tension relaxes until it reaches a final constant value, lower than its initial plateau value (insert Figure 3.5b). For high concentrations ($C > C^*$), the surface tension remains constant after volume reduction, indicating no relaxation of the interface. In that case, wrinkles are also seen at the interface (Figure 3.5c). The crosslinker/catalyst concentration at which the relaxation is blocked (0.05 $< C <$ 0.1 mol% for this system) correlates well with the results from the emulsion stability experiment Section 2.5 and Figure 3.2 and Figure 3.3 b.

3.4 Discussion

Let us first summarise the different observations made throughout Section 2.5 and Chapter 3.

In Section 2.5 in Chapter 2, we discussed that there were four chemical reactions at the PEG/MHDS interface in the presence of the crosslinker/catalyst molecule (Figure 2.13). Out of these four, two

are responsible for the crosslinking of the MHDS molecule (reactions (1) and (3b)), and the two others create surface active molecules, a hydroxy terminated silicone and a PDMS-b-PEG copolymer (reactions (2) and (3a)). We then studied the impact of the crosslinker/catalyst concentration C on the PEG-in-MHDS emulsion stability (Figure 2.14). We concluded that the emulsions were unstable for concentrations $C < C^*$ and indefinitely stable for concentrations $C > C^*$ where C^* is a critical crosslinker/catalyst concentration in the PEG.

In order to fully understand and control the emulsion stability and the existence of C^*, we studied the PEG/MHDS interface in the presence of the crosslinker/catalyst through the measurement of the interfacial tension. In Figure 3.1 a, we observed a diminution of the interfacial tension between the PEG and the MHDS with time in the presence of the crosslinker/catalyst, which we attributed to the presence of the hydroxy terminated silicone and especially the PDMS-b-PEG copolymers at the interface, until a plateau is reached. In Figure 3.1 b, we reported the value of the interfacial tension in the plateau for each crosslinker/catalyst concentration C, for different systems where we changed the PEG and MHDS molecular weight, the number of reactive sites on the MHDS, or the value of $F(Pt)$. We were able to identify two regimes: a first regime where the equilibrium value of interfacial tension decreases with C, and a second where γ_{eq} is constant with C. The transition between these regimes appears, for the M2000-25/P400, $F = 0.02$ system, at the same concentration C^* than for the emulsion stability observed with the same system. In Figure 3.2, we changed the representation of Figure 3.1b to get the equilibrium interfacial tension against the platinum concentration C_{Pt}. From this representation, we saw that the different systems collapsed into two master curves with the same behaviour but different values of C^*. This will be discussed in detail in Section 3.4.1.

The characteristic time of the relaxation of the interfacial tension was measured and shown in Figure 3.3b. It also indicated a transition between two regimes at concentrations close to the value of C^* observed in Figure 3.1 b. From this, we concluded that the overall reaction kinetics at the interface changes with C with a transition at C^*.

In Section 3.3, we studied the relaxation of the PEG/MHDS interface under static and dynamic compression for the system M2000-25/P400, $F = 0.02$. We observed an increase of the dilatational surface elasticity with time and with the crosslinker/catalyst concentration C (Figure 3.4) which we attributed to the increase of the molecular weight of the molecules at the interface. We also noted in Figure 3.5 that when compressing a PEG/MHDS interface in the presence of a concentration C of crosslinker/catalyst molecule and allowing it relax, we see the interfacial tension increase again slowly for $C < C^*$ when it stays constant for $C > C^*$. This supports the observation of the two regimes in Figures 2.14, 3.2 and 3.3.

From all these observations, we know that there is a clear transition between two regimes, visible both on the emulsion stability and the behaviour of interfacial tension, which happens at the critical crosslinker/catalyst concentration C^*. Our hypothesis is that this behaviour is the signature of the formation of a skin-like layer at the interface above C^* as shown on the scheme in Figure 3.6. For $C < C^*$, the crosslinking of the interface via reactions (1) and (3b) is not fast enough for the molecules at the interface to be large enough to prevent diffusion out of the interface. On the contrary, for $C > C^*$ we can assume that the MHDS at the interface will be linked to the other chains close to it to form a molecule of higher molecular weight before it can desorb from the interface which leads to the formation a skin-like layer at the interface.

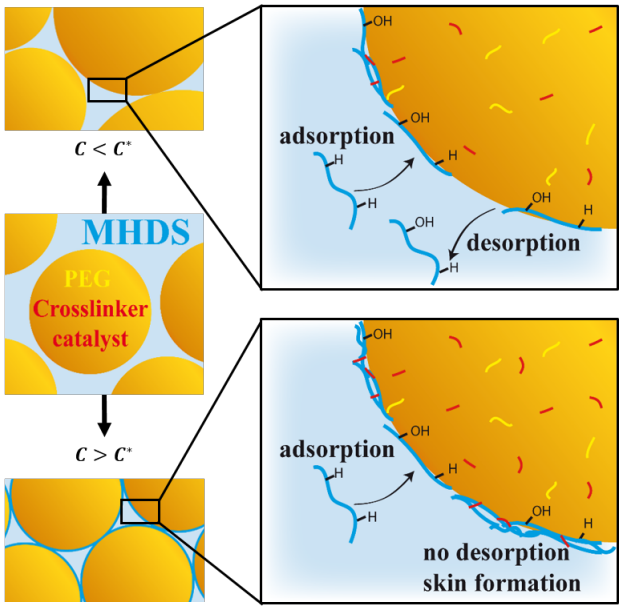

Figure 3.6: Scheme representing the stabilisation mechanisms depending on the concentration. Top: regime of adsorption/desorption of MHDS at the interface. Bottom: no desorption of MHDS from the interface, skin formation around the drop.

We therefore interpret these two regimes in terms of a competition between the kinetics of the different reactions and adsorption/desorption processes which occur at the interface. The system's global evolution is governed by two characteristic times (Figure 3.6): the reaction time τ_r of the different species at the interface, and the desorption time τ_d given by the average time a MHDS molecule remains in the vicinity of the interface. The value of C has an immediate effect on τ_r only, and different scenarios can then occur.

For the lowest values of C, the reaction rate is low, so we can assume $\tau_r < \tau_d$. The interface crosslinking increases slowly the molecular weight of the MHDS chains in the vicinity of the interface. As for polymers below the entanglement limit, as it is the case for the different MHDS molecules used in this study [3], the desorption rate is inversely proportional to their molecular weight M_w [195], the desorption of these copolymers is still possible, leading to an equilibrium between these two mechanisms. This is shown at the top of Figure 3.6. The plateau value of interfacial tension depends then on C during this adsorption/desorption regime (Figure 3.1b). Inversely, for the highest values of C, we can assume that $\tau_r > \tau_d$, meaning that the MHDS at the interface will be linked to the other chains close to it to form a molecule of higher molecular weight. In this regime, the MHDS will not desorb and a skin-like layer will form at the interface, leading to the independence of the plateau value of interfacial tension on C_{Pt} at long times. This is shown at the bottom of Figure 3.6.

Besides, this hypothesis explains the complete inhibition of the ageing processes (coalescence and Ostwald ripening) in the emulsions, making them indefinitely stable for $C > C^*$ (Figure 2.14). It also explains the increase of the dilatational surface elasticity with C (Figure 3.4) along with the fact that the interfacial tension does not relax after a rapid compression for $C > C^*$ (Figure 3.5). Indeed, we believe the relaxation for $C < C^*$ to be due to the desorption of the HO-MHDS or PDMS-b-PEG copolymers from the interface because of steric effects. This means that the onset of the plateau in

[3] For PDMS, the critical molecular weight for entanglement is given between 20 and 35 kg/mol, depending on the study [194].

Figure 3.2 - and hence C^* - can indeed be associated with the creation of a continuous skin around the drop. Moreover, if there is effectively a competition between two kinetic processes leading to two governing characteristic times τ_r and τ_d, then it explains the change in behaviour of the characteristic time of evolution of interfacial tension in Figure 3.3b as well. We can make the hypothesis that, since we deal with several reactions having different impacts on the interfacial tension, the importance of one reaction over the others changes depending whether we find ourselves in the regime $C < C^*$ or $C > C^*$.

We therefore summarise here our hypothesis on the behaviour of interfacial tension at long times, for which the critical crosslinker/catalyst concentration C^* marks the separation of two regimes:

- At $C < C^*$ the reactions at the interface lead to a reduction in interfacial tension and to a global increase in molecular mass of the MHDS, but the interface remains liquid-like.
- On the contrary, at $C > C^*$, the crosslinking reactions lead to the formation of an elastic skin around the droplet which also correlates with the formation of stable emulsions (Section 2.5 and Figure 3.2).

In order to analyse this hypothesis in more depth, we study in detail in Section 3.4.1 the dependency of the transition between the two regimes $C < C^*$ and $C > C^*$ on the parameters of the reactive molecules at the interface such as their molecular weight M_w, their percentage of reactive sites Mole%(MeHSiO) and the value of $F(Pt)$. We then investigate in Section 3.4.2 the kinetics of evolution of the interfacial tension via theoretical models developed in Chapter 2 Section 2.2.3 in order to determine whether we do observe a change in the importance of one reaction over the others in the two regimes. Indeed, if our hypothesis is correct, for $C < C^*$ the preponderant reaction is reaction (3a) which creates the surface active PDMS-b-PEG copolymers at the interface while the crosslinking reactions are negligible, and we should be able to apply these models. For $C > C^*$, the inverse would occur, and the crosslinking reactions are preponderant. As these are not responsible for the evolution of interfacial tension, the models should not apply.

3.4.1 Dependency of the transition between the two regimes $C < C^*$ and $C > C^*$ on the parameters of the reactive molecules at the interface

We now compare the equilibrium value of interfacial tension obtained for different systems or MHDS and PEG molecules with the platinum concentration C_{Pt}. From Figure 3.2, we observe that the plateau value of interfacial tension seems to be independent of the molecular weight of the MHDS (red and orange markers) and the PEG (red and dark blue markers), within the error bars, as all the concerned data follow a single master curve. This is coherent with our hypothesis that the interfacial tension evolution is the result of the reactions (2) and (3a). One should note here that the number of reactive sites per chain on the MHDS 2000-25 and 13000-3.5 are approximately equal (7.5 and 6.1 in mean respectively).

When decreasing $F(Pt)$ by a factor 10 (green markers), the final plateau value stays the same within the error bars, but we lower the concentration C^*_{Pt} at which the plateau is reached. Upon a decrease of $F(Pt)$ we promote the hydrosilylation (reaction (1)) over the oxidation reaction (reaction (2)) [183]. For the same amount of Pt in the two M2000-25/P400, F=0.02 and F=0.002 systems, the crosslinking

of the interface is therefore more efficient in the latter case, and consequently the plateau value is reached at a lower C_{Pt} since the crosslinking will prevent the Si-OH bonds or the PDMS-b-PEG copolymers to desorb from the interface or new ones to be added.

The same observation is made when the number of Si-H bonds on the MHDS backbone changes with a fixed MHDS size (light blue markers Figure 3.2): the creation of the skin occurs at a lower concentration. In this case, the different reaction kinetics are the same since the ratio $F(Pt)$ is constant, meaning that for a given time, there will be as many sites that have reacted for the MHDS 2000-25 and the MHDS 2000-6.5, and we can then consider only the hydrosilylation reaction for this interpretation. As there are less reactive sites on the MHDS 2000-6.5, less crosslinker molecules are needed to connect all the MHDS chains at the interface, thus the lower C^*_{Pt} value. This also means that these sites will react with other sites on chains that are farther away than in the case of the MHDS 2000-25.

The critical concentration at which the emulsions are stable can thus be tuned by varying two parameters: the number of reactive Si-H sites along the MHDS backbone and the ratio of platinum over siloxane molecules in the crosslinker/catalyst $F(Pt)$.

3.4.2 Kinetic of evolution of the interfacial tension: comparison with theoretical models

To be able to apply known theoretical models on the kinetics of evolution of interfacial tension at a reactive interface, we first need to lay down the characteristics of our system, and we limit ourselves here to the M2000-25/P400, $F = 0.02$. The first important point to make is that we do not know the reactivity of the reactive molecules used in this study. Indeed, we know that the catalyst is active at ambient temperature, but this does not inform us on whether the reaction is diffusion-controlled (high reactivity of the reactants) or reaction-controlled (low reactivity). Both should then be considered here.

Another crucial element lies in the concentration of the reactive molecules in the bulk phases. Until then, we considered only the concentration of crosslinker/catalyst C, or platinum C_{Pt}, because it was our preferential variable. But the theoretical models in Chapter 2 involve the concentrations of each reactive molecule. In our case, the evolution of interfacial tension is mostly due to reaction (3a) involving the PEG and the MHDS without the crosslinker, and we deal with polymer melts having 2 reactive sites for the PEG-400 and 7-8 for the MHDS 2000-25. In the case of reactive melts, low concentrations in reactive sites are usually defined as the reactive sites being spaced on average by a distance that exceeds the radius of gyration R_g, which in the gaussian chain model in a random coil gives $R_g = a \cdot \sqrt{N/6}$ where a is the monomer size and N the number of monomers. For the MHDS 2000-25, $N_{MHDS} \approx 30$, which gives $R_g(MHDS) \approx 2.25\ a_{MHDS}$ and for the PEG-400 we obtain $R_g(PEG) \approx 1.2\ a_{PEG}$ with $N_{PEG} \approx 9$. This means that for both molecules, the reactive sites are not distant of at least R_g and we can only consider theories that do not rely on low concentrations of reactive sites. In that regard, we will not try to apply the model of Fredrickson and Milner [142] for diffusion-controlled reactions, which is applicable only for low concentrations in reactants.

Most models are in theory applicable only to flat interface, which, though it is applicable for co-extrusion processes, is never the case in an emulsion. However, multiple experimental studies or simulations on emulsions were interpreted with these models, which comforts us into using them also in our case (cf. Section 2.2.3).

Diffusion-controlled kinetics

In the case of a high reactivity of the molecules at the interface, the overall kinetic should be diffusion-controlled. Since the model of evolution of the surfactants surface coverage in reactive stabilisation processes by Fredrickson and Milner [142] is applicable only to low concentrations of reactants and we are in no way close to this assumption, we cannot apply this model which is the only model for diffusion-controlled reactions. In Section 2.2.3, we discussed that if the reaction is fast compared to the diffusion time for the reactants to diffuse toward the interface, then this diffusion is the only limiting factor of the kinetics of evolution of the interfacial tension, linked with the probability of finding a reaction partner. Since we are in a high concentration of reactants regime, we can assume that the probability to find a reaction partner is high. In that case, we might be able to apply the same diffusion-controlled model as for pre-made surfactants absorbing at a non-reactive interface. This model, called the Ward and Tordai model for diffusion-controlled kinetics of evolution of interfacial tension at non reactive interfaces [74], was derived by Miller, Fainerman and Makievski [85] into Equation 2.6 in Chapter 2 Section 2.2.3, called the Ward and Tordai equation which we recall here

$$\gamma_{t\to 0} = \gamma_0 - 2nRTc\sqrt{\frac{Dt}{\pi}}, \tag{2.6}$$

where D is the diffusion coefficient of the surfactant.

Figure 3.7 is a log-log representation of the interfacial tension with time measured for the M2000-25/P400, F=0.02 system, for each C and for several measurements. Each data set is compared to the Ward and Tordai equation (black solid line) and a linear evolution with the time t (black dashed line). The deviation between experiment and theory clearly shows that the Ward and Tordai model which expects an evolution of γ with $\sqrt{t}$ for $t \to 0$ fails to capture the kinetic evolution of interfacial tension at reactive interfaces. It shows however that the behaviour is close to $\gamma \sim t$. We also verified that the values of γ_0 and t_0 did not have an influence on the evolution of the plot $log(\gamma_0 - \gamma(t)) = log(t - t_0)$ (cf. Appendix II).

We measured the slope α of the curves $log(\gamma_0 - \gamma(t)) = log(t - t_0)$ for $t \to 0$ for each C and for the different systems available. The results can be seen in Figure 3.8. This confirms that, within the error bars, we find $\alpha = 1.10 \pm 0.05$, meaning a $\gamma \sim t^{1.1\pm0.05}$ dependency for the M2000-25/P400, F=0.02 system. For both the M2000-25/P200, F=0.02 and M2000-6.5/P400, F=0.02 systems, we also find α close to 1. However, the M2000-25/P400, F=0.002 system shows a more complex evolution with a power law coefficient α closer to 0.5 at low C and closer to 1 at high C. The system with a longer MHDS chain, M13000-3.5/P400, F=0.02, shows a behaviour close to $\alpha \approx 0.70 \pm 0.06$.

From these observation, we can say that the slope α seems to depend on the platinum ratio $F(Pt)$ and the size of the MHDS. The former is not surprising since it influences directly the kinetic of all the chemical reactions at play here. However, the size of the MHDS should not have an impact on α, but only on the prefactor which depends on the diffusion constant D. In any case, the interfacial tension at the PEG/MHDS interface does not follow the Ward and Tordai equation. Currently, no theories allow to understand why we find $0.5 < \alpha < 1$.

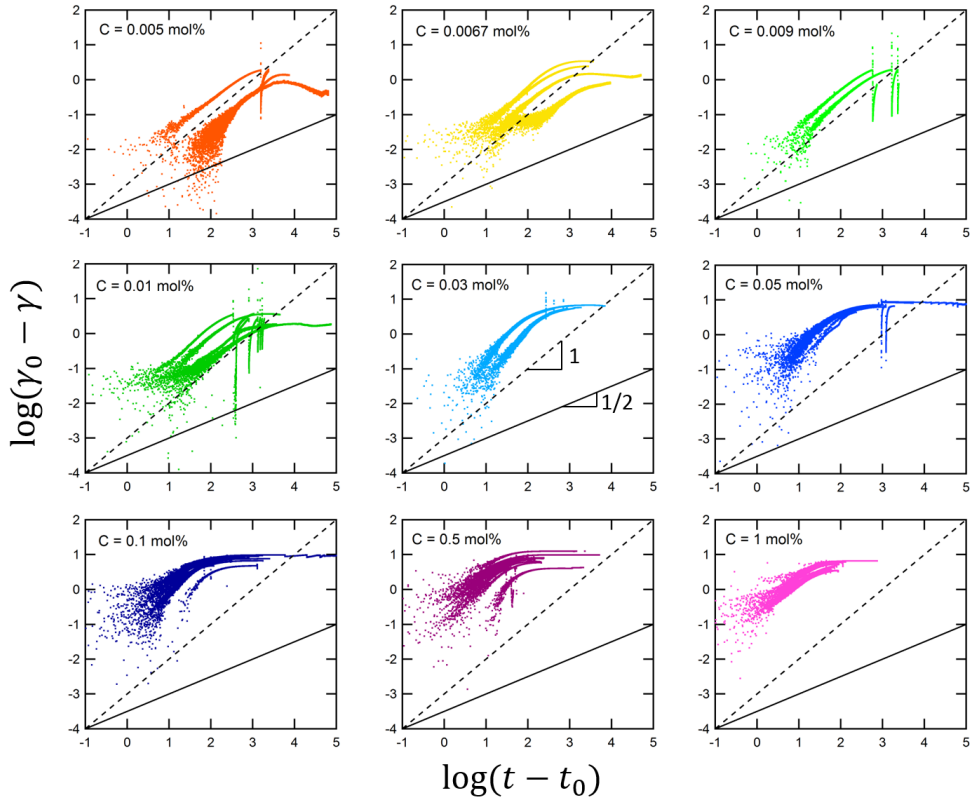

Figure 3.7: Logarithmic representation of the evolution of interfacial tension at the MHDS 2000-25/PEG 400 interface with time for different concentrations C. The solid black line corresponds to the 0.5 slope expected by equation 2.6. The black dotted line corresponds to a slope 1.

Reaction-controlled kinetics

In Chapter 2, we detailed different modelisations which capture the evolution of interfacial tension at reactive interfaces, for both diffusion and reaction-limited systems. The Ward and Tordai model does not capture the evolution of interfacial tension γ for our system. In the eventuality that the reactivity of the reactants is low compared to the diffusion time of the molecules toward the interface, we can assume that the system might be reaction-limited. In that case, we refer to the models developed by O'Shaughnessy *et al.* [144] and Oyama *et al.* [134]. These models give the dependence between the interfacial coverage Γ of the *in-situ* formed copolymer on time. In our case, in order to apply these theories, we need to obtain Γ from the interfacial tension measurements. To do so, Chi *et al.* [123] used the Gibbs equation to measure the value of Γ at long times (i.e. when the system is at equilibrium). However, the use of the Gibbs equation is not a usual approach in reactive systems. The results given in this section are in that regard subject to caution. Chi *et al.* justify its use by stating that the reactant concentration stays constant in their study since only a few percent of reactant is consumed during the reaction. In our case, with the measure of interfacial tension, we measure the number of surface active agents at the interface. However, these surfactants are produced by the reaction mechanisms (2) and (3a) which consume only the PEG and MHDS chains which are in large excess. In that sense, we can assume a constant reactant concentration, and apply this analysis in the following manner.

The Gibbs equation, given in Chapter 2 Section 2.1.3 and recalled here, states

$$\Gamma(\gamma) = -\frac{1}{RT}\frac{d\gamma}{d\ln C}. \tag{2.5}$$

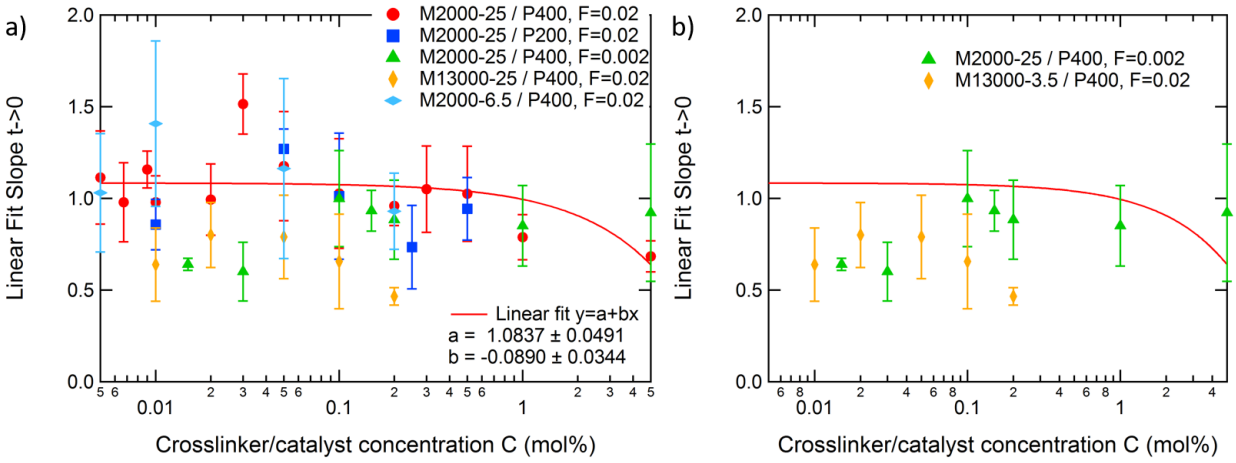

Figure 3.8: a) Slope of the $log(\gamma_0 - \gamma(t)) = log(t - t_0)$ curves for $t \to 0$ at different concentrations C and for different systems (Table 3.1). b) Same as a) with only the systems M2000-25/PEG400, F=0.002 and M13000-25/PEG400, F=0.02, for clarity.

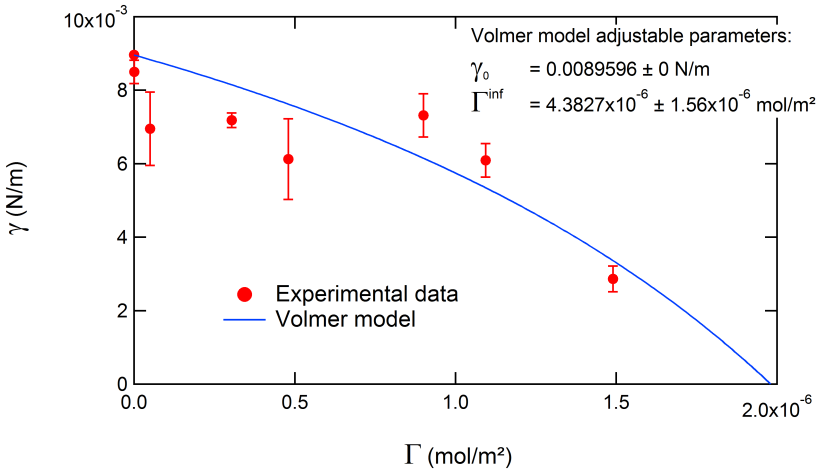

Figure 3.9: Interfacial tension vs surface concentration calculated using equation 3.1 at the interface MHDS 2000-25/PEG 400 with $F(Pt)$=0.02.

To measure the term $d\gamma/d\ln C$, we use the data points in Figure 3.2. We measure the slope for a point i between his two neighbouring points i+1 and i-1, and $\Gamma(\gamma, C)$ is finally given by

$$\Gamma(i) = -\frac{1}{RT}\frac{\gamma(i+1) - \gamma(i-1)}{\ln C(i+1) - \ln C(i-1)}. \tag{3.1}$$

The resulting $\gamma = f(\Gamma)$ curve is plotted in Figure 3.9.

This curve can be fitted by the Volmer model

$$\gamma = \gamma_0 - \frac{RT\Gamma^\infty\Gamma}{\Gamma^\infty - \Gamma}, \tag{3.2}$$

with Γ^∞ and γ_0 as adjustable parameters. Here we fix γ_0=$\gamma(C$=0 mol%$) = 8.9 \times 10^{-3}$ N/m, and a fit gives us the value of Γ^∞, the copolymer concentration at saturation of the interface. For the MHDS 2000-25/PEG 400, $F(Pt)$=0.02 system, we find $\Gamma^\infty = 4.38 \times 10^{-6} \pm 1.56 \times 10^{-6}$ mol/m^2=2.64 ± 0.96 chains/nm^2. This value of the surface coverage at saturation is high compared to values found in other studies (around 0.1-0.5 chains/nm^2). These high values may be explained by the fact that statistical

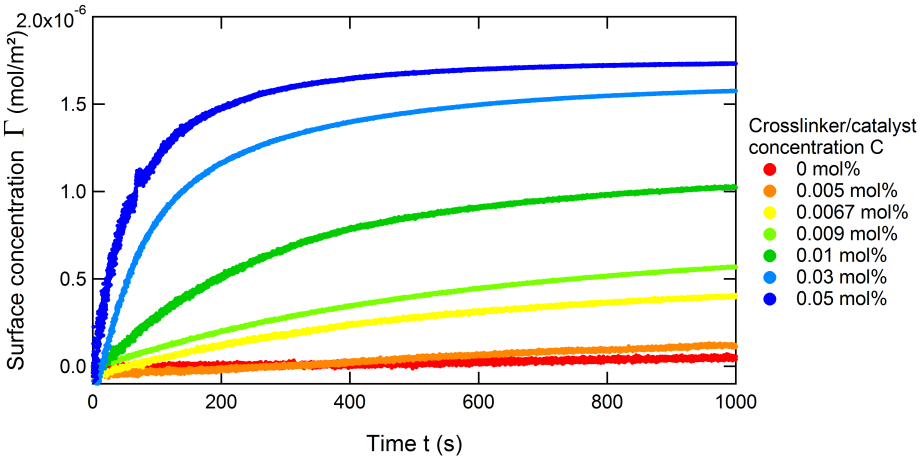

Figure 3.10: Copolymer surface concentration with time calculated using Equation 3.3 at the MHDS 2000-25/PEG 400 interface with $F(Pt)$=0.02 for different crosslinker/catalyst concentrations C.

PDMS-b-PEG copolymers with uncontrolled structure are created at the MHDS/PEG interface, while usually these measures are made for surfactants of well-defined molecular structure. Though the order of magnitude corresponds well in the following, we nevertheless concentrate only on the evolution of Γ with time and not on its absolute values.

The same analysis was made by fitting the $\gamma = f(lnC)$ curve with a second order polynomial curve and then taking the derivative of the fit to measure $d\gamma/d\ln C$ instead of using neighbouring data points. This gave the same qualitative results that we describe below in this section, the only change being in the absolute values of Γ and Γ^{∞} which we do not take into account as just discussed.

Even though the error on Γ^{∞} is important, of the same order of magnitude than its mean value, the Volmer model seems to capture the experimental values of $\gamma = f(\Gamma)$. Thus we can now use it to obtain the $\Gamma(t)$ values. Indeed, the Volmer model can be rewritten

$$\Gamma(t) = \frac{(\gamma_0 - \gamma(t))\Gamma^{\infty}}{RT\Gamma^{\infty} + \gamma_0 - \gamma(t)}. \tag{3.3}$$

Figure 3.10 shows the evolution of copolymer surface coverage Γ with time, for different initial concentrations C calculated using the Volmer model. We observe that Γ increases with time until a plateau is reached. As C increases, the characteristic time to reach this plateau decreases and the value at equilibrium Γ_{eq} increases. Here we plotted $\Gamma = f(t)$ for $C \leq 0.05$ mol% only. Indeed, we applied the Gibbs equation to the data of Figure 3.2, as long as the slope $d\gamma/d\ln C$ had a finite and non-zero value. This means that, for the system studied here (M2000-25/P400, F=0.02) we in fact considered only the data points for $C \leq C^* = 0.05$ mol%, where $\gamma = f(C)$ has a negative slope. For $C > C^*$, $\gamma(C)$ is a constant, and the Gibbs law is non applicable.

To check whether our system can be described by the kinetic models given in Chapter 2, we will look at several representations of $\Gamma(t)$. For clarity, we now focus only on intermediate crosslinker/catalyst concentrations C = 0.0067, 0.01, 0.03 and 0.05 mol%. Two models were proposed for reaction-limited dynamics at reactive interfaces: one by Oyama *et al.* [134] and another by Kramer [149]. According to Oyama *et al.* [134], for reaction limited systems Γ follows first-order dynamic[4], characterised by a

[4]The order of a reaction is defined as the exponent to which its concentration term in the rate equation is raised.

reaction rate

$$\frac{d\Gamma}{dt} = k(\Gamma^{\infty} - \Gamma(t)), \tag{3.4}$$

where k is the reaction constant which depends, among other things, on the initial reactants concentrations. By integrating this equation, Γ follows an exponential behaviour (cf Chapter 2 Section 2.2.3). Figure 3.11a reproduces Figure 3.10 with the intermediate concentrations C = 0.0067, 0.01, 0.03 and 0.05 mol% only for clarity purposes. We see that for low concentrations, namely C = 0.0067 and 0.01 mol%, the curve seems well fitted by the equation $\Gamma = \Gamma_{eq}(1 - A\exp(t/\tau_c))$. For higher concentrations however, this equation captures well the behaviour at short times, but systematically underestimates the value of the plateau Γ_{eq}. Since these concentrations are close to C^*, the change of behaviour can be the signature of the regime transition observed in Sections 3.1, 3.2 and 3.3 and discussed at the beginning of this section.

If, as implied by Figure 3.11a, Γ does follow an exponential growth at low concentrations, then we have

$$\ln(\Gamma_{eq} - \Gamma) \sim t/\tau_c. \tag{3.5}$$

Figure 3.11b shows $\ln(\Gamma_{eq} - \Gamma) = f(t)$ for the crosslinker/catalyst concentrations C = 0.0067, 0.01, 0.03 and 0.05 mol%. For this analysis, Γ_{eq} was taken as the equilibrium value of the experimental $\Gamma = f(t)$ curves. We observe for the highest C a non-linear behaviour of the curves with time, as it was suggested in Figure 3.11a. For C = 0.0067 and 0.01 mol% however, the curves follow a linear behaviour with time, which confirms the first-order dynamic implied in Figure 3.11a.

Kramer [149] applied a second-order dynamic model at a reactive polystyrene/epoxy interface. the second-order dynamic is defined by the reaction rate

$$\frac{d(\Gamma_{eq} - \Gamma)}{dt} = -k(\Gamma_{eq} - \Gamma)^2 \tag{3.6}$$

In the case where the reaction kinetics for high C followed a second-order dynamic, as assumed by Kramer for example, we should find that our experimental data obey the relation

$$\frac{1}{\Gamma_{eq} - \Gamma} \sim t. \tag{3.7}$$

Figure 3.11c plots $1/(\Gamma_{eq} - \Gamma)$ as a function of time. Since a non-linear dependency is evidenced, this shows that no agreement is found between our data and the second-order dynamic.

To summarize on the kinetics of the reactions, we find a good agreement with a pseudo first-order kinetic proposed by Oyama *et al.* at low C, if we accept the Volmer equation as a good fit for the $\gamma = f(\Gamma)$ curve. Chi *et al.* [123] made the same observations for their system: only low concentrations agreed with the pseudo first-order kinetic. As for higher concentrations, no available model allow us to describe the evolution of the interfacial tension γ or the surface coverage Γ with time.

The kinetics of evolution of γ and Γ obviously depend on the reactivity of the blend. Figure 3.3b showed a transition in the behaviour of the characteristic time of the evolution of γ, and a reaction-controlled kinetic model is applicable at low concentrations only, sufficiently apart of the critical concentration C^* for which the transition occurs. Our hypothesis here is that by increasing the crosslinker/catalyst concentration C, we promote the hydrosilylation reaction, which does not create surface active molecules,

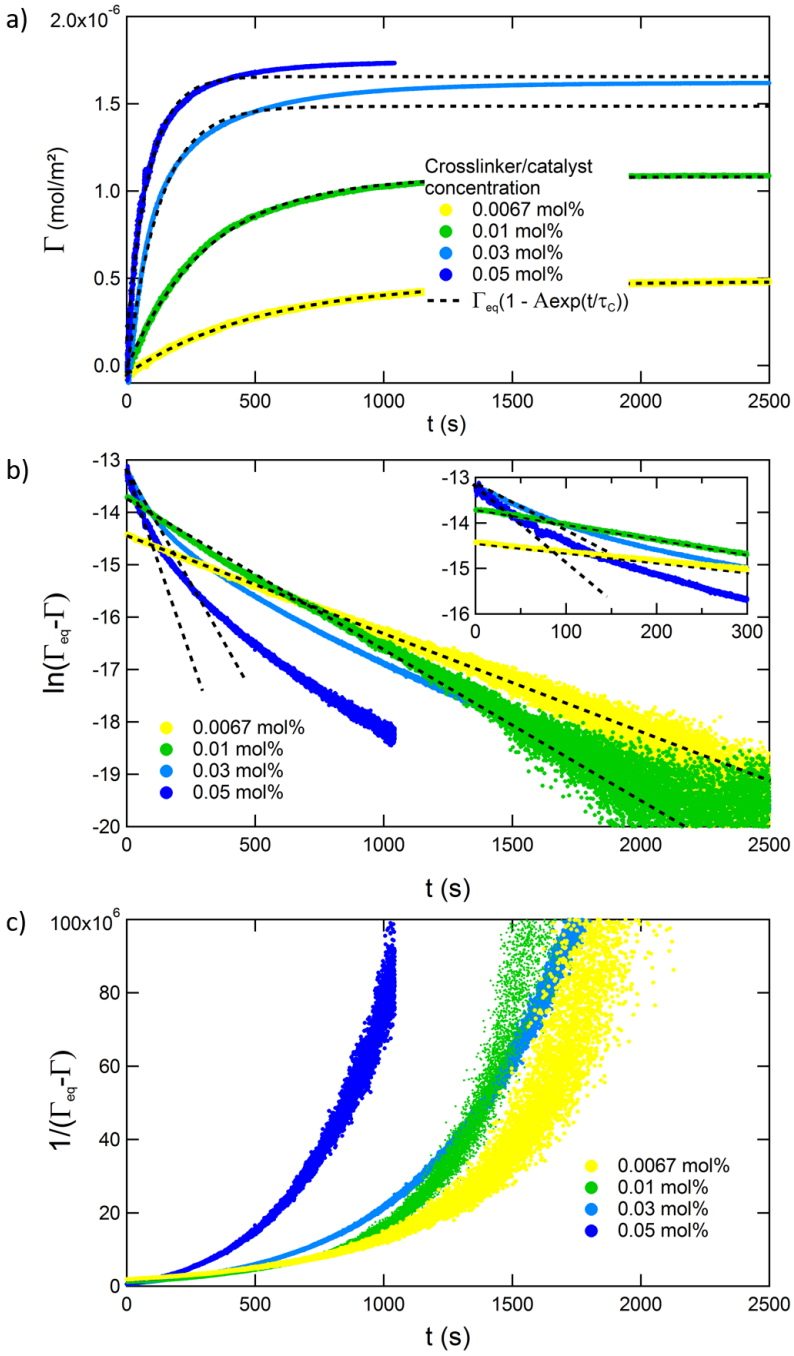

Figure 3.11: a) Copolymer surface concentration with time at the MHDS 2000-25/PEG 400 interface with $F(Pt)$=0.02 for different crosslinker/catalyst concentrations C. b) First order plot of Γ with time. The insert is the evolution at short times. c) Second order plot of Γ with time. The black dotted lines are $y_0 - y_1 \exp(t/\tau)$ fits of the data.

over the reaction which creates the PDMS-b-PEG copolymers. Indeed, at low C, the Si-H are more likely to react with the PEG rather than the crosslinker, on the account of the crosslinker being less present in the mix. In that case, an equilibrium between the creation of the copolymers at the interface and their desorption out of the interface can take place at long times. By increasing C closer to C^*, the hydrosilylation reaction is more and more promoted, creating molecules with higher molecular sizes at the interface which desorb at longer and longer time-scales than for lower C. At the transition, the molecular size of the molecules at the interface is sufficiently large to inhibit their desorption and they create a crosslinked network, or skin-like interface. If this is true, for low C, the hydrosilylation reaction rate is negligible compared to the rate of reaction (3a) and we can apply the different models available to understand the evolution of interfacial tension. However, as C increases towards C^*, the reaction rates become comparable and these theories cannot apply.

Still, as it was stated before, one can argue that the way we calculate Γ is incorrect, since it takes its basis on the Gibbs equation. The result of the fit with the Volmer model is indeed subject to caution, and as a matter of facts returns a large error on the adjustable parameter Γ^{∞}, though the robustness of the fit with the Volmer model was studied while varying the values of Γ^{∞} and Γ_{eq} (cf. Appendix II). Probably the only way to get rid of such problems is to measure directly Γ as a function of time, as we measured $\gamma = f(t)$, using XPS analysis [124, 134–138], gel permeation chromatography [139], infrared spectroscopy [148] or dynamic secondary ion mass spectrometry [140].

As for the kinetics of the hydrosilylation reaction for $C > C^*$, we cannot measure it via interfacial tension measurement since, as stated before, this reaction does not create surface active agents at the interface. However, the kinetics of formation of the skin at the interface is of great importance for stabilisation processes. One way to overcome this problem would be to measure directly the thickness of the skin with time, using interfacial rheology for example. Indeed, the interfacial elasticity E_s is related to the thickness of the polymeric skin h via the bulk modulus E_b also called the Young's modulus

$$E_s = E_b \cdot h. \tag{3.8}$$

This is under the condition that the surface elasticity E_s is greater than the surface tension γ to ensure that the resistance to deformations measured is not an effect of the surface tension. In our case and taking into account Figure 3.4, we expect to be able to measure h for $C > C^*$ only since $\gamma < E_s$ for those concentrations only. Assuming that $h = 0$ µm for very low C, only the measure of h at the transition would not be available. The measure of the skin thickness would also be useful to interpret the results that we present in Part B on the structure of the packing of drops presenting a skin at their surface.

Conclusions and perspectives of Part A

The objective of this first part was to present how to stabilise and generate emulsions with a silicone matrix. Since no surfactants are truly efficient to this day for the generation of stable silicone emulsions, we adopted the use of chemical reactions at the interface between PEG and MHDS (reactive blending approach), piloted by the concentration C of a crosslinker which creates a visco-elastic skin around the drops. The presence of this skin allows the complete inhibition of the coalescence and Ostwald ripening phenomena in the emulsions. We found in Section 2.5 that the stability behaviour of the emulsions was separated in two regimes: unstable for $C < C^*$ and stable for $C > C^*$, where C^* is the critical crosslinker/catalyst concentration (Figure 3.12).

In order to optimise the formulation and understand in detail the stabilisation mechanisms, we followed in Chapter 3 the evolution of the interfacial tension with time at the reactive PEG/MHDS interface. This way, we were able to obtain two informations about the interfacial properties:

- the analysis of the equilibrium value and the characteristic time of evolution of the interfacial tension points toward a critical concentration C^* which delimits two regimes and correlates very well with results on the emulsion stability in Section 2.5,
- the relaxation of the interfacial tension after static or dynamic compressions also falls into two regimes separated by the critical concentration C^*.

We interpreted the existence of C^* as the signature of the onset of the formation of a crosslinked interface.

To support this hypothesis, we discussed the influence of the molecular parameters of the PEG and MHDS, and showed that the evolution of the equilibrium value of interfacial tension with these parameters was coherent with the creation of a skin-like interface. We then applied a theoretical model for the kinetics of interfacial tension at reactive interfaces on our data, with the goal to find again a change of regime between $C < C^*$ and $C > C^*$. We found that the system is reaction-limited and follows a pseudo first order kinetic for $C < C^*$, while the kinetics for $C > C^*$ does not however follow any known theories. This once again supports our hypothesis that the interface is crosslinked for $C > C^*$, through the promotion of reaction (3a) at low C and of the crosslinking reactions (1 and 3b) at high C.

This study also shows that it is possible to probe indirectly and quantitatively the advancement of the different reactions by measuring interfacial properties such as interfacial tension and/or dilatational surface elasticity.

The understanding of the properties of the reactive PEG/MHDS interface is a key point in choosing the best crosslinker/catalyst concentration for the generation of emulsions. Indeed, it allowed us to

report for the first time the generation of ultra-stable closed-cell emulsions with PDMS as continuous phase, via reactive blending as a stabilisation route, with drop sizes up to the millimetre scale (which is presented in Chapter 4). We are also able to generate open-cell silicone foams via emulsion templating using the same approach. We believe this reactive blending approach to be transferable to other polymeric systems. For example, the in-situ formation of block-copolymers at droplet surfaces is routinely used for a wide range of polymer blends [39–41]. And the formation of a skin on the droplet by initiating the polymerisation from the dispersed phase is used for the generation of polyHIPEs with different polymer systems (yet with the additional use of a surfactant to avoid droplet coalescence) [196, 197]. Our work combines these two aspects.

The obtained liquid PEG-in-MHDS emulsions have a very high drop density (>97%) due to the low interfacial tension between the two phases which allows the drops to deform. This causes the study of their structural properties impossible with an in-lab X-ray tomography setup because of its resolution of $\approx$ 20 µm when the films between the drops are expected to have a 1-10 µm thickness. The use of a synchrotron X-ray tomography facility with high resolution and phase contrast analysis could allow to obtain the structure of these polyhedral drops in PDMS.

Moreover, the elastic modulus of the solidified PEG-in-MHDS emulsions is too low to manipulate them without damage during mechanical experiments, which explains why we do not have results on their mechanical properties.

By replacing the small MHDS molecules by Sylgard 184® (high molecular weight MHDS), we are able to generate solid emulsions using the same formulation, but with a higher elastic modulus and whose structural properties could be obtained with an in-lab X-Ray tomography setup. The presence of the liquid drops inside a purely elastic matrix modifies greatly the mechanical properties of the material as compared to the ones of the bare PDMS matrix. The size, organisation and volume fraction of the drops can be used to fine-tune the mechanical properties of the solid emulsion. The control of the emulsion structure and its relationship with its visco-elastic and adhesive properties are the subject of Parts B and C of this manuscript.

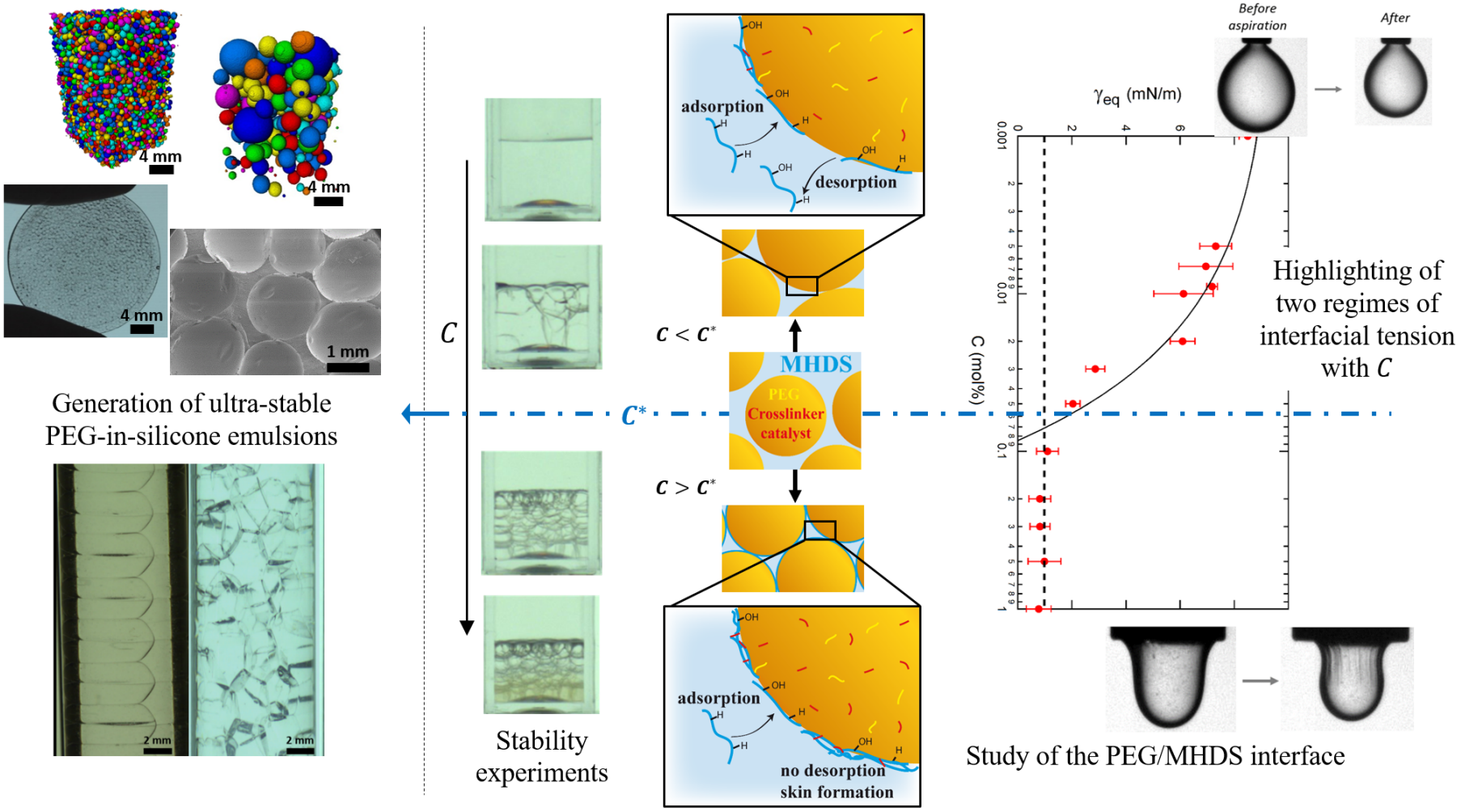

Figure 3.12: Scheme of the conclusions drawn from Part A of this thesis.

Part B

Structural properties of PEG-in-silicone emulsions

Introduction of Part B

Dispersed media are composed of two phases, one being dispersed in the other. We find dispersions of solid-in-gas (Figure 3.13d to h, j and k), an example being a sand pile (Figure 3.13k), solid-in-liquid such as wet sand (Figure 3.13n), liquid-in-liquid which is called an emulsion, gas-in-liquid making a liquid foam (Figure 3.13a and i), liquid-in-solid, or gas-in-solid for a solid foam (Figure 3.13b and c). These materials have complex mechanical properties. For example, liquid foams, emulsions and packing of hard spheres are able to keep complex shapes if no stress is applied, such as when we create a sand castle from wet sand. However, upon an applied stress, they will behave just like a fluid, which is what we observe during an avalanche (Figure 3.13l and m). Solid foams see their mechanical properties, which depend on the density of the foam, greatly modified compared to the bulk material [4]. To understand these properties, one has to look deep into the internal structure of the materials. What objects are they made of? How are they organised relative to each other? What is their size? And how do they interact with one another?

One globally distinguishes between ordered and disordered packings. In the case of ordered systems, the spatial organisation of spheres is a problem finding its mathematical origins in the work of Johannes Kepler who stated in 1611 that the most efficient ways to pack hard monodisperse spheres were the face-centered cubic (fcc) and hexagonal close packing (hcp) arrangements. The efficiency is here defined as the arrangement with the highest sphere density, which was calculated to be around 74.05% for the fcc and hcp organisations [198]. The proof of this statement was however formally given only in 2014 by Thomas Hales [199]. Of course, this problem has very concrete applications: how does the merchant can pack its apples and oranges in the market so that he can install as much fruits as possible and in a mechanically stable way?

If we know mathematically which organisation is the most efficient in ordered media, we have to know what arrangement is effectively attained by the physical objects. In the case of monodisperse hard spheres, for example grains of sand or sugar, we know that, by simply letting them fall in a container, they arrange in a disorganised manner due to their indeformability and the friction they exert one another (Figure 3.13j, k). The disordered packing of spheres are characterised by two limits: the Random Loose Packing (RLP) and the Random Close Packing (RCP). The RLP defines the lowest volume fraction of spheres at which the spheres are in contact, while the RCP defines the maximal volume fraction of undeformable spheres attainable in a disordered arrangement. The RCP volume fraction is systematically lower than the density calculated for the fcc and hcp arrangements. As a result, if the merchant simply throws its apples and oranges instead of neatly stacking them, less fruits will be in display in the market. The study of the packing of disordered hard spheres allows to answer questions such as the understanding and prediction of avalanches.

The case of soap bubbles and emulsion droplets is rather different. Indeed, they can deform and they have a negligible friction at the interface, which allows them to pack in a crystalline, i.e. ordered, manner with a higher density than their hard counterparts, up to 99.99% (Figure 3.13c). The deformability and the presence or absence of friction between the spheres has thus a great impact on the packing of spheres.

Then, what about soft deformable objects that exhibit non-negligible friction at their interface? To answer this question, we study emulsions composed of liquid drops surrounded by a thin solid-like skin dispersed in a liquid, for which the formulation was studied in Part A of this manuscript. We try to understand how the interfacial properties of the drops, along with their size, influence the overall structure of the emulsions. To do so, we first review the literature in Chapter 5 about interfacial properties in dispersed media and their link with the structure of the materials for hard frictional, soft frictionless and soft adhesive spheres. Then in Chapter 6 we study the interfacial properties of PEG drops in silicone having a skin-like interface. Finally, in Chapter 7 we show the influence of the skin around the PEG drops on the overall structure of the emulsions. The link with the mechanical response of the emulsions will be investigated in Part C.

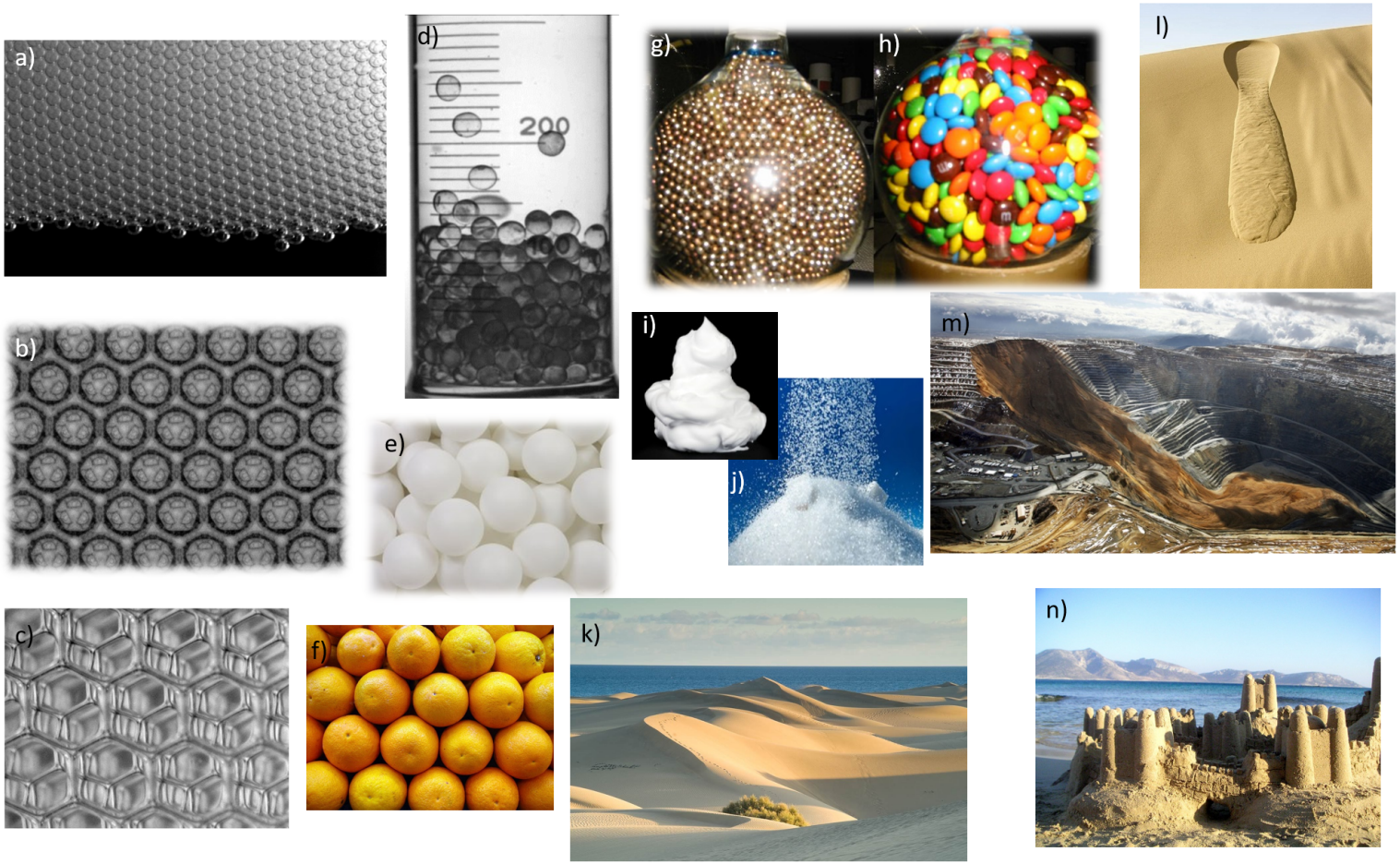

Figure 3.13: Different examples of granular media at different lengthscales. a) Liquid foam (credits from Wiebke Drenckhan). b) Closed-cell solid foam (credits from Wiebke Drenckhan). c) Open-cell solid foam (credits from Wiebke Drenckhan). d) Glass spheres falling in a sphere (credits from Antje van der Net). e) Pile of ping pong balls. f) Pile of oranges on a fruit market. g) Organisation of spherical candies. h) Organisation of elliptical candies. i) Shaving foam standing on itself. j) Pile of sugar grains. k) Sand dunes (dune of Pilat, Bordeaux, France). l) Sand avalanche on a dune. m) Kennecott Utah Copper Bingham Canyon Mine after a landslide in Bingham Canyon, Utah (Photograph by Ravell Call/Deseret News). n) Sandcastle (credits from freepik.com).

Chapter 4

Generation and imaging of PEG-in-silicone emulsions

Using the results of the emulsion stability experiments in Section 2.5 in Chapter 2 and the measurements of interfacial tension and surface elasticity in Chapter 3, we can optimise the formulation of the emulsions. For our standard formulation we therefore use $C = 0.05$ mol% with $F(Pt)$=0.02. This concentration is above C^* which ensures the stability of the emulsions, while being low enough to avoid the brown colouration observed for high C (Figure 2.14a).

Different selective drop generation methods can be used depending on the desired drop size. Dripping for example allows for millimeter sized droplets, while millifluidic techniques allow to decrease the drop size down to 100 µm. All these generation methods are presented in Section 1.2 in Chapter 1. In this chapter we show how, by varying the flow rates and/or the geometric dimensions of the different devices, we are able to generate stable emulsions with a wide range of volume fractions and with a wide range of drop radii (100 µm up to several millimetres depending on the flow rates). Once we control the drop sizes and volume fraction, we can generate various types of materials, by using different liquids and/or by solidifying the continuous phase or not.

4.1 PEG-in-MHDS liquid emulsions

By choosing $C = 0.05$ mol%, we generated PEG-in-MHDS liquid emulsions. They serve as template for some of the solid emulsions described in Section 4.2.

Figure 4.1a and b show PEG-400 in MHDS 2000-25 liquid emulsions just after generation by dripping (a) and after several months (b). This illustrates that no ageeing processes (coalescence or Ostwald ripening) occurred, i.e. that the emulsions are highly stable.

Varying the aspect ratio of the container-to-drop size we can change the overall organisation of the emulsion drops. When the ratio of the container-to-drop size is low ($R_{tube}/R_{drop} = 2$ in Figure 4.1a and b), the emulsions are ordered. On the contrary, for higher ratio of container-to-drop size, the emulsions are disordered ($R_{tube}/R_{drop} = 3$ and 4.6 respectively in Figure 4.1c and d).

It is also possible to change the liquid inside the drops of the emulsions, for example to generate transparent emulsions using a dispersed phase of similar refractive index as the MHDS. Mixing water and

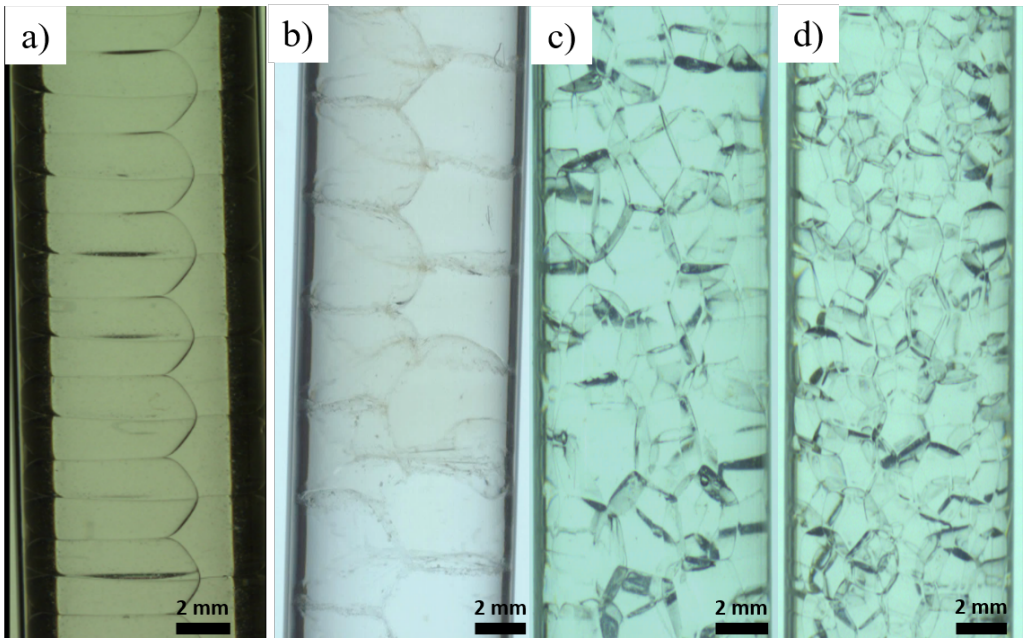

Figure 4.1: Liquid PEG-in-MHDS emulsions. a) and b) ordered emulsions respectively just after generation and after a few months, with high drop content and tube diameter over drop diameter ratio 2, c) and d) disordered emulsions with high drop content and tube diameter over drop diameter ratio 3 and 4.6 respectively.

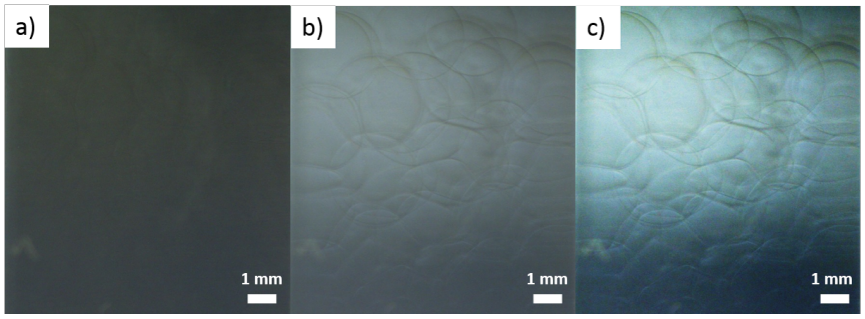

Figure 4.2: Liquid (water(52%)-PEG400(48%))-in-MHDS emulsions under a) no light, b) and c) white light.

PEG with a 52%/48% ratio, along with the crosslinker/catalyst, allows to obtain the same refractive index as for MHDS 2000-25. Figure 4.2 shows such a stable index-matched emulsion, with different lighting conditions to be able to observe the drops thanks to curvature effects.

4.2 Emulsion solidification

Finally, the solidification of the MHDS phase was done by the addition of another platinum-based crosslinker (platinum cyclovinylmethylsiloxane complex, Table 1.1 in Chapter 1) in the silicone phase prior to emulsification, which is active at moderate temperatures and which we call here the "solidifier". Even if the same hydrosilylation reaction is responsible for the crosslinking of the MHDS/PEG skin-like layer and the solidification of the MHDS matrix, we believe that the addition of the solidifier does not interfere with the different chemical processes discussed before in Section 2.5. Indeed, the liquid emulsions – and the stabilising layer - are generated at ambient temperature and at time-scales which are shorter than the solidifier reaction time at this temperature. We therefore generate the liquid emulsion at room temperature with the same interfacial properties as discussed in Section 2.5 and

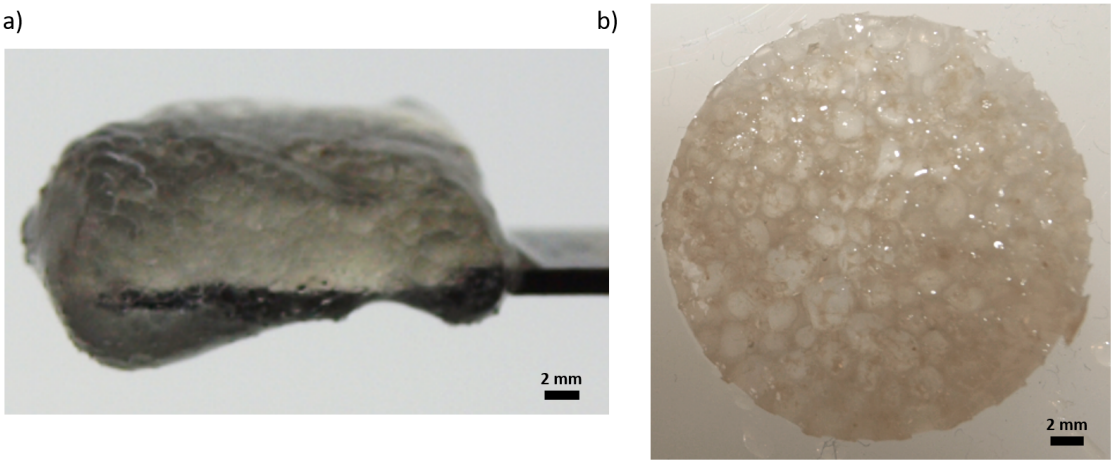

Figure 4.3: Solid emulsions generated with a) MHDS 2000-25 and PEG400 with drop radius of approximately 350 µm and b) MHDS 13000-3.5 and PEG400, with drop radius of approximately 1 mm.

Chapter 3. These are then cured for a few hours at 60°C in an oven. The presence of the skin-like layer ensures that no coalescence occurs between the drops during the curing stage.

By solidifying the MHDS phase of a liquid PEG-in-MHDS emulsion, one obtains a macro-cellular elastomer, which we call a "solid emulsion" composed of a PDMS matrix with liquid PEG inclusions. Figure 4.3 shows such emulsions generated with MHDS 2000-25 and PEG400 (Figure 4.3a) and MHDS 13000-3.5 and PEG400 (Figure 4.3b). The liquid drops are maintained in order to create a "solid emulsion" but may eventually be removed to obtain a porous material (silicone foam) as shown later in this section. The solidification of the MHDS with low molecular weight M_w does allow to obtain solid-like materials, as visible on these pictures, but their elastic modulus is too weak to allow to manipulate them without damage.

The use of Sylgard 184® allows to obtain solid emulsions with a higher elastic modulus as seen in Figure 4.4. Indeed, the MHDS chains in the Sylgard 184® curing agent allow to keep the same approach as studied throughout Part A of this manuscript. We keep $C = 0.05$ mol% which, though we did not make the entire study again for the Sylgard 184®, allows to obtain emulsions that are stable over the solidification time. The same generation techniques can be used to generate the PEG-in-Sylgard 184® emulsions a for the PEG-in-MHDS emulsions: millifluidic techniques allow to obtain monodisperse drops with radii below 500 µm (Figures 4.4a, b, e and f), while the dripping technique allows to obtain millimetre-sized drops (Figures 4.4c, d, h, i, j and k).

Figure 4.4i to k are Scanning Electron Microscopy (SEM) (cf Section 1.4.1 in Chapter 1) images of a solid emulsion with drop radius of approximately 1 mm after cutting in the center of the sample and removing the liquid inside the drops. Figure 4.4j shows the overall organisation of the drops. We see that the pores are all closed. We also see that the thickness between two drops seems to take only two values: either of the order of 3 µm (Figure 4.4k) or of 300 µm (Figure 4.4 i).

Understanding the structural properties of the liquid PEG-in-Sylgard 184® emulsions stabilised by reactive blending is the subject of the second part of this manuscript. They serve as liquid template for the solid PEG-in-Sylgard 184® emulsions that are studied in the third part of this manuscript about the adhesion properties of elastomers enhanced by the presence of liquid inclusions in their structure.

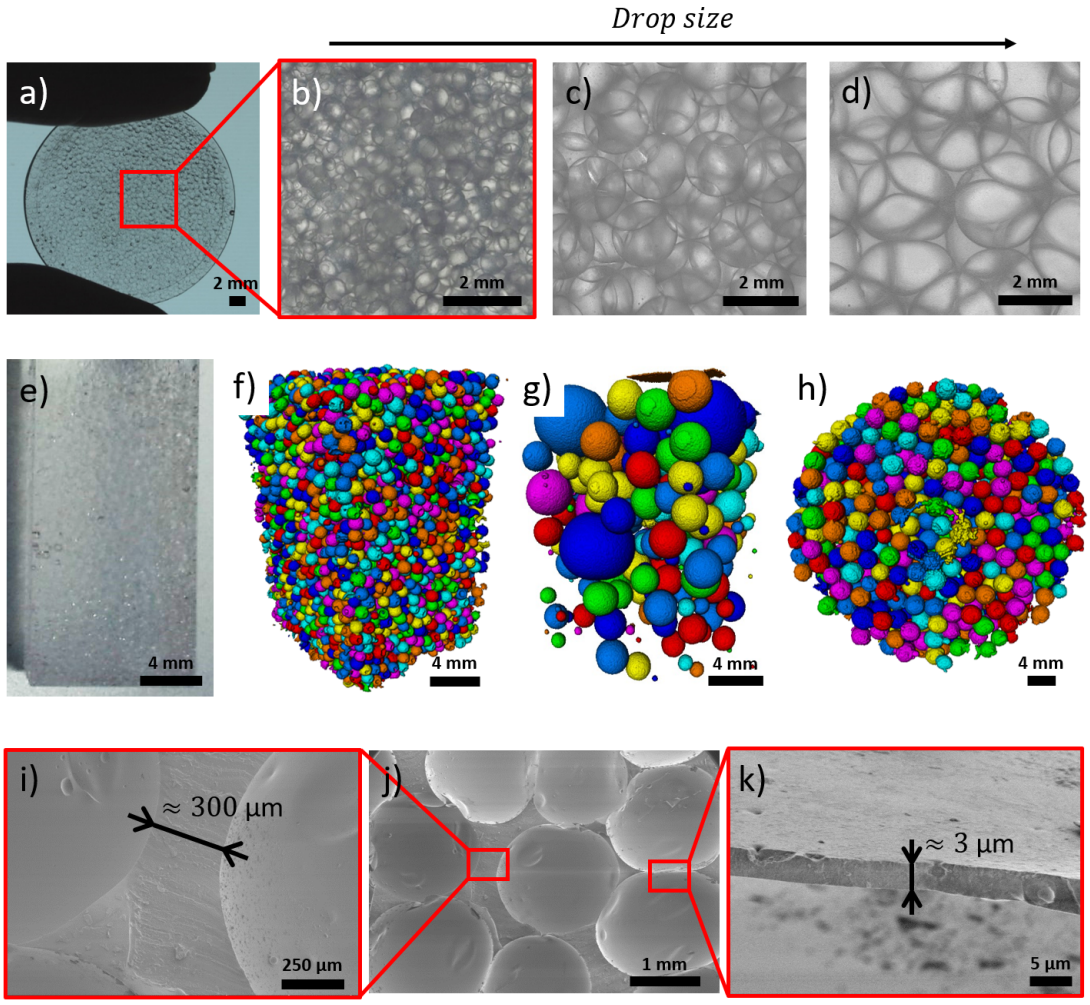

Figure 4.4: a), b), c) and d) Solid emulsions generated with Sylgard 184® and PEG-400, with drop radius of 335 µm (a and b), 850 µm (c) and 1390 µm (d). e) Solid emulsion generated with Sylgard 184® and PEG-400, with drop radius of 330 µm, with its 3D rendering volume (f) obtained by absorption contrast X-Ray tomography showing separated droplets marked by different colours after image processing. g) and h) 3D rendering volumes obtained by absorption contrast X-Ray tomography of a polydisperse solid emulsion (f) and the solid emulsion in c). i), j) and k) Images of a solid emulsion with drop radius of ≈ 1 mm after removal of the liquid in the drops obtained by Scanning Electron Microscopy. i) and k) are close-ups of two separating films of different thicknesses between two droplets.

Solid silicone foams

By replacing the PEG inside the drops by water (or any other hydrophilic liquid that evaporates through PDMS at ambient temperature) in which the crosslinker/catalyst is dissolved (as previously in the PEG), we were able to create a water-in-PDMS solid emulsion. After evaporation of the water, a silicone foam is obtained whose structure can be tuned in the same way as the emulsions (Figure 4.5). Looking at the silicone foam through a microscope shows it has an open-cell structure, as seen in Figure 4.5c. This may be due to the fact that in the absence of PEG no copolymers are generated at the drop surfaces. This may lead to the formation of much thinner and fragile films between the drops which break.

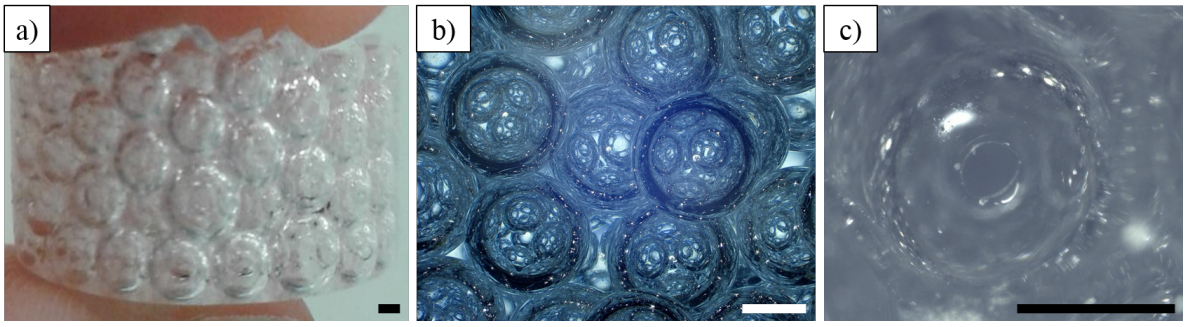

Figure 4.5: a) and b) Solid silicone foams made from a water-in-Sylgard 184® template. c) Zoom on an open pore of a silicone foam generated by emulsion templating obtained with a microscope.

4.3 Characterisation of the emulsion structure

Imaging the volume of the emulsions can be made using different techniques. For example, confocal microscopy could be used, however we would need to work only with index-matched emulsions. To avoid this, we used X-ray tomography. The principle of the technique and the experimental details of the setup used are given in Section 1.4.4 in Chapter 1. X-ray tomography allows to reconstruct the structure of the samples, using the software *Octopus*, based on the atomic number and density differences between the different phases composing it. As shown in Figure 4.4f, g and h, we are then able to separate the PEG droplets from the continuous phase. Using the software *Avizo*, we can measure the volume, positions and deformations of each individual drop, in order to study the structural properties of the emulsions.

For every sample with Sylgard 184® as continuous phase, the difference in absorbance between the PDMS and the PEG was sufficient to be able to analyse the radiographs, the PDMS being more absorbant than the PEG (Figure 4.6a). Unfortunately, no Voltage-Current configurations allowed to detect an absorption difference between the two phases for the PEG-in-MHDS emulsions (Figure 4.6b). This is in all probability due to the thickness of the films between the PEG drops that are thinner than the resolution of the technique (of ≈ 17 µm depending on the magnification). The use of a synchrotron facility (Tomcat beam at the Paul Scherrer Institute in Switzerland) allowed to image these emulsions with a better resolution. In Figure 4.6c, we can see by eye the thin films between the drops. This makes it possible to analyse the structure as seen in Figure 4.6d, however the quality of the analysis is still rather poor, and more importantly the size of the sample that can be imaged at such a resolution is too small to be able to analyse a statistically significant number of drops in this example, since the drops are large ($R \sim 1$ mm). The study of the structure of the liquid PEG-in-MHDS emulsions could be the focus of a following study, which would require time in a synchrotron facility and smaller drop sizes.

In this study, we thus focused on PEG-in-Sylgard 184® emulsions, with large droplets ($R \sim 1$ mm). The study of a packing of spheres requires a large number of objects in a recipient large enough to avoid boundary effects. The generation of emulsions with controlled drop sizes in a viscous continuous phase and with a significant number of drops requires several hours. This makes the study of solid PEG-in-Sylgard 184® difficult since the solidification takes place at the same time-scale as the emulsion generation. To avoid this, we study a model emulsion of PEG drops containing the crosslinker/catalyst molecule in Sylgard 184® base only (see Section 1.1.1 in Chapter 1). We mimic the viscosity of the

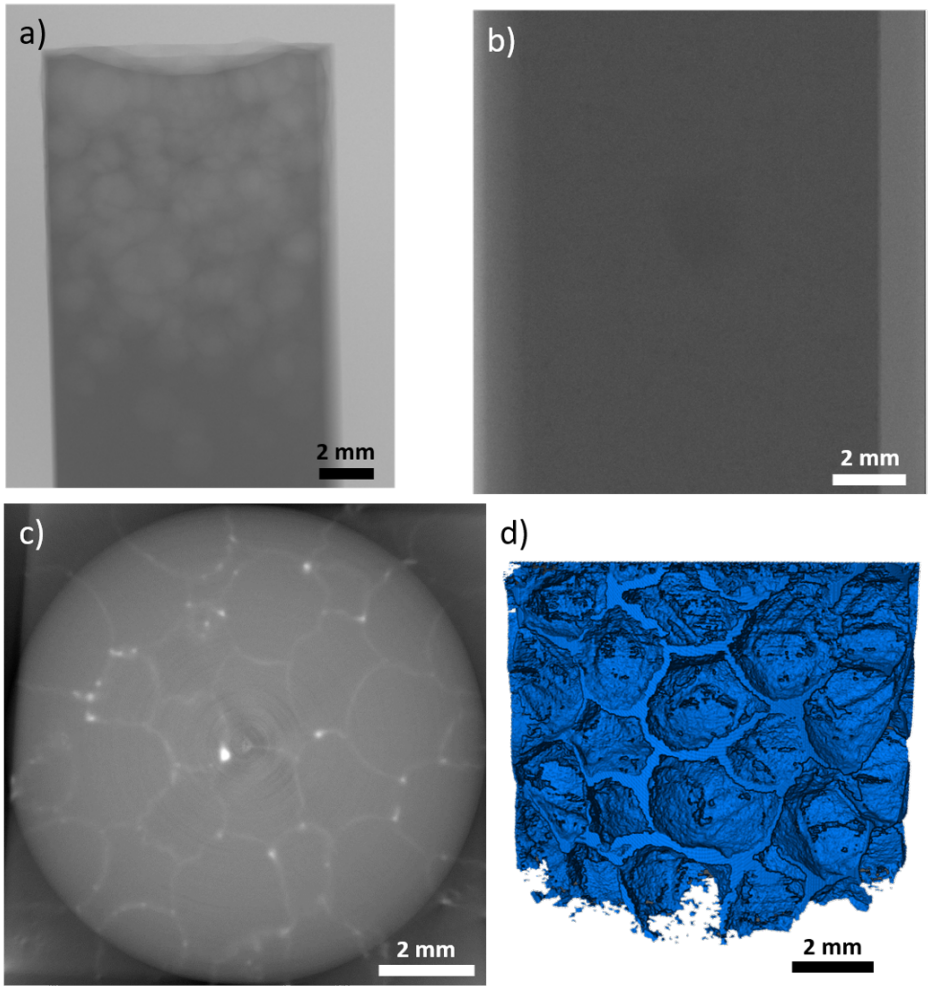

Figure 4.6: a) Example of a radiograph of a solid PEG-in-Sylgard 184® for a 60 kV filament voltage and a 500 µA intensity. b) Example of a radiograph of a liquid PEG-in-MHDS sample for a 60 kV filament voltage and a 166 µA. c) Tomograph of a liquid PEG-in-MHDS emulsion taken in a synchrotron facility. Image taken by Francisco García-Moreno (HZB Germany). d) 3D rendering of the liquid PEG-in-MHDS emulsion in c) (image taken by Gaetan Dalongeville (ICS Strasbourg).

Sylgard 184® by adding the non-reactive equivalent of the molecule which constitutes the majority of the Sylgard 184® crosslinker (the solidifier in this manuscript), the octamethylcyclotetrasiloxane, also called D_4. This way the generation and the packing is not disturbed by the solidification of the continuous phase. However, there are no reactive Si-H groups in the base of the Sylgard 184® to react with the crosslinker/catalyst. This means that the creation of the polymeric skin at the surface of the drops has to be made through a different process, which we discuss in Appendix III.

Chapter 5

Packing of spheres: the concept of jamming and the role of sphere-sphere interactions

Jamming is an idea proposed to consider disordered, athermal materials composed of many individual objects such as granular materials, emulsions, foams, and even car traffic [200] as a unique class of systems to understand their mechanical properties. Indeed, all of these materials have one common property: their viscosity and elasticity increase in a characteristic manner when increasing the objects volume fraction. When their volume fraction is lower than a critical value Φ_c, they all are liquid-like materials, but once this critical volume fraction Φ_c is reached, the system becomes solid-like, the objects are jammed. Changing the density can be achieved by adding or retrieving objects, or by changing the pressure. For example, a liquid foam with a volume fraction above Φ_c is solid-like, and is capable of supporting an applied stress below a yield stress, to which it exhibits an elastic response, meaning that it will go back to its initial shape once the stress is decreased to zero. Above the yield stress, the foam undergoes a plastic deformation, i.e. irreversible changes in its structure [201, 202]. By adding liquid in the foam, the volume fraction of bubbles decreases, and below Φ_c the bubbles are mainly independent of one another, and we then talk of a bubbly liquid (Figure 5.1a). The same holds for emulsions. Instead of changing the volume fraction by adding or retrieving bubbles or drops, it is also possible to do so by applying a pressure with a permeable membrane [203].

The case of hard spheres, sand for example, is not that far from the one of foams and emulsions. When pouring sand from a bucket, it flows just like a liquid. If a hopper is put in the way of the flowing sand, blocking part of the flow and thus creating a pressure, the grains are temporarily jammed in the hopper, until they can flow out the opening at the bottom (Figure 5.1b). When the sand grains are packed together, they collectively behave as a solid. One example to illustrate this is the fact that the sand on the beach is able to supports one's weight. The yield stress necessary for a packing of hard spheres to flow depends on the density of spheres in the material [204].

If we consider that temperature can play the same role as pressure, then glasses and colloidal systems should also be considered here. Indeed, by lowering the temperature of a glassy liquid or a colloidal suspension, we lower the thermal fluctuations and thus increase the importance of attractive interac-

tions between the individual objects (Van der Walls and depletion forces). This leads to the formation of glasses[1] and colloidal gels respectively.

The phase diagram in Figure 5.1c was proposed by Liu *et al.* [200] and then revised by O'Hern *et al.* [205]. It features the impact of the inverse density $1/\rho$, the temperature T and the pressure or load P. The jammed states are found near the origin of the graph, underneath the curves, for low temperatures, large densities and low applied loads. The variation of these parameters can unjam the disordered materials. The point 'J' materialises the fact that below the critical volume fraction Φ_c the system cannot be jammed at all, no matter the variations of T and P. To take into account the possible interactions in glasses and colloidal materials, the temperature axis is sometimes replaces with k_BT/U, where k_B is the Boltzmann constant and U the characteristic interaction energy [206].

In this work, we will concentrate on monodisperse hard spheres and soft spheres such as bubbles and drops, forming materials which we will refer to as granular materials, with objects large enough so that gravitational energies are much larger than thermal energies, which allows to stay in the density-load phase of the diagram in Figure 5.1c. This gives a lower limit to the diameter of the spheres around 10 µm, though typically the sizes of the systems considered here are seldom under 100 µm [206].

However one aspect of the packing of spheres is not dealt with in Figure 5.1c: the interaction forces between large particles. For example, sand grains have frictional interfaces while smooth glass beads are almost frictionless. This causes these systems to be mechanically stable (or jammed) at different packing fractions. Bubbles and drops can also exhibit different interfacial properties (frictionless, adhesive, etc.), leading to the same result. Moreover, sand grains and glass beads are hard, non-deformable spheres, when bubbles and drops are soft and deformable, which also imposes different densities for the onset of rigidity of emulsions and foams. The density and organisation of the spheres at jamming in granular materials, which dictates their mechanical properties, is a direct consequence of both the interfacial properties of the spheres and their deformability, i.e. elastic modulus. In this chapter, we first discuss the different types of interactions that can exist between the spheres and how to control and measure them in Section 5.1. In Section 5.2, we analyse the impact of these interactions on the packing of the spheres in the material.

5.1 Interactions between spheres

From our personal experience, we have some idea of the different interactions between hard grains: the glass beads we played with as children were slippery to the touch, while the sand grains we build sand castle with were much rougher. In the case of foams and emulsions, our experience of interactions between the bubbles or drops is way more limited, and only if there is some aggregation can we "feel" them. These interactions can be divided between normal and tangential forces (Figure 5.2). In this section, we first detail the normal and tangential forces possible between two spheres in different systems, and how we can control them. Then, we provide different experimental methods to measure directly or indirectly the amplitude of these interactions.

[1] In the case of glasses, the temperature at which the transition occurs in called the glass transition.

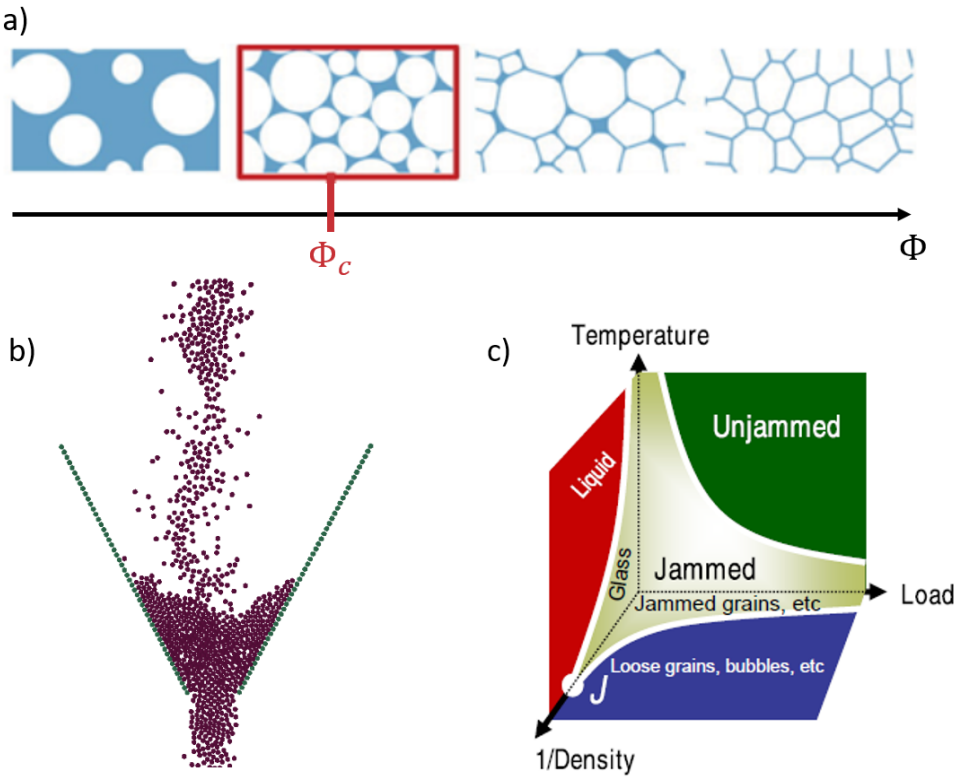

Figure 5.1: a) Scheme of the transition from a bubbly liquid to a solid-like foam by increasing the volume fraction of bubbles Φ (i.e. the density of bubbles) either by adding more bubbles or by application of pressure. Φ_c is the critical volume fraction at which the transition occurs. Adapted from [2]. b) Discrete element method simulations of hard particle filling and flow in a hopper in 3D. From [207]. c) Jamming diagram proposed by Liu *et al.* [200], and revised by O'Hern *et al.* [205].

5.1.1 Normal forces

Repulsive interactions

Since the objects considered here have diameters above 10-100 µm, the effect of Van der Walls forces on two spheres that touch each other is negligible compared to the other forces. Two glass beads colliding will then only be subjected to a strong steric repulsion because of the high elasticity of the spheres. This steric repulsion linked to the elasticity is also present for bubbles and drops, where the elastic modulus is lower but the interfacial tension resists the compression (deformation) of the spheres. Repulsive interactions between bubbles and drops can also occur because of the stabilising agent [208]. For example, steric repulsion between the spheres can come from the repulsion between polymers at the interface, or electrostatic repulsion if charged surfactants were used for the stabilisation. Repulsive interactions between bubbles or drops have long been approximated by pair-wise power laws, as in the case of hard spheres interactions [209]. However, much recent work [210] is pointing towards the non-local nature of bubble/bubble or drop/drop interactions with much more complex interaction potentials.

Attractive interactions

A simple way to add attractive forces between hard spheres is the addition of liquid in the material. The liquid forms "bridges" at the contact points between the grains (Figure 5.3a). The surface energy

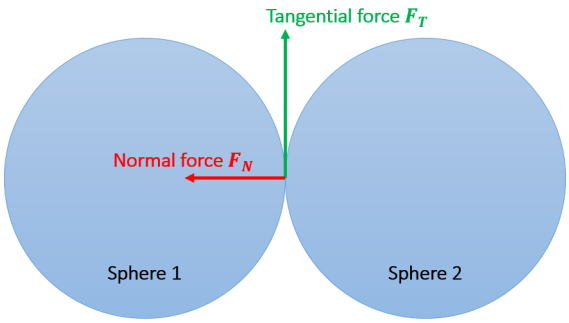

Figure 5.2: Scheme of the normal and tangential forces between two spheres (either hard spheres, bubbles or drops).

of those capillary bridges leads to an attractive force, which is absent between dry hard spheres. Therefore, wetting changes a granular system from one with only repulsive inter-sphere interactions to one with both repulsive and attractive interactions [211–215]. This effect explains how one can build sand castles [216].

The capillary bridge attraction was used by Hemmerle *et al.*to generate a cohesive material with tunable elasticity [217]. The idea is to add a curable polymer to the granular material, where it will form liquid bridges, to then solidify it (Figure 5.3b). The final material is much like a wet packing of hard spheres, only with a higher bond strength. By varying the mass ratio of base to crosslinker of the curable polymer, this strength varies.

The idea of creating adhesive bridges between the spheres was also used in emulsions by different teams. Hadorn *et al.* [218] used specific and reversible binding of DNA strands to generate clusters of emulsion droplets able to dissociate by changing the temperature or the emulsion composition. Feng *et al.* [219] also used complementary DNA strands which bind together to stabilise the drops in an emulsion (Figure 5.3c). In another study, Pontani *et al.* [220] stabilised an emulsion with lipids which can bind to proteins present in the continuous phase when a load is applied on the emulsion. In that case, the lipids organise themselves into patches at the surface of the drops, the number of which can be tuned by changing the drop size or the lipid composition [221].

Also, Jorjadze *et al.* [222] used silicone oil-in-water emulsions with varying concentrations of the charged stabilising agent in the continuous phase to change the attractive depletion forces between the drops, and were able to correlate the intensity of the attractive force to the packing of the drops. Depletion is a frequently used mechanism to generate attractive forces between spheres, for example by adding polymers or micelles in the continuous phase [223]. Since the space between the spheres is narrow, the polymers or micelles cannot enter, which creates an osmotic pressure which leads to an effective attraction of the spheres.

5.1.2 Tangential forces

Tangential forces come from the presence of friction at the interface between the spheres. It is quantified either by the static friction coefficient $\mu_s \geq F_t/F_n$, or by the dynamic friction coefficient $\mu_d = F_t/F_n$

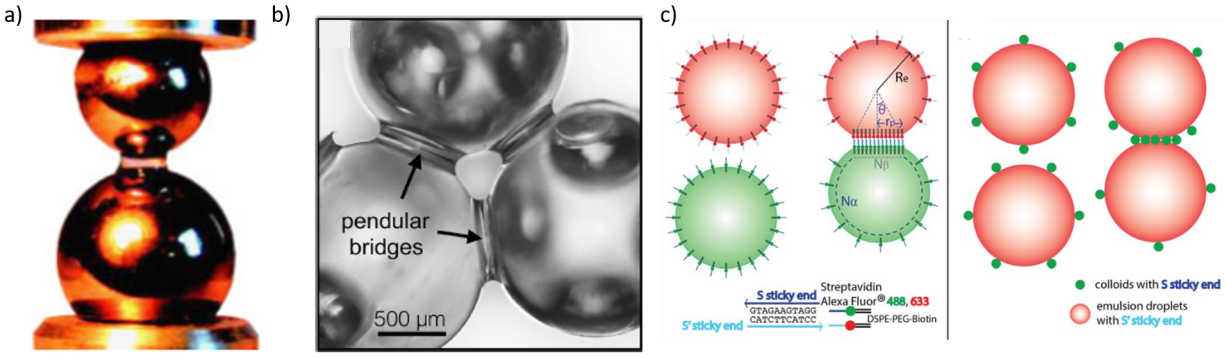

Figure 5.3: a) Liquid bridge between two stainless steel balls of different sizes [211]. b) Three beads are shown connected by polymer bridges in the form of pendular rings, at a polymer content of W = 2.7%. Other bridges, which have debonded from their neighbours, are also visible [217]. c) Top left: silicone oil droplets stabilised with phospholipids, some of which are labeled with fluorescent streptavidin that allows the grafting of two different DNA strands S and S' on green and red streptavidins respectively. The complementary S and S' sticky ends then bind and form adhesion patches enriched in DNA tethers between the droplets. Top right: colloids coated with the S sticky end and dyed in green stick to S' functionalised droplets and eventually bridge to droplets together through a colloidal patch [219].

with F_t the tangential force and F_n the normal force. In the case of hard spheres, the grains can either be frictionless ($\mu \approx 0$) or frictional ($\mu > 0$) depending on the roughness of their interface. For foams and emulsions, friction can be added to the interface thanks to modifications of the interface, for example by using nano-particles to stabilise the bubbles or drops during the generation. The impact of the friction at the interface was highly investigated in the case of rigid spheres [224–227], for which the friction coefficient was varied systematically, but never (to our knowledge) for soft deformable systems. Foams and emulsions are usually treated as almost frictionless systems ($\mu \approx 0$).

Frictionless spheres are able to slide over each other, which means that the global material will change its arrangement more easily. If the system is composed of frictional grains, then the energy required to reorganise in order to attain a more dense packing is higher. As a result, tangential forces add a mechanical constraint which allows to stabilise a packing of spheres with a lower number of contacts between the spheres.

The shape of the beads was also discussed as a motor of friction by Anthony *et al.* [224]. However we will concentrate in this manuscript on monodisperse spherical objects only.

There are different ways to vary the friction at the interface between two spheres. One way is to simply change the material, comparing glass bead with sand grains for example, but this usually also changes the shape of the spheres (sand grains are not spherical). Blair *et al.* [228] used hydrogen fluoride (HF) to etch the surface of glass beads [229] and vary the tangential forces between the spheres. However, HF is very dangerous for the user, and harmful to the environment. Utermann *et al.* [230] proposed to etch the surface of hard spheres using ammonium bifluoride which releases only a little HF. They also used sodium hydroxide NaOH to make the spheres smoother, using a protocol developed by Shellenberger *et al.* [231].

In Sections 5.1.3 and 5.1.4, we suggest a few methods that were used to evidence the presence of interactions between the objects composing a granular medium, and sometimes quantify their intensity.

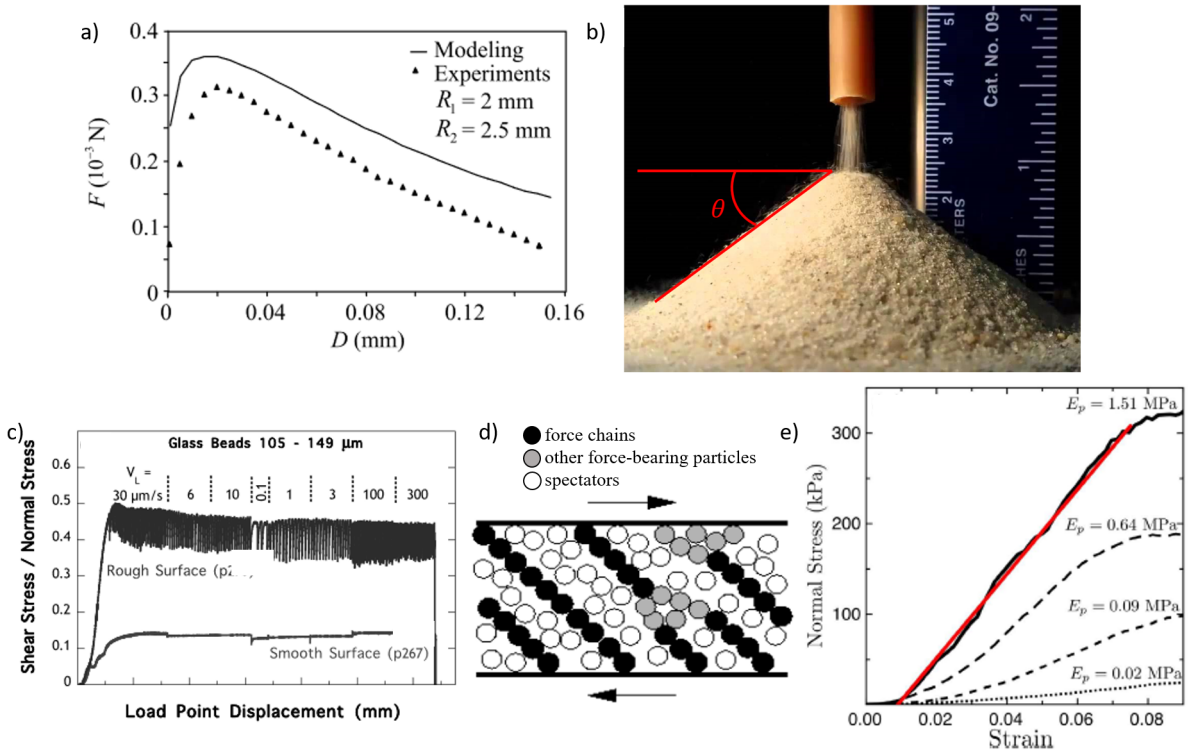

Figure 5.4: a) Force–distance plot for a capillary grain-pairs with a volume $V = 3$ mm^3 of the liquid bridge [211]. b) Angle of repose shown with a sand pile. Extracted from `https://www.youtube.com/watch?v=SIkRUv39SoI`. c) Comparison of the friction coefficient $\mu = F_t/F_n$ as a function of load point displacement for experiments consisting of smooth or rough glass beads (105–149 mm). Note the stick-slip instabilities that occur for rough surfaces. Loading velocity V_L is varied throughout the experiment. Adapted from [224]. d) Scheme of force chains inside a sheared granular material. From [232]. e) Typical stress-strain curves of the cohesive granular material, as measured for various stiffnesses of the polymer forming the bridges for W = 2.3%. The Young's modulus of a sample, E, is found by a least-squares fit to the linear region of its stress-strain curve, as demonstrated by the red line. From [217]

5.1.3 Characterisation of normal forces between spheres

Direct measurement of the normal forces between two spheres

A straightforward way to know if there are interaction forces between two objects is to measure it directly. For example, Soulie *et al.* [211] designed an experiment which allowed them to measure the force acting between two spheres in the presence of a liquid bridge (Figure 5.3a) as a function of the distance between the spheres using a high precision balance (Figure 5.4a). They found that the force is positive (attractive) and increase as the spheres are brought closer, until a maximal force is reached and steric effects appear, causing the force to decrease and change direction. This is a clear evidence of the attractive effect of the liquid bridge between the steel balls.

The idea of this method has a lot in common with atomic force microscopy (AFM), but allows measures with macroscopic objects which suits better the field of granular matter.

Measure of the material's elasticity

By quantifying the elasticity of a granular material, either by measuring the shear modulus $\mathcal{G}$ (see Section 8.1.1 in Chapter 8), or the young's modulus E during a compression experiment (see Section

1.5.1 in Chapter 1), one can have access to the magnitude of the normal forces between the spheres. Hemmerle *et al.* [217] measured the normal stress during compression experiments, and found that by increasing the elastic modulus of the polymer forming the solid bridges between beads (described in Section 5.1.1), they were able to directly influence the elastic modulus of the global material (Figure 5.4e).

It is important to note here that the initial volume fraction of the material also impacts the value of E or $\mathcal{G}$ [233–235]. The two notions are linked: the presence of normal and tangential forces induces a lower volume fraction (as it will be discussed in Section 5.2), thus a lower elasticity of the material.

5.1.4 Characterisation of tangential forces between spheres

Angle of repose

Granular materials can behave both as a liquid or a solid. When sand is poured from a bucket, it flows just like a liquid. However, it does not spread on the floor but instead forms a pile, like a solid. This pile is the result of interactions between the grains which allow to obtain a mechanically stable pile, in that case the static friction [236]. However, attractive processes, if they exists in the system, also play a role in the stability of the pile. One way to quantify these interactions is the measure of the angle of repose: the angle θ between the slope of the pile and a horizontal line passing through the top of the pile (Figure 5.4b). This method is traditionally used for systems with frictional but non-adhesive interactions as an easy and efficient way to measure the static friction coefficient since $\tan\theta \approx \mu_s$ [237–239].

When attractive forces are present, and whether there is friction or not between the spheres, no model currently exists which allows to extract a parameter which quantifies the magnitude of the attractive forces from the angle of repose. However the measure of the angle of repose is a simple and efficient way to highlight the existence of attractive and/or tangential forces between the spheres.

The way that one particular insect decided to use the angle of repose is captivating. The antlion lives in the Namib desert and needs to stay buried in the sand to avoid the extreme heat, at the risk of starvation since its preys remain at the surface. To answer this problem, the antlion builds sand cones and waits patiently at the bottom of it. When an hotrod ant goes down the cone, it cannot go up again because of the mechanical instability of the first layers of sand under its legs, which instantly goes down. The cone serves as a trap for the antlion which then just has to wait for its prey to fall at the bottom where it savagely kills it for food[2].

Shear flow through a tube

Tangential forces between spheres in granular media were also quantified by measuring the pressure needed to push granular objects through a tube with a piston. Anthony and Marone [224] measured the ratio of the shear stress over the normal stress, equal to the coefficient of friction, for glass beads with smooth and rough surfaces with the same size distribution and for different loading velocities

[2] A very short but breathtaking documentary about this is made available by the BBC at `https://www.youtube.com/watch?v=QSYpWaFsIRY`.

(Figure 5.4c). They observed a succession of stick-slip instabilities when shearing the system composed of rough glass beads, while these events only sporadically occurred when shearing the smooth glass beads. The force needed to move the beads is also higher for rough beads than for smooth beads (≈ 3 times higher). The mechanism proposed to explain the stick-slip events is the building of force chains from one side of the container to the other inside the granular material because of the inability of the beads to slide over each other (Figure 5.4d), which finally fail for a sufficient stress and allow the beads to move until another force chain is formed [240–242].

After this review of the normal and tangential interaction forces found between the spheres which compose granular medium, we discuss in Section 5.2 their impact on the global structure of the materials.

5.2 Structure of granular media

The macroscopic properties of granular materials are directly linked to their internal organisation, i.e. to the way the spheres are arranged in relation to one another. The control over this arrangement is then of crucial importance in order to control the mechanical or acoustic properties of the materials. Here, we first enumerate the different structural parameters of importance, then we discuss how the interactions between the individual spheres composing the material influence its organisation.

5.2.1 Introduction of the key structural parameters

The volume fraction Φ and local volume fraction Φ_l

The volume fraction of spheres, bubbles or drops Φ is a global parameter which measures the quantity of the solid, air or dispersed liquid phase respectively, present in a volume V of a granular material. It is defined as

$$\Phi = \frac{V_d}{V_d + V_c}, \tag{5.1}$$

where V_d is the volume of the dispersed phase (the hard spheres, the bubbles or the drops) and V_c the volume of the continuous phase. It is also called density of spheres, bubbles or drops. It is usually measured using imaging techniques such as tomography or confocal microscopy, or by measuring the weight of the material if one of the phases has a negligible weight and the density of the other phase is known (for foams and packing of hard spheres).

In random packings, the volume fraction of the material fluctuates locally, and it is then appropriate to use the local volume fraction Φ_l which quantifies the ratio of the volume of a sphere, bubble or drop and the available or free volume around that object. The measure Φ_l is made through the Voronoi tessellation, which is normally defined as the partitioning of a surface into regions based on distance to points. In 3D and replacing points by spheres of finite radius (or deformed objects), this gives the partitioning of the volume V of the material based on the distance between the surfaces of the spheres (Figure 5.5a). From this calculation, we obtain 3D cells of volume $v_{i,c}$ in which only one sphere, bubble or drop of volume v_i is present, and the local volume fraction of one object i is then $\Phi_l(i) = v_i/v_{i,c}$. The width of the distribution of Φ_l is an indication of the local fluctuations of volume fraction inside the material. Aste *et al.* [243] showed that the distribution of the volume of the Voronoi cells V calculated

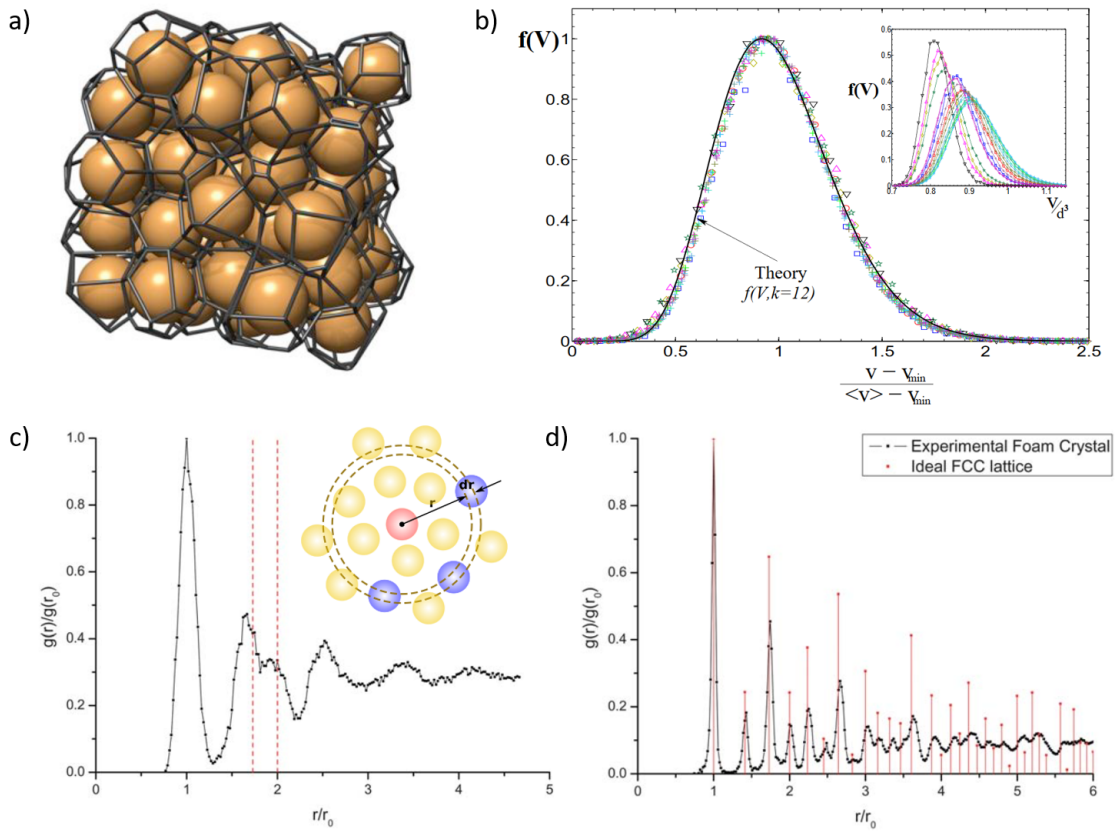

Figure 5.5: a) Packing of spherical beads with black wire frame to indicate the Voronoi cells of the beads. From [244]. b) Distributions of the Voronoi cell volumes V plotted against $(V - V_{min})/(\langle V\rangle - V_{min})$, where V_{min} is the minimal value of V and $\langle V\rangle$ its average value, collapse onto a universal curve, for different shape of the beads and different global volume fractions Φ. The insert shows the distributions plotted versus V/d^3 with d the sphere diameter. From [243]. c) Normalised $g(r)$ of a non-crystalline foam. From [245]. d) Normalised $g(r)$ of a foam crystal. From [245]. The insert in c) is a scheme of the calculation of $g(r)$ (image from the radial distribution function page of Wikipedia).

for the packing of hard beads plotted against $(V - V_{min})/(\langle V\rangle - V_{min})$, where V_{min} is the minimal value of V and $\langle V\rangle$ its average value, collapsed onto a single universal curve independently of the shape of the beads and the global volume fraction Φ of the packing (Figure 5.5b).

The global volume fraction Φ can be calculated as the harmonic mean of the local volume fraction Φ_l, i.e.

$$\Phi = \frac{1}{N}\sum_{i=1}^{N}\Phi_l(i), \tag{5.2}$$

where N is the number of objects in the material.

The coordination number z

In an arrangement of spheres, bubbles or drops, the mechanical stability is provided by the load applied by the objects on each other. For any cellular material, it is then possible to count the number of spheres, bubbles or drops bearing a load on a particular object i, which we will denote as z_i. The

coordination number of a material, or average number of contacts $\langle z \rangle$, defined as

$$\langle z \rangle = \frac{1}{N} \sum_{i=1}^{N} z(i), \tag{5.3}$$

quantifies the mean value of the distribution of the number of contacts per object throughout the material.

The radial distribution function $g(r)$

Another way to measure the density fluctuations inside a granular material is to calculate the radial distribution function $g(r)$, also called pair correlation function, which describes the density fluctuations as a function of distance r from a reference object. In other terms, it is the probability of finding an object in between the distances r and $r+\mathrm{d}r$ from a reference object, averaged over the entire material (insert Figure 5.5b). The shape of the function, i.e. the existence of peaks at particular positions, is characteristic of the overall organisation of the material and allows to differentiate random from crystalline organisations of objects. For example, Figure 5.5b shows the $g(r)$ for a foam slightly above the jamming transition exhibiting non-crystalline ordering with a set of characteristic peaks, and Figure 5.5c the $g(r)$ for a crystalline foam characterised by the presence of several tens of peaks.

5.2.2 Structural features of surfactant-stabilised emulsions and foams

We now look at the structural parameters Φ, Φ_l, $\langle z \rangle$ and $g(r)$ of monodisperse, surfactant-stabilised emulsions and foams, i.e. in the case of monodisperse, soft, frictionless spheres[3].

Volume fraction Φ Figure 5.1a shows an example of a foam floating on top of its foaming solution. We can see in this image that the drops are spherical at the bottom, and are increasingly deformed as we go up. This is a very important aspect of the volume fraction of emulsions and foams: it varies with the foam/emulsion height h since the bubbles/drops are compressed by buoyancy [1–3] (Figure 5.6 b). An analytical approximation of this variation was given by Maestro *et al.* [1] as

$$\tilde{h}(\phi) = k(\sqrt{\phi_c} - \sqrt{\phi})(3 + \frac{\sqrt{\phi_c^3}}{\sqrt{\phi}}) + \frac{k}{2}(3 - 2\phi_c - \phi_c^2) \ln\left[\frac{(\sqrt{\phi}+1)(\sqrt{\phi_c}-1)}{(\sqrt{\phi}-1)(\sqrt{\phi_c}+1)}\right], \tag{5.4}$$

where $\phi = 1 - \Phi$ is the volume fraction of continuous phase, $\tilde{h} = hR_{32}/l_c^2$ is the reduced height with $R_{32} =< R^3 > / < R^2 >$ the Sauter mean radius of the bubbles or drops and $l_c = \sqrt{\gamma/\Delta\rho g}$ the capillary lenght, and $k = 7.3$ for ordered and 3.2 for disordered foams and emulsions.

Because of the bubble's and drop's ability to deform, large variations of Φ can be accessed in foams and emulsions. Imagine a liquid with isolated drops or bubbles. By applying a pressure with a permeable membrane for example, i.e. by decreasing the volume accessible to the objects, we can bring them closer to each other, thus increasing the volume fraction Φ. The bubbles or drops are almost frictionless, which means that they are able to slide over each other in order to avoid bearing pressure. This

[3] In order to be realistic, the term frictionless should be interpreted as almost frictionless.

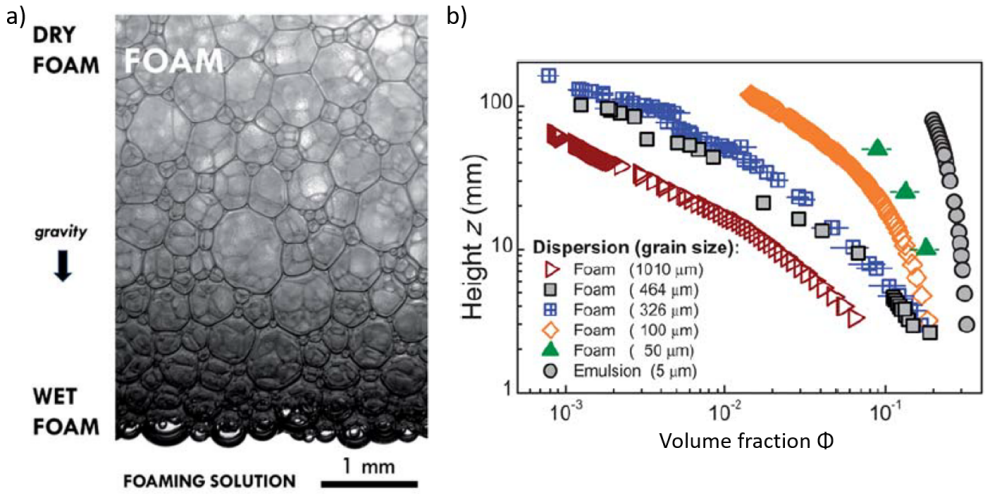

Figure 5.6: a) Example of a liquid foam floating on top of its foaming solution (in this case the detergent "Fairy Liquid"). Liquid drainage under gravity results in a gradient of volume fraction of liquid $(1 - \Phi)$. At the top (dry foam) the bubbles take on polyhedral shapes while at the bottom (wet foam) they are nearly spherical. From [248]. b) Examples of volume fraction profiles for different grain types and sizes. From [1].

rearrangement will be possible until a critical concentration Φ_c is attained and the objects are in contact in the densest arrangement possible without being deformed. Φ_c was given theoretically for crystalline organisations. For a hexagonal close-packed (fcc), or a face-centered cubic (fcc) lattice of equal-size spheres for example, $\Phi_c \approx 0.74$ [199, 203]. For random organisations, Φ_c, also called in that case the *Random Close Packing* (RCP) volume fraction Φ_{RCP}, is lowered, and experimental and numerical work showed that $\Phi_c = \Phi_{RCP} \approx 0.64$ [246]. Upon increasing Φ, the bubbles or drops deform to form an arrangement of polyhedral objects. When $\Phi \to 1$, a foam is called *dry* and for emulsions, the term *concentrated emulsion* is common. Below the limit $\Phi_{RCP} \approx 0.64$ for random packings or $\Phi_c \approx 0.74$ for crystalline arrangements, we speak of bubbly liquid or isolated droplets. It is noteworthy that the polydispersity of the bubbles or drops increases the value of Φ_c [247].

Coordination number $\langle z \rangle$ The mechanical stability of the packing at jamming is given by the repartition of the applied pressure inside the material through the contacts between the spheres. To the value of Φ_c is thus added the value of the isostatic number of contacts $\langle z_c \rangle$ to define the jamming transition. In other words, $\langle z_c \rangle$ is the lowest number of contacts needed for the mechanical stability of the material. Figure 5.7a shows a simulation result for the evolution of the coordination number $\langle z \rangle$ with the volume fraction of drops Φ in a surfactant-stabilised emulsion made by Zhang *et al.* [249]. It shows that for a randomly organised frictionless system, $\Phi_c \approx 0.645$ independently of construction history and $\langle z_c \rangle = 6$. This observation can be derived by isostaticity arguments [205, 209].

Above the jamming, the relation between $\langle z \rangle$ and Φ has been shown to follow a power law

$$\langle z \rangle - \langle z_c \rangle = z_0 \cdot (\Phi - \Phi_c)^{\beta}. \tag{5.5}$$

They found $\beta = 0.5$, and this value for the exponent of the power law was also found numerically by Durian [250] and Katgert *et al.* [251] for polydisperse frictionless foams, and experimentally by Brujic *et al.* [247].

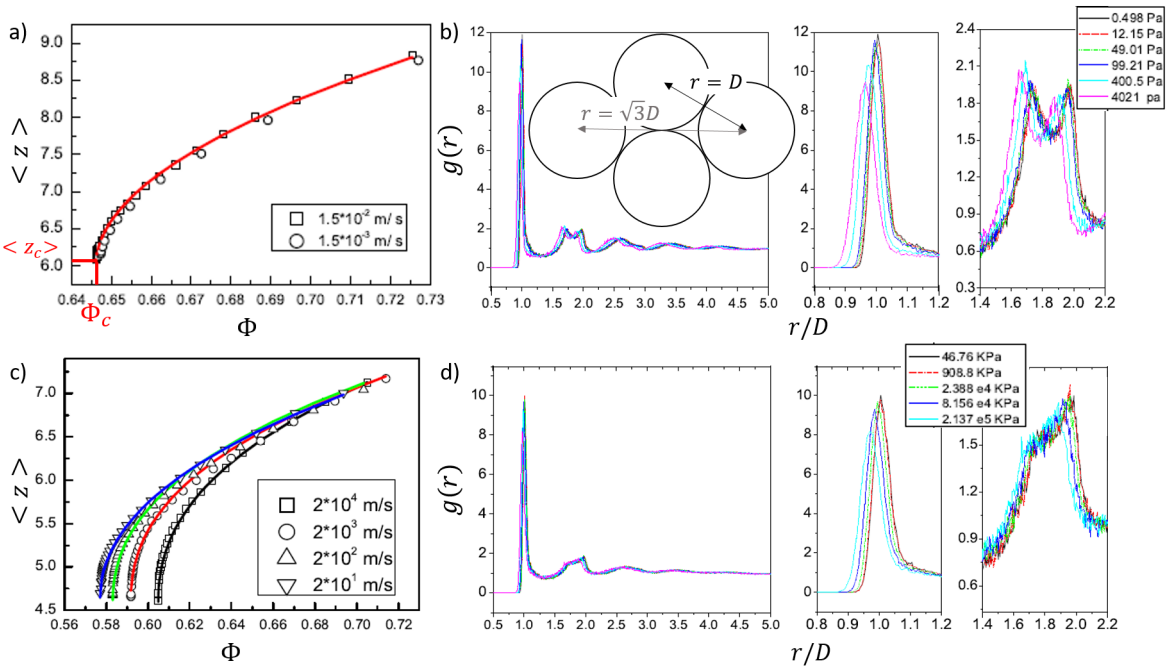

Figure 5.7: a) Evolution of the coordination number $\langle z \rangle$ with the volume fraction Φ in a surfactant-stabilised emulsion. The symbols are the data from the simulations and different symbol corresponds to different compression rates. b) Radial distribution function $g(r)$ for different applied pressure for a surfactant-stabilised emulsion, with close ups on the peaks. Insert is a scheme of the arrangement of the drops. c) Evolution of the coordination number $\langle z \rangle$ with the volume fraction Φ in a packing of hard frictional spheres with $\mu = 0.3$. The symbols are the data from the simulations and different symbols corresponds to different compression rates. d) Radial distribution function $g(r)$ for different applied pressure for a granular system, with close ups on the peaks. From [249].

Radial distribution function $g(r)$ Figure 5.7b shows the radial distribution function $g(r)$ as a function of the distance r normalised by the diameter of the drops D, for a numerical simulation of a packing of frictionless drops under increasing pressures. The radial distribution function exhibits three peaks at $r = D$, $r = \sqrt{3}D$ and $r = 2D$. The first peak at $r = D$ corresponds to the presence of objects in direct contact (or almost), called the first neighbours. As the pressure increases, this peak shifts to the left, indicating that the spheres are overall closer to each other in the material. The second peak at $r = \sqrt{3}D \approx 1.7D$ is attributed to local four-particle hexagonally close-packed arrangements. These three peaks were also found in other studies for soft frictionless systems, numerically [252] and experimentally for foams [245].

5.2.3 Packing of hard spheres

Volume fraction Φ For granular materials, the global volume fraction Φ of spheres is constant with the height of the material, contrarily to the evolution of Φ in surfactant-stabilised foams and emulsions. This is due to the Janssen effect: the contact forces between the spheres redirect the weight, i.e. te pressure, towards the walls of the container, and therefore the pressure in the bulk in a constant with the height [253]. When the spheres are poured in a recipient, they arrange driven by gravity and interacting via normal repulsive forces and friction forces at their interface (cf section 5.1). An

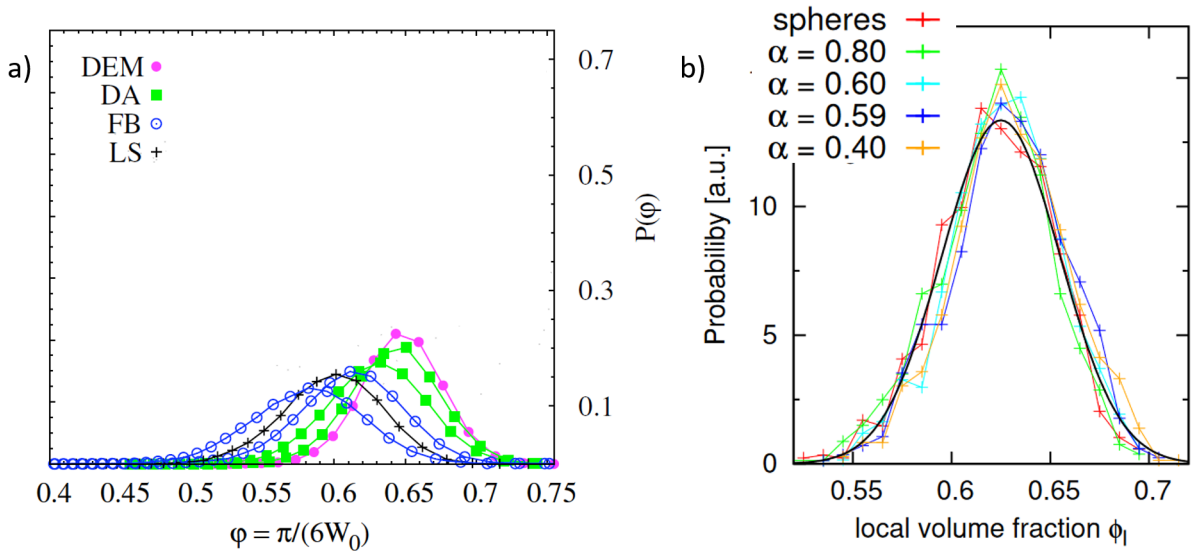

Figure 5.8: a) Distribution of the local volume fraction of packing of spheres $(\pi/6)/W_0$, where W_0 is the volume of the Voronoi cells, for packings obtained by different protocols: glass beads prepared by fluidized bed (FB), dry acrylic beads prepared by tapping/compression (DA), realistic frictional beads simulated by discrete element method (DEM) and ideal frictionless beads using the Lubachevsky-Stillinger Algorithm (LS). The six datasets shown here have global packing fractions $\Phi = 0.567$ (FB), 0.598 (FB), 0.636 (DEM), 0.630 (DA), 0.617 (DA) and 0.585 (LS). Note that the global volume fraction Φ is given as the average $\langle(\pi/6)/W_0\rangle$ over all Voronoi cells. Adapted from [244]. b) Scaling properties of the local volume fraction distribution of ellipsoidal beads $P(\Phi_l)$, for a given global volume fraction $\Phi \approx 0.625$. The black line is a Gaussian fit. From [263].

ensemble of spheres with a too low volume fraction simply collapses until it reaches mechanical stability. However, even if the packing after simple pouring may be mechanically stable, it is not necessarily the densest possible packing. Complex tapping, vibrating or fluidisation procedures, which give energy to the systems, are required to increase step by step the density to a more optimal value [254–258]. This causes the volume fraction of granular materials to be in-between two limits: the upper RCP limit measured at $\Phi_{RCP} \approx 0.634$ for both hard and deformable spheres [259, 260], and the lower RLP limit at $\Phi_{RLP} \approx 0.54$ [261]. The two limits are set by the presence of additional tangential forces between the spheres (friction). For frictionless spheres, mechanical stability is obtained for $\Phi \geq \Phi_{RCP}$. Upon increasing the friction at the interface, the lowest value of Φ for which mechanical stability of the packing is obtained decreases towards $\Phi_{RLP} = \lim_{\mu_s \to \infty} \Phi$, with the coefficient of friction μ_s defined in Section 5.1.2 [262].

Local volume fraction Φ_l The local volume fraction Φ_l is commonly used to measure the fluctuations of volume fraction is packing of hard spheres. Figure 5.8a shows different distributions of Φ_l for the packing of monodisperse, hard spheres with different global volume fractions Φ. The local volume fractions can usually be fitted by a symmetric Gaussian function. Interestingly, Schaller *et al.* [263] showed that the distribution of local volume fraction could also be fitted by a Gaussian curve for packings of ellipsoidal beads with different aspect ratio α (Figure 5.8b).

Coordination number $\langle z \rangle$ Zhang *et al.* [249] compared their results for frictionless drops with frictional spheres with $\mu = 0.3$. Figure 5.7c shows the evolution of $\langle z \rangle$ with Φ for the hard frictional

spheres and for different compression rates. They show that, as for soft frictionless bubbles and drops, the contact number also follows Equation (5.5) with $\beta = 0.5$ (Figure 5.7c). O'Hern *et al.* [205] studied numerically monodisperse and bidisperse granular systems, in both 2D and 3D, at the jamming transition and found the same results. Majmudar *et al.* [264] studied experimentally bidispere packings of spheres, and also found $\beta = 0.5$.

Zhang *et al.* [249] looked at the influence of the friction at the interface on the values of $\langle z_c \rangle$ and Φ_c. They determined that if frictionless systems jam at $\Phi_c \approx 0.64$ and are mechanically stable for $\langle z_c \rangle = 6$, the addition of friction decreases the values of both these parameters. They state that for $\mu \to \infty$ and as $\Phi \to \Phi^+_{RLP} \approx 0.57$, $\langle z_c \rangle \to 4$, well below the isostatic point in 3D. This was also reported by Silbert *et al.* [265].

Radial distribution function $g(r)$ Figure 5.7d shows the radial distribution function for a packing of frictional spheres with $\mu = 0.3$ [249]. Here also, the similarities with the frictionless drops and bubbles are striking, with three peaks at $r = D$, $r = \sqrt{3}D$ and $r = 2D$. By looking closely at the impact of the applied pressure on the position of the peaks, we can see that the variations of the position of the peaks are less pronounced as they are for soft spheres (Figure 5.7b).

5.2.4 Adhesive emulsions

The observation of interfacial forces between large ($R > 10 - 100$ µm) bubbles or drops has not been extensively treated in the literature. Only the presence of cohesive forces (adhesion) was reported by Brujic *et al.* [219–222, 266] and Hadorn *et al.* [218].

Volume fraction Φ Brujic *et al.* [266] observed the sedimentation of drops under a confocal microscope and reported that drops having adhesive patches at their interface reached mechanical stability at volume fractions $\Phi \approx 0.55$, while their non-adhesive counterparts exhibited a volume fraction $\Phi \approx 0.64$, as expected. In another study [222], they used silicone oil-in-water emulsions stabilised by a charged molecule (SDS) for which they varied the concentration of SDS in order to change the intensity of the attractive depletion forces $< F_d >$ between the drops. Still using confocal microscopy, they measured the local volume fraction of each individual drop after creaming of the emulsion, shown in Figure 5.9a. They could show that by varying $< F_d >$, they were able to vary the mean local volume fraction from $\Phi \approx 0.74$ down to $\Phi \approx 0.6$. For $< F_d > = 0$ N, they measure $\Phi_v > 0.64$, which can be explained by the polydispersity of the emulsion which increases the value of Φ_{RCP}. Interestingly, for low but non-zero values of $< F_d >$, they measure local volume fractions higher than the *RCP* value for $< F_d > = 0$ N, until a critical force is attained and Φ decreases as shown in the inset in Figure 5.9a.

Coordination number $\langle z \rangle$ Figure 5.9b gives the distribution of the number of contacts with varying $< F_d >$ for the silicone oil-in-water emulsions of Brujic *et al.* [222]. For $< F_d > = 0$ N, the isostatic value of the coordination number for frictionless spheres $\langle z \rangle = 6$ is measured. For $< F_d >> 0$ N, $\langle z \rangle$ follows the same evolution as Φ for this systems, it first increases above the isostatic value, then decreases again down to $\langle z \rangle \approx 4$ on average. This decrease is possible because attractive forces allow to locally stabilise structures with fewer than four contacts by creating force chains [267]. The mechanical stability with fewer contacts is consistent with the evolution of Φ in Figure 5.9a.

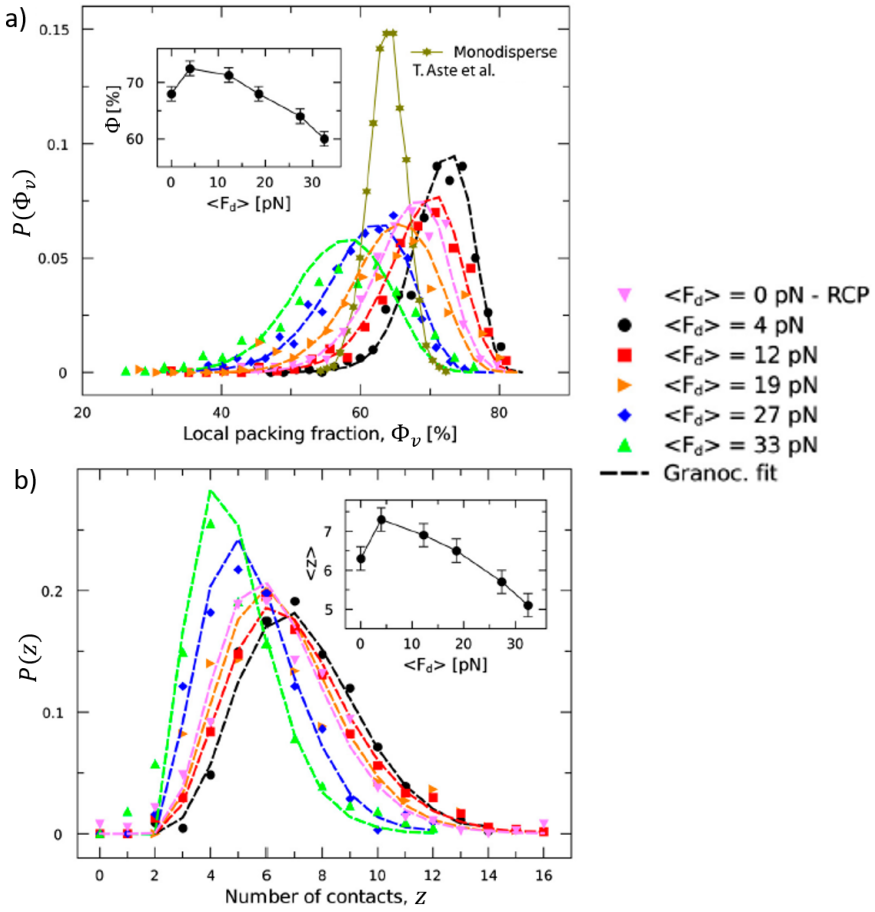

Figure 5.9: Probability density distributions of the local quantities $P(\Phi_v)$ (a), and $P(z)$ (b) are shown as a function of $< F_d >$, whereas the insets present the dependency of the corresponding average values. The dashed lines are fits with the "granocentric" model given in [268]. From [222].

5.2.5 Packing of hard cohesive beads

As we saw in Section 5.1.1, attractive forces in the packing of hard spheres can come from the presence of liquid [211] or solid bridges [217] between the beads. The presence of these forces surely impacts the volume fraction Φ and number of contacts $\langle z \rangle$ in these cohesive granular materials. Liu *et al.* [269] compared the volume fraction and contact number of wet beads depending on the surface tension γ of the wetting liquid. They showed that the volume fraction decreased with the surface tension (Figure 5.10a) below the limit of $\Phi(\mu_s \to \infty) \approx 0.54$. This is coherent with the evolution of Φ with the friction at the interface: interfacial forces, either cohesive or frictional, form mechanically stable packings at lower volume fractions.

5.3 What about tangential forces between drops?

In this chapter, we reviewed the preponderant role of interactions between the spheres on the overall structural properties of granular materials. Frictionless and non-adhesive spheres jam randomly at a

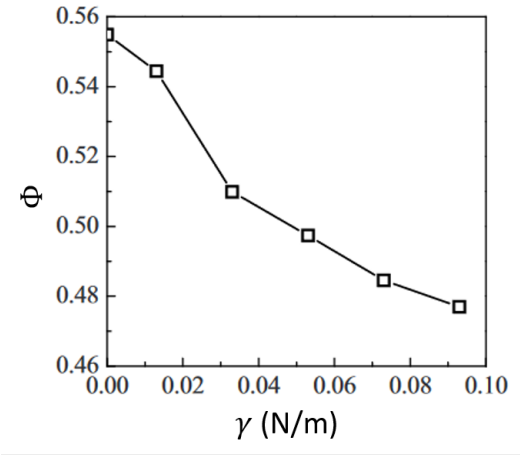

Figure 5.10: a) Mean volume fraction of beads Φ as a function of the surface tension γ of the wetting liquid. b) Mean coordination number $\langle z \rangle$ as a function of the surface tension γ. From [269].

volume fraction $\Phi_c = \Phi_{RCP} \approx 0.64$ regardless of their deformability and with a number of contacts $\langle z_c \rangle = 6$. Both these values of Φ_c and $\langle z_c \rangle$ decrease when tangential or attractive forces are added between the spheres, down to $\Phi_c \approx 0.48$ and $\langle z_c \rangle = 4$. We summarise these structural properties in Table 5.1.

These known and studied systems can be reported on a diagram depending on the deformability of the spheres, and the friction and/or adhesion between them. For clarity, only 2D diagrams were represented. In Figure 5.11a, we first represented a diagram classifying the systems depending on the deformability of the spheres and the magnitude of the interaction potential (tangential and normal forces) between the spheres, while Figure 5.11b classifies them depending on the magnitude of friction and adhesion between the spheres separately. We see that in both these diagrams, a part is unexplored for soft frictional and adhesive spheres.

In Part A of this manuscript, we reported the generation of ultra-stable PEG-in-MHDS emulsions. The stability was discussed to be the result of the creation of a polymeric skin around the PEG drops. The question we ask ourselves in this Part B is: *What is the impact of a polymeric skin around emulsion drops?* Indeed, polymers interact greatly with each other in a melt because of entanglement. We can then imagine that when two drops whose interface is made of a polymeric skin approach each other during the emulsion generation, the polymers at the surface of one will interact with the polymers at the surface of the other. The entanglement is known to create both friction and adhesion forces at interfaces. Would we then be able to fill the unexplored part of the diagrams in Figure 5.11 with our system? To answer that question, we first study in Chapter 6 the interactions between two drops presenting a polymeric skin at their surface. Then, in Chapter 7 we investigate the influence of these interactions on the structural properties of the emulsions.

System	Interactions	Φ_c	$\langle z_c \rangle$
Surfactant-stabilised foams and emulsions [249]	$\mu \approx 0$ No adhesion	0.64 $\Phi(h)$ [1]	6
Hard spheres [249]	$\mu \approx 0$ No adhesion	0.634 $\Phi = cst$	6
	$\mu > 0$ No adhesion	$0.54 < \Phi_c < 0.634$ $\Phi = cst$	$4 < \langle z_c \rangle < 6$
	$\mu \to \infty$ No adhesion	≈ 0.54 $\Phi = cst$	4
Adhesive emulsions [222]	$\mu \approx 0$ Adhesion	$\Phi_c < 0.64$	$\langle z_c \rangle \to 4$
Hard adhesive spheres [269]	$\mu \approx 0$ Adhesion	$\Phi_c \approx 0.48$	4

Table 5.1: Summary of the structural characteristics of the different systems studied in this chapter (monodisperse spheres in disordered arrangements)

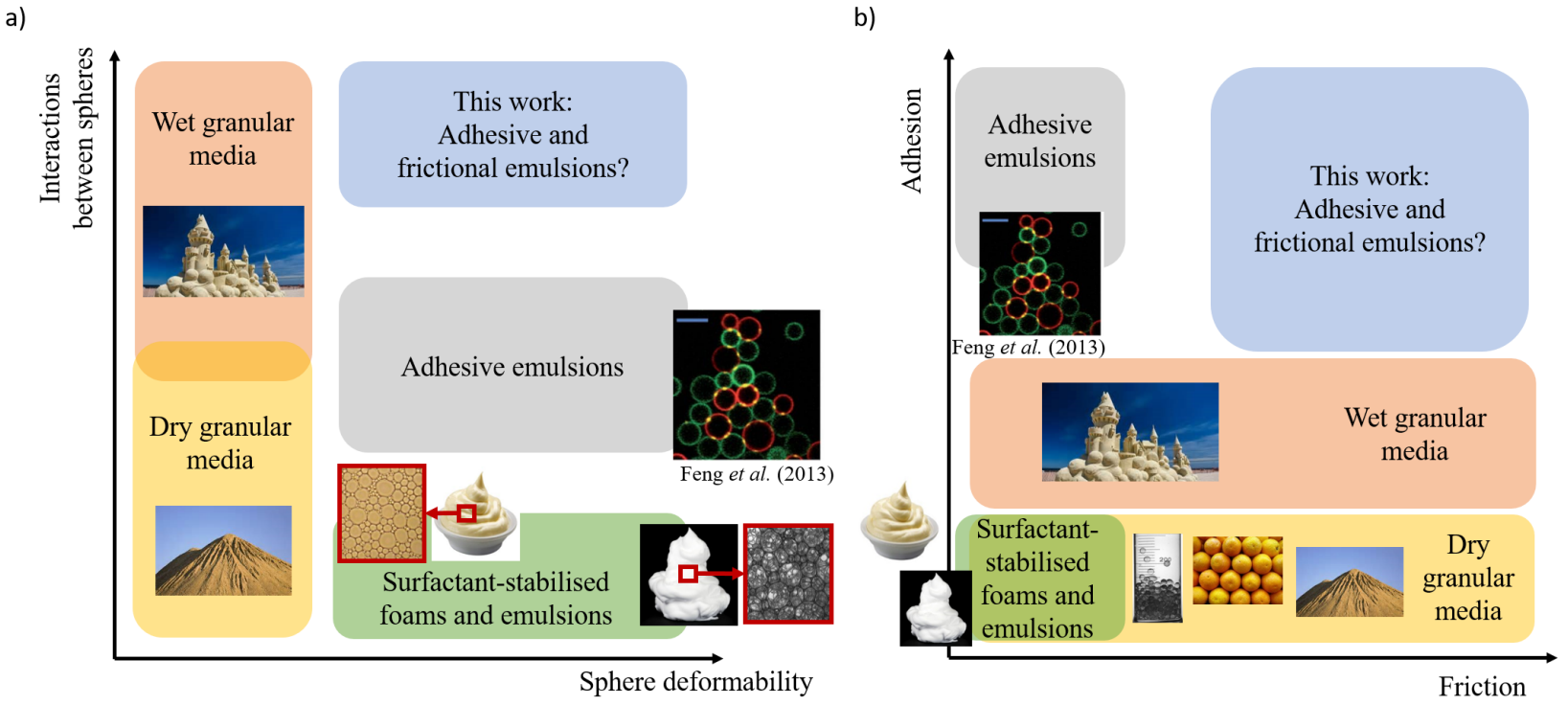

Figure 5.11: Graphical representations of granular systems studied depending on a) the deformability of the drops and the magnitude of interactions between the drops (friction and/or adhesion) and b) the friction or adhesion at the interface of the spheres. This study aims at characterising the structural properties of emulsions composed of deformable drops presenting both friction and adhesion at their interface.

Chapter 6

Interactions between droplets presenting a polymeric skin at their surface

In Chapter 5, we determined that the normal and tangential forces between individual spheres in a granular material have a great impact on the way they pack. At the jamming transition, the packings are more dense for frictionless and non-adhesive spheres than for frictional or adhesive spheres. The aim of this part is to characterise and control the packing of PEG drops surrounded by a polymeric skin in a liquid silicone matrix. For this purpose, we use here PEG-in-Sylgard 184® emulsions.

Here, we always refer to drops of PEG-400 containing a crosslinker/catalyst concentration $C = 0.05$ mol%, generated using the methods described in Section 1.2 in Chapter 1, and a continuous phase composed of Sylgard 184® base and D_4 (cf Section 1.1.1 in Chapter 1). In order to change the density difference between the drops and the continuous phase, we added dodecane, a solvent of the Sylgard 184®, into the continuous phase with three different concentrations (0%, 5% and 10% in weight %). We will also investigate its effect on the structural properties of the packing in Chapter 7.

We study the interfacial properties of the PEG droplets surrounded by a polymeric skin, inside the liquid silicone matrix. We first show in Section 6.1 how the presence of interactions between the drops is evidenced macroscopically. Then, we try to quantify the normal and tangential forces between two individual drops in Sections 6.3 and 6.2 respectively. Finally, we discuss in Section 6.4 the influence of the dodecane on the magnitude of the normal and tangential forces. In Chapter 7, we will analyse the influence of the drop interactions on the emulsion structure.

6.1 Macroscopic evidence of the presence of interactions

In granular media, one way to evidence and measure the friction at the interface between the grains is to measure the static or dynamic angle of repose, as explained in Chapter 5 Section 5.1.4. We then naturally measured the dynamic angle of repose θ made by the drops in the continuous phase, during the generation as shown in Figure 6.1. The experimental protocol of the measure is detailed in Chapter 1 Section 1.4.2. Table 6.1 gives the values of θ measured for three concentrations of dodecane in the continuous phase: 0, 5 and 10%. First of all we can notice that θ is low but non negligible for 0% of dodecane in the continuous phase. θ increases greatly with the addition of dodecane from $\approx 10°$ up to

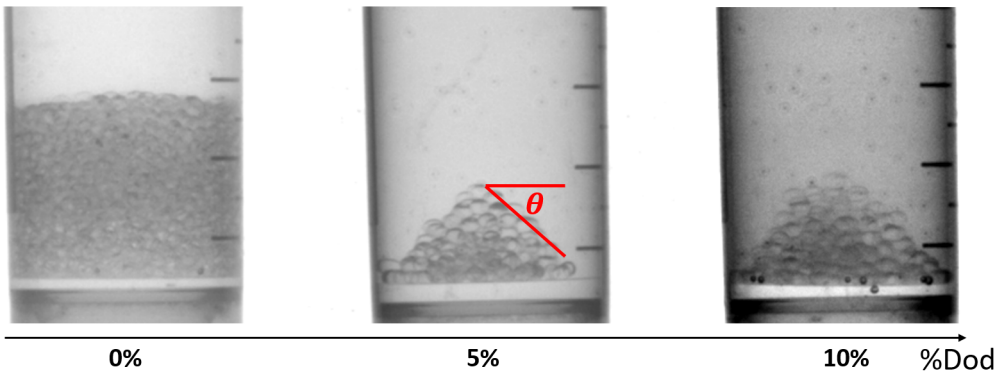

Figure 6.1: Images of the emulsions during the generation for 0, 5 and 10% dodecane in the continuous phase showing the unusual measure of a finite contact angle. b) Dynamic angle of repose measured for each dodecane percentage measured during the generation of the emulsions.

$\%Dod$	θ (°)
0%	10.8 ± 0.5
5%	40.8 ± 2.1
10%	43.4 ± 2.3

Table 6.1: Dynamic angle of repose measured for each dodecane percentage during the emulsions generation as shown in Figure 6.1.

$\approx 40°$. This indicates the presence of adhesive or tangential forces between the drops with and without dodecane, and the increase of the importance of these interactions in presence of dodecane. Note that the observation of a finite θ is highly unusual for emulsions. The difference between the value of θ at 5 and 10% of dodecane is not statistically significant in this experiment. To see whether there is a significant difference or not, we should vary the dodecane concentration in a more detailed manner.

The angle of repose is usually used to quantify the coefficient of friction of the objects with the equation $\tan\theta \approx \mu$. However in our case we expect both tangential and adhesive forces at the interface due to the presence of the polymeric skin. As the decrease of the volume fraction and number of contacts in sticky emulsions suggests [222, 266], adhesive forces should also impact the value of θ, and we are then not able to differentiate the role of each interaction in this experiment. In the following, we attempt to characterise these interactions using the double drop experiment (DDE) (Section 1.4.3 in Chapter 1).

6.2 Characterisation of the adhesion between two drops

Probing the presence of adhesion forces between the drops can be done by separating two drops initially in contact and observing the deformations of the drops. We do this using the double drops experiment (DDE) presented in Section 1.4.3 in Chapter 1. This experiment was developed during this thesis work, and we are thus able to present here only preliminary results.

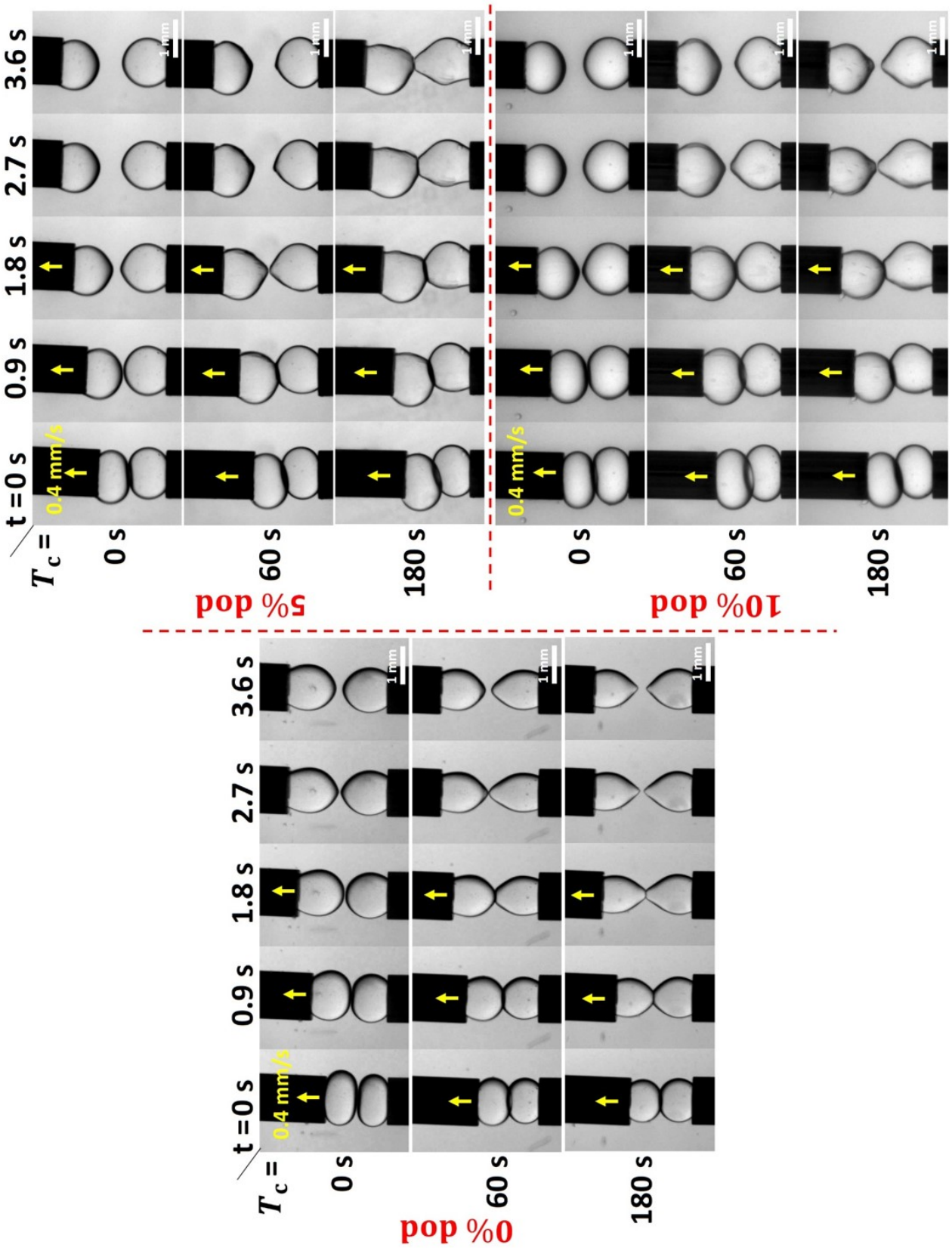

Figure 6.2: Image sequences of the separation of the drops for 0, 5 and 10% of dodecane in the continuous phase, at speed $v_t = 0.4$ mm/s after a contact time between the drops of either $T_c = 0$ s, $T_c = 60$ s and $T_c = 180$ s.

As it will be discussed in Section 8.1.2 in Chapter 8, adhesion processes can be dependent on the traction speed. Therefore, we present here a traction experiment between two drops performed at low (Section 6.2.1) and high (Section 6.2.2) drop separation speeds. Unfortunately, this experiment does not allow to measure the force needed to separate the drops. However, we can look at other parameters to highlight the presence of adhesion.

6.2.1 Drop separation at low speed

In a first attempt to observe the signature of adhesive forces between two drops of volume $V = 2$ µL initially in contact ($d_{min} = 1.5$ mm) which are pulled apart from each other, we first separated the drops at low traction speed v_t 0.4 mm/s after a stabilisation time $T_s = 120$ s (during which the drops are not in contact) and a contact time $T_c = 0$, 60 or 180 s, with either 0, 5 or 10% dodecane added in the continuous phase. Images sequences of the traction are shown in Figure 6.2. We can see that for $T_c = 0$ s, we systematically cannot see any resistance to detachment since nothing particular happens at the interface between the drops. However, for $T_c = 60$ s, we notice the apparition of wrinkles at the interface (for 5 and 10% of dodecane in the continuous phase), accompanied by large deformations of the drop compared to its equilibrium spherical shape. These are even more pronounced as T_c increases to 180 s.

6.2.2 Drop separation at high speed

In this section, we probe the behaviour of the drops separated at high traction speed v_t. As in Section 6.2.1, we generate two drops of volume $V_d = 2$ µL each, in the continuous phase with either 0, 5 or 10% of dodecane. We let a stabilisation time $T_s = 180$ s, then bring them in contact at speed $v_c = 0.1$ mm/s (compression) and leave them in contact for the contact time $T_c = 120$ s at $d_{min} = 1.5$ mm. After this time, they are abruptly separated at speed $v_t = 4$ mm/s (traction).

Figure 6.3a, b and c show image sequences of the separation of the two drops with time for respectively 0%, 5% and 10% of dodecane in the continuous phase. The first image on the left is before separation, the second image is the first image right after separation, and the needle does not move for the following images. In this experiment, the separation of the needles is sudden, and we see for each percentage of dodecane that the two drops deform and are still in contact right after the separation. However, the deformations are much more pronounced in the case of 5% and 10% of dodecane, and we also see wrinkles at the surface of the drops for 5% of dodecane. As an attempt to quantify the interactions at the interface, we measured the evolution of the radius of the surface of contact R_c with time, which gave the relaxation times indicated in Figures 6.3a, b and c, i.e. the time needed for the drops to separate. These indicate that R_c relaxes faster in the case of the continuous phase with 10% of dodecane than with 0%, and that both of them relax faster than with 5% of dodecane. However, the amount of dodecane in the continuous phase changes its viscosity and density, and in order to take this into account, we normalise the time t with the characteristic time τ_r needed for a drop to recover a spherical shape driven by the surface tension between the two phases in the case where there is no interactions with the other drop. This characteristic time is calculated by taking into account the effects of the surface tension γ and the viscosity of the continuous phase η only, which gives

$$\tau_r = \frac{\eta R}{\gamma}, \tag{6.1}$$

where R is the radius of the drop (estimated here as $(3V/4\pi)^{1/3}$), $V = 2$ µL its volume, and $\gamma = 5$ mN/m. We normalised R_c with the initial contact radius $R_{c,i}$, and the evolution of the normalised radius of contact $R_c/R_{c,i}$ with the normalised time t/τ_r is shown in Figure 6.3d, $t/\tau_r = 0$ corresponding to the moment right after separation (second image from the left in Figure 6.3a, b, and c). First, we can see that R_c relaxes in the same manner for both 0% and 10% of dodecane, while the relaxation for 5% of dodecane is much slower. Finally, we see that for 0% of dodecane in the continuous phase, the normalised time needed for the drops to separate t_f/τ_r is higher than 1, i.e. we could think that there are interactions at the interface between the drops, as it was suggested by the measure of the finite angle of repose in Figure 6.1. This suggests that the addition of dodecane in the continuous phase induces higher adhesion (attractive normal) forces between the drops, though there seems to exist an optimal concentration. The more rapid relaxation of the system with 10% of dodecane may be the result of less adhesive forces, or of an increase of the skin elasticity, which is not taken into account in our scaling, i.e. the surface tension would have to be replaced by a restoring stress crossing surface tension and surface elasticity. More systematic experiments would be required to distinguish between the different contributions.

6.3 Quantification of the tangential forces between the drops

Here we attempt to quantify the tangential forces acting between the drops. Indeed, we showed in Section 6.2 that there are adhesive forces acting at the interface between the drops, responsible for parts of the behaviour observed in Section 6.1. In this Section, we investigate whether tangential forces, i.e. friction, are also present at the interface.

Figure 6.4a shows an image sequence of the experiment. Two 2 µL drops are created in the continuous phase with either 0, 5 or 10% of dodecane. They do not touch during the stabilisation time $T_s = 120$ s. At the end of this stabilisation time, they are brought in contact during[1] $T_c = 0$ or 60 s. Then, the bottom needle is moved to the left, and the drops slide over each other. Once the needle stops moving, we quantify the relaxation towards the equilibrium position of the drop on the top by measuring the left θ_L and right θ_R angles between the drop and the needle as shown in Figure 6.4b. An example of the measure of $\theta_L(t)$ and $\theta_R(t)$ is given in Figure 6.4c, for 0% of dodecane in the continuous phase and $T_c = 60$ s. The $\theta(t)$ curves can both be fitted by an exponential function $\theta(t) = \theta_f + \theta_0 \exp(-t/\tau)$, and this allows to extract the final value θ_f and the relaxation time τ towards θ_f, for both θ_L and θ_R. To analyse the dynamics of the evolution of the angles towards the final values, while getting rid of the influence of the volume of the drops on the final angle[2], we consider the relaxation in time of the angles normalised by the mean of their final values

$$\bar{\theta}(t) = \frac{\theta_{L,R}(t)}{\langle \theta_f \rangle}, \tag{6.2}$$

where $\langle \theta_f \rangle = \frac{\theta_{L,f} + \theta_{R,f}}{2}$.

[1] $T_c = 0$ s means that the movement towards the left starts as soon as the needle stops moving vertically. The contact time is then negligible, but not strictly equal to 0.

[2] The motor controlling the volume of the drops is not sensitive enough in this experiment, so that we have some drop size variations between experiments.

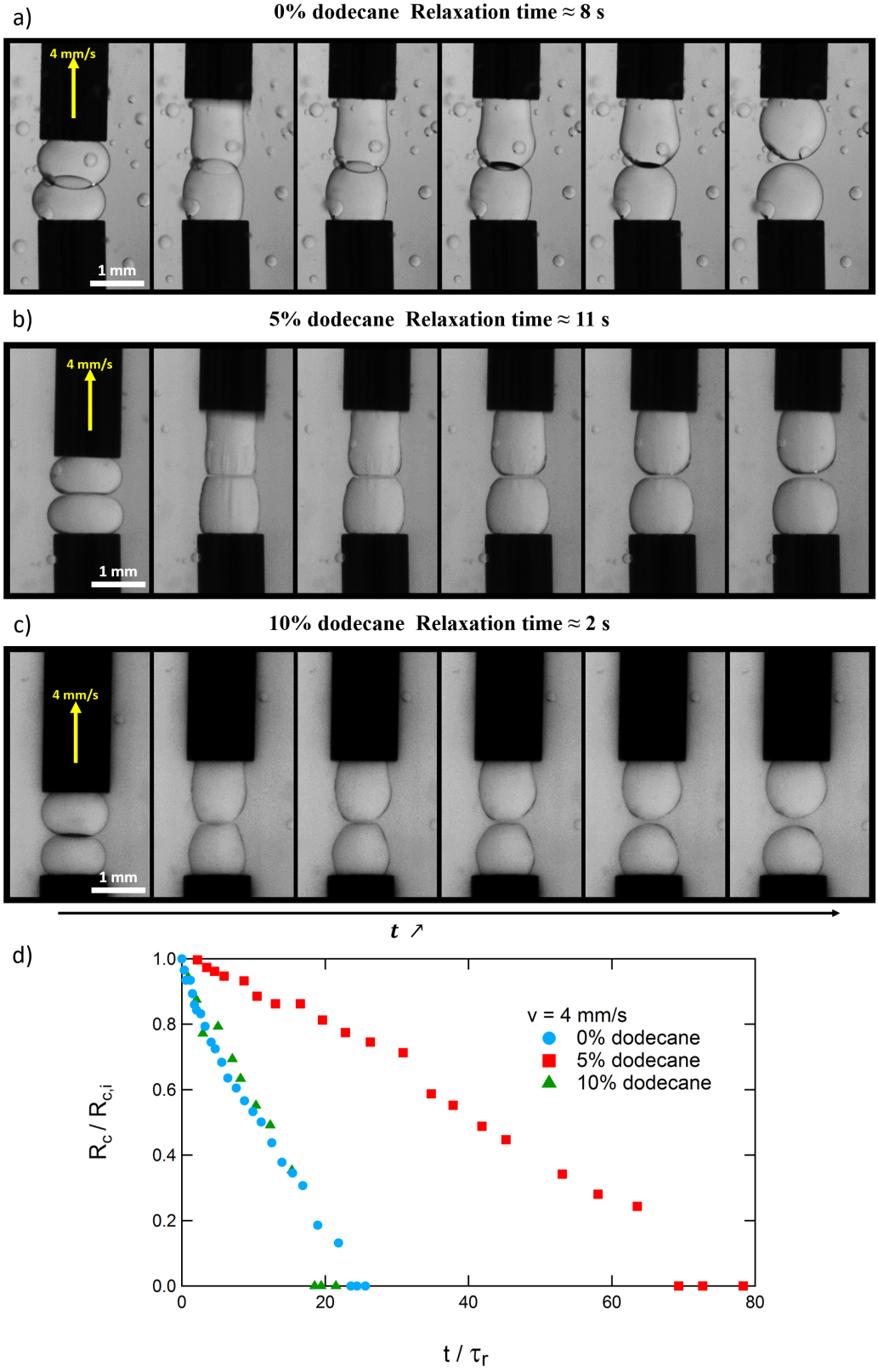

Figure 6.3: a), b) and c) Image sequences of the fast separation of the drops followed by the relaxation for 0% (1 image every 1.6 s), 5% (1 image every 2.2 s) and 10% (1 image every 0.4 s) respectively. d) Evolution of the radius of the surface of contact between the drops R_c normalised by the initial radius $R_{c,i}$ after the separation of the needles.

Figure 6.4d shows the evolution of $\bar{\theta}$ with time for $T_c = 60$ s. The different dodecane concentrations in the continuous phase are separated by color. We can see in this graph that the difference between the final angles is more and more pronounced as the dodecane concentration increases, while the relaxation time towards the final value remains the same for each concentration. Figure 6.4e shows the evolution of the difference between the final angles $\theta_{R,f} - \theta_{L,f}$ with the concentration of dodecane and for two different contact times $T_c = 0$ and 60 s. We can see that for $T_c = 60$ s (which is the representation of the final state of Figure 6.4d), on the one hand the difference $\theta_{R,f} - \theta_{L,f}$ increases with the dodecane percentage, and mostly that the difference is not zero for 0% of dodecane, indicating interactions between the drops even without dodecane in the continuous phase. For $T_c = 0$ s, $\theta_{R,f} - \theta_{L,f}$ is close to zero for 0 and 5% of dodecane, and increases to $\theta_{R,f} - \theta_{L,f} \approx 20°$ for 10% of dodecane, indicating that the mechanisms at hand are faster for high dodecane concentrations.

The experiments in Sections 6.2 and 6.3 seem to show that the magnitude of the interactions between the drops increases with both the contact time between the drops the amount of dodecane in the continuous phase. In Section 6.4, we discuss these results and the possible mechanisms responsible for this effect.

In Figure 6.5, we compared the images of the sliding experiment with simulations (superimposed in red) using the program Surface Evolver[3]. Surface Evolver is used for the modelling of liquid surfaces shaped by various forces and constraints at equilibrium. It searches for the configuration of a given system with the minimal energy. We used it to find the equilibrium shape of the drops sliding on each other as in the right image of Figure 6.4a, assuming that only surface tension is acting on the drops, i.e. no surface elasticity, no adhesive forces and no friction at the interface. This is the condition one would expect for "ordinary" emulsion drops stabilised by low molecular weight surfactants.

6.4 Discussion

In Section 6.1, we showed that the packing of the PEG-400 drops containing a concentration $C = 0.05$ mol% of crosslinker/catalyst, in the Sylgard 184® base/D_4 mix formed different angle of repose depending on the presence of dodecane in the continuous phase. From this, we deduced that there should be tangential and/or adhesive interactions at the interface between the drops, as the review of the literature on packings of spheres showed in Chapter 5. These macro-scale interactions between the drops would be the result of micro-scale interactions between the polymeric skins around the drops discussed in Appendix III. Indeed, polymers entangle, which causes energy dissipations when attempting to separate them. When a drop surrounded by a polymeric skin falls on another one during the emulsion generation, the polymer forming the skin of the first drop interact with the polymers around the second drop, and resist their movement with respect to each other. However, this experiment at the macro-scale did not allow to separate between tangential and attractive normal forces.

[3]available at `http://facstaff.susqu.edu/brakke/evolver/evolver.html`

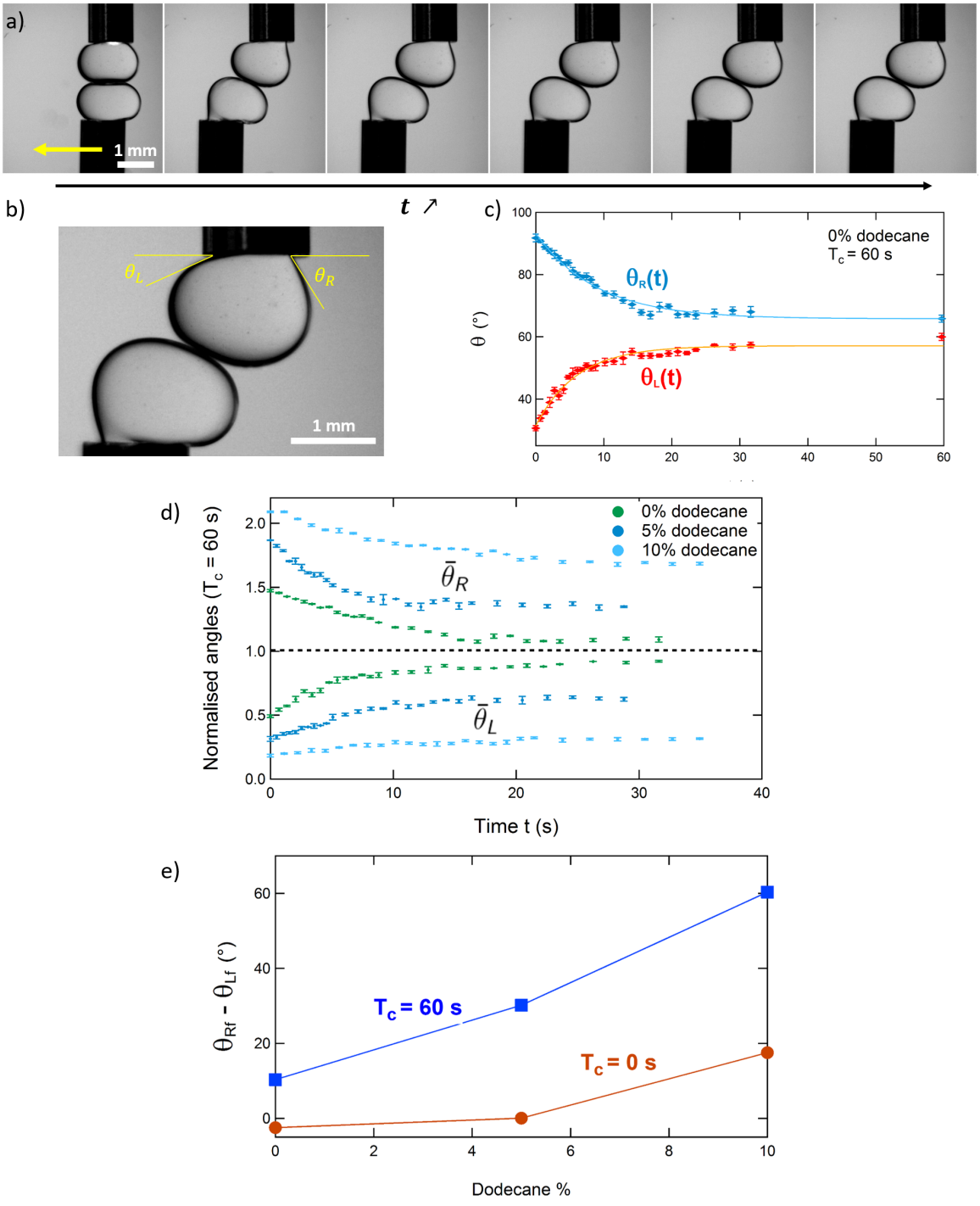

Figure 6.4: a) Image sequence of the interfacial friction experiment: the drops are put in contact for either $T_c = 0$ or 60 s, then the bottom drop is moved towards the left and slides over the top drop. The interfacial friction is quantified by the measure of the evolution of the left θ_L and right θ_R angles between the top drop and the needle with time as shown in b). c) Evolution of θ_L and θ_R with time for 0% of dodecane and $T_c = 60$ s. $t = 0$ s is the time at which the bottom needle stops moving. Both curves are well fitted by an exponential. d) Evolution of $\bar{\theta}$ with time for $T_c = 60$ s. e) Evolution of the difference between the final values of θ_R and θ_L $\theta_{R,f} - \theta_{L,f}$ with the percentage of dodecane in the continuous phase, for $T_c = 0$ s and $T_c = 60$ s.

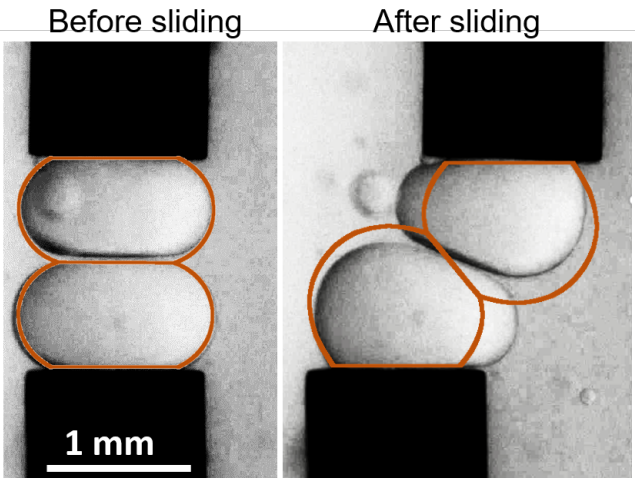

Figure 6.5: Superimposition of experimental images and shape profile of simulations using Surface Evolver of the sliding of drops, for 5% of dodecane in the continuous phase. The simulations assume no adhesive or frictional forces between the drops.

In Section 6.2, we looked at the deformations of the interface of drops initially in contact and separated perpendicular to the interface at low and high speed in order to probe the normal forces. For systems with 5 and 10% of dodecane in the continuous phase, we were able to see large deformations of the drops, and even wrinkles at the interface, which both indicate a resistance to the separation, for finite contact times T_c. The wrinkles at the surface of the drops are the signature of the surface elasticity intrinsic to the polymeric skin. This skin is stretched between the top needle pulling the drop upwards and the bottom drop attached to an immobile needle. This shows that with these traction experiments we observe adhesive forces between the drops. By analysing the radius of the surface of contact between the drops, we were able to show that its relaxation time does not increase monotonously with the dodecane percentage but rather that it reaches a maximum for a concentration below 10%. The quantification of the forces between the drops during the separation are still out of reach with this experimental protocol. However, the addition of a force sensor to the experiment seems feasible for future investigations. We would expect forces in the order of magnitude of the nN or μN.

The tangential forces at the interface between the drops were investigated in Section 6.3. We studied the resistance to sliding of two drops on each other by measuring the relaxation of the angles formed between the top drop and its needle. We noticed that for negligible contact times (T_c = 0 s), we could only measure a resistance to sliding for the highest dodecane concentration (10%), while for T_c = 60 s, a resistance to sliding was measured for all concentrations, but increased significantly with the dodecane percentage.

The movements of the drops in the experiments (downwards, then sideways) are made at a speed v = 0.1 mm/s comparable to the speed of the falling drops in the continuous media, which are estimated equal to respectively 0.06, 0.13 and 0.21 mm/s for 0%, 5% and 10% of dodecane by balancing gravity and viscous drag using the Stokes law. The value of T_c to take as a reference to explain the results in Chapter 7 however decreases with the amount of dodecane in the continuous phase: values close to T_c = 0 s are representative of the case where 10% of dodecane are added in the continuous phase, and longer values should be considered to explains the results with 0 and 5% of dodecane. Experiments of the separation of the drops for T_c = 0 s do not show the signature of normal attractive forces between the drops. However, we were able to see them for higher values of the contact time, which

implies that the magnitude of these forces are dependent on the contact time for a given dodecane concentration. We can thus already have access to informations about the interactions at the interface, and the role of adhesion and/or friction. As we will develop in Chapter 7, the drops are created in the air, outside of the continuous phase, into which they fall and go down distances between 10 and 40 mm. Assuming a distance of 40 mm, this gives falling times of $\approx$ 670, 300 and 190 s for 0%, 5% and 10% of dodecane respectively, that we mimic with the stabilisation time T_s in our experiments. Here, we took systematically $T_s = 120$ s, which is below the estimations for all concentrations, for a preliminary study. This allows to compare all dodecane concentrations without taking into account viscosity effects which probably also impact the reaction rate at the interface. Future studies should however look at the impact of the variation of the stabilisation time.

6.4.1 Impact of the contact time for a given dodecane concentration

For 0% of dodecane in the continuous phase, we saw that the drop returns to its equilibrium position with $\theta_{L,f} = \theta_{R,f}$ (Figure 6.3e), i.e. the drops are able to slide over each other, for $T_c = 0$ s. This is coherent with the finite but low angle of repose measured in Section 6.1 indicating very low tangential and/or adhesive forces between the drops. Upon increasing the contact time ($T_c = 60$ s), we increase the interactions at the interface. Looking at the separation of two drops with 0% of dodecane in the continuous phase (Figure 6.3d), we see that the relaxation of the surface of contact takes a longer time than it would assuming only surface tension effects. The fact that no deformations or wrinkles at the interface are seen in the image sequence in Figure 6.2.1 shows however that the magnitude of attractive interactions stays low.

In the case of 5% of dodecane in the continuous phase, the measure of the angle of repose during the emulsion generation shows unambiguously the presence of strong interactions at the interface between the drops. However, for $T_c = 0$ s, the measure of the final values of the left and right angles of the top drop during the sliding experiment shows a complete relaxation of the angles (Figure 6.4e), and the drop separation experiment shows no visual sign of adhesive forces between the drops (Figure 6.2.1) for this value of T_c. Upon increasing T_c, the complete relaxation of the angles is prevented (Figure 6.4e), and strong adhesive forces are indicated by large deformations and wrinkles at the interface in Figure 6.2.2b.

Finally, for 10% of dodecane, we can see in Figure 6.4e that the complete relaxation of the angles is not observed even for $T_c = 0$ s, which correlates well with the measure of the angle of repose in Figure 6.1. This effect is even more pronounced for $T_c = 60$ s, and deformations of the drops in Figure 6.2.2c for $T_c = 120$ s during separation of the drops for 10% dodecane in the continuous phase are also observed.

For a given concentration of dodecane, the mechanisms responsible for the interactions between the drops seem to be dependent on the contact time. A first hypothesis is given by the fact that we have polymeric gels at the drop surface which penetrate each other with time. As the contact time increases, entanglement is made easier between the polymers of each drop. The impact of the contact time on the magnitude of the interaction between drops is thus easy to interpret. Also, since the reaction at the interface between the drops is not stopped after the stabilisation time, and thus continues during contact, an hypothesis would be that the reaction occurs between the skin at the surface of each drop, "connecting" them chemically. However, the strength of the bond between the two drops would still

be lower than the strength of the bonds between the polymers at the interface of one drop since the reaction time is lower.

6.4.2 Impact of the dodecane concentration

The measure of the angle of repose in Section 6.1 seems to indicate that the concentration of dodecane does not play a measurable role in the macroscale properties of the packing of spheres, only the absence or presence of it. The importance of the concentration of dodecane on the packing of the drops is studied in detail in Chapter 7. However, in Section 6.2 we saw that the forces resisting the separation of the drops were higher for 5% of dodecane rather than for 10%, while in Section 6.3 the measure of the angles between the drop interface and the needle showed that the sliding of one drop over the other was more efficiently blocked at 10% of dodecane in the continuous phase rather than 5%. The fact that the conclusions drawn by these two experiments do not coincide seems counter-intuitive. This could however be explained by a different surface elasticity between the system with 5% of dodecane and the system with 10%. Assuming that the surface elasticity of the polymeric skin at the surface of the drop is higher for 10% of dodecane than for 5%, there would be a higher restoring force in the separation process in the experiments in Section 6.2 resisting the deformation of the drops, which we would need to take into account in the scaling proposed in Equation (6.1).

An important question for this chapter is whether we can talk separately about adhesion and/or friction at the interface. Experiments in Section 6.2 unambiguously show adhesive processes between the drops. Now we need to determine whether we can say that the phenomena observed in Section 6.3 are frictional forces or not. Indeed, adhesion could also prevent the sliding of the drops on each other. Granular materials with lower volume fraction were indeed observed in the presence of adhesive forces between drops in an emulsion with no friction between the drops [222]. In granular materials, friction is added between the spheres by surface roughening of the beads, while adhesion forces are kept equal to zero. In our case, the forces are induced by the presence of the polymeric interface and their magnitude seems to vary by the presence of dodecane in the continuous phase. In polymeric materials, either polymer melts or elastomers (crosslinked network of polymer chains), frictional and adhesive processes can both arise from entanglement and chemical or physical bonding of the polymer chains at the interface. This means that in our case, we cannot truly separate the contributions of adhesion and friction. Indeed, the friction between two materials depends on many parameters [270]: surface roughness (as said before, the most, if not only, used in granular matter), surface chemistry (linked to the thermodynamic work of adhesion W of the system, cf Chapter 8), lubrication, environment, temperature, etc. In our case, the interface is not roughened at the interface scale, though it is at the molecular scale. The lubrication is important in our system, where it is provided by the continuous phase in between the two drops. The viscosity of the continuous phase is thus important, and could explain the differences seen between the different dodecane concentrations in the experiment where two drops slide on each other for a given contact time. The dodecane, being a solvent of the PDMS[4], also changes the surface chemistry of the interface by swelling the polymeric skin. This might make it easier for polymers to entangle at the interface when the drops are in contact, which would explain why the adhesion between the drops depends on the dodecane concentration in the continuous phase.

[4]This is easily verified by putting a piece of crosslinked PDMS in dodecane and measuring its dimensions before putting it in the solvent and after.

Finally, as the addition of a solvent in the continuous phase changes its density and viscosity, the reaction rate might change at the interface. Indeed, the reaction rate depends on the diffusion coefficient of the molecules involved, which, in a liquid, is inversely proportional to the viscosity. Lowering the viscosity of the continuous phase increases the reaction rate at the interface and thus the number of covalent bonds between two drops for a given contact time.

To summarise, the DDE allowed to investigate the role of the dodecane on the interactions between the drops, and we were able to draw several conclusions:

- the presence of the polymeric skin completely inhibits coalescence between the drop, for any dodecane concentration;
- the drop detachment experiment in Section 6.2 puts in evidence adhesive forces, which seem to have a maximum for 5% of dodecane in the continuous phase;
- the drop sliding experiment in Section 6.3 evidences the resistance to sliding, i.e. tangential forces, between the drops, which increase with the dodecane concentration. For our system, friction and adhesion are likely coupled;
- the role of these tangential and attractive normal forces are also reflected in the measure of the angle of repose.

The presence of tangential and attractive normal forces between the drops is all very different from "ordinary" emulsion drops stabilised by low molecular weight surfactants. And while much more systematic investigations need to be done in the future, it seems clear that the amount of dodecane in the continuous phase increases the frictional and adhesive forces between the drops for this formulation.

If the dodecane is responsible for the adhesive and frictional processes at the interface between the two drops in our system, changing the solvent could be a way of tuning the magnitude of the frictional and adhesive forces and thus the structural properties of the emulsions. For example, we measured the swelling ratio $S = D/D_0$ of PDMS in dodecane, with D and D_0 the diameter of the piece of PDMS respectively after and before staying in a dodecane bath, and found $S = 1.31$, while the swelling ratio of PDMS in diisopropylamine has been measured at $S = 2.13$ [193].

In this chapter, we were able to show the presence of interactions forces between the drops, that can be characterised as adhesive and frictional forces. In Chapter 7, we study the impact of these interactions on the packing of drops presenting a polymeric skin at their surface.

Chapter 7

Packing of frictional and adhesive emulsion drops

From the results presented in Chapter 6, we know that the presence of a polymeric skin around the drops induces interactions between two touching drops in the form of friction and adhesion. In this chapter, we study the impact of these interactions on the packing of the droplets, more precisely on the volume fraction and the mechanical stability of the packing. We generate the PEG/crosslinker/catalyst drops in the Sylgard 184® base and D_4 mix using the dripping technique (cf Section 1.2.2 in Chapter 1). Dodecane is added to the continuous phase at either 5% or 10%, which varies the intensity of the interactions as seen in Chapter 6.

The structural properties (the volume fraction Φ, the local volume fraction Φ_l, the distance between drops δ and the radial distribution function $g(r)$) in this chapter are for the most part obtained by performing X-Ray tomography on the emulsions (cf Section 1.4.4 in Chapter 1). The analysis of the tomographs using the software *Avizo* allowed to obtain the drop volumes and positions in space. Image analysis of the tomographs using *Pomelo*[1] [271] allowed to obtain the Voronoi tesselation based on the surfaces of the drops (and not only the centers as regular Voronoi tesselations work) to measure the local and global volume fractions of the packings. The program *Karambola*[2] was used to measure the Minkovski tensors of the drops.

Most of the analysis presented here was performed in close collaboration with Matthias Schröter and Simon Weis of Erlangen University, Germany.

Here, we first present the emulsions studied in this chapter in Section 7.1. Then in Section 7.2 we analyse the volume fraction of drops in the emulsions. In Section 7.3 we investigate the pair correlation function characteristic of the overall organisation of the drops. In Section 7.4, we analyse the shape of the drops in the packings and we look at the distance between the drops. Finally, we discuss the results obtained in this chapter with respect to the results obtained in Chapter 6 on the interaction between two drops.

[1] software available at `http://theorie1.physik.uni-erlangen.de/research/pomelo/`

[2] Minkowski tensor software available at `http://theorie1.physik.uni-erlangen.de/research/karambola/`

Sample name	$\%Dod$	η (Pa.s)	$\langle R \rangle$ (µm)	σ_R (µm)	PI	$\langle \Phi_l \rangle$	σ_{Φ_l}	$\langle \beta_0^{20} \rangle$	σ_β
5%-S	5%	0.83	903.6	22.9	2.5%	0.486 ± 0.002	0.073 ± 0.003	0.680 ± 0.004	0.16 ± 0.01
5%-L	5%	0.83	1162.7	70.3	6.0%	0.541 ± 0.003	0.091 ± 0.005	0.600 ± 0.006	0.17 ± 0.01
10%-S	10%	0.52	930.2	28.3	3.0%	0.354 ± 0.001	0.123 ± 0.002	0.574 ± 0.008	0.25 ± 0.02
10%-L	10%	0.52	1054.0	196.9	18.7%	0.408 ± 0.009	0.185 ± 0.016	0.389 ± 0.009	0.22 ± 0.02

Table 7.1: Characteristics of the emulsions studied in this chapter, with %Dod the dodecane percentage in the continuous phase, η the viscosity of the continuous phase, R the radius of the drops, PI the polydispersity index of the drop sizes in an emulsion, $\langle \Phi_l \rangle$ the average value and σ_{Φ_l} the width of the distributions of the local volume fraction Φ_l obtained by fitting the distributions with Gaussian functions, and $\langle \beta_0^{20} \rangle$ the average value and σ_β the width of the distributions of the parameter β_0^{20} characterising the drop deformations.

7.1 Presentation of the emulsions

In this chapter, we study the packing of PEG-400 drops presenting a polymeric skin at the interface in a viscous continuous phase composed of Sylgard 184® base and D_4 and either 5 or 10% of dodecane (cf Section 1.1.1 in Chapter 1). In Table 7.1, we give the average equivalent radius $\langle R \rangle$ of the drops and the associated error σ_R (given by the standard deviation) for each sample, measured from the distribution of the equivalent radius[3] R in Figure 7.1a, the polydispersity index $PI = \sigma_R / \langle R \rangle$ of the drops and the amount of dodecane added in the continuous phase $\%Dod$ (in weight %). For simplicity, in the rest of the study we refer to the drop size as either S (small, $R \approx 930$ µm) or L (large, $R \approx 1150$ µm). The images of the samples given in Figure 7.1b are 3D volume renderings obtained from X-ray tomography. The colors of the drops have no other purpose than being able to separate the different droplets. We also indicated in this figure the color code used in the rest of the study of each emulsion.

The samples 5%-S, 5%-L and 10%-S have a low polydispersity index PI. However, the sample 10%-L has a high PI due to the presence of many smaller drops in the emulsions as seen in Figure 7.1a, which might have been created during the generation. The results given for this sample are therefore to be interpreted cautiously.

The absence of emulsions with 0% of dodecane in the continuous phase is due to the instability of these emulsions. Indeed, they are sufficiently stable to be able to measure the angle of repose during generation as shown in Section 6.1 in Chapter 6, and to solidify the continuous phase in an oven at 60°C. Unfortunately, they were not stable enough for transporting and imaging with X-Ray tomography in Berlin.

[3]The equivalent radius consists in calculating the radius R of the drop from its volume V which is known thanks to X-ray tomography by the relation $V = \frac{4}{3}\pi R^3$, i.e. by considering that the drop is spherical, even though we know that they are deformed.

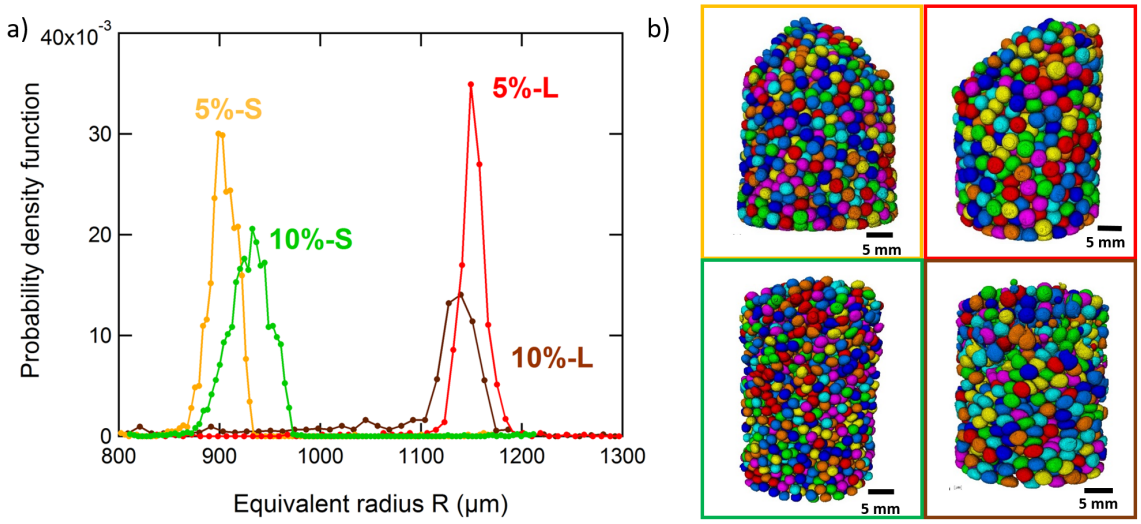

Figure 7.1: a) Distribution of the equivalent radius of the drops in the different emulsions. b) 3D volume rendering of the emulsions obtained from X-ray tomography, using the color code used in a) and in the rest of the study. The different colors of the drops have no meaning and are only here to separate the drops.

7.2 Volume fraction

7.2.1 Local volume fraction Φ_v

In Chapter 5, we discussed the global and local volume fraction for different systems of soft and hard spheres. To measure the distributions of the local volume fraction Φ_l of the frictional and adhesive emulsions, we calculated a tesselation of the systems close to a Voronoi tesselation though based on the surface-to-surface distances instead of the center using the program Pomelo (cf Section 5.2.1 in Chapter 5 for the definition of the local volume fraction).

Figure 7.2a shows the distributions of the local volume fraction of the frictional and adhesive emulsions in Figure 7.1. We see that they all follow Gaussian distributions, though in the case of the samples 5%-S and 5%-L we can see an overpopulation of loosely packed drops (tail-like structure) on the left side of the distribution. As the polydispersity indexes for these samples are low, we assume that it does not come from the polydispersity of the drops, though we cannot give another explanation at the moment. Future investigations will have to clarify if this is a real effect. The distribution of the 10%-L sample is noisy but can still be described with a Gaussian function. The average value $\langle\Phi_l\rangle$ and width σ_{Φ_l} of the distributions are indicated in Table 7.1. Both the value of $\langle\Phi_l\rangle$ and σ_{Φ_l} seem to depend on the dodecane percentage for a given drop radius.

In order to compare these distributions independently of the value of $\langle\Phi_l\rangle$, we looked at the rescaled local volume fraction RLVF defined by

$$\text{RLVF} = \frac{\Phi_l - \langle\Phi_l\rangle}{\sigma_{\Phi_l}}. \tag{7.1}$$

The result is shown in Figure 7.2b together with the same distributions measured for hard frictional spheres (data from Matthias Schröter and Simon Weis) and frictionless emulsion drops (from [243]). We can see that they all collapse within the scatter of the data on one master distribution curve

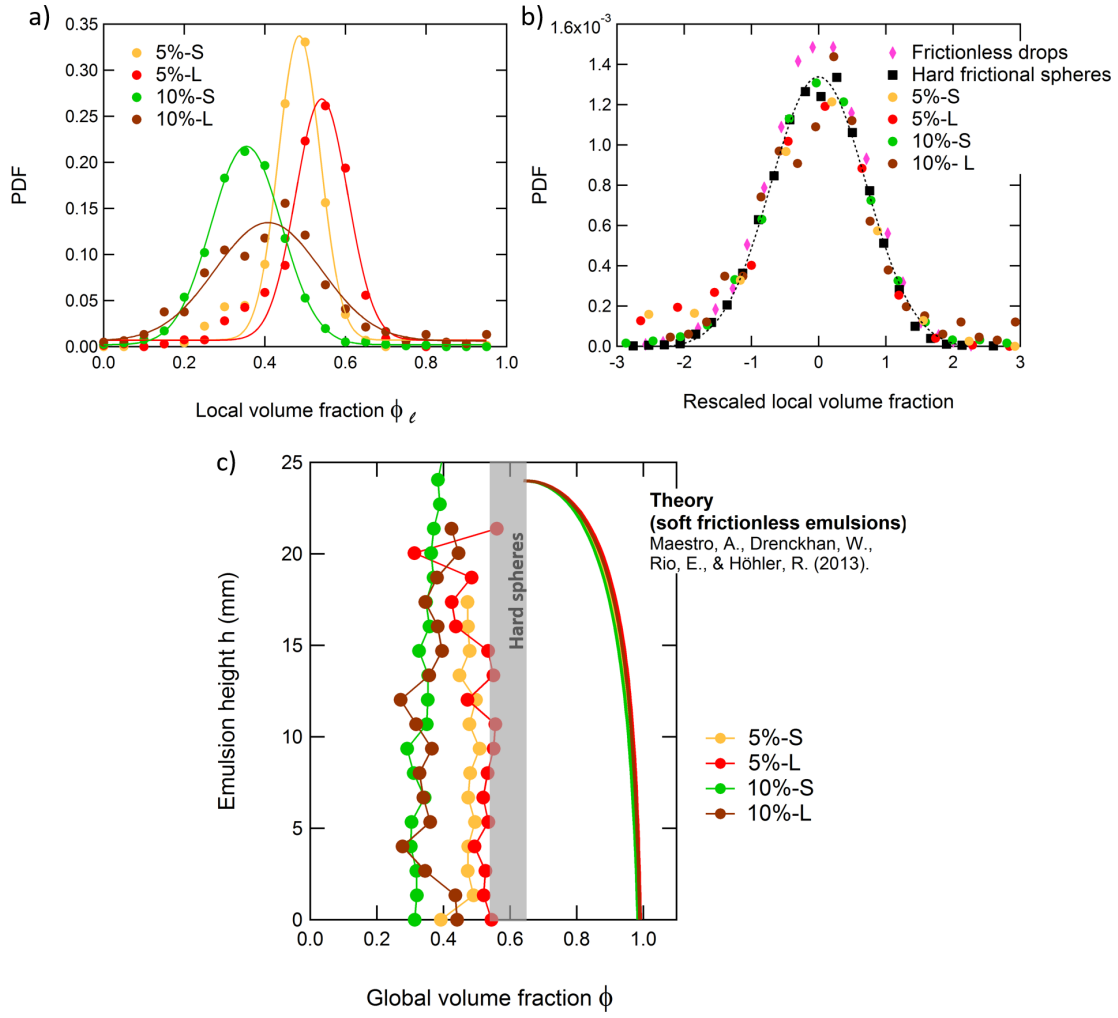

Figure 7.2: a) Distribution of the local volume fraction, fitted with a Gaussian function. b) Rescaled distribution of the local volume fraction (using Equation (7.1)), compared with the distributions obtained with frictionless emulsion drops [243] and hard frictional spheres. c) Evolution of the global volume fraction Φ with the emulsion height measured for the emulsions presented in Figure 7.1. The theory for soft frictionless spheres developed by Maestro *et al.* [1] is also shown, along with the range of values of the global volume fraction for hard spheres (in gray).

(black dashed line). This means that the distribution of the local volume fraction of our system is not distinguishable from a packing of hard frictional spheres or soft frictionless drops. This representation of the local volume fraction is thus independent of the interactions between the spheres and of the global volume fraction of the packings within the error bars of our experiments.

7.2.2 Global volume fraction of drops Φ

By calculating the harmonic mean of the local volume fraction $\frac{1}{N}\sum_{n=1}^{N}\Phi_l(n)$, with N the number of drops in a sample, as a function of the height of the emulsion, we obtain the locally resolved global volume fraction Φ (which is close, but not equal to $\langle\Phi_l\rangle$). Figure 7.2c shows the evolution of Φ with the emulsion height h for the samples shown in Figure 7.1. We can clearly see that Φ does not follow the theoretical model given by Maestro *et al.* [1] for surfactant-stabilised frictionless emulsions. On

the contrary, our profiles seem to be constant with h. However, Maestro *et al.*took into account only surface tension effects and neglected the surface elasticity of the bubbles and drops in their model. In our system, however, we know that the surface elasticity of the drops is not negligible and will resist strongly the drop deformations (Chapter 6). Moreover, the seemingly constant volume fraction with the emulsion height is the same behaviour as the one known for hard spheres, independently of their friction coefficient. For hard spheres, this is called the Janssen effect [253]: the contact forces between the spheres redirect the weight, i.e. the pressure, towards the walls of the container, and therefore the pressure in the bulk is constant with the height. Here, we therefore assume that the elasticity of the drops and the tangential forces between them have act simultaneously to explain the constant volume fraction Φ with the emulsion height h. A closer analysis of the drop deformation and organisation in Sections 7.3 and 7.4 will support this hypothesis.

We also observe low values of Φ compared to the lowest values of the global fraction $\Phi_{RLP} \approx 0.54$ known for hard spheres with a non-zero friction coefficient. However, as detailed in Section 5.2.5 in Chapter 5, values of Φ below this limit were observed by Liu *et al.* [269] for hard spheres connected by liquid bridges, i.e. in the presence of adhesive forces between the spheres. As we saw in Chapter 6, the presence of the polymeric skin around the droplets in the emulsions induces both friction and adhesion in the presence of dodecane. These values of Φ are in that sense not incoherent.

Figure 7.2c also seems to show that the amount of dodecane in the continuous phase has an impact on the global volume fraction of drops in the emulsion. Indeed, the values of Φ for 10% of dodecane are lower than the values for 5% of dodecane, with a difference of $\Phi(5\%) - \Phi(10\%) \approx 0.15$ between the values of $\Phi(h)$ for a given drop radius. As we saw in Section 7.2.1, the width σ_{Φ_l} of the distributions of the local volume fraction also depend on the dodecane percentage. The study of the drop-drop interactions in Chapter 6 showed that their magnitude depend on $\%Dod$, and studies in the literature show that the global volume fraction decreases with the magnitude of the sphere-sphere interaction (as shown for example in Figure 5.9 in Chapter 5 for adhesive emulsions). The decrease of Φ with $\%Dod$ in our case can thus easily be explained by the increasing interaction between the drops. The width of the distributions also increases with the strength of the adhesion between emulsion droplets in Figure 5.9 in Chapter 5, which correlates well with our result.

7.3 Overall droplet organisation in the emulsions

To probe the local fluctuations in density in the emulsions, we can calculate the pair correlation function $g(r)$, which is often called the radial distribution function (defined in Section 5.2.1 in Chapter 5). Figure 7.3 shows the $g(r)$ for the frictional and adhesive emulsions, compared with the $g(r)$ obtained by Zhang *et al.* [249] from simulations of a frictionless emulsion, and with the $g(r)$ for a packing of hard frictional spheres (data from Matthias Schröter and Simon Weis), as we did for Figure 7.2c. In the case of the frictionless drops and the frictional hard spheres, we can clearly observe a sharp peak at $r/r_0 = 1$ and the two peaks at $r/r_0 = \sqrt{3}$ and $r/r_0 = 2$ characteristic of the random ordering of monodisperse spheres (see Figure 5.7 in Chapter 5). In the case of the drops presenting both friction and adhesion at the interface, the first peak at $r/r_0 = 1$ is broad, with a width $\sigma_g \approx 0.45$ independently of the $\%Dod$. This cannot be due to the polydispersity of the drops since as shown in Table 7.1 the PI are low for the samples represented in Figure 7.3. We also notice the absence of any characteristic peak

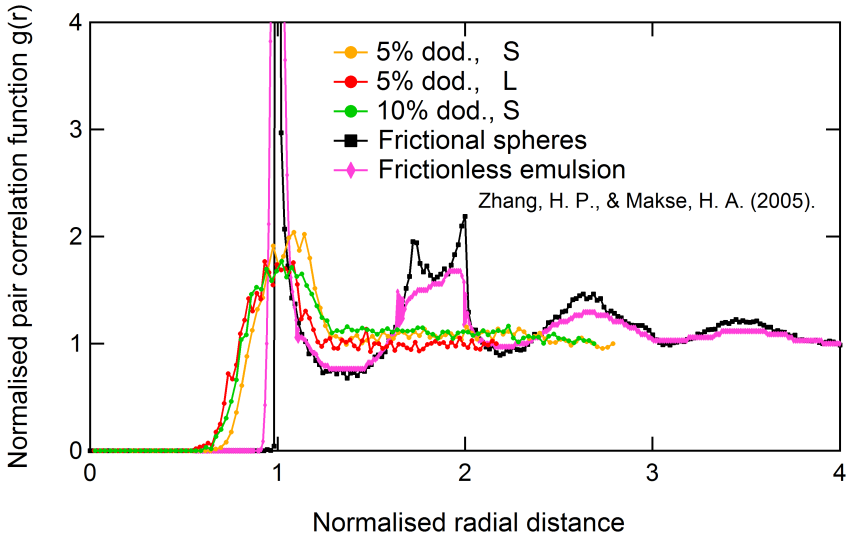

Figure 7.3: Normalised pair correlation function $g(r)$ of the frictional and adhesive emulsions, compared with the function obtained for both frictionless emulsions [249] and frictional hard spheres.

in the $g(r)$ of the frictional and adhesive emulsions, which indicates no correlations in the position of the drops with respect to each other in the packing.

However we can notice that the peak at $r/r_0 = 1$ for the soft frictionless drops is broader than the one for the hard frictional spheres, which is due to the deformability of the emulsion drops. The large peak calculated for the frictional and adhesive emulsions could be the result of the deformation of the drops. We thus study the shape of the drops in Section 7.4.

7.4 Deformations of the drops in the packing

Anisotropies in the shape of objects are often measured using the Minkovski Tensors [272]. Here, we concentrate on the parameter β_0^{20} defined as

$$\beta_0^{20} = \frac{|\varepsilon_{min}|}{|\varepsilon_{max}|} \in [0, 1], \tag{7.2}$$

which measures the degree of anisotropy through the ratio of the minimal ε_{min} to maximal ε_{max} eigenvalue of the Minkowski tensor W_0^{20} characterising the volume distribution of the object. $\beta_0^{20} = 1$ means that the volume is isotropic. For these systems, the capillary length λ_c defined as $\lambda_c = \sqrt{\gamma/\rho g}$ with γ the interfacial tension between the dispersed and continuous phase, ρ the density of the PEG and g the gravitational acceleration, and which defines the limit above which gravity can deform the system, is $\lambda_c \approx 0.7$ mm (using $\gamma = 5$ mN/m). Since the drops in the emulsions studied in this chapter have radii above this limit, we conclude that gravity alone can deform the drops, and that compression by other drops can overtake the surface tension which tends to keep the drops spherical. The measure of the distributions of β_0^{20} for each drop of the frictional and adhesive emulsions was made using the program *Karambola* by Simon Weis (Erlangen University), and they are shown in Figure 7.4a. We can see that the distributions are indeed systematically large, and centred on low values of β_0^{20}. Table 7.1 gives the average value $\langle\beta_0^{20}\rangle$ and the width σ_β of each distribution grossly fitted with a Gaussian

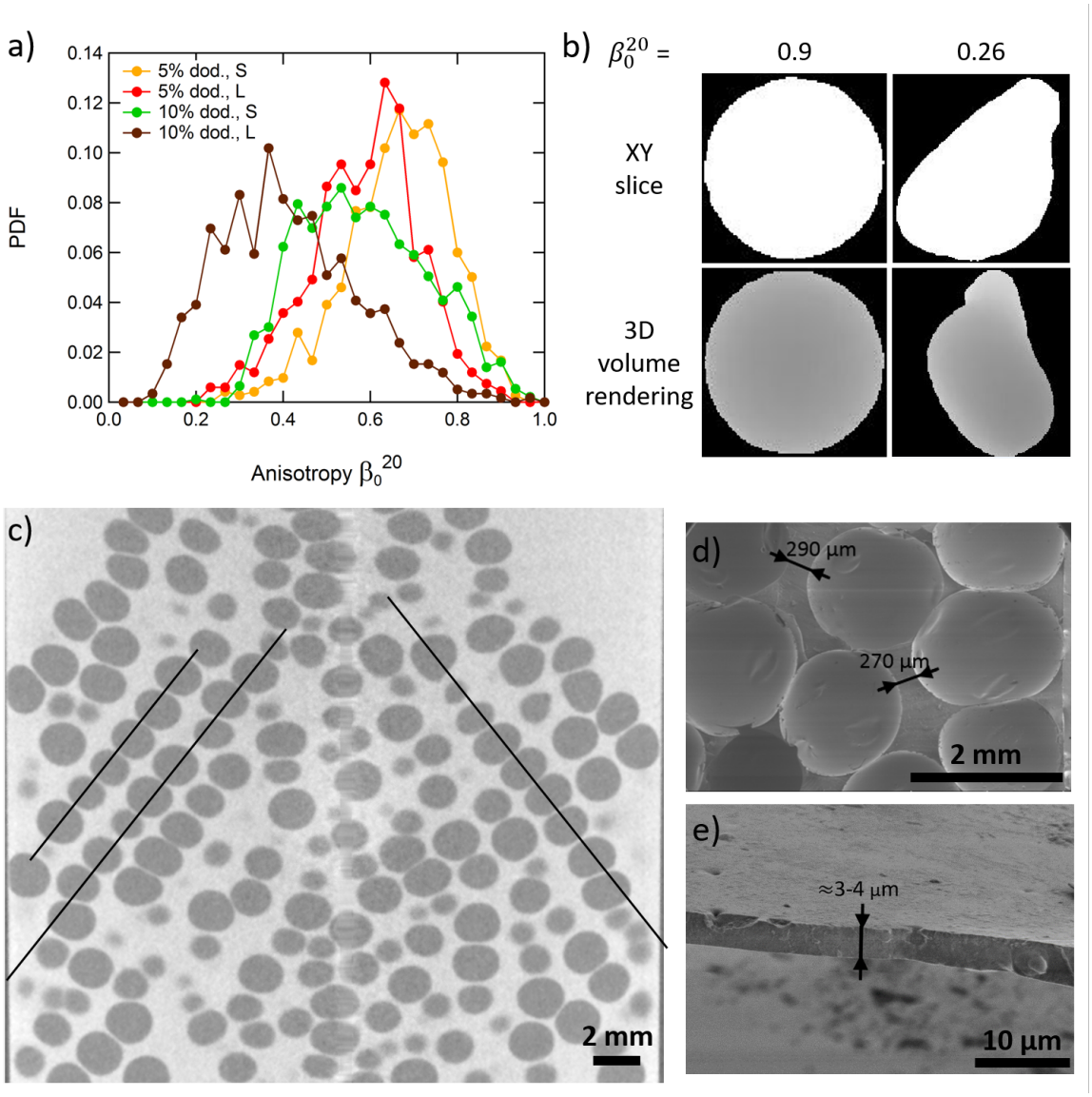

Figure 7.4: a) Distribution of the measured values of β_0^{20} in the four samples. b) XY slice and 3D volume rendering of drops with two extreme values of β_0^{20} from the sample 5%-S. c) Vertical slice at the center of the reconstruction of the volume of the 5%-S sample using X-ray tomography showing the presence of force chains (indicated by black lines). d) SEM image of a solid emulsion after removal of the liquid PEG in the drops. e) Zoom on a thin film between two drops on image d).

function. Here, the amount of dodecane in the continuous phase does not seem to have a large impact on $\langle\beta_0^{20}\rangle$. Indeed, except for the sample 10%-L for which the average value of $\beta_0^{20} = 0.39$, the other samples exhibit values relatively close to each other around $\beta_0^{20} = 0.7$. The highly deformed drops of the sample 10%-L are probably due to another mechanism which would also be responsible to the high polydispersity of this drop packing. Figure 7.4b shows two examples of drops with extremal values of $\beta_0^{20} = 0.9$ and 0.26 from the sample 5%-S. These high deformations of the drops can explain the broad peak at $r/r_0 = 1$ and the missing structure peaks at $r/r_0 > 1$ of the pair correlation function in Figure 7.3.

To understand how the drops pack and deform with respect to their neighbours, we looked at a vertical slice at the center of the reconstruction of the volume of the 5%-S sample obtained using X-ray tomography, shown in Figure 7.4c. In this figure, we can distinguish lines of drops whose deformations

follow a single direction (some of them indicated by black lines), which are similar to force chains observed in packings of hard spheres (cf Figure 5.4d in Chapter 5). The formation of such neat force chains is not observed in uncompressed packings of frictional hard spheres, which indicates that the adhesive forces between the drops might be responsible for the creation of these structures during the emulsion generation.

Looking closely at Figure 7.4c, we can see that it is complicated to define a number of contacts in this packing. Indeed, none of the drops in this image are directly touching each other, since we can always distinguish by eye a separation[4] of approximately 150 µm $< \delta <$ 300 µm. However, we know that the polymeric skin at the interface of the drops is made of crosslinked molecules in the Sylgard 184® base. X-ray tomography is sensitive to the density difference between two phases in the sample, and to the atomic number of each phases. Crosslinking the Sylgard 184® base does not significantly change its density which means that in the reconstructed images, the polymeric skin appears in the same color as the continuous phase. We would then need to know the skin thickness at the surface of the drops and substract it to the distance between drops to be able to determine the average number of contacts $\langle z \rangle$ of the packing. This would need systematic experiments of the minimal distance between the drops found in the packing as a function of the time left for the skin to be created (which we referred to as stabilisation time T_s in Chapter 6). However, since the skin is created with a chemical reaction, there is no reason for the reaction to stop once the drops are in contact, which would influence the magnitude of the force between them, by increasing the network density of the skin.

In order to have an idea of the typical distances between the drops while avoiding the problem of the always growing polymeric skin at the surface of the drops, we stopped the reaction at the interface by solidifying the continuous phase via a crosslinking reaction at a temperature $T \approx 60°$C by adding the Sylgard 184® curing agent in the continuous phase before the emulsion generation (cf Section 1.2.4 in Chapter 1). It takes approximately 30 min to reach the gel point of the continuous phase at this temperature (Figure 1.11). The solidification "freezes" the distance between the drops at a given time (with an error corresponding to the solidification time in regard to the reaction rate, which is unknown here). An example of the organisation of drops in a section of a solid emulsion is shown in Scanning Electron Microscopy (SEM, cf Section 1.4.1 in Chapter 1) images in Figures 7.4d and e, after removal of the liquid PEG inside the drops. We see that all the pores are closed, i.e. the drops are always separated by a polymeric film. However, we can distinguish two characteristic length-scales between the drops in Figures 7.4d and e: the thickness of the polymeric skin $\delta \approx$ 3-4 µm and a larger thickness $\Delta \approx 280$ µm. In that example the lower thickness $\delta \approx$ 3-4 µm is far from the values of 150 µm $< \delta <$ 300 µm given above for the liquid 5%-S emulsion, but the chemistry at the interface is different in this case because of the addition of the curing agent. This makes the comparison between the two systems difficult. However, it is interesting to note that we also find two characteristic length-scales in the liquid emulsions, as Figure 7.4c seems to indicate. This, together with the drop deformations, would explain the absence of the peaks at $r/r_0 = 2$ and $\sqrt{3}$ in the pair correlation function in Figure 7.3.

[4]Though this image is a slice which means that we might not look at the vertical plane in which the drops are actually touching, the probability that this is the case for every single drops in this slice is low.

7.5 Discussion

In this chapter, we presented a new granular system composed of soft frictional and adhesive drops. We characterised the drop-drop interactions in Chapter 6, and we analyse the structural properties of the emulsions in comparison with those of known systems: hard frictional spheres and soft frictionless emulsion drops. While some of our investigations remained on a descriptive level, we can already draw some important conclusions about this new system.

We showed in Section 7.2.1 that by looking at the local volume fraction Φ_l of a packing of soft frictional and adhesive drops, we cannot distinguish them from a packing of hard frictional spheres or soft frictionless emulsions. Indeed, the distributions of the local volume fraction of the frictional and adhesive emulsions can be fitted by a Gaussian function (Figure 7.2a), like for the hard frictional spheres and soft frictionless emulsions, and all the distributions of the rescaled local volume fraction collapse on a single master curve (Figure 7.2b). Since the interactions between the spheres are quite different between these different systems, this shows that the rescaled local volume fraction is not very sensitive to the sphere-sphere interactions. We looked at the global volume fraction Φ as a function of the emulsion height h (Section 7.2.2) and observed that Φ is a constant with h (Figure 7.2c). This is in contradiction with the evolution of Φ with h for frictionless emulsions which decreases with the height. However, packings of hard spheres have a constant density of spheres with the vertical axis, which is explained by the Janssen effect. Our hypothesis here is that, as for hard spheres, the friction between the drops redirects the pressure towards the walls of the container and that the elasticity of the droplets skin resists to some of the deformation. The analysis of the global volume fraction thus showed that the frictional and adhesive emulsions do not behave like frictionless emulsions. However, it did not allow to differentiate its behaviour with the one of the packing of hard spheres.

We thus calculated in Section 7.3 the pair correlation function $g(r)$ of the frictional and adhesive emulsions, and compared it to the $g(r)$ for frictional hard spheres and frictionless drops (Figure 7.3). We saw that none of the characteristic peaks that can be observed for hard spheres and frictionless drops are present in the $g(r)$ of the frictional and adhesive emulsions. Also, the first peak at $r/r_0 = 1$ of the $g(r)$ of our system is much broader than for the other systems, which we cannot explain with the polydispersity of the drops in the samples. To understand this, we measured the anisotropy of the shape of the drops inside the packing using the Minkovski parameter β_0^{20} which quantifies the degree of anisotropy of an object. The distributions of β_0^{20} for the drops surrounded by a polymeric skin are given in Figure 7.4a, and images of drops with extremal values of β_0^{20} in the sample 5%-S are shown in Figure 7.4b. This way, we established that the drops in each packing were strongly deformed, independently of the dodecane percentage, which could explain the broad peak at $r/r_0 = 1$ and the absence of peaks for $r/r_0 > 1$ in the pair correlation function $g(r)$.

The absence of the peaks at $r/r_0 = 2$ and $\sqrt{3}$ can also be explained by the distances between the drops in the packings. We found that the drops were never completely in contact with their neighbours in the tomographs, because of the presence of the polymeric skin around the drops which has the same absorption coefficient as the continuous phase, making them undistinguishable from one another. To avoid this issue, we imaged a solidified emulsion using SEM and looked at the distances between the drops. We found two characteristic distances in the packing, which we can also qualitatively see in the tomograph in Figure 7.4c. Both the existence of two characteristic lengths and the drop deformations could explain the absence of peaks for $r/r_0 > 1$ in the pair correlation functions.

The tomographs also reveal the formation of very neat force chains in the packings, which is usually not observed to that extent in uncompressed packings of hard spheres. These are characteristic of strong interaction forces.

Conclusions and perspectives of Part B

The aim of this part was to present a new granular material to fill-in the blank spaces of the graphs proposed in Figure 5.11 in Chapter 5. This system is composed of soft emulsion drops surrounded by a polymeric skin, made via chemical reactions at the interface which create a network of crosslinked polymers at the surface of the drops. The presence of this skin-like interface is responsible for the introduction of both attractive normal and tangential forces between the drops. By varying the concentration of solvent in the continuous phase (dodecane in this study), we managed to tune the strength of these interactions between the drops in order to explore a system which may be placed in between the extreme cases of soft frictionless bubbles/drops and hard frictional spheres. To study this new system, we analysed both the interaction properties of two drops in contact and the structure of packings of drops using X-ray tomography (Figure 7.5).

In Chapter 6, we studied the interfacial properties of the drops surrounded by a polymeric skin. The measure of the dynamic angle of repose allowed us to highlight the presence of strong attractive normal and tangential forces between the drops. Using the two-drops experiment, we investigated the separation of two drops initially in contact depending on the amount of dodecane in the continuous phase. This showed a net increase of the adhesive forces between the drops in the presence of dodecane. We also quantified the relaxation towards its equilibrium position of a drop sliding on another one, as a way to probe the tangential forces. Here also we showed that an increase of dodecane in the continuous phase reduced the ability of the drops to slide over each other. To understand the impact of the concentration of dodecane, we proposed different possible explanations. First, the addition of a solvent might swell the polymeric skin, making the loose chains of the skin more apt to entangle with the polymers of the skin on the other drops. We furthermore suggest that the diminution of the viscosity of the continuous phase has an effect on the lubrication during the sliding of the drops over each other. Indeed, if the viscosity decreases, the lubrication between the two interfaces is less effective, and the entanglement of the polymers on the skin of both drops is more likely to happen. Also, since the presence of dodecane decreases the viscosity and density of the continuous phase, the reaction rate increases at the interface because of the dependence of the diffusion coefficient of molecules on the viscosity of the liquid. By increasing the number of molecules that react between two interfaces in contact for a given time, the magnitude of the force required to separate them is thus enhanced.

Having characterised the impact of the dodecane on the interaction forces between drops, we studied in Chapter 7 the structural properties of the packings of frictional and adhesive drops. We demonstrated a number of properties specific to this system. First of all, as all granular systems, emulsions are sensitive to the construction history, i.e. the way the emulsions are generated impacts the final structure of the material as shown by the slope at the top of the emulsion in Figure 7.5. It is a direct result of

the presence of strong interactions between the drops, such as the high angle of repose measured in Chapter 6. Also, the global volume fraction of drops is a constant with the emulsion height, which is usually characteristic of the packing of hard spheres instead of soft emulsion drops. Looking at the local volume fraction distribution, we were not able to find any distinguishable characteristic from other systems like hard frictional spheres or soft frictionless emulsion drops. However, we noticed that the global volume fraction is low compared to the volume fraction of random loose packings of hard spheres ($\Phi < \Phi_{RLP} \approx 0.54$). We were able to measure even lower volume fraction as for systems of hard frictional spheres presenting adhesive forces because of liquid bridges between the grains [269]. This is also very well explained by the strong interactions between the drops which allow the mechanical stability of the packings with a low number of contact (below isostaticity), i.e. low density of drops. The packing fraction also decreases with the increase of the amount of dodecane in the continuous phase, which agrees well with the increase of the strength of the drop-drop interactions as the concentration in dodecane increases. The analysis of the overall organisation of the drops with the calculation of the pair correlation function $g(r)$ indicated no correlation in the position of the drops beyond the nearest neighbours because of the total absence of characteristic peaks at $r/r_0 = 2$ and $\sqrt{3}$, which are normally found for random organisations of hard frictional spheres and soft frictionless drops. We explained this with the deformation of the drops and the lack of a well-defined drop-drop separation. Finally, we noticed the presence of force chains of drops forming in the emulsions, which is not observed in granular materials unless a pressure is applied. The flat pair correlation function and the presence of force chains are thus characteristics of the packing of soft frictional and adhesive drops.

Several aspects remain in need of more investigations. More systematic experiments are needed to fully understand and control the interactions forces between the drops, for which the control of the thickness of the polymeric skin would be of utmost importance. To do so, one might try to stop the reaction at the interface, for example by replacing the continuous phase by a non-reactive PDMS after a given stabilisation time. Also, changing the solvent instead of its concentration in the continuous phase might be another way to tune the interactions between the drops. Finally, we were not able to measure the average number of contacts $\langle z \rangle$ between the drops because of the inability of the X-ray tomography technique to differentiate between the polymeric skin and the continuous phase. One way to count the contacts could be to correlate the deformations of a drop with the positions of its closest neighbours.

In Chapter 4, we pointed out that we had not been able to image the emulsions with a high volume fraction of drops obtained with MHDS molecules of low molecular weights with the X-ray tomography lab setup because of resolution issues. The use of a beamline in a synchrotron facility with a higher resolution showed that these emulsions could be imaged (Figure 4.6 in Chapter 4), which shows promise for the study of the topology of high volume fraction emulsions with frictional and adhesive interfaces.

Globally, we could show that soft frictional and adhesive emulsions present some interesting features with respect to their more traditional cousins (frictionless drops and frictional hard spheres). It will be of interest in the future to avail of systems which provide independent control of the skin elasticity, the friction and the adhesion between the drops.

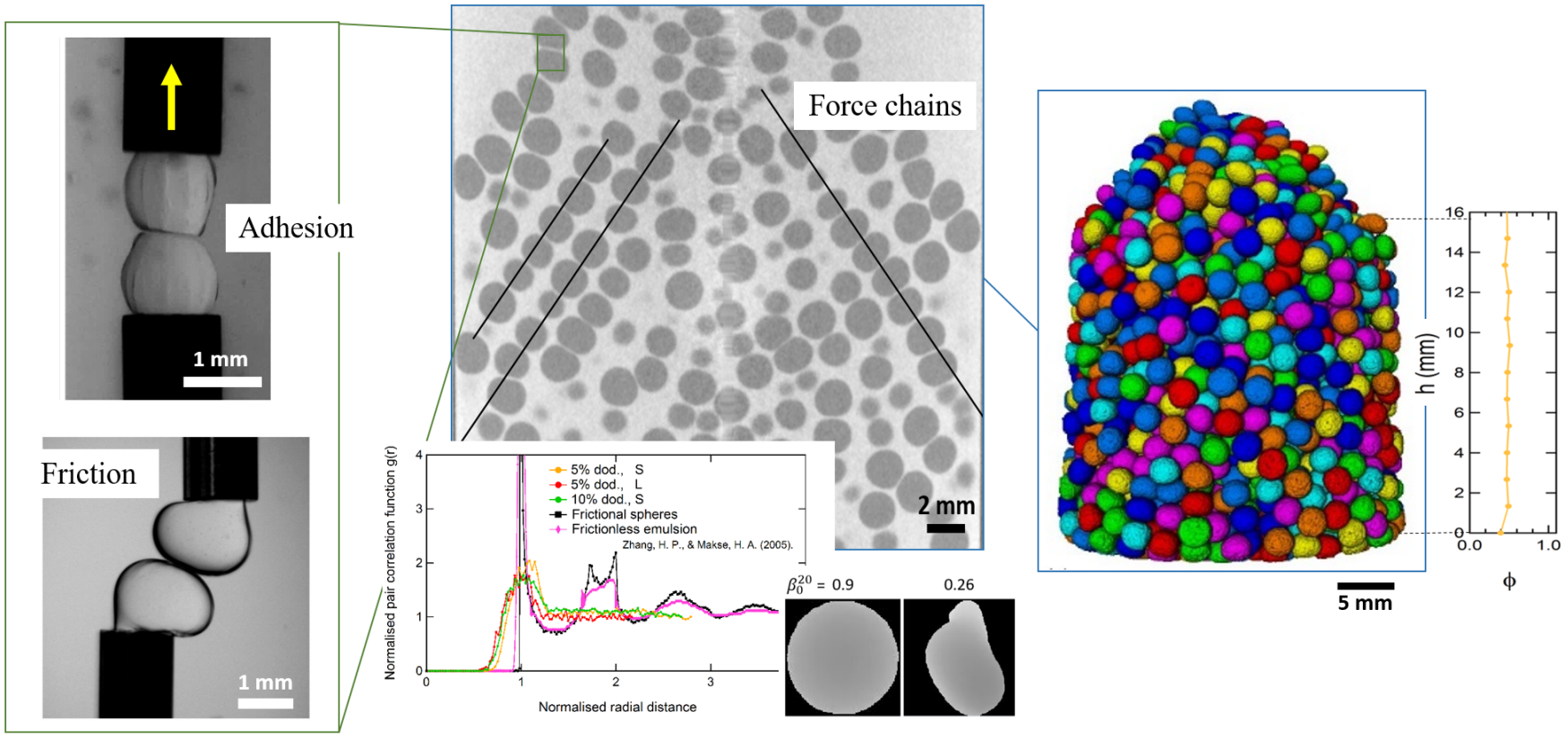

Highlighting of tangential and normal forces between the drops

Study of the structural properties of the packing of the drops

PEG-in-Silicone emulsions stabilised by a polymeric skin

Figure 7.5: Conclusions drawn from Part B of this manuscript.

Part C

Mechanical and adhesive properties of solid PEG-in-silicone emulsions

Introduction of Part C

Adhesion is a recurring problematic in industry, whether it is to generate multi-layered films while preventing the film lamination in the food industry or to offer a large choice of glues for different types of materials and loads to clients in the adhesives industry. Also in nature, some animals are able to climb walls and trees easily, such as the now famous in adhesion science gecko, or to stick to a rock even under crushing waves like mussels.

If the interesting finality for both the salesperson or the mussel is whether it will stick or not, to sell or to survive, the actual mechanisms reveal a diversity and a complexity which has deserved its share of the scientific literature [273–277]. For example, intermolecular forces can be the motor of adhesion, such as covalent bonding when a chemical reaction occurs at the interface, Van der Walls forces, hydrogen bonding, electrostatic forces or entanglement of the molecules at the interface. Surface microstructure has also been shown to increase the energy release rate G needed to detach the surfaces, for instance the microstructured paw of the gecko which allows him to climb walls (Figure 7.6). Also, adhesion can come from mechanical forces, when two pieces of fabric are sewed together. All these happen at the surface only. Another source of adherence, and the one we are mostly interested in for this study, is the viscoelasticity of the bulk which allows irreversible energy dissipations in the volume of the material.

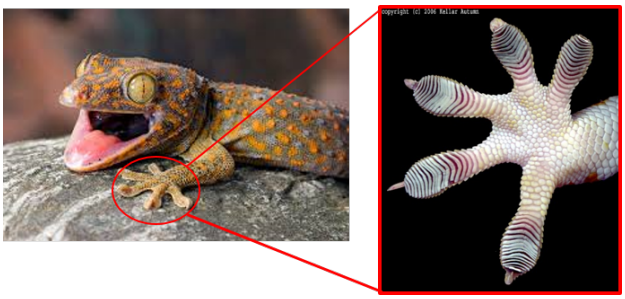

Figure 7.6: Picture of a gecko with a zoom on the microstructure on its paw which allows him to climb on walls.

In this part of this manuscript, we focus on the adhesive properties of solid PEG-in-PDMS emulsions. These are generated by using a liquid template stabilised by a reactive blending approach which we studied in Part A, and then solidifying the continuous phase, leading to a solid material with liquid inclusions inside its volume (cf Section 4.2 in Chapter 4). We are interested in the influence of the structural properties of the emulsions, i.e. the number of drops inside the volume and their density, and of the traction speed on the mechanical and adhesive properties of the overall material.

The details about the materials and methods used in Part C are given in Chapter 1. In Chapter 8, we go through the theoretical background needed about the mechanics and adhesive properties of simple

liquids, solids, and cellular materials. We then study the mechanical and rheological properties of the solid emulsions in Chapter 9. Finally, we investigate their adhesive properties in Chapter 10.

Chapter 8

Mechanical and adhesive properties of elastic solids

As mentioned in the introduction of this part, adhesion is the result of many different mechanisms arising simultaneously from surface and volume effects. Since the surface does not change in-between the samples we use, we will focus mainly on volume effects. In this chapter, we first introduce in Section 8.1 the theory of elasticity of solids and the notion of adhesion between two solids, and detail the different contact mechanics experiments at hand to measure both the elastic and adhesive properties of a material. In Section 8.2, we develop the notion of viscoelasticity, which gives the relation between the elastic and viscous dissipative contributions in a material, and which are the mechanisms we focus on in this part of the manuscript. Finally, in Section 8.3, we provide a short review of the literature on the mechanical and adhesive properties of cellular materials such as foams and solids with liquid inclusions which correspond to the limit cases of the solid emulsions we study.

8.1 Elastic solids

8.1.1 Theory of elasticity

The elasticity of a solid quantifies its resistance to deformation. Here, we will limit ourselves to isotropic solids and also to small deformations, meaning that we probe the regime of linear elasticity of the materials. Moreover, the small deformations allows to stay in a regime where deformations are reversible, i.e. the solid comes back to its initial dimensions without hysteresis once the applied force vanishes. An elastic solid can thus be modelled by a spring subjected to small forces, with a "spring constant" related to E called tensile modulus or the Young's modulus [278]. It's behaviour under tensile stress σ_t (Figure 8.1a) is given by the *Hooke*'s law

$$\sigma_t = E \cdot \epsilon, \tag{8.1}$$

where $\epsilon = L/L_0$ is the tensile strain[1]. In the case of a shear stress σ_s (Figure 8.1b), the *Hooke*'s law becomes

$$\sigma_s = \mathcal{G} \cdot \tau, \tag{8.2}$$

[1]This equation is similar to the force/displacement relationship of a spring: $F = k\Delta x$ with F the applied force, k the spring constant and Δx the deformation.

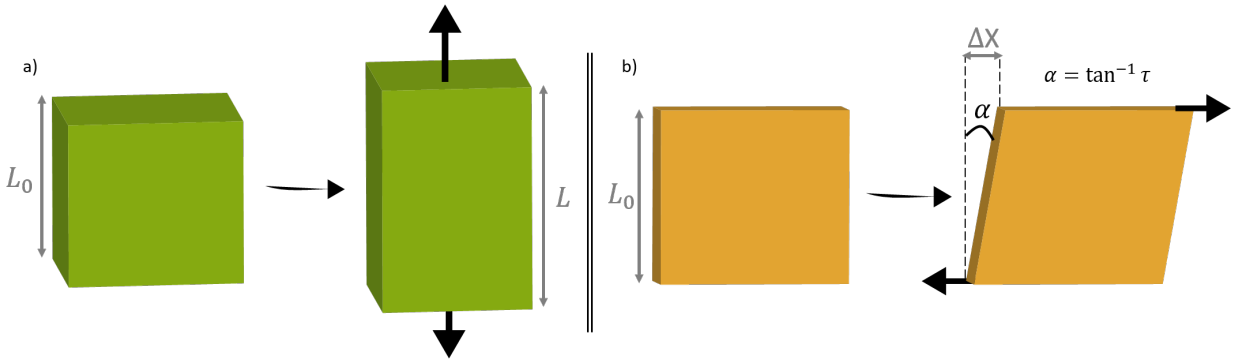

Figure 8.1: Scheme of a uniaxial traction of an elastic solid.

where $\mathcal{G}$ is the shear modulus and γ the shear.

The relation between E and $\mathcal{G}$ is given via the Poisson ratio ν characteristic of the material

$$E = 2(1+\nu)\mathcal{G} \tag{8.3}$$

with

$$\nu = \frac{1}{2}[1 - (\frac{1}{V})\frac{dV}{d\epsilon}]. \tag{8.4}$$

where V is the volume of the elastic solid, and $\frac{dV}{d\epsilon}$ the compresibility of the volume V. For incompressible solids, ν=0.5.

Elasticity of elastomers

Elastomers and rubbers, which are crosslinked polymers of very high molecular weight, are capable of sustaining large deformations without rupture, up to five to ten times their unstretched lenght, which truly differentiate them from other solids [279]. Indeed, polymer chains, that are initially in randomly coiled arrangement, are capable to rearrange to highly extended configurations. Another remarking ability is the spontaneous recovery of the polymers to their initial configuration, allowing the elastomer to retrieve its initial dimensions.

The polymer chains can be connected by chemical (covalent) bonding in which case reactive polymer chains are used and are paired with a curing agent also called a crosslinker which links the reactive chains via a crosslinking reaction. Another possibility is to use physical interactions to form the polymer gel, such as hydrogen bonding or electrostatic forces. The crosslinked polymer is represented in a schematic form in Figure 8.2. At the molecular scale, it is almost unrecognisable from an entangled polymer melt[2]. The chains are linked at points called the nodes, and the molecular mass between nodes M_c, or the number of monomers between nodes N_c defines the elastic properties of the elastomer.

By calculating the impact of the deformations of a polymer chain on the free energy of the system, we obtain the Young's modulus of elastomers

$$E = \frac{3Nk_BT}{V} = \frac{3\rho k_BT}{M}, \tag{8.5}$$

[2]One way to distinguish them is to put them in a good solvent: the uncrosslinked polymers will dissolve when the crosslinked elastomer will only swell.

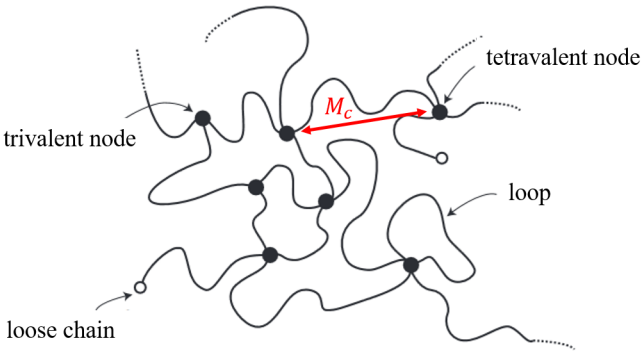

Figure 8.2: Scheme of a crosslinked polymer. Adapted from [280].

with ρ the polymer density and M the molecular weight of the polymer. In the case of a crosslinked elastomer, the same expression is applicable while changing M by the molecular weight between two nodes M_c[3] (see Appendix IV for the detailed calculation). From this expression, it is obvious that the elastic modulus of elastomers depends on the temperature: the higher the temperature, the stiffer the elastomer. This model is in good agreement with experimental data for deformations up to 50% [282].

Deviation from this model can however occur from different reasons. For example, the affine deformations model assumes that the nodes in the crosslinked elastomer are attached only to one chain, which does not allow them to fluctuate in space, and is not the case of a real network. The *phantom network* model does take this into account [283, 284]. It is also important to note that the polymer chains are always considered as highly monodisperse in size, and polydispersity will cause deviations from these models. Loops and loose chains which have not reacted with a crosslinker can be present and are also not taken into account here. These are responsible for decreasing the elastic modulus of the elastomer [279, 285, 286], and adding a non-negligible viscous component to the overall modulus of the material (cf Section 8.2).

Elastic dissipations in the volume of an elastic solid can enhance its adherence to substrates. In Section 8.1.2, we thus define the adhesion between two materials and we detail the possible mechanisms responsible for the enhancement of the adhesive properties.

8.1.2 Adhesive properties of elastic materials

Separating two materials in intimate contact costs energy, as everyone can easily experience. Historically, this energy was first estimated to be due to the balance between the energetic cost of the creation of two new material/air interfaces and the energetic cost of the interface between materials 1 and 2 first in contact (Figure 8.3). This energy per unit of surface is called the thermodynamic work of adhesion W, expressed in N/m^2 and given by the Young-Dupré equation

$$W = \gamma_1 + \gamma_2 - \gamma_{12}, \tag{8.6}$$

where γ_1 and γ_2 are the surface energies of materials 1 and 2 respectively and γ_{12} the interfacial tension between them[4]. Its origin is discussed below.

[3] The molecular weight between nodes M_c can be measured by measuring the swelling ratio of the elastomer in a good solvent [281].

[4] the notion of interfacial tension has been described in Part A Chapter 1

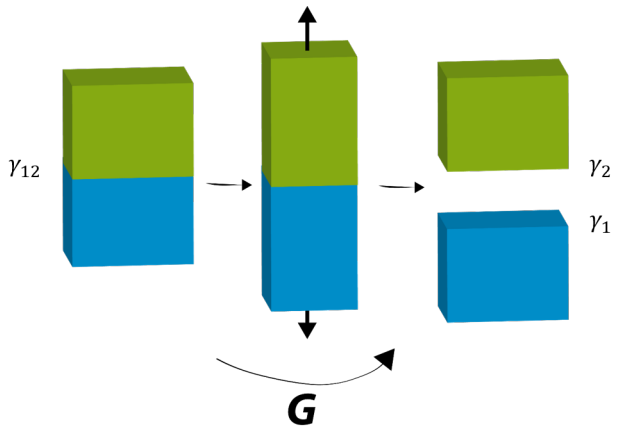

Figure 8.3: Scheme of the creation of an interface between two materials 1 and 2 with respective surface tension γ_1 and γ_2 with air and an interfacial tension $\gamma_{1,2}$ between the two materials. G is the energy required to separate the materials, called the energy restitution rate.

However, experiments showed that the measured energy needed to separate the materials was rate and temperature dependent [287]. Surface energies and interfacial tensions are indeed temperature dependent, but the variations of the rate should not have an impact if we consider only W as the motor of adhesion. For high rates and low temperature, W was usually much lower than the measured energy per unit of surface needed to separate the materials, which we call the energy release rate G (Figure 8.3)

$$G = W(T) + D(T, v, ...), \tag{8.7}$$

where D is the dissipated energy per unit of surface responsible for the increase of G. It depends on different parameters such as the rate v and the temperature T and potentially others. For some systems, D is a function of W and G is given as $G = W(1 + f(v))$ [288]. The origins of the dissipations can be numerous and are discussed below.

Mechanisms of adhesion

Both the thermodynamic work of adhesion W and the dissipations of energy D find their origins in various processes which we will briefly cite. For more details, we refer the reader to the work of Nicolas Amouroux [289].

Molecular origin of the work of adhesion W As the sum of surface and interfacial tensions, the thermodynamic work of adhesion W finds its origin at the molecular scale. Interfacial tension is the result of Van der Walls interactions, hydrogen bondings, polar interactions, etc. between molecules on each side of the interface. Details about the Van der Walls forces can be found in [290]. In that regard, any surface treatment, use of molecules at the interface that are able to form covalent, hydrogen or electrostatic bonds, is a way of modulating the thermodynamic work of adhesion W. As discussed throughout Chapter 2, changing the nature of the molecules at the interface via a chemical reaction changes the interfacial tension γ_{12} over time. However, this might also change the values of γ_1 and γ_2, i.e. changes in the value of W are not trivial in that case.

Surface patterning Geckos, along with many other vertebrates and insects, have inspired a great load of academic research due to their incredible ability to climb on almost any type of surface, smooth or rough [14, 291–296]. This is thanks to the fibrillar structure of the surface of their paws. Fibrillar structures, also called textured or patterned surfaces, present number of advantages regarding adhesion compared to smooth surfaces [297]. They are more resistant to peeling because the strain energy stored in a fibril right before pull-off is not available to drive the detachment of the next fibril, i.e. the crack has to be initiated for every fibril. They also conform themselves to rough surfaces which allows better contact with the substrate. The contact between a substrate and a textured surface is more tolerant of defects than with a smooth interface. All of this contributes to a greater adhesion energy of the patterned surface over a smooth one, depending on the size of the fibrils and the distance between them, though the chemistry of the contact is unchanged.

Also, the maximum sustainable force for a material is inversely proportional to the square root of its compliance C, and the compliance of a fibril is higher than the compliance of the volume for a same material [298]. This means that for a given force, the deformation of a fibril is larger than the deformation of a bulk material. Fibrillar structures thus improve the adherence of a system by increasing the deformation sustainable for the system. This should also be the case when the fibrillar structure is buried inside the bulk of the material. Solid foams for example are a succession of fibrils linked to each other to form a 3D structure. The role of their lower compliance on the maximum sustainable force during traction should increase the adhesion properties of the solid foams compared to the sole bulk material.

Dissipative processes in adhesion Dissipations in adhesion arise from irreversible processes during the separation of the materials, both at the interface or in the volume. In the case of polymeric materials, entanglement can occur at the interface, and the detachment, either by fracture [299] or reptation [281] of the polymers, causing energy dissipations. Plastic dissipations also occurs through the creation of new crack surfaces and additional yielding around the crack front [300]. The viscoelasticity of materials is also a motor of dissipations in the volume during deformations, which happens before the separation of the interfaces. This will be detailed in Section 8.2.

There are several experiments allowing to measure the adhesive and mechanical properties of a material. In our study, we used the JKR experiment and the probe tack test, which we detail now.

8.1.3 The JKR model

Using a strictly mechanical analysis, Hertz gave in 1882 the theory of the non-adhesive contact between two spheres of radius R_1 and R_2 or between a plane and a sphere of radius R, for which the two objects can be separated without apparition of adhesive forces [301]. The Hertz theory is valid under certain assumptions:

- the strains are within the elastic limits of the materials,
- the surface of contact has a radius $a \ll R$,
- the surfaces are frictionless,
- there are no adhesive forces between the two surfaces.

The detail of the Hertz theory is given in Appendix V, and conducted towards the definition of the force F_H and the indentation δ_H as a function of the contact radius a for a non-adhesive contact

$$a^3 = \frac{RF_H}{K}, \tag{8.8}$$

and

$$\delta_H = \frac{a^2}{R}, \tag{8.9}$$

where R is the radius of the sphere used to indent the material and $\frac{1}{K} = \frac{3}{4}(\frac{1-\nu_1^2}{E_1} + \frac{1-\nu_2^2}{E_2})$ where K is the effective modulus of the system.

However, Roberts and Kendall showed experimentally that for systems of two rubber spheres or two glass spheres, the contact area at low loads were considerably larger than what was predicted by the Hertz theory. Along with Johnson [302], they expanded the Hertz theory to include the effect of surface energy in the contact between elastic spheres, which we detail here.

Johnson, Kendall and Roberts [302] developed the theory for adhesive contacts based on an energetic point of view. They consider the case of a sphere of radius R, with a Young's modulus E_1 and a Poisson ratio ν_1, and a plane made of a material of Young's modulus E_2 and a Poisson ratio ν_2. They state that the contact radius a between the objects is a function of the total energy of the system U_T, and that at equilibrium the total energy should be minimal (Figure 8.4a).

This total energy of the system is made up of three terms: the stored elastic energy U_E, the mechanical potential energy U_P and the surface energy U_S.

When adhesive forces are present, the same contact area πa^2 is obtained with an applied force $F < F_H$ where F_H is the force predicted by Hertz for this value of a. To calculate the elastic energy U_E, we can then separate it in two contributions: a Hertzian compression phase (path between O and A in Figure 8.4b) where the surface forces are zero ($W = 0$), followed by a decompression at constant contact radius a (between A and B Figure 8.4 b) where W has a finite value. During the compression, and combining Equations (8.8) and (8.9), the Hertz theory predicts

$$\delta_H = \frac{F_H^{2/3}}{K^{2/3}R^{1/3}}, \tag{8.10}$$

and the elastic energy U_H is then given by

$$U_H = \int_0^{F_H} F_H \, \mathrm{d}\delta = \int_0^{F_H} \frac{F_H^{2/3}}{K^{2/3}R^{1/3}} \, \mathrm{d}F_H = \frac{2}{5}\frac{F_H^{5/3}}{K^{2/3}R^{1/3}}. \tag{8.11}$$

During the decompression with constant radius a, the force goes from F_H to F. Since the radius is constant, the force-indentation relation is given by the Boussinesq theory[5] [303]:

$$\delta = \frac{2}{3Ka}F. \tag{8.12}$$

[5] which gives the relations for the contact between an elastic half space and an elastic indenter.

In that case, the elastic energy U_B is then given by

$$U_B = \int_{F_H}^{F} \frac{2F}{3Ka}\,\mathrm{d}F = \frac{F^2 - F_H^2}{3Ka} = \frac{F^2 - F_H^2}{3K^{2/3}R^{1/3}F_H^{1/3}}. \tag{8.13}$$

Finally, the total elastic energy U_E is

$$U_E = U_H + U_B = \frac{\frac{1}{15}F_H^{5/3} + \frac{1}{3}F^2F_H^{-1/3}}{K^{2/3}R^{1/3}}. \tag{8.14}$$

The potential energy U_P is simply given by

$$U_P = -F\delta_1 = -F\left[\delta_H - \frac{2(F_H - F)}{3Ka}\right] = -\frac{F}{K^{2/3}R^{1/3}}\left(\frac{1}{3}F_H^{2/3} + \frac{2}{3}FF_H^{-1/3}\right). \tag{8.15}$$

Last, the surface energy U_S is expressed as a function of the thermodynamical work of adhesion

$$U_S = -WS = -W\pi a^2 = -W\pi\left(\frac{RF_H}{K}\right)^{2/3}, \tag{8.16}$$

where S is the surface area of contact.

The minimisation of the total energy

$$\frac{\mathrm{d}U_T}{\mathrm{d}a} = \frac{\mathrm{d}U_T}{\mathrm{d}F_H} = 0, \tag{8.17}$$

gives

$$(F_H - F)^2 = 6\pi WRF_H, \tag{8.18}$$

which, using Equation (8.8), translates into

$$F = \frac{Ka^3}{R} - \sqrt{6\pi Wa^3K}. \tag{8.19}$$

One should note here that in the case where $W = 0$, Equation (8.19) gives $F_H = F$ and $a^3 = RF/K$, i.e. the JKR theory includes the Hertz theory. Also, at zero applied load $F_H = 0$ (during a compression phase), the contact radius has a finite value $a^3 = \frac{6\pi WR^2}{K}$.

Equation (8.19) is written

$$F = \frac{Ka^3}{R} - \sqrt{6\pi Ga^3K}, \tag{8.20}$$

when the surfaces are separated instead of pressed against each other, where G is the energy release rate as seen in Section 8.1.2. Equation 8.20 implies that when F_H reaches zero during a traction phase, the contact radius is given by $a^3 = \frac{6\pi GWR^2}{K}$, i.e. has a different value as during the approach of the two objects. Then, when F_H is negative (still during the traction phase), a decreases from that value, and finally falls down to zero for a minimal load, also called the pull-off force

$$F_{min} = -\frac{3}{2}\pi GR, \tag{8.21}$$

which is independent of the elastic modulus.

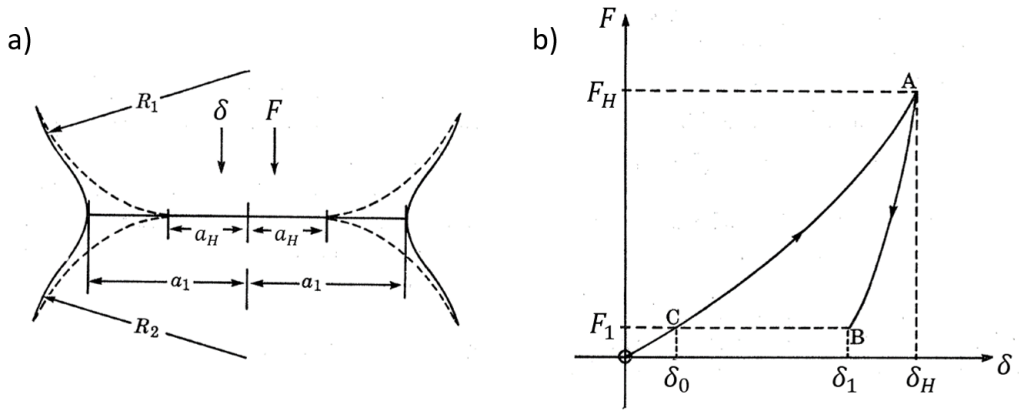

Figure 8.4: The contact between two elastic solids both in the presence (contact radius a_1) and absence (contact radius a_H) of surface forces. a) shows the contact between two convex bodies of radii R_1 and R_2 under a normal load of F; δ is the elastic displacement. b) indicates the distribution of stress in the contacting spherical surfaces. When surfaces are maintained in contact over an enlarged area by surface forces the stresses between the surfaces are tensile (T) at the edge of the contact and only remain compressive (P) in the centre. Distribution A is the Hertz stress with $a = a_1$ and $F = F_H$; distribution B the actual stress (Johnson 1958) with $a = a_1$ and $F = F_1$ and distribution C the Hertz stress with $a = a_H$ and $F = F_H$. c) represents the load-displacement relation for the contacting surfaces.

It is useful to rescale F and a into new parameters $\tilde{F}$ and $\tilde{a}$ called the pseudo force and the pseudo contact radius as

$$\tilde{a} = \frac{a^{3/2}}{R\sqrt{6\pi}}, \tag{8.22}$$

and

$$\tilde{F} = \frac{F}{\sqrt{6\pi a^3}}. \tag{8.23}$$

This finally gives the rescaled linear relations between $\tilde{F}$ and $\tilde{a}$ for the loading phase and the unloading phase respectively

$$\tilde{F} = K\tilde{a} - \sqrt{WK} \qquad \text{(loading)}, \tag{8.24}$$

and

$$\tilde{F} = K\tilde{a} - \sqrt{GK} \qquad \text{(unloading)}. \tag{8.25}$$

With this, we linearise the representation shown in Figure 1.17g, and we obtain two lines of equations $\tilde{F} = A \cdot \tilde{a} + B$ for the loading and $\tilde{F} = C \cdot \tilde{a} + D$ for the unloading. The slope A or C (which should be equal) of the compression or decompression curves give the effective modulus K of the system, while the intercepts B and D give the values of $\sqrt{WK}$ and $\sqrt{GK}$ respectively, from which we deduce W and G.

We detailed the experimental protocol for the measure of W and G using the JKR theory in Section 1.5.2 in Chapter 1.

8.1.4 The probe tack experiment

The probe tack test is very commonly used to characterise the adhesive properties of soft materials, also called their tackiness. We detailed the experimental protocol in Section 1.5.1 in Chapter 1, and

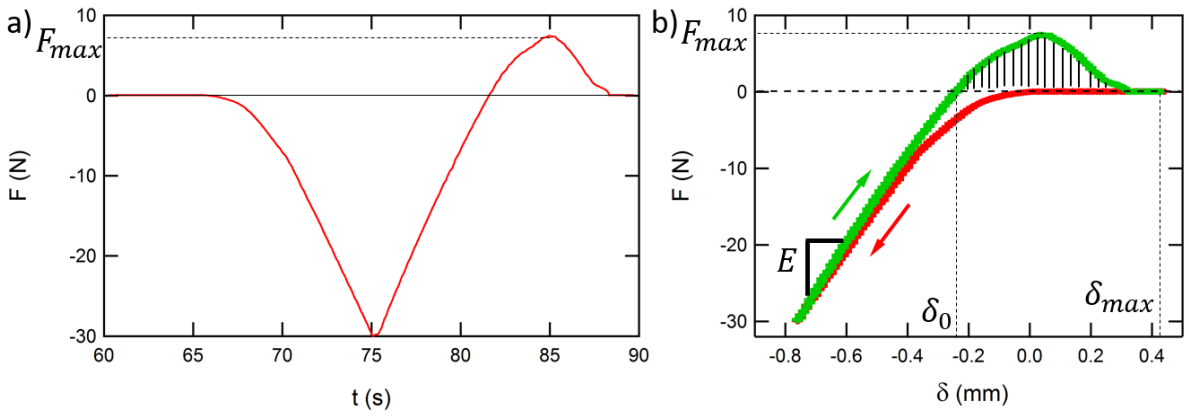

Figure 8.5: a) and b) Evolution of the force F with time (a) and δ (b) during a cycle of compression/decompression/traction.

the principle is the following. An indenter, in our case the solid emulsion sample[6], is approached with a speed v against the surface of a glass plate, larger than the sample, for a given distance d, while we measure the force F and the indentation $\delta = d - d_c$ where d_c is the distance at which the glass plate and the sample are in contact (Figure 1.16a in Chapter 1). Once the indenter has reached its maximal given distance d, it is retracted, in our case at the same speed v as during the compression phase, until there is debonding between the glass and the sample. During the compression phase, the force is negative and decreases with time and with δ, then F increases again while staying negative during the decompression phase, to finally becoming positive during the traction phase until the contact breaks between the glass lens and the sample and $F = 0$ N again (Figure 8.5a and b).

The dissipated energy D during the cycle is usually measured by integrating the curve $F = f(\delta)$ for $F > 0$ N,

$$D = \int_{\delta_0}^{\delta_{max}} F(\delta)\,\mathrm{d}\delta, \tag{8.26}$$

where δ_0 is the indentation when F becomes positive and δ_{max} the maximal indentation. The measured integral is indicated by a striped region in Figure 8.5b, and roughly corresponds to the hysteresis of the curve if we admit that the difference between the compression and decompression curves for small δ is negligible. It allows to quantify the dissipative processes in the bulk during the traction phase, i.e. the adhesive properties of the sample.

Figures 8.5a and b also give us the value of the force when the contact between the sample and the glass breaks, called the maximal force at rupture F_{max}. Finally, the slope of the compression curve in Figure 8.5b gives the Young's modulus E of the sample, following the theory given in Section 8.1.1.

The advantage of the probe-tack test compared to the JKR experiment is that it can be performed at any traction speed v, allowing to probe the rate-dependent adhesion mechanisms at play in the studied system. One of these mechanisms are viscous dissipations in viscoelastic materials such as elastomers (as stated in Section 8.1.2). Since the solid emulsions that we study in this part are composed of liquid drops in a solid elastomer, viscous dissipations will in all probability play a role in their adhesive

[6]Usually in a probe tack experiment the indenter is a solid with a high elastic modulus and the tested surface is soft and larger than the indenter. We use the opposite configuration, which should not change anything *a priori*, and showed no exotic results as shown in Chapter 10.

properties. In the next section, we thus present the notion of viscoelastic materials and their rheological properties.

8.2 Viscoelastic behaviour of polymers

All the materials used in this study, both for the drops and the continuous phase, are polymers. These are molecules made of the repetition of n small units (called monomers) with a certain molecular mass M_w, which added together ranges between a few units and $M_w \sim 100$ g/mol (in which case the term oligomer is used[7]) and up to large n and $M_w \sim 1000000$ g/mol. Depending on their size, polymers in melted form have different behaviour regarding their mechanical response. Short polymeric chains display a purely viscous behaviour. Long polymer chains on the other hand are entangled, which constrain their movement and thus their response to mechanical deformations.

8.2.1 Viscosity of liquids

The dynamic viscosity of a liquid quantifies the resistive forces to deformation by shear stress, causing energy dissipations in the bulk. These forces can be of different nature: Van der Walls forces, hydrogen bonding, electrostatic interactions, or entanglement when dealing with long chains. The dynamic viscosity, denoted either as η or μ and expressed in Pa.s, depends strongly on the temperature (the viscosity of water for example goes from 1.79 mPa.s at 0°C to 0.28 mPa.s at 100 °C). Depending on their behaviour to shear, liquids are classified in different categories.

Newtonian fluids

If η is constant for all shear rates, then the liquid is called *Newtonian* and follows Newton's law:

$$\sigma = \eta\dot{\gamma}, \tag{8.27}$$

where σ is the shear stress in Pa and $\dot{\gamma}$ the shear rate[8] in s^{-1} (which is a velocity gradient). Common examples of Newtonian fluids are water, air, milk, or alcohol. The polyethylene glycols (PEG-400 and PEG-200) used in this study are also Newtonian fluids (Figure 1.6b in Chapter 1).

Non-Newtonian fluids

Non-Newtonian fluids categorize liquids which do not have a constant viscosity for all shear rates. Among these, subcategories classify them between shear-thinning, thixotropic, shear-thickening and yield stress fluids (Figure 8.6b).

Shear-thinning fluids are defined by a decreasing viscosity when increasing the shear rate. This effect is commonly observed for polymer solutions and molten polymers, and also for common liquids like

[7]The definition of oligomer given by the International Union of Pure and Applied Chemistry (IUPAC) is "a molecule of intermediate relative molecular mass (...)" which "has properties which do vary significantly with the removal of one or a few of the units".

[8]Note here that we use γ to define the shearing deformations as customary, while γ is also used to denote the interfacial tension.

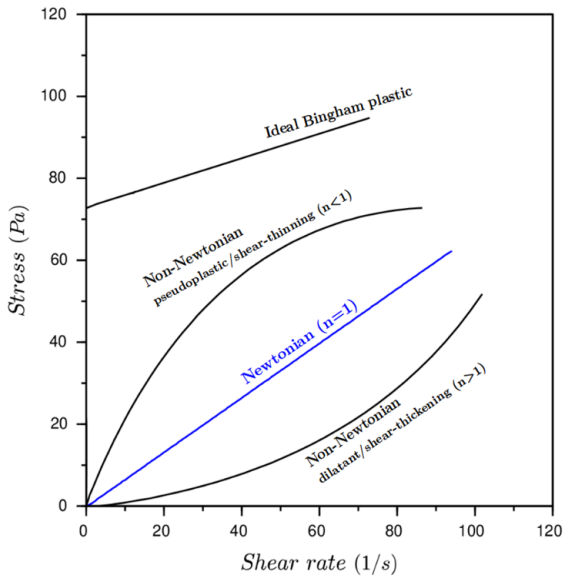

Figure 8.6: A typical stress-strain plot for non-Newtonain fluids. Adapted from https://www.simscale.com/.

ketchup, whipped cream, blood or paint. On the contrary, shear-thickening fluids have a viscosity which increases with increasing shear rate. This effect is usually observed with suspensions rather than pure fluids. For example, water-soaked sand exhibits shear-thickening properties, along with mixtures of water and cornflour. These two types of fluids usually follow a simple power law $\sigma \sim \dot{\gamma}^n$ called the *Ostwald-de Waehle* law [304].

Thixotropy is a time-dependent effect where the liquid's viscosity decreases under shaking, agitation or shear. It is not to be confused with shear-thinning, since in this case once the lower viscosity is obtained it is the same for all shear rates. Examples are found in yoghurt, ketchup and some clays.

Yield stress fluids are fluids which are solid-like at low shear rates, i.e. which do not flow below a critical stress σ_c ($\dot{\tau} = 0$ for $\sigma < \sigma_c$). In the simplest case, the fluid is Newtonian above σ_c and the *Bingham* model applies: $\dot{\gamma} = \frac{\sigma - \sigma_c}{\eta}$ for $\sigma > \sigma_c$. If the fluid is non-Newtonian above σ_c, then it is described by the *Herschel-Bulkley* model: $\sigma = \sigma_c + k\dot{\gamma}^n$ with k a constant.

8.2.2 Viscoelasticity

Some materials show both the elastic properties of solids and the viscous properties of fluids. Examples can be found in polymer melts, skin tissue or even wood. Under stress, these materials do not fully recover their initial shape, and the stress-strain plot display an hysteresis (Figure 8.7a). This means that some of the energy injected into the system is dissipated because of the viscosity. These complex materials are called viscoelastic, and their description is possible only with phenomenological models.

As it was said before in Section 8.1.1, elastic solids which follow *Hooke*'s law are characterized by the stress-strain relation $\sigma_t = E \cdot \epsilon$ for a tensile stress or $\sigma_s = \mathcal{G} \cdot \gamma$ for a shear stress. The most simple way to describe this behaviour is to modelled it by a spring of spring constant related to E or $\mathcal{G}$ (Figure 8.7b). In the case of a rapid strain imposed on the spring, its response is instantaneous and without phase.

For viscous fluids, we saw in Section 8.2.1 that Newtonian fluids followed the law $\sigma_t = \eta\dot{\epsilon}$ where $\dot{\epsilon}$ is the deformation rate during a tensile stress, or $\sigma_s = \eta\dot{\gamma}$ for a shear stress. This is modelled by a

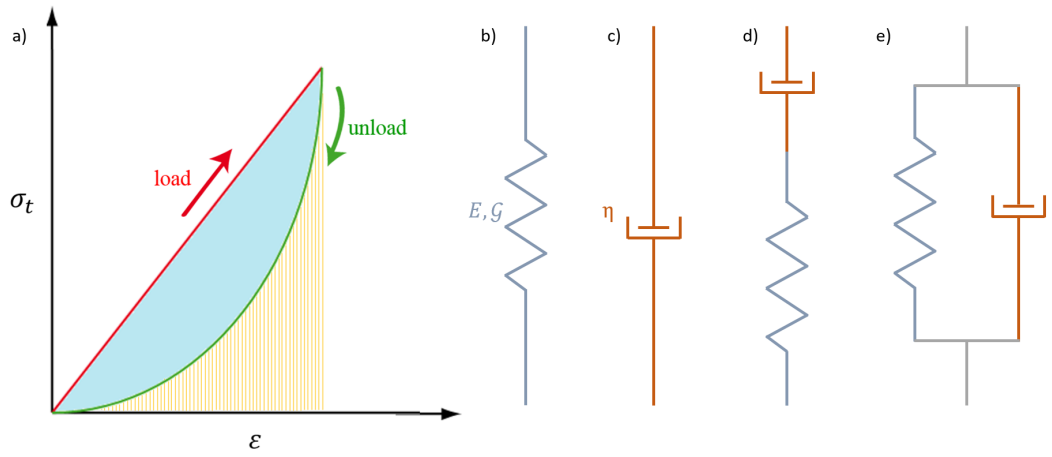

Figure 8.7: a) Schematic tensile stress-strain plot for a viscoelastic material. The hysteresis, in pale blue, is the energy lost by inner friction inside the bulk. The yellow striped part represents the energy recovered by the material. b) to e) Modelisations of visco-elastic behaviours of materials: b) solid elasticity by a spring, c) liquid viscosity by a dashpot, d) Maxwell model and e) Kelvin-Voigt model.

dash-pot, i.e. a piston moving in a container filled with a fluid of viscosity η (Figure 8.7c). This time, the dash-pot will resist a rapid strain and after the release of the stress will impose a relaxation time proportional to η.

To take into account both the elasticity and the viscosity of the material, models have been developed using the spring-dash-pot analogy with different variations. Here, we will present only two, the Kelvin-Voigt model and the Maxwell model (Figure 8.7d and e). Other more sophisticated models exist when these two fail to predict the behaviour of a material.

Here, we will develop these models only for shear stresses in oscillatory experiments, though the equations are commutable between E and $\mathcal{G}$.

The Maxwell model

In the Maxwell model (Figure 8.7d), the spring and the dash-pot are in series combination. This implies that the total deformation γ is equal to the sum of the respective deformations for the spring (γ_{el}) and the dash-pot (γ_{visc})

$$\gamma = \gamma_{el} + \gamma_{visc}. \tag{8.28}$$

Since the elements are in series, the tensile stress has to be the same in both of them and can be written

$$\sigma_t = \mathcal{G} \cdot \gamma_{el} = \eta \dot{\gamma}_{visc}. \tag{8.29}$$

From equations (8.28) and (8.29), we get the differential equation

$$\frac{d\gamma}{dt} = \frac{\sigma}{\eta} + \frac{1}{\mathcal{G}} \frac{d\sigma}{dt}, \tag{8.30}$$

for which we can look for solutions when oscillations of the form

$$\sigma(t) = \sigma_0 \exp(i\omega t), \tag{8.31}$$

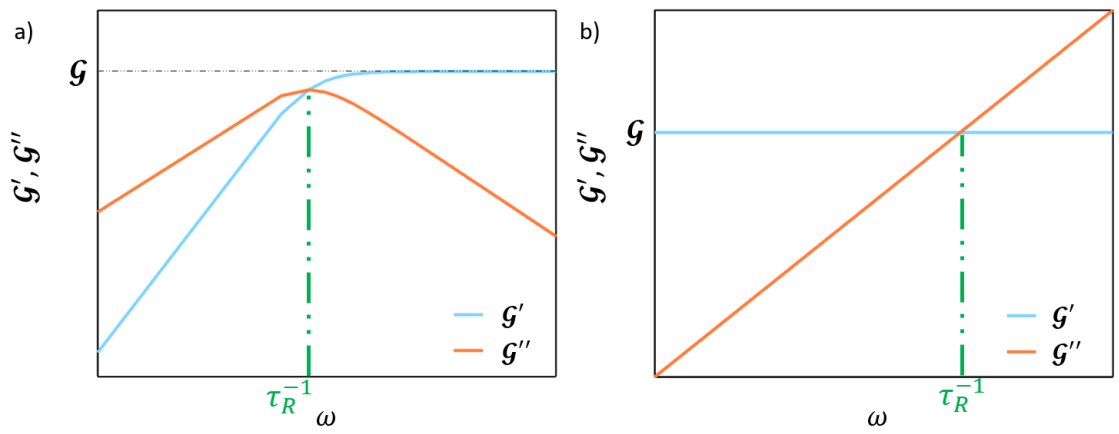

Figure 8.8: a) Log-log representation of $\mathcal{G}'$ and $\mathcal{G}''$ with the frequency ω in the Maxwell model. b) Linear representation of $\mathcal{G}'$ and $\mathcal{G}''$ with the frequency ω in the Kelvin-Voigt model.

are imposed to the system. Injecting Equation (8.31) in Equation (8.30), we get, after integration

$$\gamma(t_2) - \gamma(t_1) = (\frac{\sigma_0}{i\eta\omega} + \frac{\sigma_0}{\mathcal{G}}) \exp(i\omega(t_2 - t_1). \tag{8.32}$$

Since the complex modulus $\mathcal{G}^*$ is defined as

$$\mathcal{G}^* = \mathcal{G}' + i\mathcal{G}'' = \frac{\sigma(t_2) - \sigma(t_1)}{\tau(t_2) - \tau(t_1)}, \tag{8.33}$$

we get

$$\mathcal{G}' = \mathcal{G}\frac{\tau_R^2\omega^2}{1 + \tau_R^2\omega^2}, \tag{8.34}$$

and

$$\mathcal{G}'' = \mathcal{G}\frac{\tau_R\omega}{1 + \tau_R^2\omega^2}, \tag{8.35}$$

where $\tau_R = \eta/\mathcal{G}$ is the Rouse relaxation time of the material.

$\mathcal{G}'$ is called the storage modulus and measures the elastic response of the material, which is in phase with the excitation. $\mathcal{G}''$ is called the loss modulus, measuring the viscous response of the material, i.e. the energy dissipations and is out of phase with the excitation. They are both represented in Figure 8.8a. At low frequencies, $\mathcal{G}'' > \mathcal{G}'$ which means that the material behaves as a viscous liquid. Both moduli are equal for $\omega = 1/\tau_R$. At higher frequencies, $\mathcal{G}'$ increases and saturates at the value $\mathcal{G}$ higher than $\mathcal{G}''$, i.e. elasticity prevails and the material is solid-like. The Maxwell model is then good in characterising viscoelastic liquids.

The Kelvin-Voigt model

We now do the same analysis this time with the Kelvin-Voigt model (Figure 8.7e). The spring of constant $\mathcal{G}$ is now in parallel combination with the dash-pot of viscosity η. In that case, the deformations are equal in each element

$$\gamma = \gamma_{el} = \gamma_{visc}, \tag{8.36}$$

and the total stress is the sum of the elastic and viscous contribution

$$\sigma = \mathcal{G} \cdot \gamma_{el} + \eta \dot{\gamma}_{visc}, \tag{8.37}$$

which gives

$$\sigma = \mathcal{G}\gamma + \eta\dot{\gamma}. \tag{8.38}$$

We apply the same oscillation as in Equation (8.31), and we look for the expression of $\mathcal{G}^*$. All calculations made, we find

$$\mathcal{G}' = \mathcal{G}, \tag{8.39}$$

and

$$\mathcal{G}'' = \eta\omega. \tag{8.40}$$

Both are represented in Figure 8.8b. With the Kelvin-Voigt model, $\mathcal{G}'$ is a constant equal to $\mathcal{G}$, and $\mathcal{G}''$ is a linear function of ω. Both moduli are again equal for $\omega = 1/\tau$. This time, at low frequencies, it is the elasticity that prevails on the viscosity, the material behaves as a solid. At high frequencies however, $\mathcal{G}'' > \mathcal{G}'$ and the material behaves like a liquid. The Kelvin-Voigt is then a simple modelisation for viscoelastic solids.

Both these models are the most simple way to describe viscoelastic liquids and solids. Evidently, they can fail to predict the behaviour of more complex materials. Indeed, they only describe the transition between two regimes, liquid-like and solid-like, with only one relaxation time τ. However, polymers for example often exhibit several relaxation times and more than one phase transition between three possible states: viscous liquid, rubber and glassy polymers. Other models include the superposition of several Maxwell or Kelvin-Voigt models, or go down to the molecular scale to model the dynamics of the melts. We will not however go into more details here since we will use the viscoelasticity of a material only as a motor of adhesive processes, as it was discussed in Section 8.1.2.

8.3 Properties of cellular materials

8.3.1 Elastic properties of cellular materials

Cellular materials are a class of materials composed of spherical or polyhedral cells of gas, liquid or solid inside a liquid or solid matrix. They are found in a great variety of human-made applications, from thermal and acoustic insulation in the construction industry to the pleasure and enjoyment in the food and cosmetic industry. Nature also designed cellular materials for various reasons such as wood, sponge, bones and coral.

This work is dedicated to the study of the mechanical and adhesive properties of solid emulsions composed of viscous drops inside a solid polymeric matrix. In order to interpret the results, we need to address the results obtained with similar materials. In that regard, we will discuss here the literature on the mechanical properties of solid foams and emulsions only. The adhesive properties of these materials will be reviewed in Section 8.3.2.

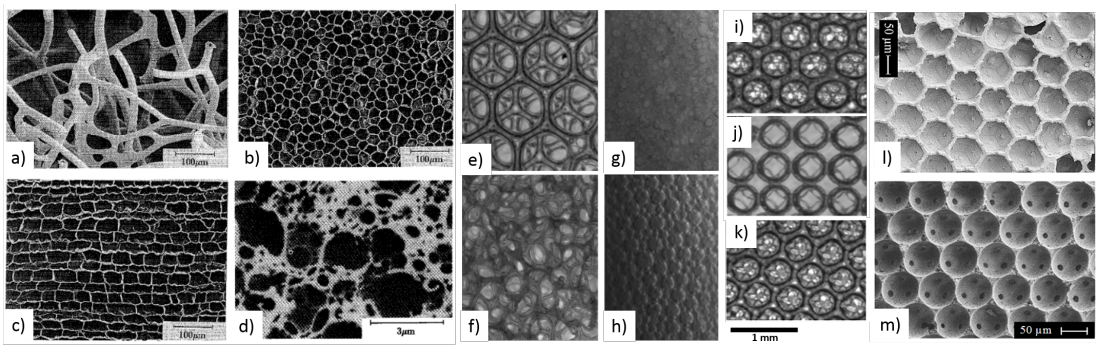

Figure 8.9: Various examples of cellular materials (depicted by scanning electron microscopy): (a) sponge formed by interconnected edges, although not arranged in polyhedral cells; (b) tangential section of cork (perpendicular to the radius of the tree); (c) section of cork containing the radius of the tree; d) bread (a), b), c) and d) extrated from [5]); e) monodisperse ordered polyurethane foam; f) monodisperse random polyurethane foam; g) polydisperse polyurethane foam; h) bidisperse polyurethane foam; i) crystalline HCP lattice; j) crystalline square lattice; k) crystalline FCC lattice; l) monodisperse closed-cell polystyrene foam; m) monodisperse open-cell polystyrene foam.

Mechanics of solid foams

Solid foams possess remarkable properties. Their low density with high stiffness is interesting for building large portable structures. They also allow to build flotation devices. Depending on the material used, they can offer thermal or acoustic insulation. Compliant foams can absorb impacts, or bring comfort for a cushion. Out of these properties, we focus here on the mechanical properties of solid foams.

The structure of a solid foam takes various forms (Figure 8.9): the cells can be monodisperse (most of the time for human-made foams) or polydisperse , open or closed. They can be arranged randomly of in a crystalline lattice. The role of these properties has been the subject of many studies, of which we give a rapid review in this section.

Usually, the parameters which are the most looked into in solid foams are its density ρ^* which measures the relative quantity of continuous phase in the foam, or inversely its void volume fraction ϕ^* which measures the relative quantity of gas, and its elastic modulus (or Young's modulus) E^*. These are considered along with the properties of the cell material such as its density ρ_s and its elastic modulus E_s. Studies looked at the impact of this quantity on the Young's modulus of the foam. Figure 8.10 gives a schematic representation of a stress-stress plot during a uniaxial compression of a solid foam. This curve can be separated in three regimes [6]. First, all foams show a linear elasticity regime (regime I Figure 8.10), where $\sigma_t^* = f(\epsilon^*)$ follows Hooke's law and is due to the bending of the cell material. Then, a plateau is reached during the second regime called the buckling regime (regime II Figure 8.10), which is due to the elastic collapse of the cells for elastomeric foams, the formation of plastic hinges in a yielding foam (metallic foams for example), and brittle crushing in a brittle foam such as ceramic foams. A third regime called compaction (regime III Figure 8.10) then follows where all the cells have collapsed and the stress rapidly increases. The exact form of the $\sigma_t = f(\epsilon)$ curve depends on the type of solid foam, for example the plateau appearing during the buckling of the foam will show strong fluctuations around the mean value in a brittle foam.

The linear elasticity regime We focus here on the linear elasticity regime, which is the one we will stay in for our experiments. Theoretical predictions of the Young's modulus of solid foams have

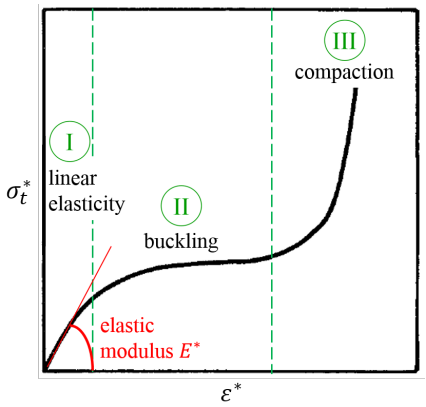

Figure 8.10: Schematic representation of a stress-strain plot of a solid foam under uniaxial compression. Adapted from [5].

been given by several studies [4,6]. Instinctively, the elasticity of a solid foam depends on the fraction of voids in the material: a high volume fraction of voids leads to a more compliant material and vice versa. Gibson and Ashby [6] proposed to separate the elastic behaviour of open-cell and closed-cell solid foams, where two additional contributions to the elasticity arise for the closed-cell foam compared to the open-cell.

In a open-cell solid foam, the elastic behaviour is driven by the elasticity of the cell materials, though their bending and the transmission of the applied force through the cells network. Considering this, Gibson and Ashby [6] give

$$\frac{E^*}{E_s} = C_1(1-\phi^*)^2, \qquad \text{(open-cell)} \tag{8.41}$$

where C_1 is a constant. Fitting the data from [7,8,305], they find $C_1 \approx 1$.

In the case of a closed-cell foam, additional contributions to the elasticity of the material cause a deviation from Equation (8.41). This time, the material structure is determined, besides the volume fraction of voids ϕ, by the face-to-edge content ratio $\psi = V_f/V_e$ in the cell, where V_f is the volume of material in the face of the cell and V_e the volume of material in the edge. Indeed, foaming processes usually cause the accumulation of material in the edges rather than in the faces of the cells. This parameter ψ induces a different contribution to the bending of the edges of the cell during the compression. Also, during the deformation of the foam, the faces are stretched in the direction perpendicular to the applied stress, which needs to be taken into account in the foam elasticity. Finally, the compressibility of the gas trapped inside the cells adds a third contribution to the global elasticity of the foam. All this results in the relative elastic modulus

$$\frac{E^*}{E_s} = C_1\psi^2(1-\phi^*)^2 + C_1'(1-\psi)(1-\phi^*) + \frac{p_0(1-2\nu^*)}{E_s\phi^*}, \qquad \text{(closed-cell)} \tag{8.42}$$

where p_0 is the initial pressure inside the cell and ν^* is the Poisson ratio of the foam which is approximated as non-dependent of ϕ and $\nu^* \approx 1/3$, as for open-cell foams. Using data from [7,306–314], they give $C_1 = C_1' \approx 1$.

Heitkam *et al.* [4] ran finite elements simulation in order to predict the mechanical behaviour of monodisperse solid foams presenting different crystalline order, with open or closed cells depending on the value of ϕ^*. They found that for any global organisation of the foam, the $E^*/E_s = f(\phi^*)$ curve

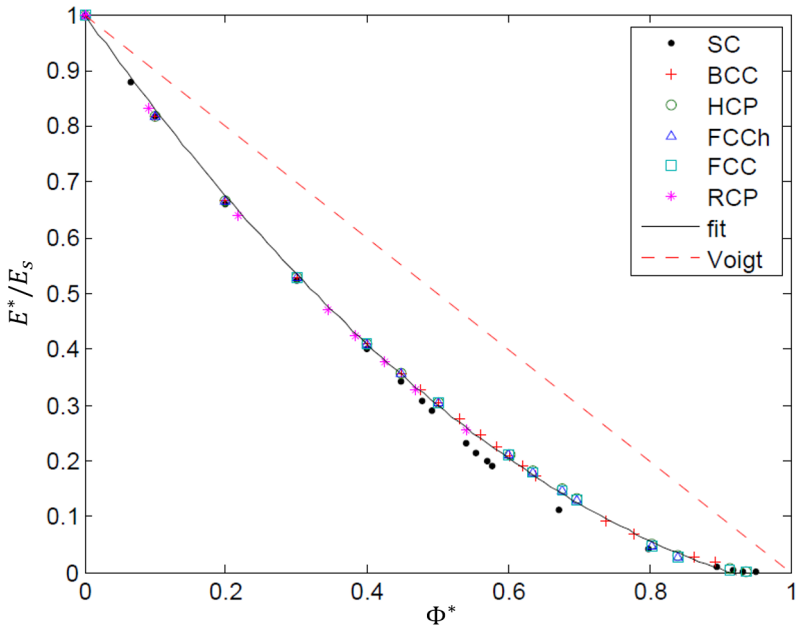

Figure 8.11: Mean Young's modulus over a range of void fractions ϕ for different arrangements of spherical voids. The solid line represents the fitting curve from Equation 8.43 while the broken line represents Voigt's upper bound [4].

was well fitted by the equation (Figure 8.11)

$$E^* \approx 0.74\phi^{*2} - 1.77\phi^* + 1. \tag{8.43}$$

This implies that, in the linear elasticity regime, no arrangement of spherical voids in a regular lattice would yield more advantageous properties than others for any given volume fraction of voids. Heitkam *et al.* use systems with air at atmospheric pressure (0.1 MPa) inside the either open or closed cells. Assuming a material's modulus in the order of the MPa ($E_s \approx 1$ MPa for the softest rubbers and up to $E_s \approx 10\,000$ MPa for polycarbonate and even higher for metals), the third term of Equation (8.42) gives a dependence in the volume fraction of $\approx 0.03/\phi^*$ at most, i.e. does not contribute much to the foam elasticity especially since closed-cells mean low ϕ in their study.

A higher air pressure, or the use of an incompressible liquid inside the cells should however greatly impact the elastic properties of the cellular material. We will now review the results on the elastic properties of solids with liquid inclusions.

Liquid inclusions in solids

The case of liquid inclusions in a solid or solid-like matrix is different than the case of solid foams because of the incompressibility of the liquid in the cell. Intuitively, a solid with a volume fraction ϕ^* of liquid cells has a higher elastic modulus than a solid foam with the same volume fraction. The prediction of the elastic modulus in such a composite material was first proposed by Eshelby [315] for solids containing isolated droplets. He stated that, for a solid of elastic modulus E_s containing a volume fraction ϕ^* of isolated and incompressible droplets, the elastic modulus of the composite material E^* should follow

$$E^* = \frac{3E_s}{3 + 5\phi}. \tag{8.44}$$

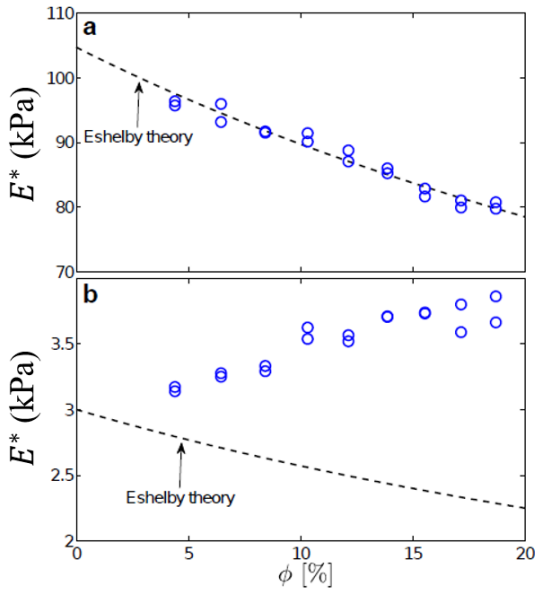

Figure 8.12: Young's modulus of soft composites E^* as a function of liquid content ϕ. (a,b) Glycerol droplets embedded in E_s ∼3, 100 kPa silicone gels respectively. Dashed curves show Eshelby's predictions for incompressible liquid droplets in an incompressible solid of stiffness E_s [9].

This behaviour implies that the presence of isolated liquid inclusions inside a solid matrix decreases the elastic modulus of the material. Hill [316] extended this result for any concentration of liquid inside the solid matrix and proposed

$$E^* = \frac{E_{mean} - E_l E_s / 4\mu^*}{1 - E_{mean}/4\mu^*}, \tag{8.45}$$

with

$$E_{mean} = \phi E_l + (1-\phi) E_s, \tag{8.46}$$

where $E_{l,s}$ are the Young's modulus of the included liquid and the solid phase respectively, and μ^* the shear modulus of the composite material.

Both these predictions however do not take into account any surface tension effects at the interface between the inclusions and the matrix. As explained in Part A of this manuscript, the surface tension γ tends to minimize the surface of a given volume. When this volume is stretched, during compression/traction or shear, surface tension tends to resist the deformation. This resistance has an impact on the deformation of solids at lengthscales $L \leq \gamma/E_s$. Style *et al.* [9] experimented this effect with two matrices of different elastic modulus E_s, for which, with the same droplet radius R, either $R > L$ (Figure 8.12a) or $R < L$ (Figure 8.12b). They showed that if Eshelby's theory predicted very well the elastic modulus of the composite when the surface tension is negligible compared to the elastic modulus of the matrix, it completely failed to describe the behaviour of the composite in the opposite case, where the presence of liquid inclusions even increased the elasticity of the material.

Style *et al.* proposed a new equation taking into account surface tension effects for the Young's modulus of the solid matrix with isolated droplets in its structure

$$E^* = E_s \frac{1 + \frac{5}{2}\frac{\gamma}{E_s R}}{\frac{5}{2}\frac{\gamma}{E_s R}(1-\phi) + (1 + \frac{5}{3}\phi)}, \tag{8.47}$$

which is identical to Eshelby's Equation 8.44 when $\gamma = 0$ N/m. They showed that their equation effectively allows to capture the increase of composite stiffness observed Figure 8.12b for E_s= 3 kPa.

Mancarella *et al.* used two approaches to predict the behaviour of composite materials for higher volume fraction of drops (up to 60%) [317, 318] which both use interfacial tension effects at the liquid/solid interface. Both studies were consistent with the results of Style *et al.* for very low ϕ (isolated droplets), and also found an increase of the elastic modulus of the composite when γ is not negligible compared to E_s. Wang *et al.* [319] used finite element simulations to get the behaviour of composite materials and showed that their results agree with the predictions of Mancarella *et al.*.

8.3.2 Adhesive properties of cellular materials

In Section 8.1.2, we saw that the adhesion energy of a material could be fine-tuned by a structuration of the interface in contact with the substrate. In this Part, we ask the question: *does a 3D bulk structuration influences the adhesive properties of a material, while its surface is kept unchanged?* In Section 8.3.1, we detailed how the volume fraction of gas or liquid inclusions in a cellular material changes its elastic modulus. In this section, we review the results obtained on their adhesive properties.

Gas inclusions

Quite surprisingly, no literature could be found on the adhesive properties of solid foams. Only patents where solid foams were used as a part of a removable adhesive tape were found [320, 321], and their role in the adhesion of the material was not discussed. We will then here not discuss the evolution of the adhesive properties of the solid foams with the volume fraction of gas inclusion as we did for their mechanical properties.

However, 2D cellular materials that can be seen as 2D solid foams were studied by Noderer *et al.* [11], Glassmaker *et al.* [322] and Shen *et al.* [323]. These are composed of fibrils with a variable spacing sandwiched between a large backing layer and a thin film which closes the material and serves as the surface in contact in the experiments (Figure 8.13a). Glassmaker *et al.* [322] realised peeling experiments with these materials as shown in Figure 8.13b, and measured the energy release rate G for different fibril length and spacings between the fibrils and normalised it by the value of G for the control bulk material. They found that the presence of a fibrillar sub-structure enhance the value of G of a factor up to ~ 9 compared to the bulk material (Figure 8.13c), and that there is an optimum of G at intermediate values of fibril spacing and length. The same evolution of G with the spacing between fibrils was found by Noderer *et al.* [11] and Shen *et al.* [323], though the latter noted that in their case the fibrils in the materials with the largest spacings (110 µm and 125 µm) were damaged during the test, possibly reducing the experimental value of G. Glassmaker *et al.* [322] also showed that the pull-out force needed to separate the surfaces in indentation experiments was 1.5 to 3.5 greater for fibrillar structures than for the control bulk material.

They all attribute this evolution of G with the spacing between fibrils to the pinning of the crack front at the position of the fibrils. Indeed, Noderer *et al.* [11] noticed that during an indentation, the crack front is first blocked at the front of the fibril. During this blockage, the fibril stores the energy, which is then released at once when it is sufficiently high to jump across the trapping fibril. The same phenomenon happens during retraction. The variation of the energy release rate along the axis of propagation of the front crack is shown in Figure 8.13d. In these systems, the magnitude of the

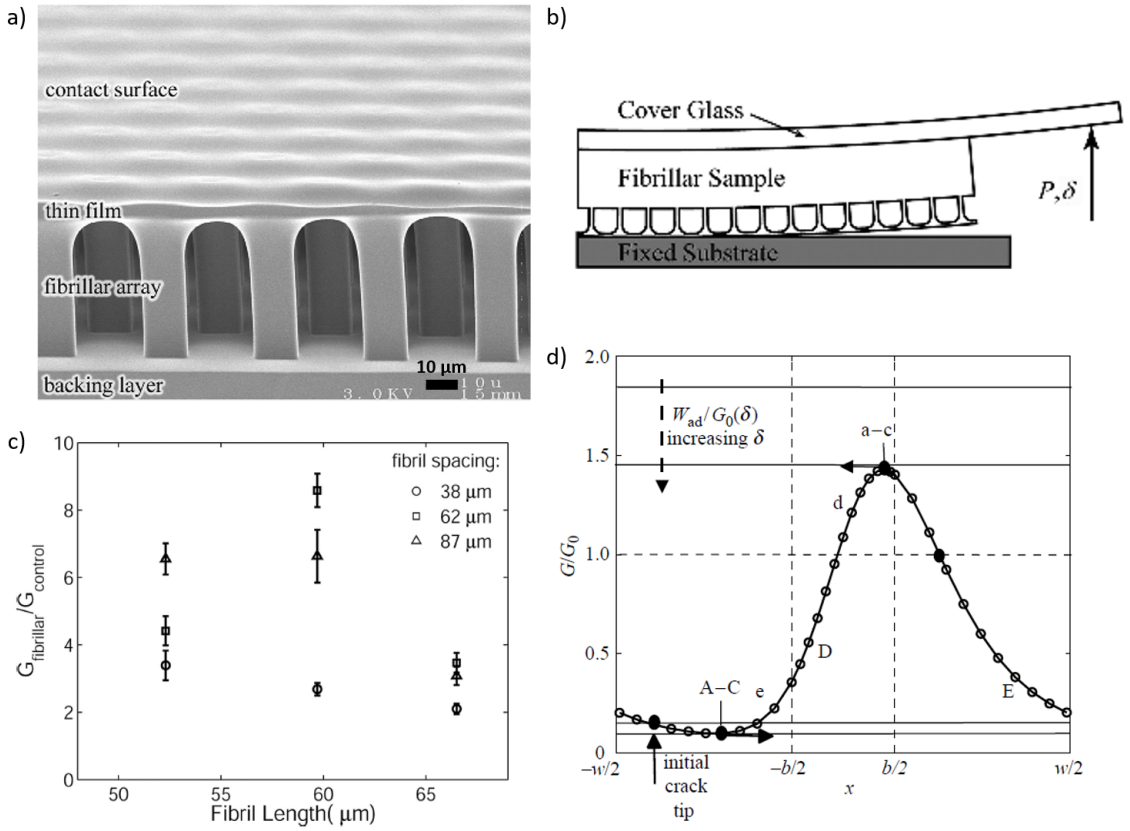

Figure 8.13: a) Synthetic fibrillar adhesion surface, including spatular features. Shown is an array of micropillars with a terminal film. b) Scheme of the sample a) during a peeling experiment. c) Normalized energy release rate G presented as a function of fibril length and spacing. Results are quotients of mean values, with five trials performed to obtain each mean. Error bars were calculated by assuming that both fibrillar and control samples have random, independent uncertainty of 1 SD. Extracted from [322]. d) Variation of normalized energy release rate G/G_0 with respect to the position of crack, x, computed with a finite element method. Points A–C and a–c represent locations where the crack is trapped during opening and healing, respectively. Extracted from [11].

energy release rate is direction dependent. Yao *et al.* [324] found that this effect could be even more significant by tilting the fibrils to an optimum angle.

Majumder *et al.* [10] used a similar approach with a different structure: they embedded channels of different diameter and with different spacings in the structure of a crosslinked PDMS sheet (Figure 8.14a and b) and measured the energy release rate necessary to detach these from a glass coverslip in a peeling experiment. They showed that the energy release rate to detach the PDMS sheet with embedded channels filled with air was up to 12 times higher than for the bare PDMS sheet, and that it was as efficient as a textured surface with comparable characteristic lengths (Figure 8.14c).

Liquid inclusions

Majumder *et al.* [10] also filled the embedded channels in the structure of the crosslinked PDMS sheets with liquids (silicone oils) of different viscosities η (Figure 8.14b). They showed that the energy release rate G during a peeling experiment was dependent on the viscosity η (Figure 8.14d), with G/G_0 up to 30 at best, where G_0 is the energy release rate of the bare PDMS sheet (Figure 8.14c). They found an optimum of G with the viscosity of the liquid. They also varied the height h of the PDMS sheet while

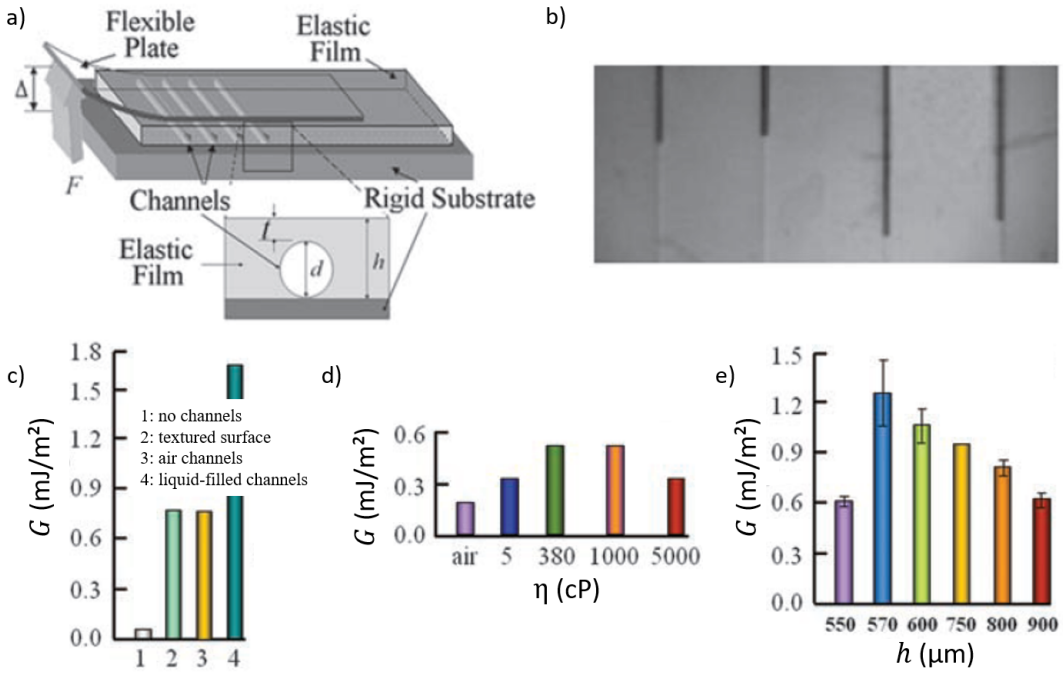

Figure 8.14: a) Schematic of the experimental setup where a flexible plate is lifted from its end off of an elastic adhesive layer with embedded microchannels. b) Top view of a typical adhesive film (h = 120 mm, d = 50 mm) with embedded channels partially filled with silicone oil of η = 380 cP. c) While on a smooth film (1), the adhesion strength is estimated as G = 60 mJ/m^2 (similar to that obtained by Johnson et al. [302]); on an incision-patterned film (2) and on a film of thickness h = 750 mm embedded with air-filled channels of diameter d = 710 mm (3), G is 750 mJ/m^2. G increases to $\sim$ 1800 mJ/m^2 when these channels are filled with liquid (4). d) h is varied systematically while keeping d = 530 mm unaltered. The channels are filled with a liquid of η = 380 cP. Error bars represent standard deviation. Extracted from [10].

keeping the channel diameter d constant, which comes down to change the thickness of the PDMS film below the channels, and showed that as h increases with constant d, G decreases, which means that the effect of the liquid channels is screened by the PDMS. The effect was also compromised for very thin thickness of PDMS above the channel (h = 550 μm against d = 530 μm). This phenomenon is interpreted as for the studies of Noderer *et al.* [11], Glassmaker *et al.* [322], Shen *et al.* [323] and Yao *et al.* [324] in Section 8.3.2: the presence of substructures inside the material causes the variation of the energy release rate with respect to the position of the crack front, which induces the pinning of the crack front at stable or unstable equilibria (Figure 8.13d). The liquid inside the channels adds viscous dissipations to the difference in the compliance of the materials compared to the gas filled substructures. Though the studies in Section 8.3.2 did not study the impact of the film thickness over the fibrils, the same effect should be measured as in Figure 8.14e.

In another paper, Majumder *et al.* [325] showed that this evolution of G with the presence of a substructure filled with either gas or silicone oil inside a PDMS sheet was independent of the environmental conditions and gave the same results in air or in water.

In this chapter, we went over the theoretical background and the associated literature to understand the mechanical properties of solids, and more precisely cellular materials with inclusions of either gas or liquid. The elastic properties of cellular materials have received much attention, and the Young's modulus of solid foams is now well known for the entire range of volume fractions of bubbles, for

any overall organisation of the bubbles. In the case of liquid inclusions in a solid compliant matrix, theoretical models now allow to predict the experimental results for volume fractions of drops up to 60%.

We also defined in Section 8.1.2 the adhesion of a material against a substrate, by giving the different mechanisms in the adhesion process, differentiating those which occur directly at the surface of contact and those which involve energy dissipations inside the bulk. In this work, we are mostly interested in the latter, more precisely *our goal is to understand how a substructure within the bulk of a material impacts its adhesive properties.* We then reviewed the associated literature in Section 8.3, where we found different studies on how a 2D fibrillar structure terminated by a continuous film enhance the adhesive properties of the material. We also presented a study of Majumder *et al.* [10] which shows that, if channels filled with air within the bulk of a material already enhance the energy release rate as previous studies did with the 2D fibrillar structure terminated by a continuous film, filling these channels with a liquid of viscosity η has an even greater impact on G. However, all of the systems described in Section 8.3.2 are 2D structures within a 3D bulk material. Our work presented in Part C of this manuscript is dedicated to going from a 2D to a 3D substructure in compliant materials. To do this, we generate solid PEG-in-PDMS emulsions (Chapter 4), of which we varied the drop radius and their number in the bulk. The description of the samples and the characterisation of their rheological and mechanical properties are given in Chapter 9. We then study their adhesive properties in Chapter 10 which we confront with the results presented in Section 8.3.

Chapter 9

Mechanical properties of solid emulsions

The goal of this part of the manuscript is to investigate the mechanical and adhesive properties of solid PEG-in-Sylgard 184® emulsions. The generation and solidification of such materials was detailed in Section 1.2 Chapter 1, and we discussed the structure of the liquid template in Part B. In this chapter, we first describe the relevant characteristics of the solid emulsions in Section 9.1. Then we investigate their rheological properties in Section 9.2 and their elastic properties in Section 9.3.

9.1 Description of the samples

The solid PEG-in-Sylgard 184® emulsions (that we call solid emulsions from now on) are composed of liquid drops of PEG-400 in a solid matrix composed of Sylgard 184® (Figure 9.1a). The generation is made as explained in Section 1.2 in Chapter 1: the drops of PEG-400 are created by dripping or using a T-junction, and they fall into a bath of Sylgard 184®, in which a percentage $\%Dod$ of dodecane (in weight %) was added (cf Section 1.1.1 in Chapter 1). We then solidify them in an oven at 60°C for at least 3 hours. They are cylinders, with a diameter $D_s = 26$ mm and a height $h_s = 8$ mm. The characteristics of the samples used for this study, such as the percentage of dodecane added in the continuous phase $\%Dod$ for the generation of the emulsions, the number of drops in the sample N, the drop radius R and the ratio of the emulsions height over the sample height h/h_s (see Figure 9.1b), are given in Table 9.1. We first looked at the impact of the number of drops N, which varies between 150 and 500, with a constant drop radius R in the sample on its rheological properties (samples 1 to 7, see Section 9.2). We then studied the impact of the drop radius, which varies between 340 µm and 1.53 mm, in samples filled with drops on the elastic properties of the materials (samples 1 and 7 to 13, see Section 9.3). The expression "filled" means that the drops fill the sample up to 90% of its height ($h/h_s = 0.9$). At least 1 mm is left without any drops on the top of the samples 8 to 13 (Figure 9.1b), in order for the surface of every sample to be smooth (not roughened by the close presence of drops), which is a strong requirement of the contact mechanics experiments to measure adhesion.

To obtain the structural properties of the solid emulsions, we imaged them using X-Ray tomography and we analysed the tomographs using the software Avizo (Figure 9.1c and d), as described in Section 1.4.4 in Chapter 1. X-Ray tomography allows to obtain the structural properties of the emulsions, such as the number of drops, their volume and their position in the volume of the sample, which makes it possible to obtain the volume fraction of drops or the distance between them.

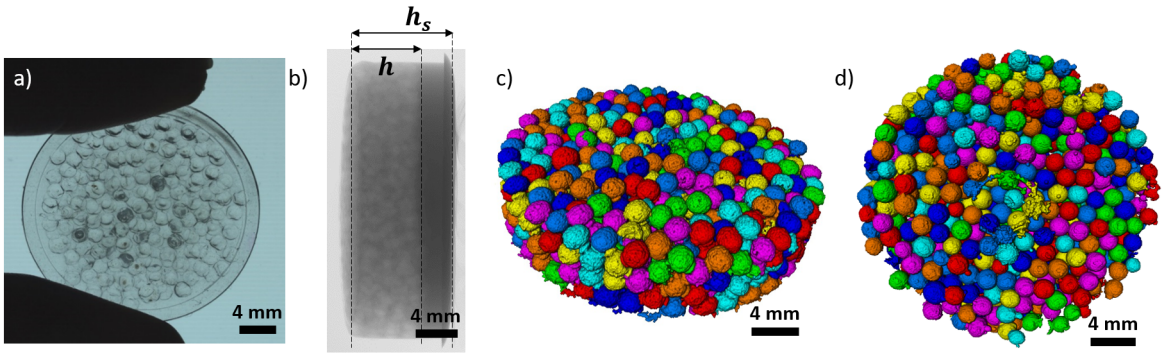

Figure 9.1: a) Optical image of solid PEG-in-PDMS emulsions with monodisperse PEG drops. b) Radiograph of the solid emulsion in a) after image normalization. c) Side view and d) top view of the 3D rendering volume of the solid emulsion in a) obtained by absorption contrast X-Ray tomography showing separated droplets marked by different colours after image processing.

Sample number	$\%Dod$	**Dispersed phase**	R **(mm)**	**Number of drops** N	h/h_s
1	0%	Bare PDMS	0	0	0
2	0%	PEG-400	1.05 ± 0.1	100 ± 5	0.2
3	”	”	1.05 ± 0.1	200 ± 5	0.4
4	”	”	1.05 ± 0.1	250 ± 5	0.5
5	”	”	1.05 ± 0.1	300 ± 5	0.6
6	”	”	1.05 ± 0.1	400 ± 5	0.8
7	”	”	1.05 ± 0.1	500 ± 5	1.0
8	5%	”	0.34 ± 0.11	4000 ± 100	0.9
9	5%	”	0.85 ± 0.11	750 ± 20	0.9
10	10%	”	0.92 ± 0.30	450 ± 50	0.9
11	0%	”	1.42 ± 0.14	220 ± 20	0.9
12	5%	”	1.48 ± 0.21	190 ± 10	0.9
13	10%	”	1.53 ± 0.30	150 ± 10	0.9

Table 9.1: Solid PEG-in-PDMS emulsions used in Part C.

9.2 Rheological properties of the solid emulsions

The rheological properties of the bare Sylgard 184® are well known, and depend on the ratio of base over curing agent of the mix [29]. For a ratio of 10:1, which is the reference sample 1 in this study,

the Sylgard 184® is a viscoelastic solid which can be approximately described by the Kelvin-Voigt model presented in Section 8.2.2 in Chapter 8. In this section, we study the impact of the presence of PEG-400 drops on the rheological properties of the samples. We thus keep a constant drop radius $R = 1.05 \pm 0.10$ mm, and we vary the number of drops N in the sample from $N = 0$ (bare Sylgard 184®) to $N = 500$. The experimental protocol of the measure of the rheological properties of the samples is explained in detail in Section 1.5.3 in Chapter 1.

9.2.1 Domain of linear elasticity

We first search for the range of shear strain of the linear elasticity domain of the solid emulsions, where the Hooke's law is valid, since we always stayed in the domain of linear elasticity in the rest of the study. For this, we varied the shear strain amplitude from $\gamma = 0.01$ % up to $\gamma = 0.9$ % for sample 3 ($N = 200$ drops, $h/h_s = 0.4$) and from $\gamma = 0.05$ % up to $\gamma = 15$ % for sample 6 ($N = 400$ drops, $h/h_s = 0.8$). The evolution of the storage $\mathcal{G}'$ and loss $\mathcal{G}''$ moduli as a function of the angular frequency ω and for each value of the amplitude γ is shown in Figure 9.2a for sample 3 and Figure 9.2b for sample 6. In both figures, all the curves for each γ are superimposed. Figures 9.2c and d show the evolution of $\mathcal{G}'$ and $\mathcal{G}''$ separately as a function of ω for sample 6. Figure 9.2c shows that the curves of $\mathcal{G}' = f(\omega)$ superimpose perfectly for $0.05\ \% \leq \gamma \leq 1\ \%$, and then separate from the pack for $\gamma > 1$ %. In the case of the evolution of $\mathcal{G}'' = f(\omega)$, we can see in Figure 9.2d that even at high amplitudes the curves do not separate except at very low angular frequencies.

We can calculate the amplitude needed to create a displacement of 1 mm at the perimeter of the sample, which we find equal to $\gamma_{1\text{mm}} = 1.2$ %. This means that the range of the elastic domain lies within solicitations of the drops lower that their radius. However, the separation of the curves of $\mathcal{G}' = f(\omega)$ for $\gamma > 1$ % is still negligible even for high solicitations ($\gamma = 15$ %). In light of these results, we chose for the rest of the study to keep $\gamma = 0.01$ % (corresponding to a displacement of 8 µm at the periphery of the sample) since it is enough to probe the response of the samples to oscillations and it allows to make sure that the samples are not deteriorated during the experiments.

9.2.2 Evolution of $\mathcal{G}'$ and $\mathcal{G}''$ with the number of drops N

Keeping $\gamma = 0.01$ %, we now look at the evolution of $\mathcal{G}'$ and $\mathcal{G}''$ with the number of drops N in the samples. Figure 9.3a shows a log-log representation of the storage and loss moduli of samples 1 to 7 and of the PEG-400 as a function of the angular frequency ω. For samples 1 to 7, the storage modulus is almost constant with ω and stays higher than the loss modulus for every angular frequency between 0.1 and 100 rad/s, while the loss modulus increases with ω. Their evolution is very close to the Kelvin-Voigt model, which means that the presence of drops in the PDMS matrix does not change the fact that the samples can be described as viscoelastic solids. For the PEG-400, which is a liquid, the storage modulus is lower that the loss modulus, and both increase with ω. For $\omega < 2$ rad/s, the value of $\mathcal{G}'$ is below the sensitivity of the rheometer, which explains the artefact at low angular frequencies.

The curves of the evolution of $\mathcal{G}'$ and $\mathcal{G}''$ as a function of ω of all samples can be described by power laws $y = y_0 + A \cdot x^{pow}$, of which the parameters of each samples are given in Table VI.1 in Appendix VI. For the solid samples (i.e. not the PEG-400), the values of y_0 and A decrease with N, while the

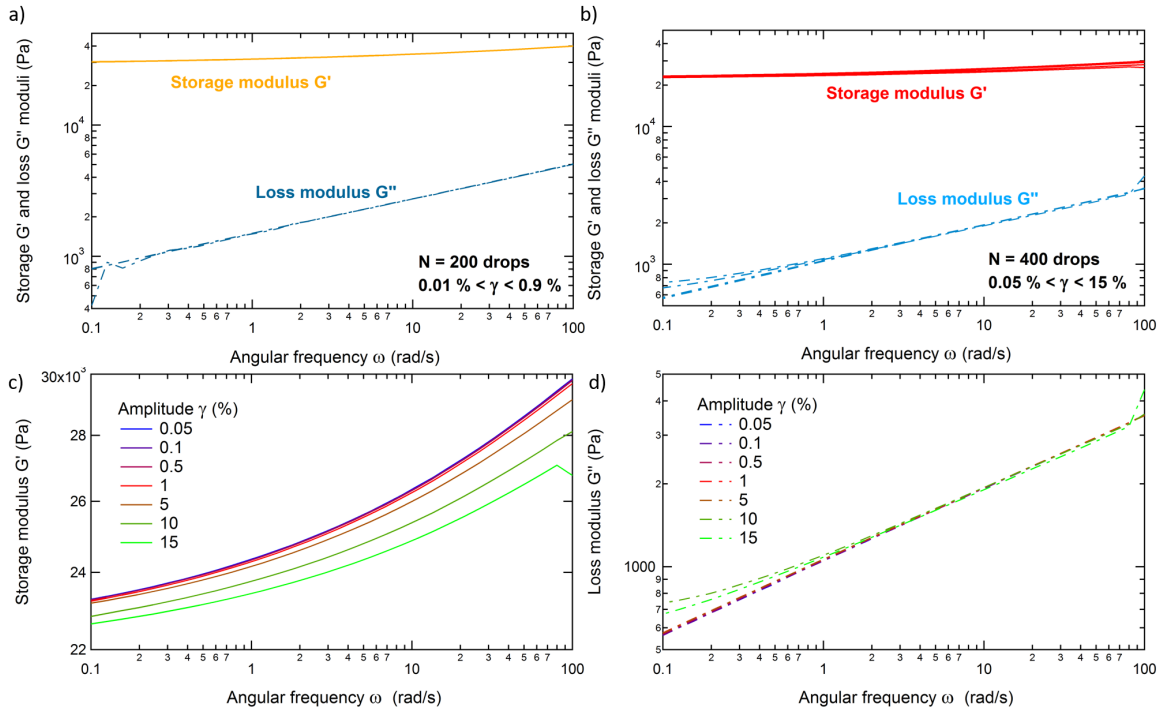

Figure 9.2: a) Storage $\mathcal{G}'$ and loss $\mathcal{G}''$ moduli as a function of the angular frequency ω for different shear amplitude γ for sample 3 (N = 200, $h/h_s = 0.4$). b) Storage $\mathcal{G}'$ and loss $\mathcal{G}''$ moduli as a function of the angular frequency ω for different shear amplitude γ for sample 6 (N = 400, $h/h_s = 0.8$). b) Zoom on $\mathcal{G}'$. c) Zoom on $\mathcal{G}''$.

value of *pow* is constant with N and we obtain $pow(\mathcal{G}') = 0.276 \pm 0.011$ and $pow(\mathcal{G}'') = 0.270 \pm 0.011$. The presence of the drops in the Sylgard 184® matrix thus changes the values of $\mathcal{G}'$ and $\mathcal{G}''$ but not the power law that describes their behaviour with ω, which means that we should be able to rescale the curves $\mathcal{G}' = f(\omega)$ and $\mathcal{G}'' = f(\omega)$ using the number of drops N or the volume fraction of drops Φ in the samples.

To illustrate this, we plotted the values of $\mathcal{G}'$ and $\mathcal{G}''$ at the angular frequency $\omega = 1.16$ rad/s as a function of N (Figure 9.3b). We clearly see that both $\mathcal{G}'$ and $\mathcal{G}''$ decrease with N for a given frequency ω. In Figure 9.3c, we plotted the ratio of $\mathcal{G}'/\mathcal{G}''$ for $\omega = 1.16$ rad/s and $\omega = 100$ rad/s as a function of N. Both curves can be fitted by a constant line $y = y_1(\omega)$ where $y_1(\omega = 1.16 \text{ rad/s}) = 19.90 \pm 0.83$ and $y_1(\omega = 100 \text{ rad/s}) = 7.76 \pm 0.18$. Viscoelastic materials are conventionally defined as purely elastic solids if $\mathcal{G}'/\mathcal{G}'' > 10$. In our case, and except for high frequencies ($\omega = 100$ rad/s) for which this ratio is lower than 10, though still close, we can indeed show that even by increasing the number of drops in the samples N we keep this ratio constant and above the elastic solid limit.

The increase of the number of drops in the samples thus changes the absolute values of the storage and loss moduli, but not the rheological behaviour of the solid emulsions. Since both the storage and loss moduli of the PEG-400 are much lower than for any of the samples, we can assume that we probe here the rheological properties of the PDMS matrix only. The increase of the number of drops causes the diminution of the quantity of PDMS inside the samples, and mostly it implies the presence of thin PDMS films between the drops whose stiffness is lower than the stiffness of the bulk PDMS. This explains well the diminution of both $\mathcal{G}'$ and $\mathcal{G}''$ with N. By changing the viscosity of the drops, we might be able to reduce the difference between the values of the moduli of the crosslinked PDMS and the liquid, and thus to probe also the rheological response of the liquid for the solid emulsions.

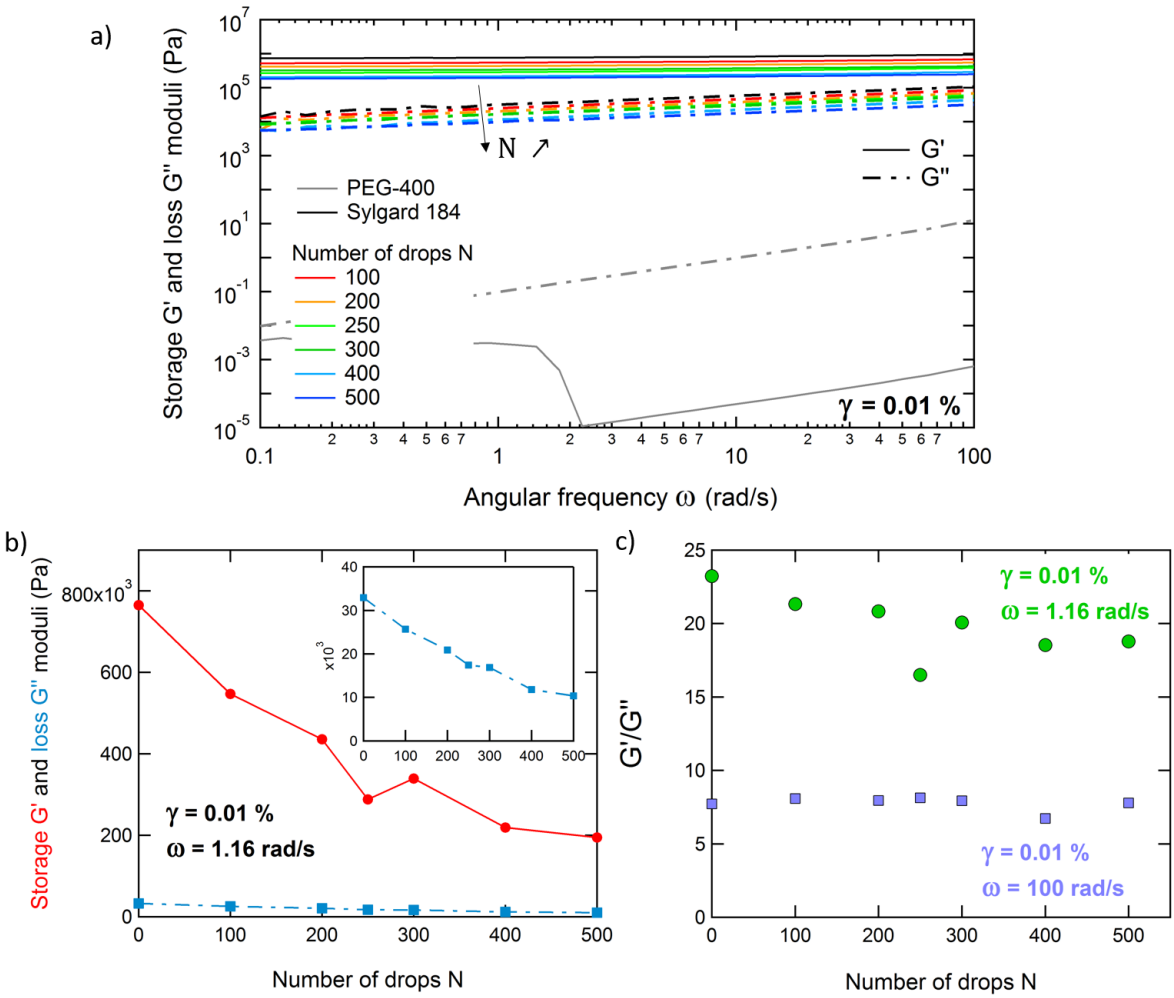

Figure 9.3: a) Storage $\mathcal{G}'$ and loss $\mathcal{G}''$ moduli as a function of the angular frequency ω for bare Sylgard 184® (sample 1), PEG-400, and for different number of drops N (samples 2 to 7), for a shear strain $\gamma = 0.01$ %. b) Evolution of the storage $\mathcal{G}'$ and loss $\mathcal{G}''$ moduli as a function of the number of drops N (samples 1 to 7), for a shear strain $\gamma = 0.01$ % and at the angular frequency $\omega = 1.16$ rad/s. The insert is a zoom on $\mathcal{G}''$. c) Evolution of $\mathcal{G}'/\mathcal{G}''$ as a function of N, for a shear strain $\gamma = 0.01$ % and at the angular frequencies $\omega = 1.16$ rad/s and $\omega = 100$ rad/s

9.3 Evolution of the Young's modulus E in the presence of drops

In Chapter 8, we presented two experiments to measure the elastic properties of materials: the JKR experiment and the probe-tack test. In this section, we show the evolution of the Young's modulus E of the samples 8 to 13 in Table 9.1, for which we keep the ratio h/h_s constant while the radius of the drops varies from 340 µm up to 1.53 mm.

9.3.1 JKR experiment

The theory from Johnson, Kendall and Roberts, called the JKR theory, was developed in Chapter 8. In this chapter, we use it as a way to obtain the effective bulk modulus K. We measure the contact between a glass lens and the surface of the solid emulsions in compression/decompression cycles as described in Chapter 1 Section 1.17, which allows to obtain the force vs. contact radius $F(a)$ curves as shown in Figure 1.17g. By linearising the force and the contact radius using Equations (8.22) and

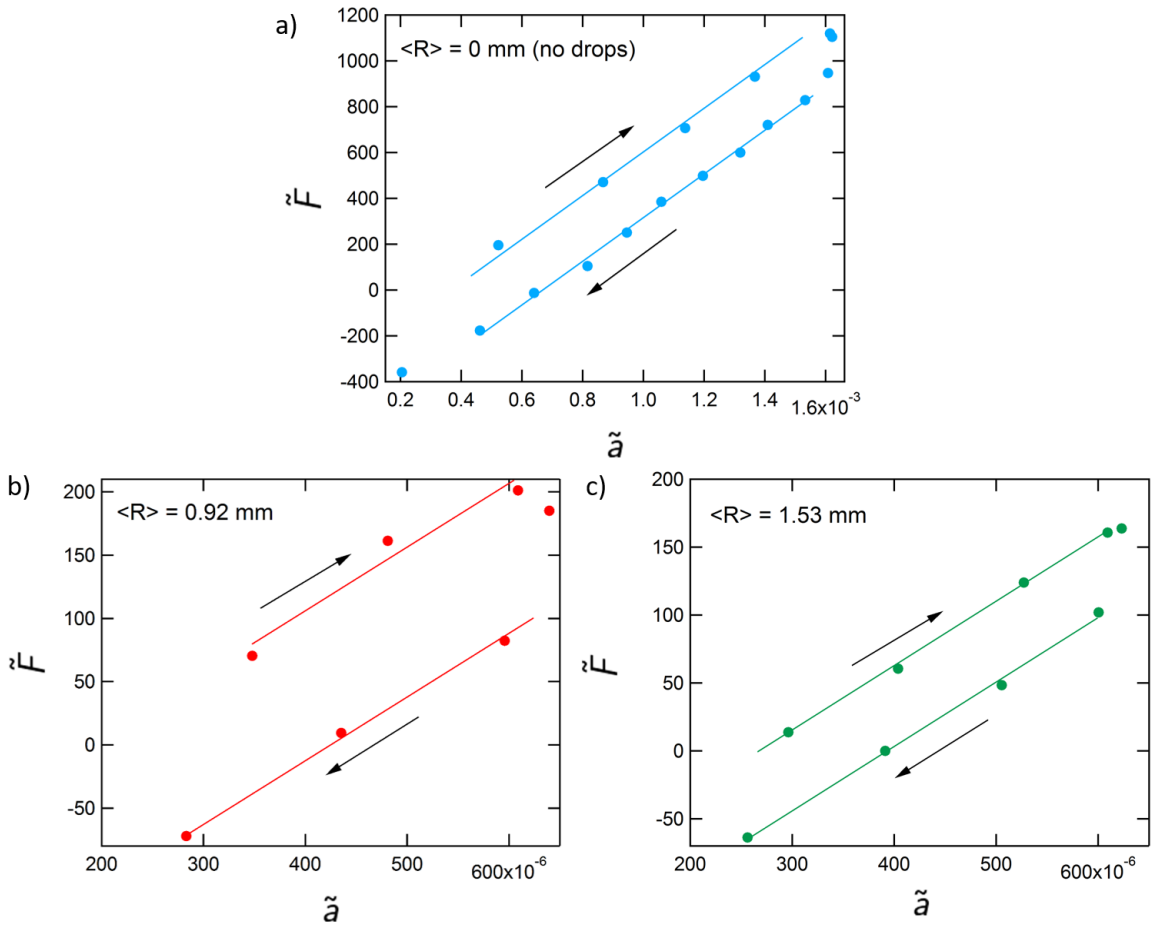

Figure 9.4: Evolution of $\tilde{F}$ with $\tilde{a}$ during a JKR experiment for a) bare PDMS, b) solid PEG-in-PDMS emulsion with $\langle R \rangle = 0.92$ mm (sample 10) and c) solid PEG-in-PDMS emulsion with $\langle R \rangle = 1.53$ mm (sample 13).

(8.23) (with $R \approx R_{lens} = 39.24$ mm since the surface of the samples are planes), we obtained Equations (8.24) and (8.25) which allow to obtain K by measuring the slope of the linear curves.

Figure 9.4 shows the evolution of the pseudo-force $\tilde{F}$ as a function of the pseudo-contact radius $\tilde{a}$ for sample 1 (bare Sylgard 184®) and samples 10 and 13. For each samples, we obtain two linear curves corresponding to the compression (increase of $\tilde{F}$ with the increase of $\tilde{a}$) and the decompression (decrease of $\tilde{F}$ with the decrease of $\tilde{a}$), with the same slope but different intersections with the y-axis. By measuring the slope of the compression and decompression curves for each system, we obtain the value of K for each samples, given in Table 9.2. The value of K for $\langle R \rangle = 0$ mm is the effective bulk modulus of the bare Sylgard 184®, for which the Young's modulus given by the manufacturer is 1.84 MPa. We saw in Chapter 8 that $\frac{1}{K} = \frac{3}{4}((1-\nu^2_{sample})/E_{sample} + (1-\nu^2_{glass}/E_{glass})$, however in our case $E_{sample} \ll E_{glass}$ which means that $E_{sample} \approx \frac{3}{4}K \cdot (1-\nu^2_{sample})$. The Poisson ratio of the Sylgard 184® is 0.5, and we find $E_0 = 3.1 \pm 0.2$ MPa. This value is higher than the value given by the supplier, but still is of the same order of magnitude, and could be explained by the fact that slight differences in the amount of curing agent in the Sylgard 184® or in the temperature at which the sample is solidified can change significantly the Young's modulus.

Comparing the value of K for the bare PDMS with its values for the samples with $\langle R \rangle = 0.92$ mm

Sample number	**Drop radius** R **(mm)**	**Number of drops** N	**Bulk Modulus** K **(Pa)**
1	0	0	$5.53\times10^6 \pm 3.59\times10^5$
10	0.92 ± 0.30	450 ± 50	$5.00\times10^5 \pm 1.00\times10^5$
13	1.53 ± 0.30	150 ± 10	$4.70\times10^5 \pm 1.10\times10^4$

Table 9.2: Values of the effective bulk modulus K of the systems measured with a JKR experiment.

and $\langle R \rangle = 1.53$ mm (samples 10 and 13 in Table 9.1), we can see that there is a factor 10 between the sample without drops and the samples with drops. However, the size and the number of drops does not seem to have an impact on K. As we do not know the values of the Poisson ratio of the emulsions, we are not able here to give the values of the Young's modulus E of the samples with drops.

9.3.2 Probe-tack experiment

As stated in Section 8.1.4 in Chapter 8, the Young's modulus of the solid emulsion in contact with a glass plate can be measured from the slope of the compression part of the force-indentation $F-\delta$ curve. Figure 9.5a shows the evolution of the Young's modulus E of the samples 1 and 8 to 13 normalised by the Young's modulus of sample 1 (bare PDMS) E_0 with increasing mean drop size radius $\langle R \rangle$. We can see that we measure a factor 10 between the Young's moduli of the bare PDMS and the solid emulsions, just as we measured for K in Section 9.3.1. Here, we found $E_0 = 1.47$ MPa for sample 1, which is close to the value of 1.84 MPa given by the supplier.

If we now concentrate on the values of E for the samples 8 to 13, we can see that neither the number of drops (insert Figure 9.5a) nor their size have an impact on the elastic modulus. This was also evidenced by the JKR experiment in Section 9.3.1.

9.4 Discussion

9.4.1 Stiffness of the PDMS films between the drops

We showed in Figure 9.3 that the storage $\mathcal{G}'$ and loss $\mathcal{G}''$ moduli of the solid emulsions decreased with the number of drops N in the sample (equivalently with the increase of h/h_s). This is easily understood by the fact that as N increases, the PDMS in the bulk is "replaced" by PDMS films of finite thickness between the drops, as schematized inside the red rectangle in Figure 9.6a. If the elastic modulus E of these thin films is the same as the elastic modulus of the bulk E_0, the stiffness of a single film $k_s = \frac{AE}{L}$, with A the cross-sectional area and L the length of the film, is lower than the stiffness of the bulk PDMS. We can schematize the films has we did in the case of a single layer of drops in Figure 9.6b. As N increases, the number of layers of drops also increases, and the stiffness of multiple films in series k_m (dark blue rectangle in Figure 9.6c) is lower than the stiffness of a single film. In total, the stiffness of the whole sample decreases as N increases, and as a result its elastic modulus decreases. This explains qualitatively the results on the samples 1 to 7 for which $\langle R \rangle$ is a constant and N varies.

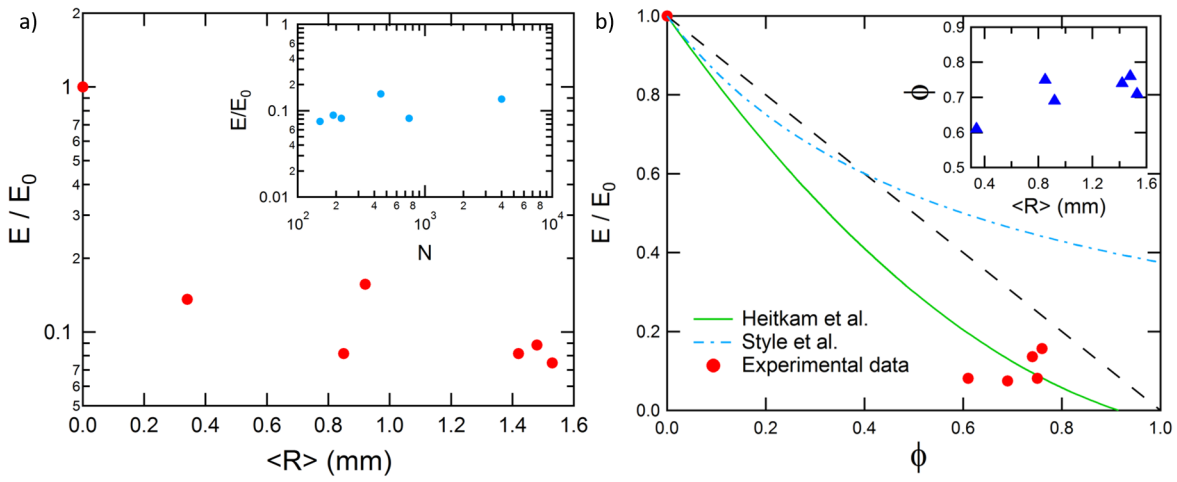

Figure 9.5: a) Log-lin representation of the evolution of the normalised Young's modulus E/E_0 of the system with $\langle R \rangle$ measured with a probe-tack experiment. Insert is the log-log representation of the evolution of E/E_0 with the number of drops N in the sample. b) Evolution of the normalised E/E_0 with the volume fraction of drops Φ of the solid emulsions compared to the numerical data given by Heitkam *et al.* [4] for solid foams (green solid line) and Style *et al.* [9] for liquid inclusions in compliant solids (blue solid line). Insert is the volume fraction of drops Φ with the mean drop radius $\langle R \rangle$.

We showed using two techniques in Section 9.3 that the Young's modulus E did not depend on the drop size for $h/h_s = 0.9$. Since increasing the drop size for a constant density of drop in a volume means decreasing the number of compliant thin films between the drops, we should measure a dependency of E on the drop size using our argument to explain the evolution of $\mathcal{G}'$ and $\mathcal{G}''$ with N. However, both experiments do not apply the same mechanical stress on the material. The measure of the rheological properties was made by shearing the samples between two plates while the measure of the Young's modulus (or the effective bulk modulus K) was made by compressing the samples. In the first case, the drops radius is larger than the capillary length[1] $\lambda_c \approx 0.7$ mm (using $\gamma = 5$ mN/m) of the system. If the drops had a diameter lower than 0.7 mm, the surface tension would oppose the shearing movement and this force would be measured by the rheometer. Since the drops have a diameter of ≈ 2 mm in the rheology experiments, they can deform under shear, and we thus probe only the rheological properties of the PDMS matrix. As N increases, more and more compliant thin films are created inside the matrix which resist less the deformation than the bulk PDMS. On the other hand, compressing the samples implies different contributions from the PDMS matrix and the PEG drops. The presence of thin films in the PDMS matrix makes it more compliant and thus less resistant to compression, but the liquid drops are incompressible. Changing the number of thin films (by changing the size of the drops while keeping the same drop density for example) does not change the ability of the material to compress under pressure, and the Young's modulus is thus a constant with the drop radius.

The fact that the solid emulsions behave differently under shear or compression means that they could be qualified as orthotropic materials, i.e. that their Poisson ratio would be different in the vertical (z axis) and horizontal ((x,y) plane) directions, where the (x,y) plane is parallel to the surface of the emulsions in contact with the indenter of the traction tester or the geometry of the rheometer. The relationship between the elastic modulus E and the shear modulus $\mathcal{G}$, defined in Section 8.1.1 in Chapter 8 in the case of an anisotropic material, would thus be more complex in the case of the solid

[1]The capillary length was defined in Part B Chapter 7 Section 7.4 as: $\lambda_c = \sqrt{\gamma/\rho g}$ with γ the interfacial tension between the dispersed and continuous phase, ρ the density of the PEG and g the gravitational acceleration

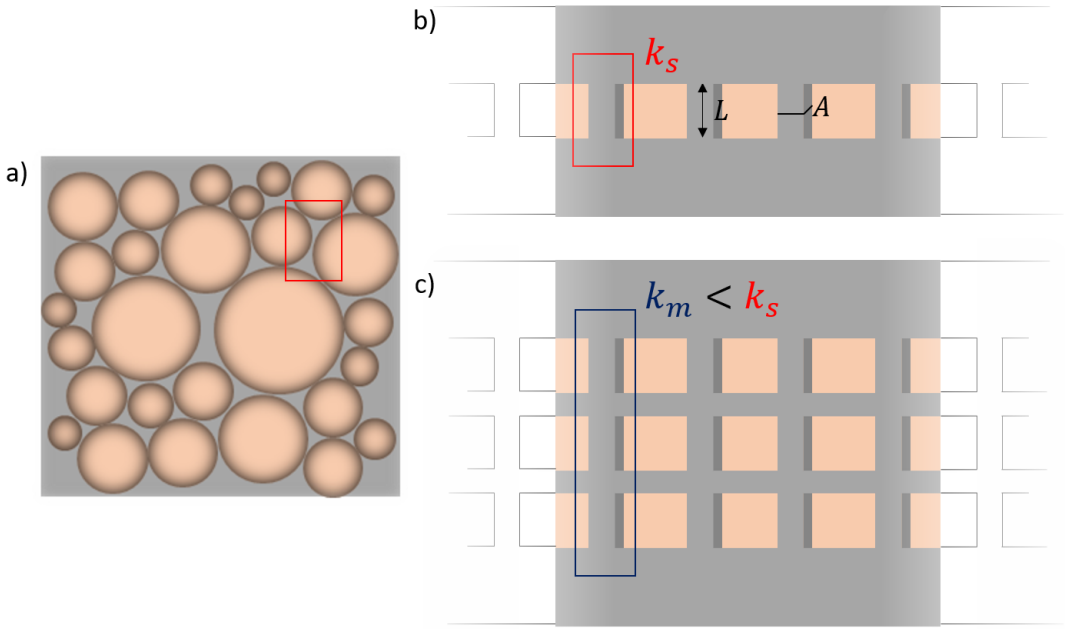

Figure 9.6: a) Scheme of a solid emulsion. b) Schematic representation of one layer of drops in a solid matrix, where the thickness between two drops has a stiffness k_1. c) By increasing the number of layers of drops in the solid matrix, the stiffness k_m of the superposition of several films decreases.

emulsions, and should be the object of further studies. For example, one might look at the dependence of the number of drops in the vertical and horizontal cross-sections.

9.4.2 Comparison with models from the literature

In Figure 9.5b, we plotted the values of E/E_0 against the volume fraction of drops Φ in the emulsions. the insert shows that the densities of drops in the volume of the samples 8 to 13 are very close to each other and do not allow an investigation of the role of the density on the elastic modulus of the sample. However we can compare these values with the values which the models proposed by Heitkam *et al.* [4] and Style *et al.* [9] would give. Though the model of Style *et al.* is valid for $\Phi < 0.6$ only, when the solid emulsions of this study have a density of drops $\Phi = 0.6 - 0.8$, we can see that this model is in any case far from capturing our experimental data points. Also, in our case we find $\gamma/(E_s R) \ll 1$ which means that the equation of Eshelby [315] would have given the same result here: the PDMS is not compliant enough in our case for the surface tension between the PEG and the PDMS to play a role in the elasticity of the cellular material. Heitkam *et al.* [4] stated that Equation (8.43) in Chapter 8 was a good approximation for the elastic modulus of solid foams with any overall organisation and for the entire range of pore density. Our data points seem closer to the curve given by this model than the curve given by the model of Style *et al.*, which is surprising in regard to the incompressibility of the liquid in the pores of the solid emulsion compared to the compressibility of the gas in the pore of the solid foams.

The formulation of the solid emulsions did not allow here to generate samples with a wide range of volume fraction of drops. In Part B, we discussed the impact of the interactions between the drops, varied by the addition of a solvent (dodecane) in the continuous phase, on the final volume fraction of drops of an emulsion. Here, the samples 8 to 13 were generated with various amounts of dodecane

in the continuous phase as a way to vary the volume fraction of drops, however in that case we were unable to see this effect. This could be explained by the much lower height of the samples used in this study of the mechanical and adhesive properties of the solid emulsions. Indeed, in Part B, we showed in Chapter 6 that the magnitude of the interactions between the drops was dependent on the time given to create the polymeric skin-like interface, and in Chapter 7 we studied emulsions for this stabilisation time was long enough for the skin to grow and thus the magnitude of the interactions to increase, which lead to differences in the volume fraction of drops between samples generated with 5% of dodecane in the continuous phase and samples generated with 10% of dodecane. In this part, during the generation the drops fall into an 8 mm high container, which means that the drops are in contact very fast, and the magnitude of the interactions between them is probably low. Other samples should be generated in the same conditions as in Part B, but with the same dimensions as here, in order to change the drop volume fraction and study its impact on the mechanical properties of the solid emulsions.

Chapter 10

Adhesive properties of solid emulsions

In Chapter 9, we studied the impact of the presence of liquid drops in the substructure of a solid matrix on its mechanical and rheological properties. We showed that the elastic modulus depends on the number of drop layers inside the sample, but not on their size. Here, we ask ourselves the same questions of the impact of the presence of the drops, but this time on the adhesive properties of the materials. In addition to the measure of the bulk and elastic moduli K and E, contact mechanics experiments allow to obtain informations on the adhesive properties on a specific substrate with the measure of the thermodynamic work W or the energy release rate G. These parameters depend on the temperature T at which the experiment is made, but the experiments used for this study were not made to allow for a precise control of the temperature. For that reason, they were performed at room temperature, however we did not notice any reproducibility issues depending on the time of the year the experiments were carried on.

Among K, W and G, only G depends on indentation speed via the energy dissipations term $D(T, v)$. As we expect the surfaces of the samples to be identical for each one of them, W should be a constant, and we are then interested in how do the dissipated energy D varies with the structural parameters of the samples described in Chapter 9, namely the number of drops N and their average radius $\langle R \rangle$, but also with external parameters such as the indentation speed v. In this chapter, we work with samples "filled" with drops (Samples 8 to 13 with sample 1 as reference, described in Table 9.1 in Chapter 9), i.e. the ratio of the emulsion height over the sample height is constant $h/h_s = 0.9$.

We carried out two types of contact mechanics experiments: a JKR experiment in quasi-static conditions ($v \to 0$), and a probe-tack test with varying speed v. The experimental details are given in Chapter 1 and the theoretical background in Chapter 8. Here, we give the experimental results of the JKR experiment in Section 10.1 and of the probe-tack test in Section 10.2. In Section 10.3, we discuss the results of both experiments together in regard to the theoretical and experimental results from the literature presented in Chapter 8.

10.1 Evolution of the adhesive properties in quasi-static conditions

The theory from Johnson, Kendall and Roberts, called the JKR theory, was developed in Chapter 8. In this chapter, we use it to obtain the thermodynamical work of adhesion W and the energy release

rate G in quasi-static conditions. To do so, we study experimentally the contact between a glass lens and the surface of the solid emulsions in compression/decompression cycles as described in Chapter 1 Section 1.17, which allows to obtain the force-contact radius $F(a)$ curves as shown in Figure 1.17g. By linearising the force and the contact radius as we did in Section 9.3.1 in Chapter 9, we were able to measure W and G for this particular contact between the surface of the solid emulsions and the glass lens by measuring the intercept between the linear curves and the y-axis. Here, we look at the values of W and G for $\mathrm{d}a/\mathrm{dt} = 0$[1].

The linearised curves obtained with the measure of the pseudo-force $\tilde{F}$ and the pseudo-contact radius $\tilde{a}$ for the samples 1, 10 and 13 (Table 9.1) were shown in Figure 9.4 in Chapter 9. We see that the curves of the compression and the decompression do not intercept the y-axis at the same value, and this for each sample, which means that W and G are not equal in quasi-static conditions. In Figure 10.1a, we plotted the evolution of W and G with the average drop radius R. The first noticeable result is that the values of W_0 and G_0 for the bare PDMS ($R = 0$ mm) are in the same range as the values found in the literature for a PDMS/glass contact [14, 326]: between 20 and 50 mJ/m^2 for W and between 100 and 200 mJ/m^2 for G.

Taking into account the error on the measurements, we can see in Figure 10.1a that W seems to not be affected by the presence of drops in the volume of the samples. Since the work of adhesion is a surface property only (cf Section 8.3 in Chapter 8), this result is an indication that the presence of the drops does not change the surface of the emulsions in between samples. Measures of the contact angle between drops of water and the surface of the samples presented in Appendix VII also goes in that direction.

The fact that the value of G is different than the value of W for the bare PDMS in quasi-static conditions is understood as the result of two possible energy dissipation mechanisms. First, we can mention the impact of adsorbed PDMS chains on the glass lens. During the traction at very low speed (500 µm/min), these chains do not have enough time to relax since the speed at which they relax is much lower than the traction speed (i.e. if the experiment is quasi-static at the macroscopic scale, it is not the case at the molecular scale). The chains are thus stretched and then break, causing energy dissipations. We expect this effect to be constant for all samples, with or without the presence of drops. By normalising the value of G, we can neglect this mechanism in our analysis. We can also indicate the presence of elastic dissipations in the bulk, which are not rate-dependent. This process of dissipation of energy linked to the elasticity of the PDMS is also present in the solid emulsions. However, in the solid emulsions, the PDMS matrix is shaped like a solid foam: it is a succession of thin PDMS films. As we discussed in Section 9.4.1 in Chapter 9, the stiffness of an elastic film increases with its thickness, which means that thin PDMS films deform more than bulk PDMS. This should cause elastic dissipations to be higher for the solid emulsions than for the bulk PDMS, i.e. we should see an increase of G between sample 1 and the two other samples studied in this section. However, we observe a decrease of G with R in Figure 10.1a. The diminution of G was also observed in the case of patterned surfaces, when a glass lens is in contact with PDMS pillars positioned on a PDMS surface (with a surface density $\Phi_s = S_p/S_t$ where S_p is the surface covered by the pillars and S_t is the total surface) [14]. Indeed, the pillars have a lower stiffness than the bulk PDMS, which should

[1]The analysis of the experiment could be made for any value of $\mathrm{d}a/\mathrm{dt}$, and in the case of finite values gives the dependency of the energy release rate on the speed.

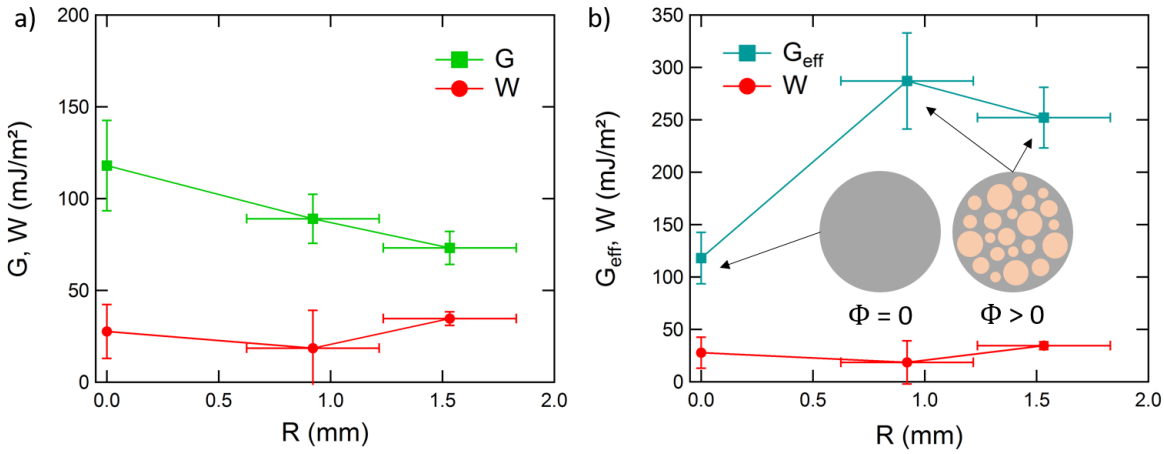

Figure 10.1: a) Evolution of the thermodynamical work of adhesion W and the energy release rate G of the system with $< R >$ measured with a JKR experiment for $\mathrm{d}a/\mathrm{d}t = 0$. b) Evolution of W and the effective energy release rate G_{eff} of the system with $< R >$. The insert are schemes of cross-sections inside the bulk of the different samples.

impose higher elastic dissipations, but the values of G measured in that case were systematically lower than for smooth PDMS surfaces. However in the case of a contact between a lens and pillars, the surface of contact is lowered compared to the case of a contact between a lens and a smooth surface, which means that G should be rescaled by the inverse of the surface density Φ_s which gives an effective energy release rate G_{eff}. Since in our case we are probing an effect which depends on the bulk density in elastic material and not the surface density, we rescale G with the cross-sectional density of solid PDMS matrix. In Chapter 7, we showed that the volume fraction of drops Φ was constant with the height of the emulsions for this systems thanks to the tangential forces between the drops, which means that the cross-sectional fraction of drops is $(1-\Phi)$ where Φ is the drop volume fraction that we defined in Part B. We thus obtain the rescaling

$$G_{\mathrm{eff}} = \frac{G}{(1-\Phi)}, \tag{10.1}$$

using the values of Φ plotted in the insert of Figure 9.5b in Chapter 9. We plotted in Figure 10.1b the effective release rate G_{eff} along with the thermodynamic work W which in our case does not change since the surface of contact is not lowered by the presence of the drops in the bulk. We can see that with this rescaling we do observe an increase of the effective energy release rate for solid emulsions compared to the bare PDMS (by a factor of ≈ 2.5). We then observe a slight diminution (though not very significant) of G_{eff} as R increases. If the effect is not really pronounced here, we can however say that this diminution would make sense since increasing the drop radius for a constant drop volume (Φ is constant in between samples 10 and 13) means that the number of elastic films between the drops decreases, and thus the magnitude of the elastic dissipations.

With this experiment, we now have a reference value at $v \approx 0$ mm/min of the thermodynamic work of adhesion $W = 26.7 \pm 14.2$ mJ/m^2 between a PDMS surface and a glass lens. We were able to show that the presence of drops in the volume of the emulsions did not change their surface properties. We however showed that it impacts greatly the energy dissipations in quasi-static conditions. This experiment will be completed by the study of the adhesive properties of the contact between glass and

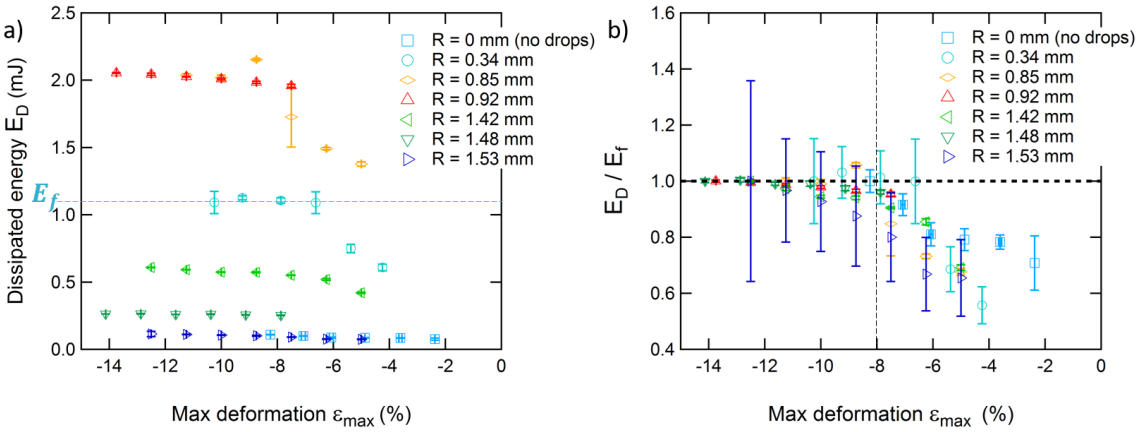

Figure 10.2: a) Evolution of the dissipated energy E_D with the maximal deformation $\epsilon_{max} = \delta_{max}/h$ for samples 1 to 7 for $v = 5$mm/min. b) Data of a) normalised by the value of the dissipated energy for the maximal compression E_f for each curve.

PDMS for $v > 0$ mm/min, reported in Section 10.2.

10.2 Evolution of the adhesive properties in dynamic experiments

The analysis of the energy release rate dependence on the speed $G(v)$ with the JKR experiment is very time consuming, and to avoid this problem, we probed $G(v)$ with a probe-tack test, for which we gave the experimental protocol in Chapter 1 and the principle of the measurement in Chapter 8. Here we explore the dependencies of G on external parameters such as the indentation δ and the speed v, and on structural parameters of the sample such as the drops radius R.

The adhesive properties of the solid emulsions are investigated here by measuring the dissipated energy E_D during a compression/decompression cycle as explained in Chapter 8 Section 1.5.1: we calculate the integral of the force-indentation $F - \delta$ curve once F becomes positive. In this section, we first give the dependency of E_D on the indentation δ for a fixed compression/traction speed v.

10.2.1 Evolution of the dissipated energy with the indentation δ

We varied the maximal indentation during compression/decompression cycles at a constant speed v = 5 mm/min. Figure 10.2a shows the evolution of E_D with the maximal deformation $\epsilon_{max} = \delta_{max}/h$ for each sample. We can see that E_D increases with increasing $|\epsilon_{max}|$ until a plateau is reached. Figure 10.2b shows the evolution of the normalised dissipated energy E_D/E_f where E_f is the dissipated energy at the maximal $|\epsilon_{max}|$ of each curve, and indicates that the plateau value is reached in all cases for $|\epsilon_{max}| = 8\%$. This effect is in all probability due to an imperfect parallelism of the two surfaces in contact: for small indentations, the surface of the sample might not be entirely in contact with the glass plate, which induces a lower dissipated energy. For all experiments with the probe-tack test, we will thus keep $|\epsilon_{max}| \geq 8\%$.

10.2.2 Evolution of the dissipated energy with the drop radius R

In Chapter 4, we generated solid emulsions with different drop sizes thanks to two generation techniques, millifluidic and dripping of the drops out of a needle. Here, we study the impact of the drop

size R on the dissipated energy during a compression/decompression cycle between a glass plate and the solid emulsions (samples 1 and 8 to 13 in Table 9.1 in Chapter 9). In Figure 10.3a, we plotted the normalised dissipated energy E_D/E_{D0}, where E_{D0} is the dissipated energy of the bare PDMS (sample 1), against the drop radius R. We observe a bell shaped curve with a maximal value of dissipated energy $E_D \approx 20 \cdot D_0$ for an average drop radius $\langle R \rangle \approx$ 0.8-0.9 mm, and which decreases back to $E_D/E_{D0} = 1$ for the highest drop radii. It is important to remember here that since the volume of the samples is always the same, and that in this chapter we study samples with $h/h_s = 0.9$ i.e. with the maximum number of drops possible in the volume without roughening the surface, changing the drop size comes back to changing the number of drops, as shown in Figure 10.3b. It is thus interesting to notice that we measure the same dissipated energy for both samples with $\langle R \rangle \approx = 0.85$ mm and $\langle R \rangle \approx = 0.92$ mm when the difference in number of drops between them is significant ($N = 750$ and 450 respectively). The density of drops Φ in the volume of the samples is on the other hand constant with $\langle R \rangle$, as shown in the insert of Figure 9.5b in Chapter 9, which means that the amount of liquid inside each samples, participating in the dissipated energy through viscous dissipations, is a constant. However, as we pointed out in Section 10.1, this also causes the number of elastic films between the drops to decrease, which means that the elastic dissipations are not constant in between samples.

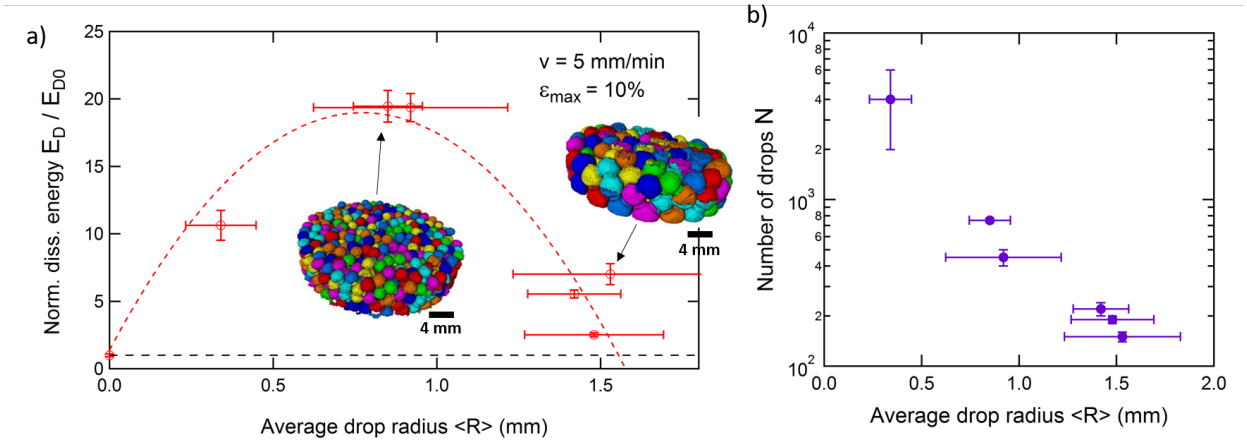

Figure 10.3: a) Evolution of the normalised dissipated energy E_D/E_{D0}, E_{D0} being the dissipated energy for sample 1 (bare PDMS), with the mean drop radius $< R >$, for a maximal deformation $\epsilon_{max} = 10\%$ and a traction speed $v = 5$mm/min. The inserted images are 3D rendering volume of the solid emulsions with $< R >$ = 0.85 mm and 1.53 mm obtained by X-Ray tomography. b) Relationship between the number of drops N in the volume of the samples and their average radius $\langle R \rangle$ (for $h/h_s = 0.9$).

10.2.3 Evolution of the dissipated energy with the traction speed v

The adhesive properties of the crosslinked PDMS against a rigid substrate (glass, steel, etc.) are known experimentally to depend on the traction speed of the indenter [327–330]. This is due to the fact that crosslinked PDMS is a viscoelastic solid, characterised by both a storage $\mathcal{G}'$ and loss $\mathcal{G}''$ modulus. Both elasticity and viscosity cause energy dissipations, however elastic dissipations are not rate dependent when viscous dissipations are, and the latter cause the rate dependency of the adhesive properties of the crosslinked PDMS.

We measured the dissipated energy for different traction speed v of the samples 1, 10 and 13, in order to confront our results to the literature. Figure 10.4a, b and c show the positive part of the force F with the indentation δ for different speeds v for each sample. These curves show an increase of F with

δ until the maximal force F_{max} is reached, then the force decreases towards zero as the surface of the sample detaches from the glass plate. Note here that if the surfaces were perfectly parallel to each other, the force should be discontinuous and fall to zero right after reaching F_{max}. For each sample, F_{max} increases with v and so does the integral below the curve. This clearly shows an impact of the speed on the measured dissipated energy for each sample. In Figure 10.4d, we compare the $F = f(\delta)$ curve of each sample for the maximal traction speed tested $v = 10$ mm/min. We see that the maximal force F_{max} for sample 10 is approximately 5 to 10 times higher than for the other samples, as Figure 10.3a showing the evolution of E_D with $< R >$ suggested.

In Section 10.1, we measured values of the thermodynamical work of adhesion W_{JKR} and the energy release rate G_{JKR} in quasi-static conditions ($v = 0$ mm/min). At very low values of the traction speed, we should in this experiment find values of G which tend towards G_{JKR}. We can measure the energy release rate G from the measure of the dissipated energy using the relation

$$G = \frac{E_D}{S}, \tag{10.2}$$

where $S = \pi R_s^2$ is the area of the samples ($R_s = 13$ mm), i.e. the area of contact between the sample and the glass plate. In Figure 10.4e, we plotted a log-log representation of the evolution of the energy release rate G with the traction speed v for samples 1, 10 and 13. We can see that the rate dependency of the energy release rate for samples 10 and 13 follows the same power law $G \sim v^{0.5}$. But this power law does not seem to capture the behaviour of $G(v)$ for the bare crosslinked PDMS, for which the rate dependency is $G \sim v^{0.25}$. Typical values of power law $G \sim v^n$ found in the literature for elastomers lie within $0.2 < n < 0.5$ [29, 289], though the power law of the rate dependency of the energy release rate depends strongly on both materials in contact, which makes it difficult to directly compare with our system. However, taking as a reference the crosslinked PDMS, this shows that the presence of the drops in the samples adds another rate dependent energy dissipation process which is not present in the bare crosslinked PDMS, and which changes the power law.

If we report in Figure 10.4e the values of G_{JKR} and W_{JKR} measured with the JKR experiment with their respective error bars, we can see that the values of G for all samples seem to tend toward the quasi-static limit for the lowest speeds.

10.3 Discussion

In this chapter, we first studied in Section 10.1 the adhesive properties of PEG-in-Sylgard 184® solid emulsions with PEG drops of different radii with a JKR apparatus, allowing us to probe the thermodynamical work of adhesion W and the energy release rate G in quasi-static conditions. We were able to show that W was a constant in between the different samples, i.e. that the presence of drops in the volume of the samples did not influence its surface properties, by inducing any roughening at the surface or changing chemically the surface for example. We measured however a great impact of the presence of the drops on G_{eff} which increases in the presence of drops in quasi-static conditions ($v \approx 0$ mm/min). We also showed that $G \neq W$, which points towards the existence of dissipative processes in the samples which are not dependent on the traction speed v. These effects will be discussed in Section 10.3.1.

In Section 10.2, we completed the study of the adhesive properties of the samples with dynamic experiments ($v > 0$ mm/min) with a probe-tack test. We first measured the dissipated energy D with the indentation δ during a uniaxial compression/decompression cycle, and we observed the existence of a plateau of dissipated energy for $\epsilon_{max} \geq 8\%$, which serves as a lower limit for all the other measurements. Then, we looked at the evolution of D with the average drop radius $\langle R \rangle$ inside the sample, or equivalently with the number of drops N, for a fixed traction speed $v = 5$ mm/min and a maximal deformation $\epsilon_{max} = 10\%$.

It showed an augmentation of the dissipated energy with $\langle R \rangle$ up to 20 times the value of the dissipated energy for the bare crosslinked PDMS. This way we showed the profound impact of the presence of liquid drops in the substructure of the samples. We also measured the impact of the traction speed v on the dissipated energy by units of surface, i.e. the energy release rate G. We showed that it followed a power law $G \sim v^n$ with values of n coherent with the literature. More importantly, we showed that the presence of the drops in the substructure of the samples changed the value of n i.e. changed the rate dependency compared to the bare crosslinked PDMS. All these observations point towards the existence of another dissipative process present for the solid emulsions only and which is rate dependent.

10.3.1 Mechanisms of dissipations in solid emulsions

In Section 10.1, we discussed the elastic dissipations at play in the volume of the bare PDMS and the solid emulsions in quasi-static conditions. These dissipations are not rate-dependent and are the result of the low stiffness of the elastomeric matrix, which implies that they will contribute to the total energy dissipations E_D of any of our sample and for any traction speed v. We will now discuss the mechanisms of dissipation of energy for a non-zero traction speed.

At constant speed $v \neq 0$ mm/min

In Section 10.2.2, we looked at the dissipated energy for a constant traction speed $v = 5$ mm/min for the samples 1 and 8 to 13. We observed a bell shaped curve of E_D with the average radius $\langle R \rangle$ of the drops in the samples. In the case of the bare PDMS (sample 1), and since the crosslinked Sylgard 184® with a ratio of 10:1 between the base and the curing agent is a viscoelastic material, a large part of the total dissipated energy is the sum of dissipations at the interface through the propagation of the crack front via the stretching of loose PDMS chains adsorbed on the glass, elastic dissipations in the bulk (as for the experiment at $v \approx 0$ mm/min) and viscous dissipations, also in the bulk, where only the bulk elastic dissipations are not dependent on the speed. Here we will neglect the dissipations due to the adsorbed chains at the interface for simplicity, and we refer to "elastic dissipations" as the bulk contribution only. As we discussed in Section 10.1, elastic dissipations are higher for the solid emulsions than for the bare PDMS because of the differences in stiffness of the PDMS matrix. In the bare PDMS, viscous dissipations come from the irreversible rearrangement of loose chains inside the bulk, and increases as the ratio of the storage modulus over the loss modulus $\mathcal{G}'/\mathcal{G}''$ of the material decreases. The contribution of the PDMS matrix to viscous dissipations should thus decrease in the solid emulsions compared to the bare PDMS since the volume occupied by the elastomer is reduced.

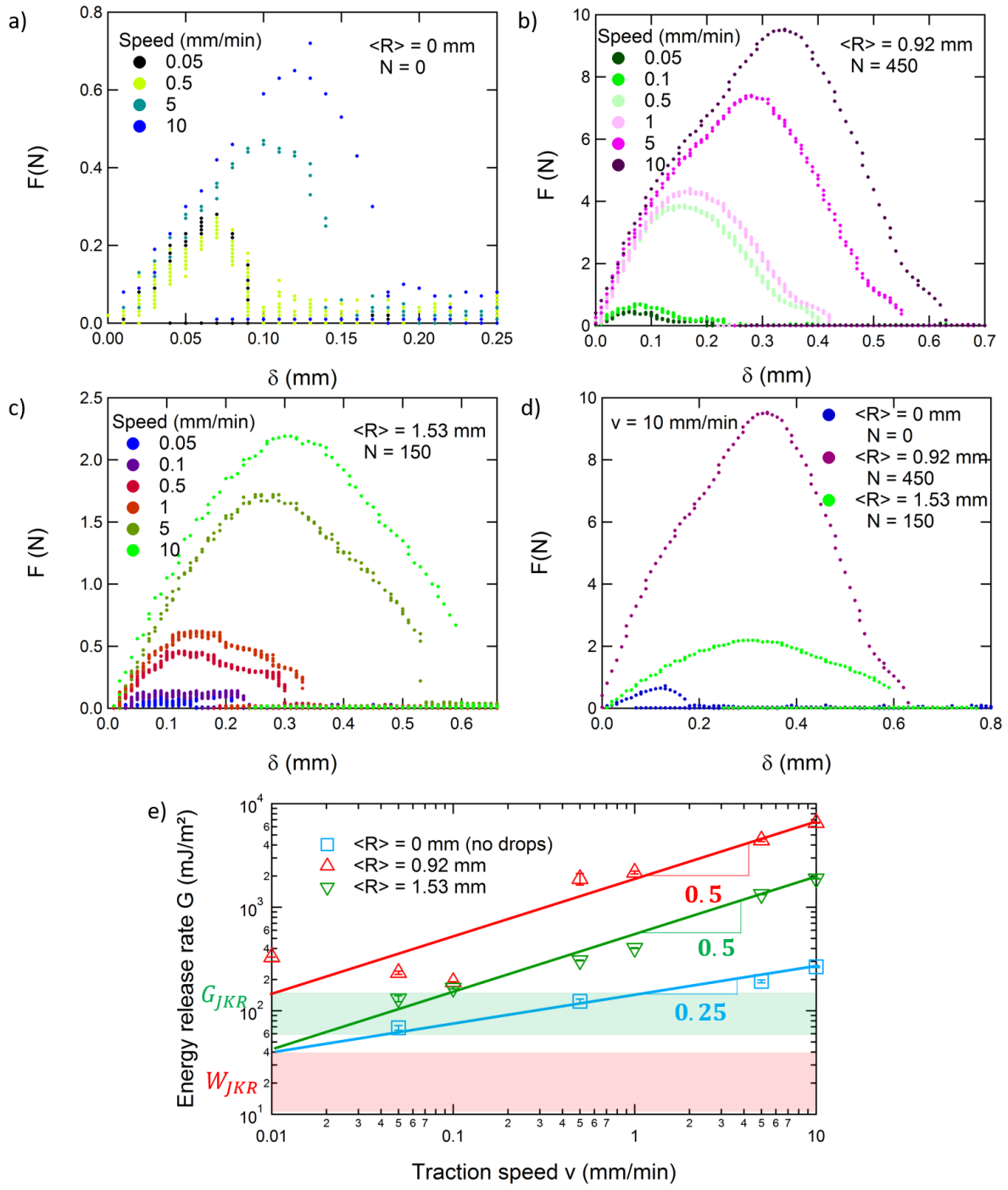

Figure 10.4: a), b) and c) Force F with the indentation δ for different traction speed for a) the bare PDMS (sample 1), b) sample 4 ($< R > = 0.93$ mm and $N = 450$) and c) sample 7 ($< R > = 1.53$ and $N = 150$). d) Comparison of the force F against the indentation δ of samples 1, 4 and 7 for $v = 10$ mm/min. e) Evolution of the energy release rate G (in mJ/m^2) during a compression/decompression cycle with the traction speed v for samples 1, 4 and 7 in comparison with the data taken from the study of Nase *et al.* [330] for PDMS in contact with steel.

However, the presence of liquid drops (characterised by $\mathcal{G}'/\mathcal{G}'' \to 0$) will increase greatly the viscous dissipations in the system.

The evolution of E_D with $\langle R \rangle$ in Figure 10.3a is thus the result of the competition between different dissipation mechanisms depending on the internal structure of the samples. Let us first put aside the solid emulsion with $\langle R \rangle = 340$ µm, and comment on the monotonous diminution of E_D from $\langle R \rangle \approx$ 0.8-0.9 mm to $\langle R \rangle \approx$ 1.4-1.5 mm. The insert in Figure 9.5b in Chapter 9 tells us that the density of drop Φ is identical for these samples, which means that the viscous dissipations linked to the presence of liquid does not change in between samples. However, as we stated in Section 10.1, by increasing $\langle R \rangle$ in a given volume, we change the number of elastic films between the drops, and their thickness since $1 - \Phi$ is also a constant. This causes the elastic contribution to D to decrease while the viscous contribution stays constant, hence the diminution of the total dissipated energy. Now, for the emulsion with $\langle R \rangle = 340$ µm, we measured a volume fraction of drops slightly below the volume fraction of drops of the other emulsions ($\Phi \approx 0.6$ instead of 0.7-0.8). This could be an explanation for the diminution of E_D for this sample. Since we were not able to explore the entire range of volume fraction, we are not able here to know if this difference in volume fraction could justify such a diminution of the dissipated energy. We can however give another argument for it which does not depend on the volume fraction of drops. In Chapter 9, we stated that the length above which the surface tension is negligible compared to gravity, and thus does not affect the shape of the drops in our system (called the capillary length), is 0.7 mm, which is approximately equal to the diameter of the drops in this sample. If surface tension opposes the deformation of the drops, and thus the stretching of the elastic films in between the drops, the elastic dissipations are reduced. The diminution of E_D in the case of the emulsion with low $\langle R \rangle$ might be a combination of the effect of both the surface tension acting against the deformations and the lower volume fraction of drops.

With increasing speed v

In Section 10.2.3, we showed in Figure 10.4e that the index n of the power law $G \sim v^n$ changed from $n \approx 0.25$ for the bare PDMS to $n \approx 0.5$ in the presence of drops in the structure of the PDMS matrix. Interestingly, values of n in between 0.2 and 0.3 were found for purely elastic materials [289], which is the case of the crosslinked PDMS considered here, while values of n closer to 0.5 were found for viscoelastic materials such as PSAs. This means that the solid emulsions studied here behave like viscoelastic materials in regard to their adhesive properties, while we established that their rheological properties were closer to that of a purely elastic material. We can imagine here that changing the viscosity of the drops might be a way of varying n, as it was the case in the study of Majumder *et al.* [10]. This would deserve other experiments.

10.3.2 Comparison with other cellular structures

In Chapter 8 Section 8.3.2, we reviewed the literature on the adhesive properties of cellular PDMS materials, with air or liquid inclusions. Noderer *et al.* [11], Glassmaker *et al.* [322] and Shen *et al.* [323] designed fibrillar structures terminated by an elastomeric film to study the impact of gas inclusions on the adhesive properties of an elastomer. They showed an increase of the energy release rate up to a factor ~ 9 which depended on the length of the fibrils and the inter-fibrils distance. Majumder *et*

al. [10] also showed a great improvement of the adhesive properties of a PDMS sheet thanks to the presence of liquid inclusions in the substructure up to a factor ~ 30, which varied with the structural parameters of these inclusions.

The systems studied by Noderer *et al.*, Glassmaker *et al.*, Shen *et al.*and Majumder *et al.*are all 2D structures, i.e. there is only one layer of gas or liquid inclusions. The adhesive properties of these structures were all interpreted as caused by the variation of the compliance of the system with respect to the position of the crack front, added to viscous dissipations in the case of the liquid inclusions studied by Majumder *et al.*. Indeed, the fact that there is only one layer of inclusions does not allow to smoothen the compliance of the system over the entire surface. The system that we studied here is the 3D case of the study of Majumder *et al.*. In our case, the variations of the compliance should be much less important thanks to the random organisation of the drops in the emulsion (showed in Part B Chapter 7). The variation of the compliance over the surface of the solid emulsions should however be studied using micro indentation experiments to confirm or infirm this claim.

To conclude, we presented here a new system of solid PEG-in-PDMS emulsions which show greatly improved adhesive properties compared to the bare PDMS, and is very easy to generate. Indeed, the fibrillar structures need several fabrication steps: photolithography to create the master of the mould, then moulding of the fibrils, followed by attachment of the terminal film. The PDMS sheet with gas or liquid inclusions used by Majumder *et al.*also needs several fabrication steps, though less than the fibrillar structures, since they drill the channels for the inclusions directly inside the PDMS sheet. As for the 2D case, the adherence of the solid emulsions can be tuned by changing their structural properties, and by changing the viscosity of the liquid in the drops, as suggested by the study of Majumder *et al.*.

Conclusion and perspectives of Part C

Following the study of Majumder *et al.* [10] who studied the impact of the structural parameters on the adhesive properties of a PDMS sheet with a 2D substructure made of liquid inclusions, we dedicated Part C to the study of the impact of the structural parameters of solid emulsions, composed of drops of different sizes in an elastomeric PDMS matrix, on their mechanical and adhesive properties (Figure 10.5). With the solid emulsions, we thus presented a 3D version of the system of Majumder *et al.*, which shows similar improvements of the adhesive properties and is much easier to generate.

In Chapter 9, we investigated the rheological and elastic properties of the solid emulsions. We first measured the response to oscillations of the solid emulsions with increasing number of drops N in their bulk, and we showed that the storage $\mathcal{G}'$ and loss $\mathcal{G}''$ moduli decreased with N, though their ratio was constant, which indicates that we probe the response of the elastomeric matrix only with this method. This is reasonable since the values of $\mathcal{G}'$ and $\mathcal{G}''$ of the PEG are several order of magnitude lower than for the crosslinked PDMS. We then studied the impact of the average drop radius $\langle R \rangle$ on the Young's modulus of the solid emulsions for a constant volume fraction of drops in all samples and a constant emulsion height over sample height h/h_s with a probe-tack test. We were able to show that the Young's modulus does not depend on the drop size, and we hypothesise that this is due to the incompressibility of the liquid. We compared our data to a theoretical model developed by Style *et al.* [9] for small densities of liquid inclusions in compliant solids, but this model was overestimating by far our experimental results. A model developed by Heitkam *et al.* [4] for solid foams gave predictions which matched better our results, though this is surprising in regard to the incompressibility of the drops.

Chapter 10 was dedicated to the study of the adhesive properties of the solid emulsions. We kept the ratio of the emulsion height over the sample height h/h_s constant and we looked at the impact of a variation of the drop radius. We first looked at the evolution of the energy release rate G in quasi-static conditions with a JKR experiment, and showed that G decreased in the presence of drops compared to the bare PDMS, which we attributed to the diminution of the quantity of PDMS in the volume of the samples. We rescaled G using the cross-sectional density of PDMS in the volume of the sample, and the rescaled energy release rate G_{eff} increased in the presence of drops. We understood this as the result of the magnitude of the energy dissipations increasing as the thickness of the elastic material decreases. We then probed the adhesive properties in dynamic conditions with a probe-tack test. We showed that we were able to tune the adherence of the emulsions up to 20 times the adherence of the crosslinked PDMS by varying the drop radius while keeping h/h_s constant. This effect was explained by the competition between elastic and viscous dissipations of energy in the volume of the samples. We also showed that the presence of drops induced a rate dependency with a different power law than for the bare PDMS.

This study is however not complete, and we suggest here a non-exhaustive list of additional experiments that would bring a better understanding of the properties of the solid emulsions. A first experiment could be to vary the viscosity of the drops. Indeed, using a liquid with higher $\mathcal{G}'$ and $\mathcal{G}''$ might make it possible to feel the response of the drops in the rheology experiments, and more importantly to tune the adhesive properties. Indeed, Majumder *et al.* [10] showed that the viscosity of the liquid in the 2D inclusions impacted the value of the energy release rate in a non-monotonous way (Figure 8.14d in Chapter 8). The viscosity of the drops might also impact the power law of the rate-dependency of the energy release rate.

As we discussed in Section 9.4.2 in Chapter 9, we were not able to vary the volume fraction of drops Φ in the samples presented in this study. Of course, the value of Φ should impact greatly both the mechanical and adhesive properties of the solid emulsions, and experiments exploring the entire range of Φ might on one hand allow to understand why we measure values of the Young's modulus so low compared to the predictions of Style *et al.* [9], and on the other hand give a new parameter to tune the adhesive properties. To obtain different values of Φ, we argued that the generation protocol of these particular samples should be reconsidered, since the way we generated the drops in the PDMS did not allow for strong interaction forces to be created between the drops, as we discussed in Part B. Also, we suggested in Chapter 6 that the use of a different solvent in the continuous phase might change the magnitude of the interaction forces. This could also be investigated.

Finally, the adhesive properties of the cellular materials presented in Section 8.3.2 in Chapter 8 were every time explained by the variations of the compliance depending on the position of the crack front. In these 2D cases, the variations were indeed important between a position above a fibril or an inclusion and a position above the bulk material only. Though we expect that in our case the amplitude of the variations should be much lower because of the random organisation of the drops in the volume, it would still be interesting to measure them using a micro-indenter. We might then be able to comment on the dissipations of energy linked to the propagation of the crack front.

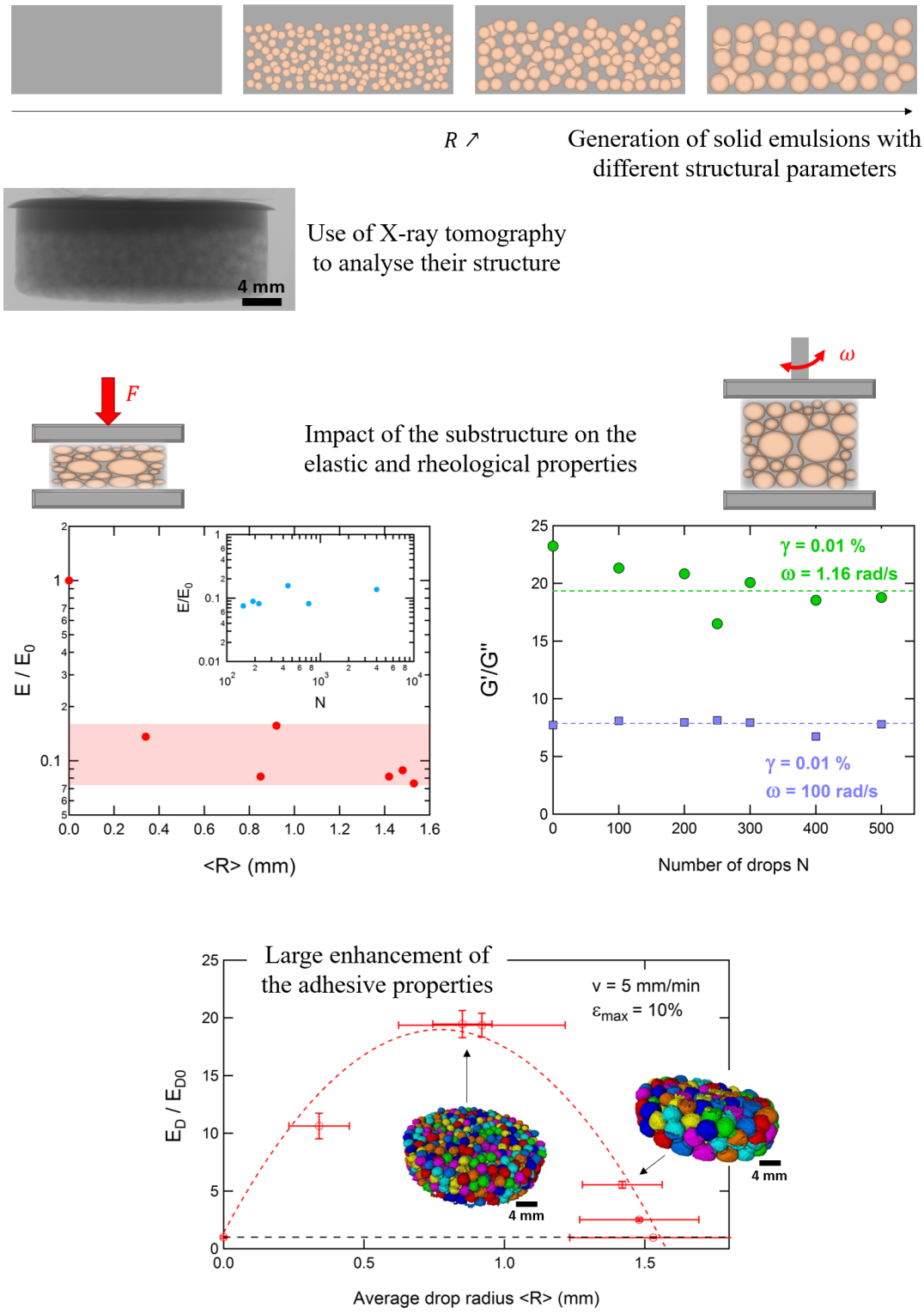

Figure 10.5: Conclusions drawn from Part C of this manuscript.

General conclusion

This work was part of the ERC POMCAPS project, which aims in generating porous materials with well-controlled structural and interfacial properties. We concentrated here on the generation of liquid and solid poly-HIPES, and on the link between their structure and their mechanical and adhesive properties. The three distinct parts of this manuscript aimed at (1) developing sufficiently stable silicone emulsions with controlled drop sizes (Part A), (2) characterising their structural properties in the liquid state (Part B) and (3) exploring their mechanical/adhesive properties after solidification (Part C).

In Part A, we started with the problematic of the stabilisation of emulsions with silicone as the continuous phase. Since no known surfactants are efficient enough to stabilise such emulsions, we chose to use a reactive stabilisation process, which creates surfactants and a polymeric skin *in-situ* at the interface thanks to chemical reactions. We showed that using a crosslinker/catalyst molecule dissolved in the dispersed phase (PEG), and a reactive PDMS (MHDS), we were able to create PDMS-b-PEG copolymers at the interface and to crosslink the interface at the same time (though with different characteristic times for each reaction). This completely inhibited the coalescence between the drops above a critical concentration of crosslinker/catalyst. We probed the evolution of the chemical reactions at the interface by measuring the interfacial tension between the PEG and the MHDS for different concentrations of crosslinker/catalyst. We put in evidence a characteristic change in its behaviour both at equilibrium and during the evolution at a concentration which coincides well with the onset of the stability of the emulsions. We associated this change with the onset of the formation of a polymeric skin around the drop. Using this result, we were able to adapt our formulation to choose the most favourable crosslinker/catalyst concentration to generate ultra-stable silicone emulsions.

Once we optimised the formulation of the emulsion, we showed that using different generation techniques, we were able to generate liquid emulsions with controlled drop sizes from 300 µm up to 1.5 mm in radius. We also demonstrated that we could solidify the continuous phase of the emulsions by adding a different crosslinker in the MHDS before the generation, and that changing the molecular weight of the MHDS allowed to obtain materials with different elastic moduli. We thus obtained what we call in this manuscript "solid emulsions", composed of liquid drops inside a solid matrix. By putting a volatile (but still hydrophilic) liquid inside the drops instead of PEG, we were able to generate solid foams with controlled pore sizes. Using X-ray tomography and Scanning Electron Microscopy we showed that if the PEG-in-MHDS solid emulsions systematically had closed cells, the solid foams generated using water as the dispersed phase had open cells. We interpreted this as the result of the absence of the PDMS-b-PEG copolymers at the interface between the water and the MHDS, which makes the films between the drops more fragile.

In the rest of the study, we concentrated on the link between the structure and the mechanical and adhesive properties of the solid emulsions. We thus chose to use Sylgard 184® as the continuous phase, which has a high enough elastic modulus to resist deformations. Since the structure of a solid material is the signature of the structure of the liquid template, we analysed in Part B liquid PEG-in-Sylgard 184® emulsions, for which we do not add the curing agent in the continuous phase. We first characterised the interactions between two PEG drops containing the crosslinker/catalyst molecule in the continuous phase in which we added 0%, 5% or 10% of dodecane. We showed that the presence of a polymeric skin around the drops, due to the stabilisation process, coupled with the addition of dodecane in the continuous phase varied significantly the strength of what we interpret as adhesive and frictional forces between the drops. Then, we showed that within an emulsion these drops do not organise in the volume as they do in surfactant-stabilised emulsions. Instead, we established that they organise more like a packing of hard spheres since the volume fraction of drops is constant with the height of the emulsion. We were able to point out some differences with hard sphere packings, such as the absence of correlation between the positions of the drops with respect to each other, which we attributed to the deformability of the drops.

We therefore provided some first answers to the question of how does the stabilisation process, in our case the creation of a polymeric skin at the surface of the drops, impacts the organisation of drops in the liquid emulsions, and we proposed a direct comparison both with systems close to ours, the surfactant-stabilised emulsions, and systems that seem very different but share common properties, the packings of hard spheres. We also reported for the first time the existence of frictional forces between emulsion drops.

After studying the structural properties of the liquid template, we investigated how the mechanical and adhesive properties of the solid emulsions depend on the number of drops, on their organisation and their size, using contact mechanics and rheology experiments. We showed that the ratio of the storage modulus over the loss modulus did not depend on the number of drops in the volume, which we understood as the fact that the presence of the drops in the volume does not change the viscoelastic properties of the material. We then showed that the elastic modulus was constant with the drop size for a constant height of drops in the material, which we interpreted as being the result of the incompressibility of the drops. Our data did not collapse with predictions of the elastic modulus of materials comporting liquid inclusions in their bulk developed by Style *et al.* [9], though it seemed quite close to the model for solid foams developed by Heitkam *et al.* [4]. We then investigated the adhesive properties of the solid emulsions with a constant volume fraction of drops. We showed that, for a constant traction speed, the drop size had a non-monotonous influence on the dissipated energy. We also measured the impact of the traction speed, and showed that the presence of liquid drops in the volume changed the power law associated with the evolution of the energy release rate with the speed.

This allowed to understand the link between the structure of the solid emulsions and their mechanical and adhesive properties. The presence of the drops in the volume of the materials impact greatly the adhesive properties, and though this had been demonstrated by Majumder *et al.* [10] for two-dimensional systems, we proposed here a 3D system which needs much less fabrication steps and shows the same efficacy.

While Parts B and C presented quite preliminary results, they show clearly that emulsions with solid-like skins are fascinating objects for investigation. They have the potential to provide soft objects with

tunable interfacial properties which may allow in the future to link more solidly the interactions between soft spheres and their organisation in dense packings. Moreover, they provide highly stable templates for solidification and therefore for the generation of two-phase materials with tunable visco-elastic properties. For the study of the structure of the emulsions, we need more systematic experiments characterising the interactions between two drops, while the study of the mechanical and adhesive properties would be more complete with experiments varying the viscosity of the drops and their volume fraction. This will be the object of future investigations.

Appendices

Appendix I

Accuracy and reproducibility of the interfacial tension measurements

In Chapter 3 Section 3.1, we study the evolution of interfacial tension γ with time, for different crosslinker/catalyst concentrations C. It is important to note that, as seen in Figure I.1 for the particular concentration $C = 0.1$ mol%, the drop volume has no impact on the kinetic of evolution of interfacial tension which shows the reproducibility of the experiments with varying the drop volume. However, if the drop is too big, it detaches from the needle before reaching the plateau value of interfacial tension (for $V = 4$ and 2 µL). One has to make sure, when using a pendant drop tensiometer, that the Bond number B_0 which balances gravitational and interfacial tension forces

$$B_0 = \frac{\Delta\rho g R^2}{\gamma}, \tag{I.1}$$

where $\Delta\rho$ is the density difference between the two phases, g the gravitational acceleration and R the drop radius, is high enough to provide a reliable measurement [331]. Usually the accuracy limit is set around $B_0 = 0.1$. In our case, the density difference between the PEG and the MHDS is low ($\Delta\rho \simeq 0.15$ g/mL), but the interfacial tension is also low ($0.5 < \gamma < 10$ mN/m), which allows for small drop volumes. Indeed, as seen in the insert of Figure I.1, for small times t the Bond number is close to the accuracy limit, but as time increases (and simultaneously γ decreases), the Bond number increases, which convinces us of the accuracy of our measurements for the rest of the study.

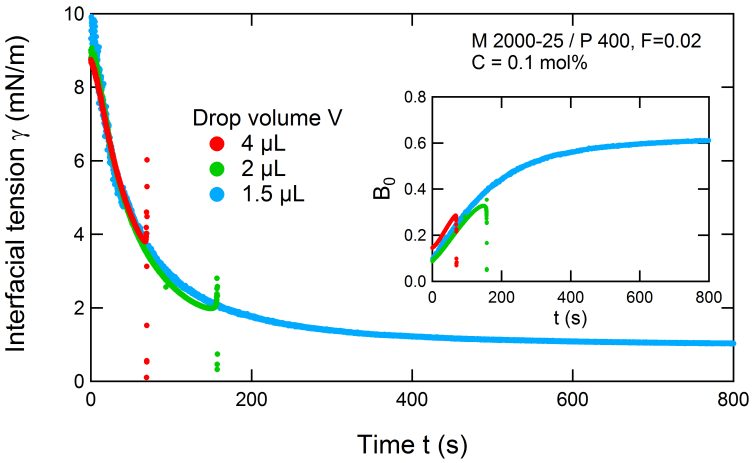

Figure I.1: Time evolution of the interfacial tension between MHDS 2000-25 and PEG400 with F(Pt)=0.02 for C=1 µL of crosslinker/catalyst in the PEG phase for different drop volumes. Insert is the respective Bond number B_0 for each volume with time.

Appendix II

Kinetics of evolution of the interfacial tension at the PEG/MHDS interface

II.1 Dependency on γ_0 and t_0 of the log-log representation of the evolution of the interfacial tension at short times

In Chapter 3 Section 3.4.2, we plot the interfacial tension γ with time as $\log(\gamma_0 - \gamma) = \log(t_0 - t)$, in order to study its evolution at short times (Figure 3.7). The two parameters γ_0 and t_0 are dependent of each other: for a value of t_0 there is a unique value of γ_0, and this duo is associated with a measurement number N of the Tracker software. Figure II.1 shows how choosing different values of the measurement number N (i.e. changing γ_0 and t_0 which are inter-dependent) does not have a large impact on the log-log curves Figure 3.7 for the particular concentration C=0.0067 mol%.

II.2 Robustness of the fit with the Volmer model

In Chapter 3 Section 3.4.2, we apply the reaction-controlled model of evolution of the surface coverage Γ at reactive interfaces on our system. In order to obtain Γ from the measurement of the interfacial tension γ, we apply the Volmer model (Figure 3.9), and find a relatively good agreement with a fixed initial surface tension γ_0 and one adjustable parameter Γ^∞. Since the error is important on the value of Γ^∞, we need to analyse whether it has an impact on the global evolution of Γ or not. Figure II.2a represents $\Gamma(t)$ for C=0.0067 mol% (yellow curve in Figure 3.10) for different values of Γ^∞ around its "true" value of $4.4 \times 10^{-6} \pm 1.6 \times 10^{-6}$ mol/m^2 (we call $\Gamma^\infty_{mean} = 4.4 \times 10^{-6}$ mol/m^2 and the plus and minus values $\Gamma^\infty_{min} = 2.7 \times 10^{-6}$ mol/m^2 and $\Gamma^\infty_{max} = 6.0 \times 10^{-6}$ mol/m^2). All these curves can be captured by an exponential fit. Figure II.2b shows the values of τ_c and A, the parameters of the fit $y_0(1 - A \cdot \exp(t/\tau))$. In this graph, the data for τ_c and A corresponding to Γ^∞_{mean} is surrounded in black, and the limiting values Γ^∞_{min} and Γ^∞_{max} are surrounded in grey.

The first thing to note is that, except for the lowest value of Γ^∞, the value of A stays constant ($A = 1.1$), which means that the pre-factor of the exponential is not dependent on Γ^∞ on a large data range. However, τ_c varies on the entire range of Γ^∞ tested. In Figure II.3a, we plotted the first order plot of the data Figure II.2. Apart from the very low value of $\Gamma^\infty = 0.17 \times 10^{-6}$ mol/m^2, the curves for all

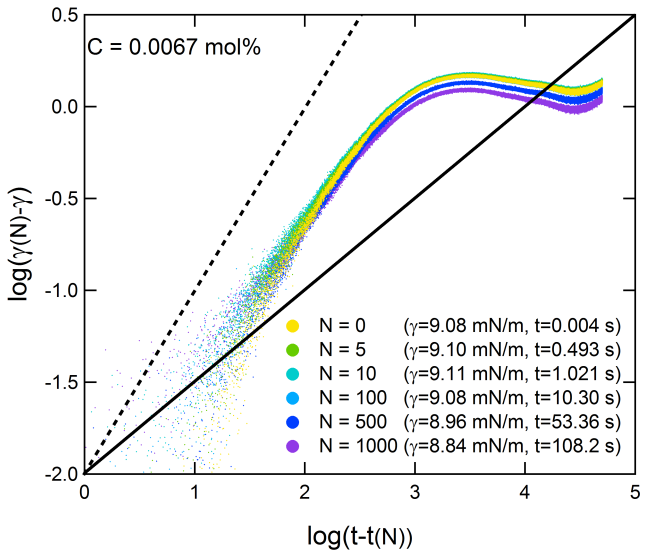

Figure II.1: Logarithmic representation of the evolution of interfacial tension at the MHDS 2000-25/PEG 400 interface for $F(Pt) = 0.02$ with time for C=0.0067 mol%, with different values of γ_0 and t_0 chosen from different measurement number N. The full black line corresponds to the 0.5 slope. The black dotted line corresponds to a slope 1.

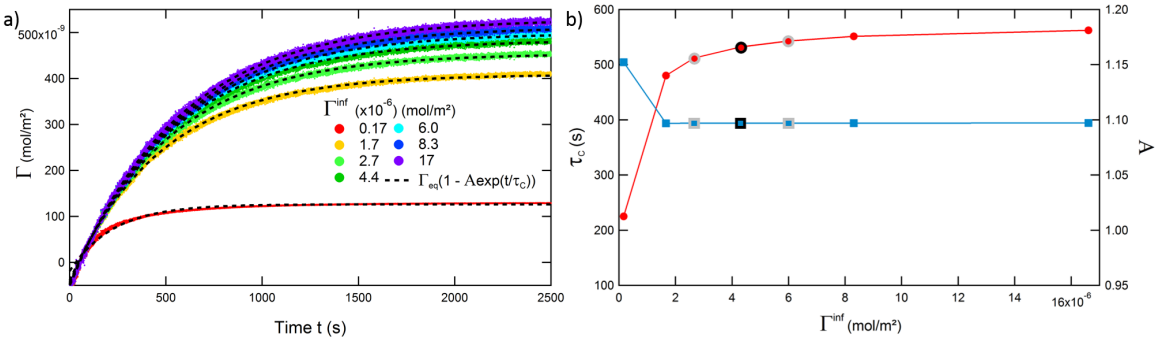

Figure II.2: Copolymer surface concentration with time at the interface MHDS 2000-25/PEG 400 with $F(Pt)$=0.02 for C=0.0067 mol%, for different values of Γ^{∞}. The marker corresponding to the central value of Γ^{∞} given by the Volmer model is surrounded in black and its minimum and maximum values in grey.

the values of Γ^{∞} at this C follow the same behaviour. From this, we deduce that in the interval given by the Volmer model, variations of Γ^{∞} do not have an impact on the evolution of $\Gamma(t)$.

In Figure II.3b, we plotted the same first order plot, this time varying the value of Γ_{eq}. In that case, the evolution of $\Gamma(t)$ seems to be more dependent on this parameter, and small variations can cause the curve to deviate from the theoretical straight line. The choice of Γ_{eq} must be made cautiously as the mean of Γ at long times.

Figures II.3c and d represent the same analysis made at C=0.0067 mol%, this time with a higher concentration C=0.03 mol%, for which the kinetic of evolution in Figure 3.11 did not seem to follow a first order dynamic. Here we show even large variations of Γ^{∞} and Γ_{eq} do not change the fact that we cannot describe the kinetic evolution of Γ with known models.

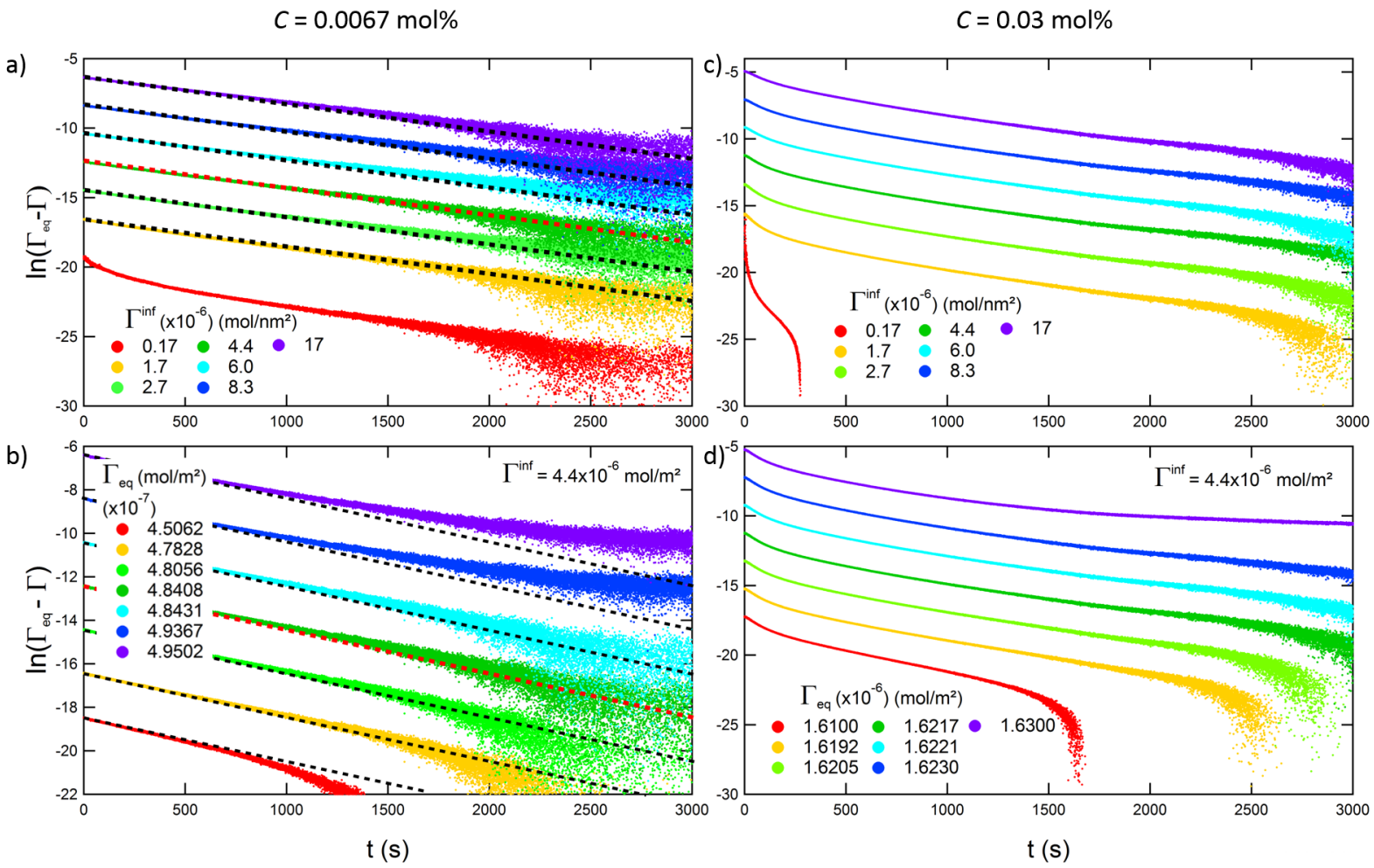

Figure II.3: First order plot of Γ with time at the interface MHDS 2000-25/PEG 400 with $F(Pt)$=0.02 for C=0.0067 mol% and C=0.03 mol%, for different values of Γ^{∞} (a and c) and Γ_{eq} (b and d). All the curves have been shifted from their original position for clarity. The red dotted lines indicate the reference parameters used for C=0.0067 mol% Figure 3.11.

Appendix III

Composition of the polymeric skin in PEG-in-Sylgard 184 base emulsions

The composition of the polymeric skin around the drops depends on the composition of the Sylgard 184® base and the reactions that can occur at the interface between the PEG and the continuous phase.

The Sylgard 184® base is composed for the main part (>60 wt%) of dimethylsiloxane, dimethylvinyl-terminated (CAS number: 68083-19-2). It also contains dimethylvinylated and trimethylated silica (CAS number: 68988-89-6) between 30 and 60 wt%, and a small quantity (between 1 and 5 wt%) of tetra(trimethylsiloxy)silane (CAS number: 3555-47-3), which is a volatile siloxane.

The dimethylsiloxane, dimethylvinyl-terminated is made to react with the dimethyl, methylhydrogen siloxane (PDMS with reactive Si-H groups), present in majority in the curing agent, upon mixing of the two parts of the Sylgard 184®. This reaction is the hydrosilylation reaction (1) in Figure 2.13 in Section 2.5. Since we do not use the curing agent here for the reasons stated in the introduction of this chapter, reactions (1) and (2) in Figure 2.13 in Section 2.5, both including the Si-H group, cannot happen at the interface between the PEG and the continuous phase composed of Sylgard 184® base and D_4, and as reaction (2) causes reactions (3a) and (3b), these should not happen either. However, we do observe the presence of a skin at the interface (as evidenced by Figure 6.2.1b), which means that a reaction takes place at the interface.

III.1 Characterisation of the Sylgard 184 base using IR spectroscopy

In order to understand the formation of the skin-like interface, we looked at the Infra-Red (IR) spectra of the Sylgard 184® base shown in Figure III.1. Figure III.1a shows the full IR spectra of the Sylgard 184® base. We can distinguish the peak at $\approx$ 2900-3000 cm^{-1} characteristic of the stretching of the Si-CH_3 liaisons present in the three molecules composing the base [15, 194]. We also see the absence of a peak at $\approx$ 2100-2300 cm^{-1} characteristic of the Si-H liaisons. It is however present in the curing agent (see Appendix III.2). Zooming on the wave numbers between 2600 and 4000 cm^{-1} (Figure III.1b), we can distinguish another peak at $\approx$ 3200-3700 cm^{-1} which is characteristic of the stretching of Si-OH liaisons. However, in the composition given by the manufacturer there is no direct indication of Si-OH liaisons in the base. Nonetheless, we know that these liaisons can only come from the presence

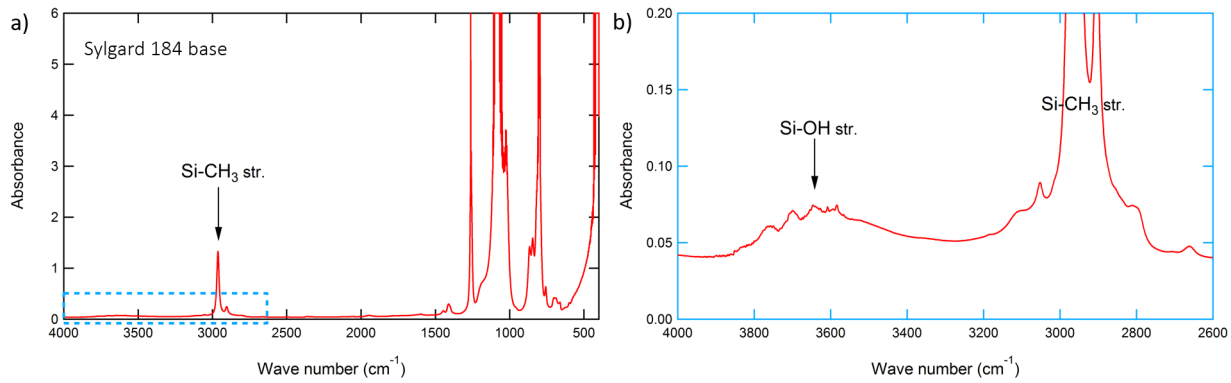

Figure III.1: a) IR spectra of the Sylgard 184® base between 400 and 4000 cm^{-1}. The dashed rectangle indicates the zone where we zoomed to observe the Si-OH str. peak. b) Zoom on the Si-OH peak for the Sylgard 184® base.

of the dimethylvinylated and trimethylated silica. Indeed, this molecule is a silicone resin, formed by branched, cage-like oligosiloxanes, used to build 3D molecular structures. It can be obtained by different processes and it is difficult to describe their real structure. The most abundant silicone resins are built of D (divalent, Me_2SiO_2) and T (trivalent, $MeSiO_3$) units or from M (monovalent, Me_3SiO) and Q (tetravalent, SiO_4) units. As not all reactive sites are treated during the reaction to build the 3D structure, some Si-OH groups can still be present at the end. Our hypothesis is that these are the ones we observe in Figure III.1b, and which react with the PEG-400 (reaction (3a) in Figure 2.13) to create PDMS-b-PEG copolymers, or with each other (reaction (3b) in Figure 2.13) which crosslinks the interface, thanks to the *Pt* catalyst present in the PEG phase.

As indicated by the IR spectra in Figure III.1b, the amount of Si-OH liaisons is low in the Sylgard 184® base. However, the dimethylvinylated and trimethylated silica are molecules usually used with high molecular weights, and our hypothesis is that this is probably enough to create the elastic skin that we observe at the interface.

III.2 Evolution of interfacial tension between the PEG and the Sylgard 184 base

Following the interfacial properties characterisation of Part A, we measured the interfacial tension γ at the interface between the PEG-400/crosslinker/catalyst and the Sylgard 184® base, with and without dodecane in the Sylgard, using the Tracker apparatus (cf Section 1.3.2 in Chapter 1). Figure III.2a shows the evolution with time of the interfacial tension for different values of the crosslinker/catalyst concentration C for this system. We can see that in all cases the interfacial tension decreases with time over timescales of $\approx$ 5-10 s, even for $C = 0$ mol%. In Chapter 3, we looked at the evolution of the interfacial tension between different systems of PEG and MHDS, with varying concentrations C. For all systems, the interfacial tension did not relax for $C = 0$ mol%, which we can interpret as an infinite characteristic relaxation time. The fact that it does relax for the PEG-400/Sylgard 184® base system brings us to think that the relaxation is due to viscosity effects. Indeed, the measurements of the interfacial tension start right after generation of the drop by the apparatus, i.e.

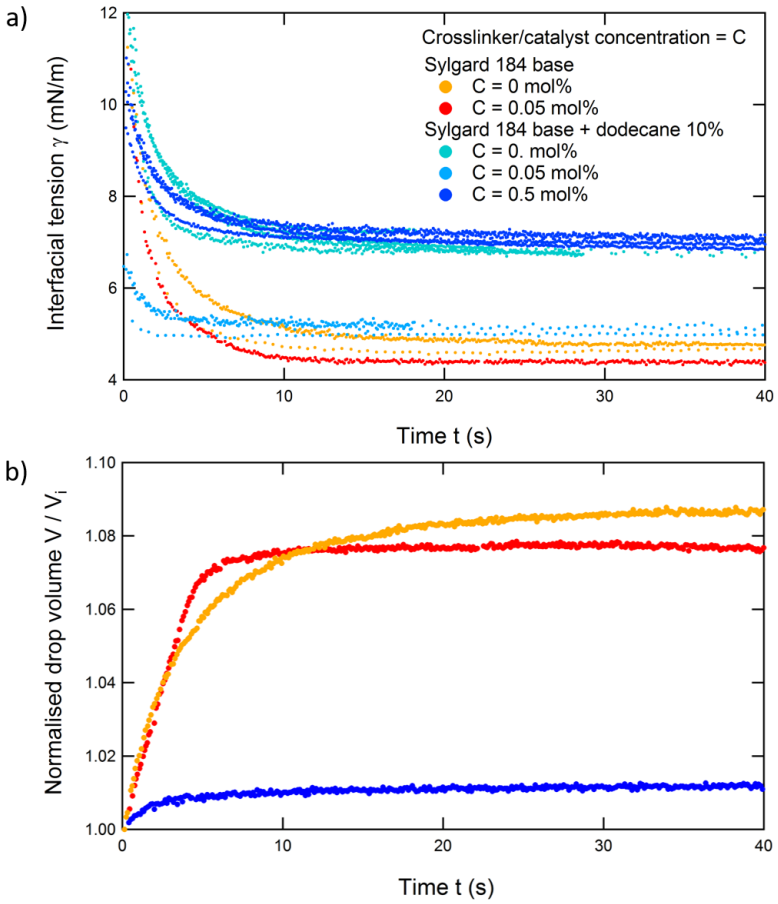

Figure III.2: a) Evolution of interfacial tension at the PEG-400/Sylgard 184® base+D_4 interface with time for different concentrations of crosslinker/catalyst C in the PEG-400 phase, with and without dodecane in the continuous phase, at 25°C. b) Evolution of the drop volume V normalised by the initial drop volume when the measurement with the tracker apparatus starts V_i with time for the same system as in a).

when the motor controlling the volume of the drop stops. However, because here the continuous phase is viscous, it resists the creation of the drop, and as a result the volume of the drop still increases when the measurement starts, as seen in Figure III.2b. The characteristic time of the evolution of the normalised drop volume V/V_i, where V_i is the volume of the drop when the measurement starts, is of the same order of magnitude as the characteristic time of evolution of the interfacial tension in Figure III.2a. We then believe that, even though the reactions do occur, as shown by the signature of elasticity at the interface in Figures 6.2.1 and 6.2.2 in Chapter 6, the effect is not captured by the measure of the interfacial tension. This is probably due to the fact that there are only a few reactive molecules in the continuous phase as shown by the IR spectrum in Figure III.1b.

We know thanks to the observations shown in Chapter 6 that a skin-like interface is created a the surface of the drops in the PEG-in-Sylgard 184® base emulsions. Here, we showed that it could only be so thanks to the presence of a few Si-OH reactive groups in the Sylgard 184® base, even though we could not deliver evidence of the reaction happening at the interface by measuring the interfacial tension at the interface with the PEG. Though the chemistry is a bit different in this case, the molecules created at the interface are not significantly different and we can assume they will play the same role as for the emulsions where Si-H groups are present.

Appendix IV

Detailed calculation of the elastic modulus of elastomers

Thermodynamically speaking, if we consider an isotherm and reversible deformation, without volume variations, then the change in free energy of the system dF is the work of the deformation dW

$$dF = dW = dU - TdS \tag{IV.1}$$

with U the internal energy of the system and S its entropy. In a metal or a glassy polymer, the number of possible configurations of the system is low leading to the variation of internal energy dU to be dominant. On the other hand, an unstretched polymer has a high entropy random coil configuration, leading to the entropy variations term TdS to be by far dominant and we can neglect the first term.

For an ideal chain under the freely-jointed chain model, we get [332]

$$S^{chain} \approx k_B \ln(P(r, N)), \tag{IV.2}$$

where k_B is the Boltzman constant and $P(r, N)$ the probability of finding the chain ends at a distance r apart as given by the following Gaussian distribution

$$P(r, N) = (\frac{3}{2\pi R_0^2})^{3/2} \exp(-\frac{3r^2}{2R_0^2}), \tag{IV.3}$$

where R_0 is the total length of the polymer chain. It comes that

$$F^{chain} = -TS^{chain} = F_0^{chain} + \frac{3k_BT}{R_0^2} r^2. \tag{IV.4}$$

For small deformations from a position $R(x, y, z)$ to $r(\lambda_x x, \lambda_y y, \lambda_z z)$, the variation of free energy $\Delta F^{chain} = F^{chain}(r) - F^{chain}(R)$ gives

$$\Delta F^{chain} = \frac{3k_BT}{R_0^2}[\lambda_x^2 x^2 + \lambda_y^2 y^2 + \lambda_z^2 z^2 - (x^2 + y^2 + z^2)]. \tag{IV.5}$$

To go from the free chain to the network, we use the affine deformation model which implies that the end points of the polymer strands in the sample undergo the same deformations as the sample itself. For

a network composed of N chains, and assuming isotropic chains, i.e. $< x^2 >=< y^2 >=< z^2 >= R_0^2/3$, we get

$$\Delta F = \frac{Nk_BT}{2}[\lambda_x^2 + \lambda_y^2 + \lambda_z^2 - 3]. \tag{IV.6}$$

We now define the deformation as uniaxial, for example along the x axis, which gives $\lambda_x = \lambda$ and $\lambda_y = \lambda_z = \lambda^{-1/2}$ for volume conservation. This allows to simplify ΔF

$$\Delta F = \frac{Nk_BT}{2}[\lambda^2 + \frac{2}{\lambda}]. \tag{IV.7}$$

From this expression of the variations of the free energy of the system, we can calculate the tensile stress $\sigma_t = f/A$ where $f\frac{d\Delta F}{dL}$ is the force applied during the deformation and A the initial area of the sample perpendicular to the deformation

$$\sigma_t = \frac{1}{A}\frac{d\Delta F}{dL} = \frac{1}{AL_0}\frac{d\Delta F}{d\lambda} = \frac{Nk_BT}{V}[\lambda + \frac{1}{\lambda^2}]. \tag{IV.8}$$

Since we assumed small deformations, $\lambda = 1 + \epsilon$ with $\epsilon \to 0$, and we finally get

$$\sigma_t = \frac{3Nk_BT}{V}\epsilon. \tag{IV.9}$$

Comparing this expression with the *Hooke*'s law, we obtain the Young's modulus for elastomers given in Equation (8.5) in Chapter 8.

Appendix V

Contact between elastic objects: the Hertz theory

Here we study the contact between a sphere and a plane without adhesive forces between the two objects.

Let us consider the case of a sphere of radius R, with a Young's modulus E_1 and a Poisson ratio ν_1, and a plane made of a material of Young's modulus E_2 and a Poisson ratio ν_2. If no pressure P, or normal force F_H[1] is applied, the contact is made only on a single point. Upon increasing of the normal force F_H between the two objects, by increasing the indentation δ, the contact area is then a circle of radius $a = \sqrt(R\delta)$. Because of the angular symmetry with θ, we choose a circular coordinate system (r,z) (Figure V.1).

In Figure V.1, the distance OH is defined by OH = δ. Near the z-axis, the distance between M (of coordinate z_1) and N (of coordinate z_2), two points on the undeformed surfaces of each object, taken vertically from each other, is given by $z_1 + z_2 = \frac{r^2}{2R}$. The non-interpenetrability of the sphere and the plane induces a sum of the deformations of the two objects in contact

$$u(z) = u_1(z_1) + u_2(z_2) = \delta - (z_1 + z_2) = \delta - \frac{r^2}{2R}. \tag{V.1}$$

The deformation $u(z)$ depends on the pressure distribution. If we assume that the pressure distribution on the contact area is represented by the ordinate of a half-sphere of radius a constructed on the surface of contact, then the total force F is given by

$$F = \frac{p_0}{a}\frac{2}{3}\pi a^3, \tag{V.2}$$

and the pressure distribution by

$$p = p_0\sqrt{1 - \frac{r^2}{a^2}}, \tag{V.3}$$

where p_0 is the maximum pressure at $r = 0$ and which verifies $p = 0$ for $r = a$. We then obtain

$$u(z) = \frac{\pi^2 p_0}{3Ka}(2a^2 - r^2), \tag{V.4}$$

[1] the H subscript denotes the expression of the normal force in the Hertz theory.

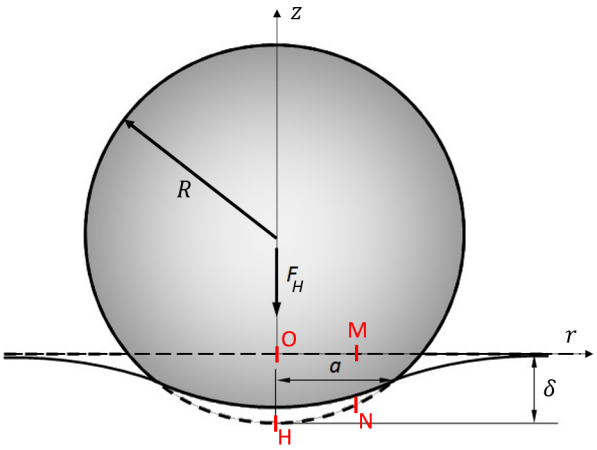

Figure V.1: Contact of an elastic sphere with an elastic half-space. Adapted from `https://commons.wikimedia.org/w/index.php?curid=35157671`.

with $\frac{1}{K} = \frac{3}{4}(\frac{1-\nu_1^2}{E_1} + \frac{1-\nu_2^2}{E_2})$ where K is the effective modulus of the system. By identification of Equations V.1 and V.4, we obtain

$$\delta = \frac{2\pi^2 p_0}{3K} a, \tag{V.5}$$

and

$$a = \frac{2\pi^2 p_0 R}{3K}, \tag{V.6}$$

which gives by combining these two equations

$$\delta = \frac{a^2}{R}. \tag{V.7}$$

Since $F = \frac{2\pi p_0}{3} a^2$ we obtain

$$F = \frac{K}{\pi R} a^3. \tag{V.8}$$

Appendix VI

Fit parameters of $\mathcal{G}'(\omega)$ and $\mathcal{G}''(\omega)$ of the solid emulsions

Sample		y_0	A	pow
PEG-400	$\mathcal{G}'$	0 ± 0	$2.6838\times10^{-6} \pm 2.27\times10^{-7}$	1.1821 ± 0.0197
	$\mathcal{G}''$	0 ± 0	$5.4009\times10^{-2} \pm 3.39\times10^{-3}$	1.1807 ± 0.0146
PDMS	$\mathcal{G}'$	$6.9228\times10^{5} \pm 1960$	70427 ± 1980	0.26508 ± 0.00481
	$\mathcal{G}''$	0 ± 0	30967 ± 241	0.26876 ± 0.00231
100 drops	$\mathcal{G}'$	$4.9303\times10^{5} \pm 427$	51721 ± 429	0.27996 ± 0.00146
	$\mathcal{G}''$	0 ± 0	24551 ± 33.1	0.26734 ± 0.004
200 drops	$\mathcal{G}'$	$3.8859\times10^{5} \pm 590$	45770 ± 595	0.26702 ± 0.00223
	$\mathcal{G}''$	0 ± 0	20037 ± 217	0.26781 ± 0.00322
250 drops	$\mathcal{G}'$	$2.5262\times10^{5} \pm 343$	33821 ± 343	0.28973 ± 0.00181
	$\mathcal{G}''$	0 ± 0	16636 ± 60.2	0.277 ± 0.00107
300 drops	$\mathcal{G}'$	$3.0206\times10^{5} \pm 445$	33573 ± 448	0.27258 ± 0.00218
	$\mathcal{G}''$	0 ± 0	16118 ± 51.4	0.26235 ± 0.00095
400 drops	$\mathcal{G}'$	$1.9284\times10^{5} \pm 867$	24639 ± 867	0.29187 ± 0.00631
	$\mathcal{G}''$	0 ± 0	11307 ± 68.9	0.29064 ± 0.00178
500 drops	$\mathcal{G}'$	$1.7194\times10^{5} \pm 480$	21927 ± 484	0.26642 ± 0.00379
	$\mathcal{G}''$	0 ± 0	9729.1 ± 25.1	0.2564 ± 0.000774

Table VI.1: Fit parameters of the power law used to describe the behaviour of $\mathcal{G}' = f(\omega)$ and $\mathcal{G}'' = f(\omega)$ in Chapter 9.

Appendix VII

Estimation of the surface energy of the samples by contact angle measurements

As said in Chapter 8, the thermodynamical work of adhesion W is a function of the surface energies of the two surfaces in contact

$$W = \gamma_1 + \gamma_2 - \gamma_{1,2}, \tag{8.6}$$

where γ_1 and γ_2 are the surface energies of materials 1 and 2 respectively and $\gamma_{1,2}$ the interfacial tension between them. In our experiments, the contact is made between a solid emulsion sample (material 1) and either a glass lens or a glass plate (material 2). This means that γ_2 never changes, but γ_1 could if the presence of drops in the volume of the sample perturbs the surface of the emulsion. One way to verify that it does not is to directly measure W as we did in Chapter 10 and show that it is a constant among the different samples, including the bare PDMS reference. Another way is to measure the contact angle θ between a drop of liquid and the surface of the sample. Indeed, the Young-Dupré law gives

$$\cos(\theta) = \frac{\gamma_{SV} - \gamma_{SL}}{\gamma_{LV}}, \tag{VII.1}$$

where $\gamma_{SV} = \gamma_1$ is the surface tension between the solid and the vapour phase, γ_{SL} the surface tension between the solid and liquid phase, and γ_{LV} the surface tension between the liquid and vapour phase. Figure VII.1 shows that the contact angle θ made by a drop of water on top of either a bare PDMS sample or a solid emulsion is the same disregarding of the sample, indicating to surface roughening induced by the presence of drops in the volume of the sample, and no change in the chemical composition of the surface either.

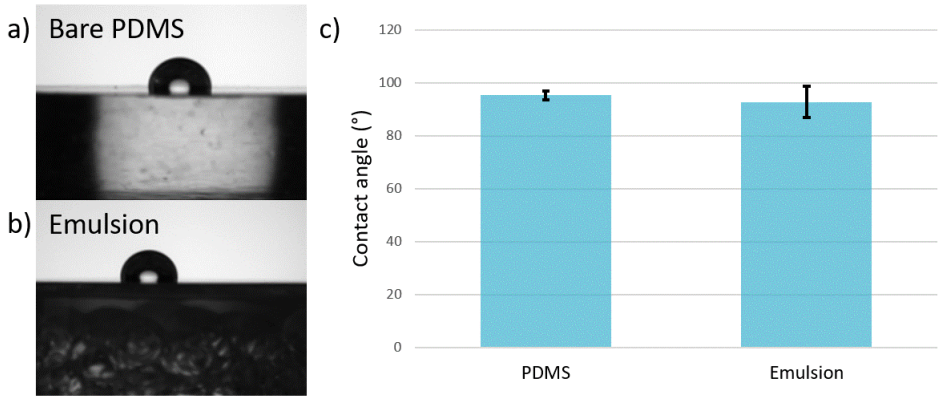

Figure VII.1: a) Photograph of a drop of water on top of a bare PDMS sample (sample 1 in Table 9.1). b) Photograph of a drop of water on top of a solid emulsion (sample 7 in Table 9.1). c) Measure of the contact angle θ between the drop of water and the surface of the samples in a) and b).

Chapter 11

Résumé en français

Les émulsions de polymères font l'objet de beaucoup de recherches du fait de leurs remarquables propriétés. Celles-ci proviennent de la structure interne du matériau, dans lequel des inclusions cellulaires d'un polymère sont compactées dans une matrice continue d'un second polymère. Généralement, l'organisation cellulaire est la signature d'un état initial liquide, dans lequel des gouttes liquides sont compactées dans une phase liquide continue, appelée matrice, et qui peut être solidifiée pour obtenir le matériau final. Comprendre et contrôler l'organisation des gouttes dans la phase continue est donc primordial pour pouvoir contrôler les propriétés finales du solide poreux, et nécessite de contrôler la taille des gouttes ainsi que leur stabilité vis à vis de la coalescence et du mûrissement d'Ostwald (Figure 11.1).

Des matériaux cellulaires ont été développés avec différents polymères pour de nombreuses applications. Par exemple, les matelas sont généralement fabriqués avec du polyuréthane ou du polyéther, et les planches de surf avec du polystyrène. Cependant, beaucoup de ces polymères posent problèmes au niveau de leur résistance au vieillissement, du manque de consistance de leurs propriétés sur une large gamme de température, de leur biocompatibilité, etc. L'utilisation du polydiméthylsiloxane (PDMS), également appelé silicone, permets de s'affranchir de certaines de ces difficultés. En effet, le PDMS est peu couteux, thermiquement stable sur une large gamme de température, perméable aux gaz, transparent sur le spectre du visible, etc., ce qui fait des élastomères silicones de très bon candidats pour de nombreuses applications de l'industrie biomédicale à l'électronique.

Cependant, la stabilisation d'une émulsion (ou mousse) où la phase continue est un silicone souffre toujours d'un manque d'agent stabilisant efficace contre le vieillissement tel que la coalescence et le mûrissement d'Ostwald. Une partie de ce travail de thèse est donc dédiée à la recherche d'une nouvelle méthode de stabilisation efficace de tels matériaux liquides. Nous avons donc développé une approche de stabilisation réactive de polyHIPE (High Internal Phase Emulsion, émulsion à haute fraction volumique de phase dispersée), qui consiste à provoquer une ou plusieurs réactions chimiques à l'interface entre les deux phases. Dans la Partie A, nous présentons le processus de stabilisation de gouttes de polyéthylène glycol (PEG) dans du silicone, et nous établissons le lien entre la stabilité des émulsions et l'évolution de la tension interfaciale entre les deux phases immiscibles, en associant ces deux phénomènes à la formation d'une "peau" élastique à la surface des gouttes.

Dans la Partie B, nous montrons dans un premier temps que nous pouvons utiliser les émulsions réactives pour générer différents types de matériaux (émulsions liquides, mousses solides et émulsions liquides) infiniment stables et avec des tailles de gouttes contrôlées. Nous caractérisons ensuite

l'organisation globale des gouttes dans les émulsions liquides grâce à la tomographie sous rayons X, et nous montrons qu'elle diffère grandement de celle d'émulsions "classiques" stabilisées par ajout de tensioactifs. En analysant les interactions entre deux gouttes, nous mettons en évidence le fait que cette organisation particulière des gouttes est une conséquence directe de la présence à la fois de forces de friction et d'adhésion entre les gouttes, du fait de la présence de la peau élastique générée par le processus de stabilisation réactive. Dans cette partie, nous traitons donc la question : **Comment le processus de stabilisation impacte-t-il l'organisation des gouttes dans une émulsion de PEG dans du silicone ?** En effet, la structure d'un empilement de gouttes d'émulsion stabilisées par ajout de tensioactifs a fait l'objet de beaucoup d'études [1–3], alors que l'étude de l'empilement de gouttes présentant des forces de friction et/ou d'attraction normale n'en est qu'à ses débuts. Nous montrons ici que l'empilement des gouttes dans nos émulsions partage beaucoup de propriétés avec l'empilement de sphères dures et frictionnelles, tout en présentant d'autres propriétés surprenantes du fait de la déformabilité des gouttes. Les systèmes comme celui que nous avons développé pourrait donc permettre de mieux comprendre comment les propriétés structurelles d'empilements de sphères athermales dépendent des interactions complexes entre elles (déformabilité, friction, adhésion).

Après avoir solidifié la phase continue de silicone, nous obtenons des "émulsions solides" dont nous étudions les propriétés mécaniques et adhésives dans la Partie C de ce manuscrit. Si les propriétés mécaniques des mousses solides ont fait l'objet de nombreuses études scientifiques pour l'intégralité de la gamme de fraction volumique de gaz du matériau [4–8], les propriétés mécaniques de solides comportant des inclusions liquides ont seulement été étudiées pour de faibles fraction volumiques de liquide [9]. Aussi, l'impact d'une sous-structure dans le volume d'un solide sur ses propriétés adhésives n'a été jusqu'à maintenant étudiée que pour des systèmes en 2D [10, 11]. Les propriétés des émulsions solides n'ont jamais été étudiées auparavant. Dans la partie C, nous nous attaquons donc à la question : **comment la présence de gouttes dans la sous-structure d'un élastomère de silicone impacte-t-elle ses propriétés mécaniques et adhésives ?** A l'aide d'expériences de rhéologie et de mécanique des contacts, nous étudions les propriétés mécaniques et adhésives des émulsions solides en fonction de leurs propriétés structurelles étudiées dans la Partie B. Nous montrons que la présence des gouttes change le module élastique, et augmente significativement les propriétés adhésives grâce à l'augmentation des dissipations d'énergie d'origine visqueuses.

D'un manière générale, nous montrons avec ce travail de thèse que l'utilisation d'une stabilisation réactive des émulsions ouvre de nouvelles voies d'étude des empilements de sphères présentant des interactions sphère-sphère complexes, ainsi que de la génération de nouveaux types de matériaux cellulaires présentant des propriétés mécaniques intrigantes. Si notre étude ne présente que des résultats préliminaires dans ce domaine vaste, ils indiquent des questions scientifiques intéressantes et importantes, dignes d'études systématiques et plus approfondies à l'avenir.

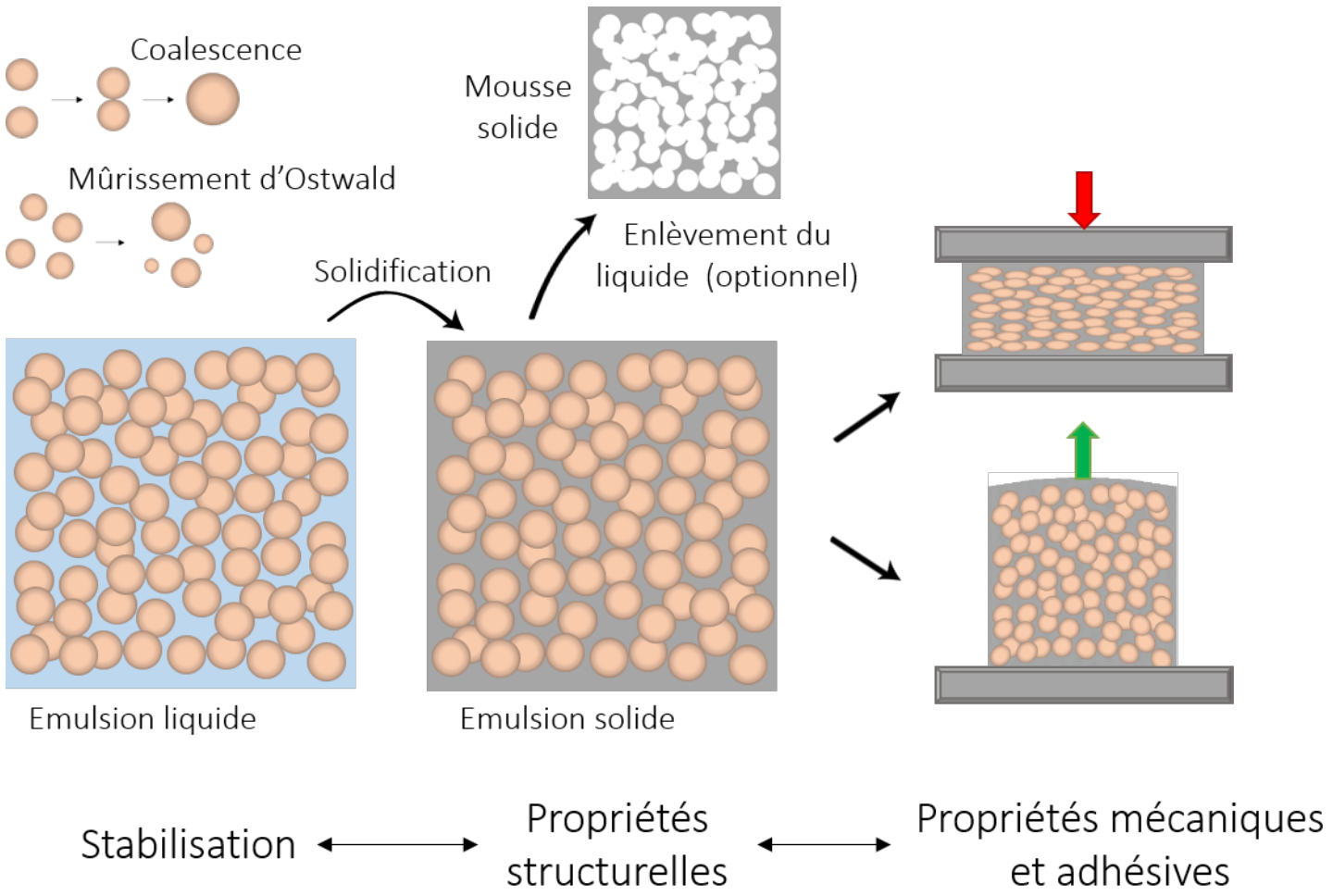

Figure 11.1: Contexte de ce travail de thèse.

11.1 Stabilité des émulsions : comportement des interfaces réactives

L'objectif de cette première partie était de présenter une méthode de stabilisation et de génération d'émulsions avec une matrice silicone. Puisqu'il n'existe aujourd'hui aucun tensioactif suffisamment efficace pour la génération d'émulsions stables de silicone, nous avons opté pour l'utilisation de réactions chimiques à l'interface entre le PEG et le MHDS (approche de stabilisation réactive), pilotée par la concentration C en crosslinker qui crée une peau visco-élastique autour des gouttes. La présence de cette peau permets de s'affranchir totalement de la coalescence et du mûrissement d'Ostwald dans les émulsions. Nous avons montré dans la Section 2.5 du Chapitre 2 que la stabilité des émulsions était séparée en deux régimes : instable pour $C < C^*$ et stable pour $C > C^*$, où C^* est la concentration critique de crosslinker/catalyseur (Figure 11.2).

Afin d'optimiser la formulation et de comprendre en détail les mécanismes de stabilisation, nous avons suivi dans le Chapitre 2.1.1 l'évolution de la tension interfaciale avec le temps à l'interface réactive entre le PEG et le MHDS. De cette manière, nous avons pu obtenir deux informations sur les propriétés interfaciales :

- l'analyse de la valeur à l'équilibre et du temps caractéristique de l'évolution de la tension interfaciale montre l'existence d'une concentration critique C^* qui délimite deux régimes et corrèle très bien avec les résultats obtenus sur la stabilité des émulsions dans la Section 2.5 du Chapitre 2,
- la relaxation de la tension interfaciale après compression montre également l'existence de deux régimes délimités par la concentration critique C^*.

Nous avons interprété l'existence de C^* comme la signature du début de la formation d'une interface réticulée.

Pour appuyer cette hypothèse, nous avons discuté l'influence des paramètres moléculaires du PEG et du MHDS, et nous avons montré que l'évolution de la valeur à l'équilibre de la tension interfaciale avec ces paramètres était cohérente avec la création d'une peau visco-élastique à la surface des gouttes. Nous avons ensuite appliqué des modèles théoriques de la cinétique de la tension interfaciale à des interfaces réactives sur nos données, avec l'idée de trouver ici encore un changement de régime entre $C < C^*$ et $C > C^*$. Nous avons montré que le système est limité par la cinétique des réactions chimiques et suit une cinétique du premier ordre pour $C < C^*$, alors que la cinétique d'évolution de la tension interfaciale pour $C > C^*$ ne suit aucune des théories connues aujourd'hui. Cela supporte notre hypothèse que l'interface est réticulée pour $C > C^*$, grâce à la promotion des réactions (1) et (3b) à concentration C élevée.

Cette étude montre également qu'il est possible de sonder indirectement et quantitativement l'avancement des différentes réactions en mesurant les propriétés interfaciales telles que la tension interfaciale et/ou l'élasticité dilatationelle de surface.

La compréhension des propriétés de l'interface réactive entre le PEG et le MHDS est un point crucial pour choisir la concentration optimale en crosslinker/catalyseur pour la génération des émulsions. En effet, cela permet de montrer pour la première fois la génération d'émulsions ultra-stables à pores fermés avec du PDMS comme phase continue, en utilisant une approche de stabilisation réactive, avec des tailles de gouttes allant jusqu'à l'échelle millimétrique (présenté en Chapitre 4). Nous sommes également capable de générer des mousses silicones présentant des pores ouverts en utilisant la même

approche. Nous pensons que cette approche de stabilisation réactive peut être transférée à d'autres systèmes de polymères. Par exemple, la formation in-situ de copolymères block à la surface de gouttes est utilisée de manière routinière pour une large gamme de mélange de polymères [39–41]. La formation d'une peau autour des gouttes en initiant une polymérisation à la surface est également utilisée pour la génération de polyHIPE avec différents systèmes de polymères, avec cependant l'ajout de tensioactifs pour éviter la coalescence des gouttes [196, 197]. Ce travail combine ces deux aspects.

Les émulsions liquides de PEG dans le MHDS ainsi obtenues ont une grande densité de gouttes (>97%) grâce à la faible tension interfaciale entre les deux phases qui permet aux gouttes de se déformer. Ceci empêche l'étude de leurs propriétés structurelles avec un appareil de tomographie sous rayons X en laboratoire à cause de sa faible résolution d'approximativement 20 µm alors que les films entre les gouttes sont attendus avec une épaisseurs de 1-10 µm. L'utilisation d'un appareil de tomographie sous rayons X dans un synchrotron avec une résolution élevée et une analyse en contraste de phase pourrait permettre d'obtenir la structure de ces drops polyédrales dans le MHDS.

De plus, le module élastique des émulsions de PEG dans le MHDS solidifiées est trop faible pour permettre de les manipuler lors d'expériences de mécanique dans les endommager, ce qui explique que nous n'avons pas de résultats à ce jour sur leurs propriétés mécaniques.

En remplaçant les chaines courtes de MHDS par du Sylgard 184® à haut poids moléculaire, nous sommes capables de générer des émulsions solides avec la même formulation, mais avec un module élastique plus important et pour lesquelles les propriétés structurelles pourraient être obtenues avec le tomographe en laboratoire. La présence de gouttes liquides dans un matériau purement élastique modifie de manière importante les propriétés mécaniques du matériau par rapport à celles du PDMS pur. La taille, l'organisation et la fraction volumique des gouttes peuvent être variées pour modifier les propriétés mécaniques des émulsions solides. Le contrôle de la structure de l'émulsion et sa relation avec les propriétés mécaniques et adhésives sont l'objet des Parties B et C de ce manuscrit.

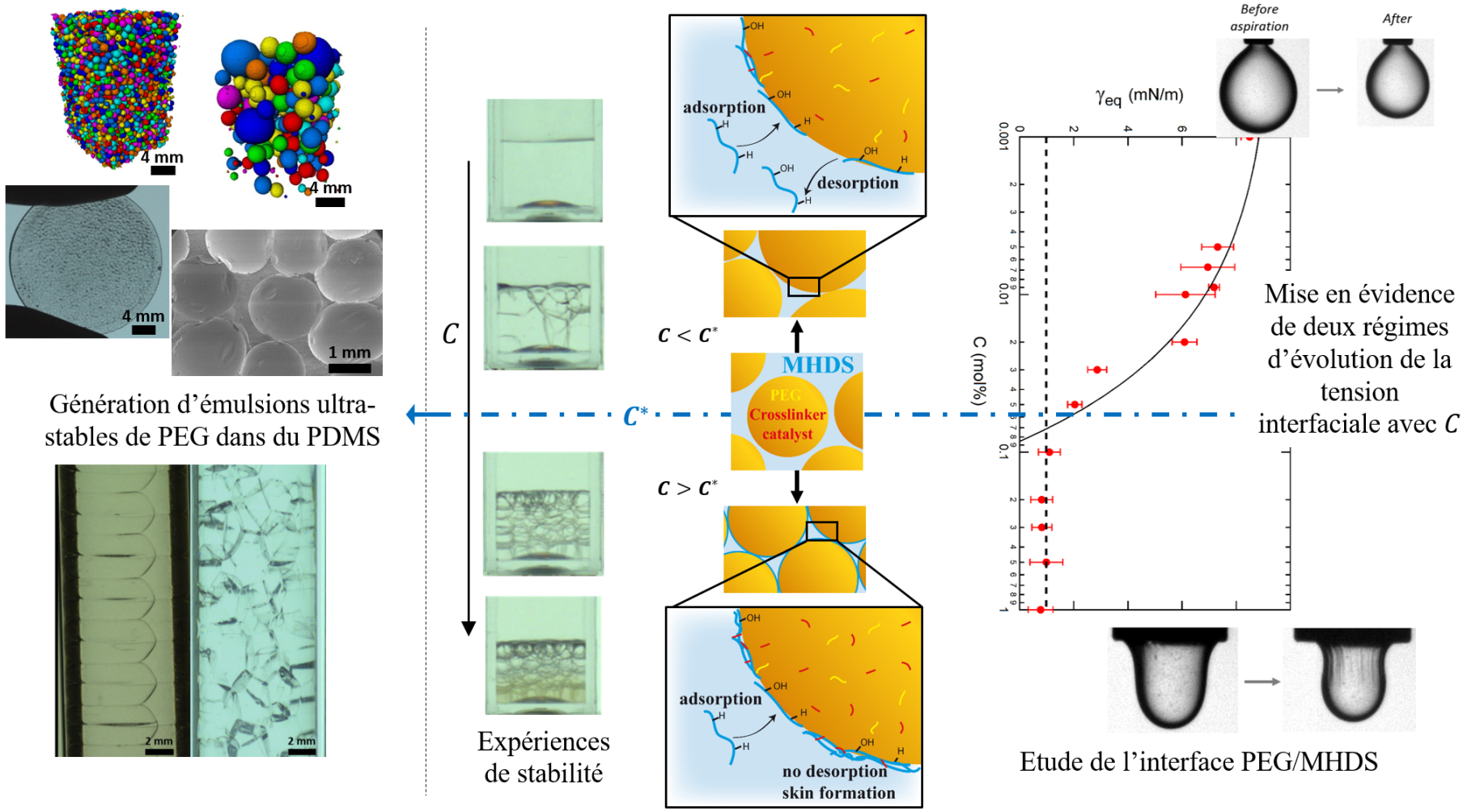

Figure 11.2: Schéma des conclusions tirées de la Partie A de ce travail de thèse.

11.2 Propriétés structurelles des émulsions de PEG dans le silicone

Dans la Partie B, nous avons présenté un nouveau type de matériau granulaire destiné à combler le vide des graphiques proposés Figure 5.11 dans le Chapitre 5. Ce système est composé de gouttes d'émulsion déformables entourées d'une peau de polymère crée par des réactions chimiques de polymérisation à l'interface avec le silicone. La présence de cette "peau" viscoélastique est responsable de l'introduction de forces normales attractives ainsi que tangentielles entre les gouttes. En changeant la concentration en solvant dans la phase continue (dodécane dans cette étude), nous avons pu faire varier l'amplitude de ces interactions entre les gouttes afin d'explorer un système qui peut être placé entre les bulles/gouttes déformables et sans friction à l'interface et les sphères dures présentant de la friction à l'interface, qui sont les deux cas extrêmes. Pour étudier ce nouveau système, nous avons analysé d'une part les interactions entre deux gouttes en contact et d'autre part la structure des empilement de gouttes grâce à la tomographie sous rayons X (Figure 11.3).

Dans le Chapitre 6, nous avons étudié les propriétés interfaciales des gouttes entourées d'une peau de polymères. La mesure de l'angle d'avalanche nous a permis de mettre en évidence la présence d'importantes forces normales attractives et tangentielles entre les gouttes. Grâce à l'expérience des "deux gouttes", nous avons étudié la séparation de deux gouttes initialement en contact en fonction de la concentration en dodécane dans la phase continue. Ceci a montré une augmentation nette des forces d'adhésion entre les gouttes en présence de dodécane. Nous avons également quantifié la relaxation vers la position d'équilibre d'une goutte en glissement sur une autre afin de sonder les forces tangentielles. De cette manière, nous avons montré qu'une augmentation de la quantité de dodécane dans la phase continue diminuait la capacité des gouttes de glisser l'une sur l'autre. Afin de comprendre l'impact de la concentration en dodécane, nous avons proposé différents mécanismes possibles. Une première explication pourrait être que l'addition de solvant gonfle la peau de polymères, rendant les chaines pendantes plus apte à s'enchevêtrer dans le réseau de polymères de l'autre goutte. Nous suggérons également que la diminution de la viscosité de la phase continue a un effet sur la lubrification lors du glissement des gouttes l'une sur l'autre. En effet, si la viscosité diminue, la lubrification entre les deux interfaces est moins performante, et l'enchevêtrement des polymères dans les peaux de chaque goutte a plus de chance de se produire. Aussi, puisque la présence de dodécane diminue la viscosité et la densité de la phase continue, la vitesse de réaction à l'interface augmente du fait de la dépendance du coefficient de diffusion des molécules en la viscosité du liquide. En augmentant le nombre de molécule ayant réagi entre deux interfaces en contact pour un temps donné, l'intensité de la force nécessaire pour les séparer augmente.

Après avoir caractérisé l'impact du dodécane sur les forces d'interaction entre les gouttes, nous avons étudié dans le Chapitre 7 les propriétés structurelles d'empilements de gouttes présentant de la friction et de l'adhésion. Nous avons démontré quelques propriétés spécifiques à ce système. Déjà, comme pour les empilements de sphères dures, les émulsions sont sensibles à la manière dont elles sont générées, comme montré par la pente présente sur le dessus de l'émulsion Figure 7.5. Ceci est une conséquence directe de la présence de fortes interactions entre les gouttes, comme pour le grand angle d'avalanche mesuré dans le Chapitre 6. Aussi, la fraction volumique de gouttes est constante avec la hauteur de l'émulsion, ce qui est généralement caractéristique des empilement de sphères dures en opposition aux gouttes d'émulsion déformables. En étudiant la distribution de la fraction volumique locale, nous avons pas pu trouver de caractéristique particulière pour les distinguer des autres systèmes.

Cependant, nous avons pu remarquer que la fraction volumique globale est faible en comparaison de la fraction volumique de sphères dures empilée de manière désorganisée et peu dense ($\Phi < \Phi_{RLP} \approx 0.54$). Nous avons pu mesurer des fractions volumiques plus faibles même que pour des systèmes de sphères dures présentant de la friction at l'interface et de l'adhésion grâce à les ponts capillaires entre les grains [269]. Cela est également très bien expliqué par la présence de fortes interactions entre les gouttes qui permettent d'obtenir une stabilité mécanique de l'empilement avec un nombre de contacts faible (en deça de l'isostaticité), c'est à dire pour une faible densité de gouttes. La fraction volumique diminue également avec l'augmentation de la quantité de dodécane dans la phase continue, ce qui corrèle bien avec l'augmentation de la force des interactions entre gouttes quand la concentration en dodécane augmente. L'analyse de l'organisation globale des gouttes grâce au calcul de la fonction de corrélation $g(r)$ a montré qu'il n'y avait aucune corrélation entre les positions des gouttes au delà des plus proches voisins, du fait de l'absence totale de pic caractéristique à $r/r_0 = 2$ et $\sqrt{2}$, qui sont normalement présents pour des organisations désorganisées de sphères dures présentant de la friction à leur interface et de gouttes déformables et sans friction à l'interface. Nous avons expliqué cela grâce à la déformation des gouttes ainsi que l'absence d'une séparation claire entre les gouttes. Enfin, nous avons remarqué la présence de chaines de force dans les émulsions, ce qui n'est pas observé dans les matériaux granulaires si une pression n'est pas appliquée. La fonction de corrélation plate après $r/r_0 = 1$ ainsi que la présence de chaines de force sont donc caractéristiques de l'empilement des gouttes déformables présentant de la friction et de l'adhésion à leur surface.

Plusieurs aspects nécessitent plus d'études. Des expériences plus systématiques seront nécessaires pour comprendre pleinement et contrôler les forces d'interaction entre les gouttes, pour lesquelles le contrôle de l'épaisseur de la peau de polymères serait d'une grande importance. Pour cela, la réaction à l'interface pourrait être stoppée, par example en remplaçant la phase continue par un PDMS non réactif après un temps de stabilisation donné. Aussi, changer le solvant dans la phase continue pourrait être une autre manière de varier les interactions entre les gouttes. Enfin, nous n'avons ici pas été capable de mesurer le nombre moyen de contacts $\langle z \rangle$ entre les gouttes du fait de l'incapacité de la tomographie sous rayons X de différencier la peau de polymère à la surface des gouttes de la phase continue. Une manière de compter les contacts pourrait être de corréler les déformations d'une goutte avec la position de ses plus proches voisins.

Dans le Chapitre 4, nous avons fait remarqué que nous n'avions pas été capables d'imager les émulsions avec une fraction volumique de gouttes élevée obtenues avec le MHDS de poids moléculaire faible avec la tomographie sous rayons X en laboratoire à cause de sa faible résolution. L'utilisation d'une ligne de synchrotron avec une meilleure résolution a démontré que nous pouvions imager ces émulsions (Figure 4.6 dan le Chapitre 4), ce qui est prometteur pour l'étude de la topologie des émulsions à haute fraction volumique présentant de la friction et de l'adhésion à l'interface.

D'une manière générale, nous avons pu montrer que les émulsions présentant de la friction et de l'adhésion à leur surface ont des propriétés intéressantes en comparaison avec les systèmes plus traditionnels (gouttes sans friction ou adhésion à l'interface et sphères dures présentant de la friction à l'interface). Il sera intéressant à l'avenir de proposer des systèmes qui permettent un contrôle indépendant de l'élasticité de la peau, ainsi que de la friction et de l'adhésion entre les gouttes.

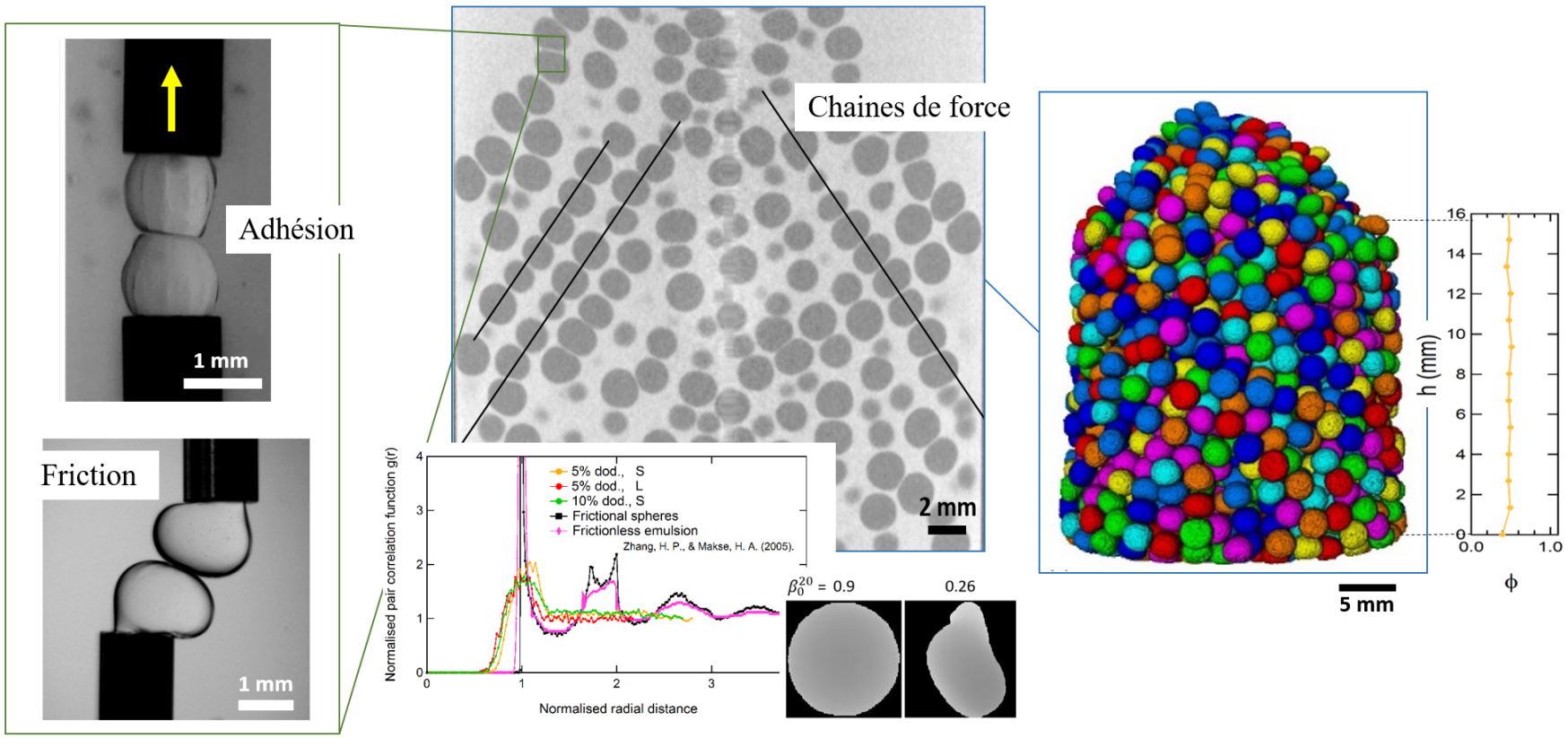

Mise en evidence de forces tangentielles et normales attractives entre les gouttes

Etude des propriétés structurelles des empilements de gouttes

Emulsions de PEG dans du silicone stabilisées par une peau de polymères

Figure 11.3: Conclusions drawn from Part B of this manuscript.

11.3 Propriétés mécaniques et adhésives des émulsions solides de PEG dans le silicone

Suite à l'étude de Majumder *et al.* [10] qui ont montré l'impact des propriétés de structure sur les propriétés adhésives d'un film de PDMS avec une substructure 2D faite d'inclusions liquides, nous avons dédié la Partie C à l'étude de l'impact des propriétés de structure d'émulsions solides, composées de gouttes liquides dans une matrice élastomère solide, sur leur propriétés mécaniques et adhésives (Figure 11.4). Avec les émulsions solides, nous avons donc présenté une version en 3D du système de Majumder *et al.*, qui montre des améliorations similaires des propriétés adhésives et dont la génération est plus simple.

Dans le Chapitre 9, nous avons étudié les propriétés rhéologiques et élastiques des émulsions solides. Dans un premier temps, nous avons mesuré la réponse des émulsions solides à des oscillations tout en augmentant le nombre de gouttes N dans le volume, et nous avons montré que les modules de conservation $\mathcal{G}'$ et de perte $\mathcal{G}''$ diminuaient avec N, quand leur ratio restait constant, ce qui indique que l'on ne sonde que la réponse de la matrice élastomère avec cette méthode. Ceci est raisonnable puisque les valeurs de $\mathcal{G}'$ et $\mathcal{G}''$ pour le PEG sont plusieurs ordres de grandeur en deçà de celles du PDMS réticulé. Ensuite, nous avons étudié l'impact du rayon moyen des gouttes $\langle R \rangle$ sur le module d'Young des émulsions solides en gardant la fraction volumique de gouttes et le ratio de la hauteur de gouttes sur la hauteur de l'échantillon h/h_s constant, grâce à un test de probe-tack. Nous avons pu montrer que le module d'Young ne dépend pas de la talle des gouttes, et nous faisons l'hypothèse que cela est dû à l'incompressibilité du liquide. Nous avons comparé nos résultats avec les modèles théoriques développés par Style *et al.* [9] pour de faibles fraction volumiques d'inclusions liquides dans un solide complaisant, mais ce modèle surestime grandement nos résultats expérimentaux. Un modèle développé par Heitkam *et al.* [4] pour des mousses solides a donné des prédictions qui capturent mieux nos résultats, ce qui est toutefois surprenant du fait de l'incompressibilité des gouttes.

Le Chapitre 10 était dédié à l'étude des propriétés adhésives des émulsions solides. Nous avons gardé constant le ratio de la hauteur de gouttes sur la hauteur de l'échantillon h/h_s, et nous avons regardé l'impact de la variation du rayon des gouttes. Dans un premier temps, nous avons mesuré l'évolution du taux de restitution de l'énergie G en conditions quasi-statiques avec une expérience JKR, et nous avons montré que G diminuait en présence de gouttes dans le volume du PDMS, ce que nous avons attribué à la diminution de la quantité de PDMS dans le volume de l'échantillon. Nous avons rescalé G en utilisant la densité de la cross-section de l'échantillon, et le taux de restitution de l'énergie rescalé G_{eff} augmentait en présence de gouttes dans le volume. Nous avons interprété cela comme le résultat de l'amplitude de l'énergie dissipée qui augmente quand l'épaisseur du matériau élastique diminue. Nous avons ensuite sondé les propriétés adhésives en conditions dynamiques avec un test de probe-tack. Nous avons montré que nous étions capable d'améliorer l'adhésion des émulsions jusqu'à un facteur 20 par rapport à l'adhésion du PDMS réticulé en variant le rayon des gouttes tout en gardant constant le ratio h/h_s. Nous avons expliqué cet effet par la compétition entre les dissipations d'énergie d'origine visqueuses et élastiques dans le volume des échantillons. Nous avons également montré que la présence de gouttes impliquait une dépendance en vitesse des dissipations d'énergie différente de pour le PDMS réticulé.

Cette étude n'est cependant pas complète, et nous suggérons ici une liste non-exhaustive d'expériences complémentaires qui permettraient une meilleure compréhension des propriétés des émulsions solides.

Une première expérience serait de varier la viscosité des gouttes. En effet, en choisissant un liquide avec des valeurs de $\mathcal{G}'$ et $\mathcal{G}''$ plus élevées pourrait d'une part rendre possible la détection de la réponse des gouttes lors des expériences de rhéologie, et d'autre part permettre de varier les propriétés adhésives. En effet, Majumder *et al.* [10] ont montré que la viscosité du liquide dans les inclusions 2D avait un impact non monotone sur la valeur du taux de restitution de l'énergie G (Figure 8.14d dans le Chapitre 8). La viscosité des gouttes pourrait également changer la dépendance en vitesse de G.

Comme nous l'avions discuté dans la Section 9.4.2 du Chapitre 9, nous n'avons pas été capable dans cette étude de varier la fraction volumique de gouttes Φ des échantillons. La valeur de Φ devrait impacter de manière significative les propriétés mécaniques et adhésives des émulsions solides, et des expériences explorant l'intégralité de la gamme de Φ pourrait d'une part permettre de comprendre pourquoi nous mesurons des valeurs du module d'Young si basses par rapport au modèle de Style *et al.* [9], et d'autre part d'avoir un autre paramètre pour moduler les propriétés adhésives. Pour obtenir différentes valeurs de Φ, nous avons discuté que la manière dont nous avons généré ces échantillons devrait être reconsidérée, puisqu'elle ne permettait pas d'obtenir de d'importantes forces d'intéractions entre les gouttes, comme nous l'avions discuté en Partie B. Nous avions aussi suggéré dan le Chapitre 6 l'utilisation d'un solvant différent dans la phase continue pour changer la force de ces interactions. Ceci devrait également être étudié.

Pour finir, les propriétés adhésives des matériaux cellulaires présentés dans la Section 8.3.2 du Chapitre 8 ont été systématiquement expliquées par la variation de la complaisance du matériau en fonction de la position du front de décollement. Dans ces cas 2D, les variations étaient effectivement importantes entre une position juste au dessus d'une inclusion et une position au dessus du matériau en volume. Bien que nous ne nous attendions pas à des variations si importantes de la complaisance du matériau en fonction de la position dans notre cas du fait que les gouttes s'empilent de manière désorganisée, il serait tout de même intéressant de les mesurer grâce à un micro-indenteur. Nous pourrions alors être en mesure de commenter sur les dissipations d'énergie liées à la propagation du front de décollement.

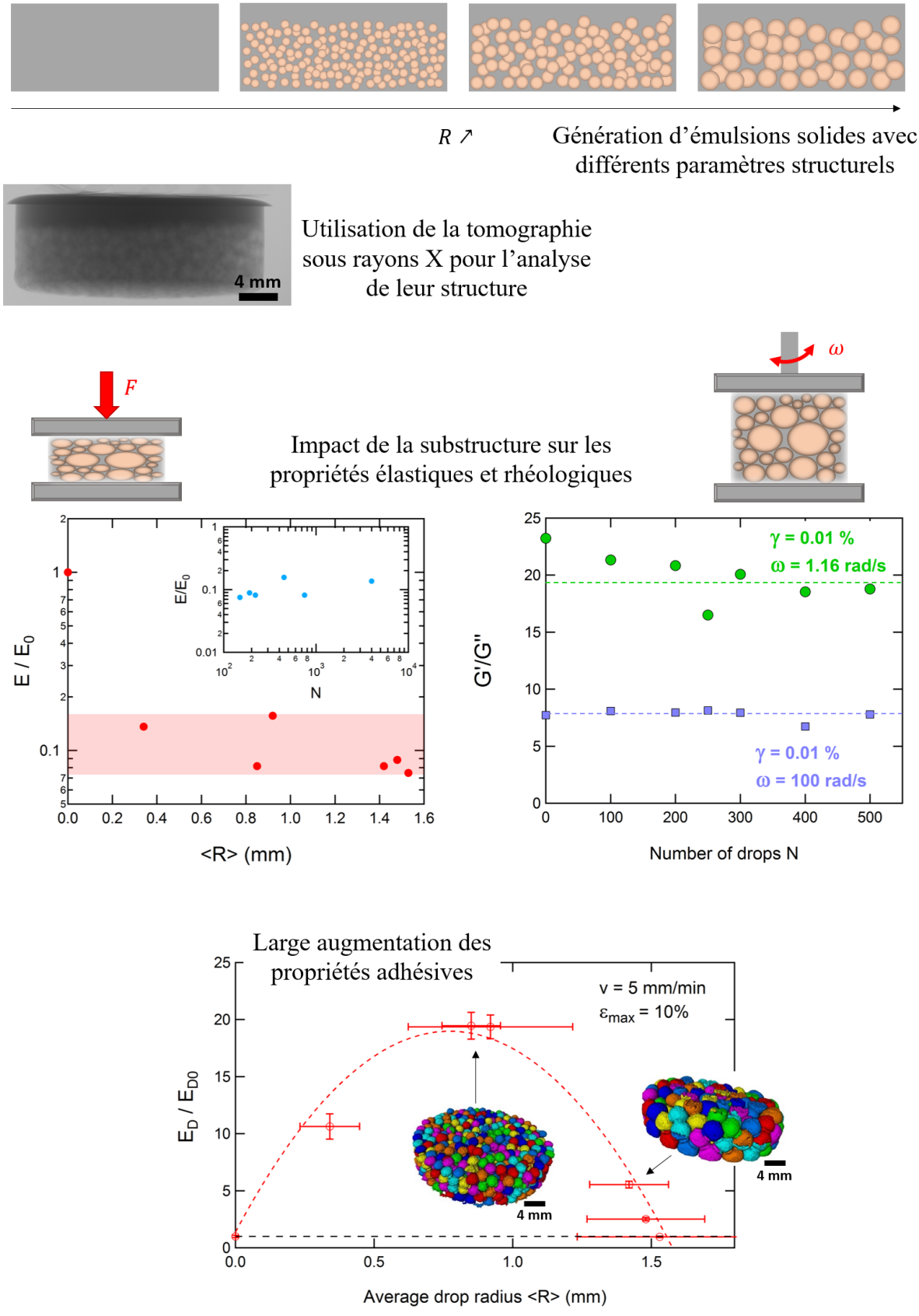

Figure 11.4: Conclusions drawn from Part C of this manuscript.

11.4 Conclusion générale

Ce travail de thèse a été effectué dans le cadre de l'ERC Pomcaps, qui a pour but la génération de matériaux poreux aux propriétés structurelles et de surface bien contrôlées. Ici, nous nous sommes concentrés sur la génération d'émulsions liquides et solides, et sur le lien entre leur structure et leurs propriétés mécaniques et adhésives. Les trois parties de ce manuscrit avaient pour but (1) de développer des émulsions ultra-stable de silicone avec des tailles contrôlées (Partie A), (2) de caractériser leurs propriétés structurelles dans leur état liquide (Partie B) et (3) d'étudier leurs propriétés mécaniques et adhésives après solidification (Partie C).

Dans la Partie A, nous avons traité la problématique de la stabilisation d'émulsions dont la phase continue est du silicone. Puisqu'il n'existe pas de tensioactifs suffisamment efficaces pour stabiliser ces émulsions, nous avons choisi d'utiliser un processus de stabilisation réactive, qui crée des tensioactifs et une peu de polymères *in-situ* à l'interface grâce à des réactions chimiques. Nous avons montré qu'en utilisant un complexe crosslinker/catalyseur dissout dans la phase dispersée (ici le PEG), et un PDMS réactif (MHDS), nous pouvions créer des copolymères PDMS-b-PEG à l'interface et de réticuler l'interface en même temps (avec toutefois des temps caractéristiques différents pour chaque réaction). Ceci a permis de totalement inhiber la coalescence entre les gouttes pour une concentration en crosslinker/catalyseur au delà d'une concentration critique. Nous avons sondé l'évolution des réactions chimiques à l'interface en mesurant la tension interfaciale entre le PEG et le MHDS pour différentes concentrations en crosslinker/catalyseur. Nous avons mis en évidence un changement caractéristique dans son comportement à l'équilibre et pendant l'évolution pour une concentration qui coïncide avec la stabilité des émulsions. Nous avons associé ce changement avec la formation d'une peau de polymères à la surface des gouttes. Grâce à ce résultat, nous avons pu adapter la formulation pour choisir la concentration en crosslinker/catalyseur optimale pour la génération d'émulsions de silicone ultra-stables.

Après avoir optimisé la formulation des émulsions, nous avons montré qu'en utilisant différentes techniques de génération nous pouvions générer des émulsions liquides avec des tailles de gouttes contrôlées, de 300 µm jusqu'à 1.5 mm de rayon. Nous avons également démontré que nous pouvions solidifier la phase continue des émulsions en ajoutant avant la génération un agent réticulant dans la phase continue, et qu'en changeant le poids moléculaire du MHDS nous pouvions obtenir des matériaux de modules élastiques différents. Nous avons donc obtenu ce que nous appelons dans ce manuscrit des "émulsions solides", composées de gouttes liquides dans une matrice solide. En changeant le liquide des gouttes (PEG) par un liquide volatile (mais toujours hydrophile), nous avons également pu générer des mousses solides avec des tailles de pores contrôlées. En utilisant la tomographie aux rayons X et la Microscopie à Balayage Electronique, nous avons montré que si les émulsions solides de PEG dans le PDMS avaient systématiquement des cellules fermées, les mousses solides générées en utilisant de l'eau pour la phase dispersée présentaient des cellules ouvertes. Nous avons interprété ceci comme le résultat de l'absence des copolymères PDMS-b-PEG à l'interface entre l'eau et le MHDS, ce qui rendrait les films entre les gouttes plus fragiles.

Dans le reste de l'étude, nous nous sommes concentrés sur le lien entre la structure et les propriétés mécaniques et adhésives des émulsions solides. Nous avons choisi d'utiliser le Sylgard 184® comme phase continue, qui a un module élastique élevé et donc résiste aux déformations. Puisque la structure

d'un matériau solide est la signature d'un état initial liquide, nous avons analysé dans la Partie B des émulsions liquides de PEG dans le Sylgard 184®, pour lesquelles nous n'avons pas ajouté l'agent réticulant dans la phase continue. Dans un premier temps, nous avons caractérisé les intéractions entre deux gouttes de PEG contenant une concentration C en crosslinker/catalyseur dans la phase continue, dans laquelle nous avons ajouté 0%, 5% ou 10% de dodécane. Nous avons montré que la présence d'une peau de polymère à la surface des gouttes, du fait du processus de stabilisation des émulsions, couplée à l'addition de dodécane dans la phase continue, permettait de varier significativement l'amplitude de ce que nous interprétons comme des forces d'adhésion et de friction entre les gouttes. Ensuite, nous avons montré que dans les émulsions les gouttes ne s'organisent pas dans le volume comme elles le font dans des émulsions stabilisées par ajout de tensioactifs. Au contraire, nous avons montré qu'elles s'organise plutôt comme un empilement de sphères dures puisque la fraction volumique de gouttes est constante avec la hauteur de l'émulsion. Nous avons pu souligner quelques différences avec les empilements de sphères dures, comme par exemple l'absence de correlation entre les positions des gouttes les unes par rapport aux autres, que nous avons attribué en partie à la déformabilité des gouttes.

Nous avons donc fourni quelques premières réponses à la question de comment le processus de stabilisation, dans notre cas la création d'une peau de polymère à la surface des gouttes, impacte l'organisation des gouttes dans les émulsions liquides, et nous avons proposé une comparaison directe avec des systèmes proches du notre, les émulsions stabilisées par ajout de tensioactifs, et d'autres systèmes qui semblent très différents mais partage des propriétés communes, les empilements de sphères dures. Nous avons également présenté pour la première fois des émulsions présentant des forces de friction entre les gouttes.

Après avoir étudié les propriétés structurelles des émulsions liquides, nous avons étudié comment les propriétés mécaniques et adhésives des émulsions solides dépendent du nombre de gouttes, de leur organisation et de leur taille, en conduisant des expériences de mécanique du contact et de rhéologie des solides. Nous avons montré que le ratio du module de conservation sur le module de perte ne dépendait pas du nombre de gouttes dans le volume, ce que nous avons interprété comme le fait que la présence de goutte ne change pas les propriétés viscoélastiques du matériau. Nous avons ensuite montré que le module élastique était constant avec la taille des gouttes pour des échantillons avec un même ratio de hauteur de l'émulsion sur hauteur de l'échantillon h/h_s, ce que nous avons interprété comme une conséquence de l'incompréssibilité des gouttes. Nos résultats expérimentaux ne suivent pas la prédiction théorique du module élastique de matériaux comportant des inclusions liquides dans leur volume développée par Style *et al.* [9], bien qu'ils soient proches des résultats du modèle développé pour les mousses solides par Heitkam *et al.* [4]. Nous avons ensuite étudié les propriétés adhésives des émulsions solides en gardant constante la fraction volumique de gouttes. Nous avons montré que, pour une vitesse de traction de l'indenteur constante, la taille des gouttes avait une influence significative sur la valeur de l'énergie dissipée (jusqu'à un facteur 20 par rapport au PDMS réticulé seul). Nous avons également mesuré l'impact de la vitesse de traction, et avons montré que la présence de gouttes dans le volume changeait la loi de puissance associée à l'évolution du taux de restitution de l'énergie avec la vitesse.

Ceci a permis de comprendre le lien entre la structure des émulsions solides et leurs propriétés mécaniques et adhésives. La présence de gouttes dans le volume a un fort impact sur les propriétés adhésives des matériaux, et bien que cela ait été démontré par Majumder *et al.* [10] pour des systèmes

2D, nous proposons ici un système 3D, qui de plus nécessite bien moins d'étapes à sa fabrication tout en montrant une efficacité similaire.

Bien que les Parties B et C présentaient des résultats préliminaires, elles permettent toutefois de clairement montrer que les émulsions stabilisées grâce à une peau de polymère sont des objets extrêmement intéressants à étudier. Elles ont le potentiel de fournir des objets déformables avec des propriétés interfaciales modulables, qui pourraient à l'avenir permettre de lier plus solidement les interactions entre les gouttes déformables et leur organisation dans des empilements denses. De plus, leur très grande stabilité en font d'excellentes candidates pour leur solidification et donc pour la génération de matériaux biphasiques avec des propriétés viscoélastiques modulables. Pour l'étude de la structure des émulsions, nous avons besoin de conduire des expériences plus systématiques pour caractériser les interactions entre les gouttes, tandis que l'étude des propriétés mécaniques et adhésives des émulsions solides serait plus complète avec des expériences faisant varier la viscosité des gouttes ainsi que leur fraction volumique. Ceci sera l'objet d'études approfondies dans un futur proche.

Bibliography

[1] Armando Maestro, Wiebke Drenckhan, Emmanuelle Rio, and Reinhard Höhler. Liquid dispersions under gravity: volume fraction profile and osmotic pressure. *Soft Matter*, 9(8):2531–2540, 2013.

[2] Wiebke Drenckhan and Arnaud Saint-Jalmes. The science of foaming. *Advances in colloid and interface science*, 222:228–259, 2015.

[3] HM Princen. Osmotic pressure of foams and highly concentrated emulsions. i. theoretical considerations. *Langmuir*, 2(4):519–524, 1986.

[4] Sascha Heitkam, Wiebke Drenckhan, Thomas Titscher, Denis Weaire, Daniel Christopher Kreuter, David Hajnal, Frederic Piechon, and Jochen Fröhlich. Elastic properties of solid material with various arrangements of spherical voids. *European Journal of Mechanics-A/Solids*, 59:252–264, 2016.

[5] D Weaire and MA Fortes. Stress and strain in liquid and solid foams. *Advances in Physics*, 43(6):685–738, 1994.

[6] Lorna J Gibson and Michael F Ashby. *Cellular solids: structure and properties*. Cambridge university press, 1999.

[7] Lorna J Gibson and Michael F Ashby. The mechanics of three-dimensional cellular materials. In *Proceedings of the Royal Society of London A: Mathematical, Physical and Engineering Sciences*, volume 382, pages 43–59. The Royal Society, 1982.

[8] AN Gent and A Gr Thomas. The deformation of foamed elastic materials. *Journal of Applied Polymer Science*, 1(1):107–113, 1959.

[9] Robert W Style, Rostislav Boltyanskiy, Benjamin Allen, Katharine E Jensen, Henry P Foote, John S Wettlaufer, and Eric R Dufresne. Stiffening solids with liquid inclusions. *Nature Physics*, 11(1):82–87, 2015.

[10] Abhijit Majumder, Animangsu Ghatak, and Ashutosh Sharma. Microfluidic adhesion induced by subsurface microstructures. *Science*, 318(5848):258–261, 2007.

[11] WL Noderer, L Shen, S Vajpayee, NJ Glassmaker, A Jagota, and C-Y Hui. Enhanced adhesion and compliance of film-terminated fibrillar surfaces. In *Proceedings of the Royal Society of London A: Mathematical, Physical and Engineering Sciences*, volume 463, pages 2631–2654. The Royal Society, 2007.

[12] Denisse Ortiz-Acosta and Crystal Densmore. Sylgard® cure inhibition characterization. *Los Alamos National Laboratory (LANL)*, 2012.

[13] LT Canham, MR Houlton, WY Leong, C Pickering, and JM Keen. Atmospheric impregnation of porous silicon at room temperature. *Journal of Applied Physics*, 70(1):422–431, 1991.

[14] Laëtitia Dies-Diverchy. *Influence d'une texturation déformable sur l'adhésion et la friction.* PhD thesis, Paris 11, 2015.

[15] BD Mistry. A handbook of spectroscopic data. In *Chemistry (UV, IR, PMR, CNMR and Mass Spectroscopy)*. Oxford Book Company, 2009.

[16] Uttandaraman Sundararaj, CW Macosko, et al. Drop breakup and coalescence in polymer blends-the effects of concentration and compatibilization. *Macromolecules*, 28(8):2647–2657, 1995.

[17] Je Kyun Lee and Chang Dae Han. Evolution of polymer blend morphology during compounding in an internal mixer. *Polymer*, 40(23):6277–6296, 1999.

[18] T Tate. On the magnitude of a drop of liquid formed under different circumstances. *The London, Edinburgh, and Dublin Philosophical Magazine and Journal of Science*, 27(181):176–180, 1864.

[19] Arthur W Adamson, Alice Petry Gast, et al. Physical chemistry of surfaces. 1967.

[20] R Kumar and NK Kuloor. The formation of bubbles and drops. *Advances in chemical engineering*, 8:255–368, 1970.

[21] Shelley L Anna, Nathalie Bontoux, and Howard A Stone. Formation of dispersions using "flow focusing" in microchannels. *Applied physics letters*, 82(3):364–366, 2003.

[22] Piotr Garstecki, Irina Gitlin, Willow DiLuzio, George M Whitesides, Eugenia Kumacheva, and Howard A Stone. Formation of monodisperse bubbles in a microfluidic flow-focusing device. *Applied Physics Letters*, 85(13):2649–2651, 2004.

[23] P Garstecki, AM Ganan-Calvo, and GM Whitesides. Formation of bubbles and droplets in microfluidic systems. *Technical sciences*, 53(4), 2005.

[24] Claudiu A Stan, Sindy KY Tang, and George M Whitesides. Independent control of drop size and velocity in microfluidic flow-focusing generators using variable temperature and flow rate. *Analytical chemistry*, 81(6):2399–2402, 2009.

[25] Y Rotenberg, Lr Boruvka, and AW Neumann. Determination of surface tension and contact angle from the shapes of axisymmetric fluid interfaces. *Journal of colloid and interface science*, 93(1):169–183, 1983.

[26] Francesca Ravera, Giuseppe Loglio, and Volodymyr I Kovalchuk. Interfacial dilational rheology by oscillating bubble/drop methods. *Current Opinion in Colloid & Interface Science*, 15(4):217–228, 2010.

[27] R Stanimirova, K Marinova, S Tcholakova, ND Denkov, S Stoyanov, and E Pelan. Surface rheology of saponin adsorption layers. *Langmuir*, 27(20):12486–12498, 2011.

[28] José Baruchel, Jean-Yves Buffiere, and Eric Maire. X-ray tomography in material science. 2000.

[29] Julia Nase. *Debonding of Viscoelastic Materials: From a Viscous Liquid to a Soft Elastic Solid.* Theses, Université Pierre et Marie Curie - Paris VI, September 2009.

[30] CJ Beverung, CJ Radke, and HW Blanch. Protein adsorption at the oil/water interface: characterization of adsorption kinetics by dynamic interfacial tension measurements. *Biophysical chemistry*, 81(1):59–80, 1999.

[31] D Exerowa, NV Churaev, T Kolarov, NE Esipova, N Panchev, and ZM Zorin. Foam and wetting films: electrostatic and steric stabilization. *Advances in colloid and interface science*, 104(1):1–24, 2003.

[32] D Varade, D Carriere, LR Arriaga, A-L Fameau, E Rio, D Langevin, and W Drenckhan. On the origin of the stability of foams made from catanionic surfactant mixtures. *Soft Matter*, 7(14):6557–6570, 2011.

[33] Srinivasan Damodaran. Protein stabilization of emulsions and foams. *Journal of Food Science*, 70(3), 2005.

[34] Aggeliki Quell, Jonas Elsing, Wiebke Drenckhan, and Cosima Stubenrauch. Monodisperse polystyrene foams via microfluidics–a novel templating route. *Advanced Engineering Materials*, 17(5):604–609, 2015.

[35] Antje van der Net, Alexander Gryson, Meik Ranft, Florence Elias, Cosima Stubenrauch, and Wiebke Drenckhan. Highly structured porous solids from liquid foam templates. *Colloids and Surfaces A: Physicochemical and Engineering Aspects*, 346(1):5–10, 2009.

[36] Irena Pulko and Peter Krajnc. High internal phase emulsion templating–a path to hierarchically porous functional polymers. *Macromolecular rapid communications*, 33(20):1731–1746, 2012.

[37] Michael Tebboth, Qixiang Jiang, Andreas Kogelbauer, and Alexander Bismarck. Inflatable elastomeric macroporous polymers synthesized from medium internal phase emulsion templates. *ACS applied materials & interfaces*, 7(34):19243–19250, 2015.

[38] Marie-Thérèse Grosse, Michel Lamotte, Marc Birot, and Hervé Deleuze. Preparation of microcellular polysiloxane monoliths. *Journal of Polymer Science Part A: Polymer Chemistry*, 46(1):21–32, 2008.

[39] Cor Koning, Martin Van Duin, Christophe Pagnoulle, and Robert Jerome. Strategies for compatibilization of polymer blends. *Progress in Polymer Science*, 23(4):707–757, 1998.

[40] Patrice Lucas and Jean-Jacques Robin. Silicone-based polymer blends: an overview of the materials and processes. In *Functional Materials and Biomaterials*, pages 111–147. Springer, 2007.

[41] Yuewen Xu, Jesse Loi, Paula Delgado, Vasily Topolkaraev, Ryan J McEneany, Christopher W Macosko, and Marc A Hillmyer. Reactive compatibilization of polylactide/polypropylene blends. *Industrial & Engineering Chemistry Research*, 54(23):6108–6114, 2015.

[42] Michael S Silverstein. Polyhipes: Recent advances in emulsion-templated porous polymers. *progress in Polymer Science*, 39(1):199–234, 2014.

[43] Neil R Cameron. High internal phase emulsion templating as a route to well-defined porous polymers. *Polymer*, 46(5):1439–1449, 2005.

[44] Jianbin Zhang, Timothy P Lodge, and Christopher W Macosko. Interfacial morphology development during ps/pmma reactive coupling. *Macromolecules*, 38(15):6586–6591, 2005.

[45] Andrea Barbetta, Neil R Cameron, and Sharon J Cooper. High internal phase emulsions (hipes) containing divinylbenzene and 4-vinylbenzyl chloride and the morphology of the resulting polyhipe materials. *Chemical Communications*, (3):221–222, 2000.

[46] G Ceglia, Laurent Mahéo, Philippe Viot, Dominique Bernard, Ali Chirazi, Isabelle Ly, Olivier Mondain-Monval, and Véronique Schmitt. Formulation and mechanical properties of emulsion-based model polymer foams. *The European Physical Journal E*, 35(4):1–11, 2012.

[47] A Imhof and DJ Pine. Ordered macroporous materials by emulsion templating. *Nature*, 389(6654):948–951, 1997.

[48] Ludwik Leibler. Block copolymers at interfaces. *Physica A: Statistical Mechanics and its Applications*, 172(1-2):258–268, 1991.

[49] Jérome Bibette and Fernando Leal-Calderon. Surfactant-stabilized emulsions. *Current Opinion in Colloid & Interface Science*, 1(6):746–751, 1996.

[50] J Eastoe and JS Dalton. Dynamic surface tension and adsorption mechanisms of surfactants at the air–water interface. *Advances in colloid and interface science*, 85(2):103–144, 2000.

[51] Francesca Ravera, Michele Ferrari, Eva Santini, and Libero Liggieri. Influence of surface processes on the dilational visco-elasticity of surfactant solutions. *Advances in colloid and interface science*, 117(1):75–100, 2005.

[52] James Goodwin. *Colloids and interfaces with surfactants and polymers*. John Wiley & Sons, 2009.

[53] Spiros H Anastasiadis. Interfacial tension in binary polymer blends and the effects of copolymers as emulsifying agents. In *Polymer Thermodynamics*, pages 179–269. Springer, 2010.

[54] Yunfei He, Pavel Yazhgur, Anniina Salonen, and Dominique Langevin. Adsorption–desorption kinetics of surfactants at liquid surfaces. *Advances in colloid and interface science*, 222:377–384, 2015.

[55] NC Liu and WE Baker. Reactive polymers for blend compatibilization. *Advances in Polymer Technology*, 11(4):249–262, 1992.

[56] Leszek A Utracki and Charles A Wilkie. *Polymer blends handbook*, volume 1. Springer, 2002.

[57] Christopher W Macosko, Hyun K Jeon, and Thomas R Hoye. Reactions at polymer–polymer interfaces for blend compatibilization. *Progress in Polymer Science*, 30(8):939–947, 2005.

[58] Arkady D Litmanovich, Nicolai A Platé, and Yaroslav V Kudryavtsev. Reactions in polymer blends: interchain effects and theoretical problems. *Progress in polymer science*, 27(5):915–970, 2002.

[59] Pierre-Gilles De Gennes, Françoise Brochard-Wyart, and David Quéré. *Capillarity and wetting phenomena: drops, bubbles, pearls, waves*. Springer Science & Business Media, 2013.

[60] A Wilhelm Neumann, Robert David, and Yi Zuo. *Applied surface thermodynamics*, volume 151. CRC press, 2010.

[61] Ganesan Narsimhan and Parul Goel. Drop coalescence during emulsion formation in a high-pressure homogenizer for tetradecane-in-water emulsion stabilized by sodium dodecyl sulfate. *Journal of colloid and interface science*, 238(2):420–432, 2001.

[62] Enda Carey and Cosima Stubenrauch. Foaming properties of mixtures of a non-ionic (c 12 dmpo) and an ionic surfactant (c 12 tab). *Journal of colloid and interface science*, 346(2):414–423, 2010.

[63] Eric Dickinson and Esra Izgi. Foam stabilization by protein-polysaccharide complexes. *Colloids and Surfaces A: Physicochemical and Engineering Aspects*, 113(1-2):191–201, 1996.

[64] I Aravind, P Albert, C Ranganathaiah, JV Kurian, and S Thomas. Compatibilizing effect of epm-g-ma in epdm/poly (trimethylene terephthalate) incompatible blends. *Polymer*, 45(14):4925–4937, 2004.

[65] Uttandaraman Sundararaj, CW Macosko, et al. Drop breakup and coalescence in polymer blends-the effects of concentration and compatibilization. *Macromolecules*, 28(8):2647–2657, 1995.

[66] Ludwik Leibler. Emulsifying effects of block copolymers in incompatible polymer blends. In *Macromolecular Symposia*, volume 16, pages 1–17. Wiley Online Library, 1988.

[67] Bernard P Binks. Particles as surfactants—similarities and differences. *Current opinion in colloid & interface science*, 7(1):21–41, 2002.

[68] K Golemanov, S Tcholakova, PA Kralchevsky, KP Ananthapadmanabhan, and A Lips. Latex-particle-stabilized emulsions of anti-bancroft type. *Langmuir*, 22(11):4968–4977, 2006.

[69] Urs T Gonzenbach, André R Studart, Elena Tervoort, and Ludwig J Gauckler. Ultrastable particle-stabilized foams. *Angewandte Chemie International Edition*, 45(21):3526–3530, 2006.

[70] Eric Dickinson. Food emulsions and foams: stabilization by particles. *Current Opinion in Colloid & Interface Science*, 15(1):40–49, 2010.

[71] Urs T Gonzenbach, André R Studart, Elena Tervoort, and Ludwig J Gauckler. Stabilization of foams with inorganic colloidal particles. *Langmuir*, 22(26):10983–10988, 2006.

[72] Timothy N Hunter, Robert J Pugh, George V Franks, and Graeme J Jameson. The role of particles in stabilising foams and emulsions. *Advances in Colloid and Interface Science*, 137(2):57–81, 2008.

[73] Rossitza G Alargova, Devdutta S Warhadpande, Vesselin N Paunov, and Orlin D Velev. Foam superstabilization by polymer microrods. *Langmuir*, 20(24):10371–10374, 2004.

[74] AFH Ward and L Tordai. Time-dependence of boundary tensions of solutions i. the role of diffusion in time-effects. *The Journal of Chemical Physics*, 14(7):453–461, 1946.

[75] Charles M Blair Jr. Time-dependence of surface tension of solutions. *The Journal of Chemical Physics*, 16(2):113–116, 1948.

[76] DJ Cooke, JR Lu, EM Lee, RK Thomas, AR Pitt, EA Simister, and J Penfold. Neutron reflection study of a double-chained sugar surfactant. *The Journal of Physical Chemistry*, 100(24):10298–10303, 1996.

[77] JR Lu, EM Lee, RK Thomas, J Penfold, and SL Flitsch. Direct determination by neutron reflection of the structure of triethylene glycol monododecyl ether layers at the air/water interface. *Langmuir*, 9(5):1352–1360, 1993.

[78] JR Lu, ZX Li, RK Thomas, EJ Staples, I Tucker, and J Penfold. Neutron reflection from a layer of monododecyl hexaethylene glycol adsorbed at the air-liquid interface: The configuration of the ethylene glycol chain. *Journal of physical chemistry*, 97(30):8012–8020, 1993.

[79] JR Lu, TJ Su, ZX Li, RK Thomas, EJ Staples, I Tucker, and J Penfold. Structure of monolayers of monododecyl dodecaethylene glycol at the air- water interface studied by neutron reflection. *The Journal of Physical Chemistry B*, 101(49):10332–10339, 1997.

[80] Julian Eastoe, James S Dalton, Philippe GA Rogueda, Esther R Crooks, Alan R Pitt, and Elizabeth A Simister. Dynamic surface tensions of nonionic surfactant solutions. *Journal of colloid and interface science*, 188(2):423–430, 1997.

[81] Pei Xun Li, Zhi Xin Li, Hsin-Hui Shen, Robert K Thomas, Jeffrey Penfold, and Jian Ren Lu. Application of the gibbs equation to the adsorption of nonionic surfactants and polymers at the air–water interface: comparison with surface excesses determined directly using neutron reflectivity. *Langmuir*, 29(30):9324–9334, 2013.

[82] Kazuo Tajima, Mitsuo Muramatsu, and Tsunetaka Sasaki. Radiotracer studies on adsorption of surface active substance at aqueous surface. i. accurate measurement of adsorption of tritiated sodium dodecylsulfate. *Bulletin of the Chemical Society of Japan*, 43(7):1991–1998, 1970.

[83] SW An, JR Lu, RK Thomas, and J Penfold. Apparent anomalies in surface excesses determined from neutron reflection and the gibbs equation in anionic surfactants with particular reference to perfluorooctanoates at the air/water interface. *Langmuir*, 12(10):2446–2453, 1996.

[84] Denver G Hall, Brian A Pethica, and Kozo Shinoda. The interpretation of surface tension data for solutions of ionic surfactants in the presence of electrolyte. *Bulletin of the Chemical Society of Japan*, 48(1):324–326, 1975.

[85] VB Fainerman, AV Makievski, and R Miller. The analysis of dynamic surface tension of sodium alkyl sulphate solutions, based on asymptotic equations of adsorption kinetic theory. *Colloids and Surfaces A: Physicochemical and Engineering Aspects*, 87(1):61–75, 1994.

[86] Shi-Yow Lin, Ting-Li Lu, Woei-Bor Hwang, et al. Adsorption-kinetics of decanol at the air-water-interface. *Langmuir*, 11(2):555–562, 1995.

[87] Shi-Yow Lin, Ruey-Yug Tsay, Lung-Wei Lin, and Shou-I Chen. Adsorption kinetics of c12e8 at the air- water interface: adsorption onto a clean interface. *Langmuir*, 12(26):6530–6536, 1996.

[88] Hong-Chi Chang, Ching-Tien Hsu, and Shi-Yow Lin. Adsorption kinetics of c10e8 at the air-water interface. *Langmuir*, 14(9):2476–2484, 1998.

[89] Julian Eastoe, James Dalton, Philippe Rogueda, Donal Sharpe, Jinfeng Dong, and John RP Webster. Interfacial properties of a catanionic surfactant. *Langmuir*, 12(11):2706–2711, 1996.

[90] Julian Eastoe, James S Dalton, Philippe GA Rogueda, and Peter C Griffiths. Evidence for activation- diffusion controlled dynamic surface tension with a nonionic surfactant. *Langmuir*, 14(5):979–981, 1998.

[91] JF Baret. Kinetics of adsorption from a solution. role of the diffusion and of the adsorption-desorption antagonism. *The Journal of Physical Chemistry*, 72(8):2755–2758, 1968.

[92] Francesca Ravera, Libero Liggieri, and Annie Steinchen. Sorption kinetics considered as a renormalized diffusion process. *Journal of colloid and interface science*, 156(1):109–116, 1993.

[93] Libero Liggieri, Francesca Ravera, and Alberto Passerone. A diffusion-based approach to mixed adsorption kinetics. *Colloids and surfaces A: physicochemical and engineering aspects*, 114:351–359, 1996.

[94] F MacRitchie and AE Alexander. Kinetics of adsorption of proteins at interfaces. part iii. the role of electrical barriers in adsorption. *Journal of Colloid Science*, 18(5):464–469, 1963.

[95] DE Graham and MC Phillips. Proteins at liquid interfaces: I. kinetics of adsorption and surface denaturation. *Journal of Colloid and Interface Science*, 70(3):403–414, 1979.

[96] Daechul Cho, Ganesan Narsimhan, and Elias I Franses. Adsorption dynamics of native and pentylated bovine serum albumin at air–water interfaces: surface concentration/surface pressure measurements. *Journal of colloid and interface science*, 191(2):312–325, 1997.

[97] Michel Cornec, Daechul Cho, and Ganesan Narsimhan. Adsorption dynamics of α-lactalbumin and β-lactoglobulin at air–water interfaces. *Journal of colloid and interface science*, 214(2):129–142, 1999.

[98] Mrityunjoy Mahato, Prabir Pal, Tapanendu Kamilya, Ratan Sarkar, and GB Talapatra. ph induced structural modulation and interfacial activity of hemoglobin at the air/water interface. *The Journal of Physical Chemistry B*, 114(1):495–502, 2009.

[99] Zhiping Du, Maria P Bilbao-Montoya, Bernard P Binks, Eric Dickinson, Rammile Ettelaie, and Brent S Murray. Outstanding stability of particle-stabilized bubbles. *Langmuir*, 19(8):3106–3108, 2003.

[100] Eric Dickinson, Rammile Ettelaie, Thomas Kostakis, and Brent S Murray. Factors controlling the formation and stability of air bubbles stabilized by partially hydrophobic silica nanoparticles. *Langmuir*, 20(20):8517–8525, 2004.

[101] Jan H Schröder, Mikheil Doroshenko, Daniela Pirner, Miriam EJ Mauer, Beate Förster, Volodymyr Boyko, Bernd Reck, Konrad J Roschmann, Axel HE Müller, and Stephan Förster. Interfacial stabilization by soft janus nanoparticles. *Polymer*, 106:208–217, 2016.

[102] Martin Uhlig, Reinhard Miller, and Regine von Klitzing. Surface adsorption of sulfonated poly (phenylene sulfone)/c 14 tab mixtures and its correlation with foam film stability. *Physical Chemistry Chemical Physics*, 18(27):18414–18423, 2016.

[103] Cosima Stubenrauch and Regine von Klitzing. Disjoining pressure in thin liquid foam and emulsion films—new concepts and perspectives. *Journal of Physics: condensed matter*, 15(27):R1197, 2003.

[104] D Langevin and E Rio. Coalescence in foams and emulsions. *Encyclopedia of surface and colloid and science. 2nd ed. New York: Taylor and Francis*, pages 1–15, 2012.

[105] R Fayt, R Jerome, and Ph Teyssie. Molecular design of multicomponent polymer systems. i. emulsifying effect of poly (hydrogenated butadiene-b-styrene) copolymers in ldpe/ps blends. *Journal of Polymer Science: Polymer Letters Edition*, 19(2):79–84, 1981.

[106] M Jayabalan and T Balakrishnan. Compatibilization of thermosetting-thermoplastic polymer blends. *Polymer Engineering & Science*, 25(9):553–561, 1985.

[107] MC Schwarz, JW Barlow, and DR Paul. Morphology of hdpe/(pec/ps) blends modified with sebs copolymers. *Journal of applied polymer science*, 37(2):403–428, 1989.

[108] Shi-Ai Xu and Chi-Ming Chan. Polystyrene/high density polyethylene blends compatibilized by a tri-block copolymer i. properties and morphology. *Polymer journal*, 30(7):552–558, 1998.

[109] Bin Chen, Tao Tang, Xiliang Li, Shengqing Xu, Xuequan Zhang, and Baotong Huang. Morphology, tensile strength and thermal behavior of isotactic polypropylene/syndiotactic polystyrene blends compatibilized by sebs copolymers. *Polymer journal*, 36(4):284–293, 2004.

[110] Clemens Auschra, Reimund Stadler, and Ingrid G Voigt-Martin. Poly (styrene-b-methyl methacrylate) block copolymers as compatibilizing agents in blends of poly (styrene-co-acrylonitrile) and poly (2, 6-dimethyl-1, 4-phenylene ether): 2. influence of concentration and molecular weight of symmetric block copolymers. *Polymer*, 34(10):2094–2110, 1993.

[111] Ho Cheol Kim, Kie Hyun Nam, and Won Ho Jo. The effect of a styrene-methyl methacrylate block copolymer on the morphological, rheological and mechanical properties of poly (2, 6-dimethyl-1, 4-phenylene ether)(ppe) and poly (hydroxy ether of bisphenol a)(phenoxy) blends. *Polymer*, 34(19):4043–4051, 1993.

[112] Eric Boucher, John P Folkers, Hubert Hervet, Liliane Léger, and Costantino Creton. Effects of the formation of copolymer on the interfacial adhesion between semicrystalline polymers. *Macromolecules*, 29(2):774–782, 1996.

[113] Eric Boucher, John P Folkers, Costantino Creton, Hubert Hervet, and Liliane Léger. Enhanced adhesion between polypropylene and polyamide-6: role of interfacial nucleation of the β-crystalline form of polypropylene. *Macromolecules*, 30(7):2102–2109, 1997.

[114] A Legros, PJ Carreau, BD Favis, and A Michel. Morphology modification by interfacial chemical reaction in a polyester/ethylene vinyl acetate/polyethylene blend. *Polymer*, 38(20):5085–5089, 1997.

[115] Claire Laurens, Costantino Creton, and Liliane Leger. Adhesion promotion mechanisms at isotactic polypropylene/polyamide 6 interfaces: role of the copolymer architecture. *Macromolecules*, 37(18):6814–6822, 2004.

[116] J Bonnet, V Bounor-Legaré, P Alcouffe, and P Cassagnau. Eva reactive blending with si–h terminated polysiloxane by carbonyl hydrosilylation reaction: From compatibilised blends to crosslinking networks. *Materials Chemistry and Physics*, 136(2):954–962, 2012.

[117] A Legros, PJ Carreau, BD Favis, and A Michel. Reactive compatibilization of polyester/vinyl acetate copolymer blends: rheological, morphological and mechanical properties. *Polymer*, 35(4):758–764, 1994.

[118] I Pesneau, P Cassagnau, and A Michel. Morphology monitoring of pe/pbt blends by reactive processing. *Journal of applied polymer science*, 82(14):3568–3577, 2001.

[119] T Barraud, F Restagno, S Devisme, C Creton, and L Léger. Formation of diblock copolymers at pp/pa 6 interfaces and their role in local crystalline organization under fast heating and cooling conditions. *Polymer*, 53(22):5138–5145, 2012.

[120] Christian Koulic and Robert Jérôme. Nanostructured polyamide by reactive blending. 1. effect of the reactive diblock composition. *Macromolecules*, 37(9):3459–3469, 2004.

[121] Gy Marosi, A Márton, I Csontos, Sz Matkó, A Szép, P Anna, Gy Bertalan, and É Kiss. Reactive surfactants–new type of additive for multicomponent polymer systems. In *From Colloids to Nanotechnology*, pages 189–193. Springer, 2004.

[122] Anaïs Giustiniani, Philippe Guégan, Manon Marchand, Christophe Poulard, and Wiebke Drenckhan. Generation of silicone poly-hipes with controlled pore sizes via reactive emulsion stabilization. *Macromolecular Rapid Communications*, 37(18):1527–1532, 2016.

[123] C Chi, YT Hu, and A Lips. Kinetics of interfacial reaction between two polymers studied by interfacial tension measurements. *Macromolecules*, 40(18):6665–6668, 2007.

[124] Li Zhaohui, Xiaomin Zhang, Shigeru Tasaka, and Norihiro Inagaki. The interfacial tension and morphology of reactive polymer blends. *Materials letters*, 48(2):81–88, 2001.

[125] Kristin Conrad Powell and Anuj Chauhan. Interfacial effects and emulsion stabilization by in situ surfactant generation through the saponification of esters. *Colloids and Surfaces A: Physicochemical and Engineering Aspects*, 504:458–470, 2016.

[126] Jin Kon Kim, Woon-Yong Jeong, Jeong-Man Son, and Hyun Kyoung Jeon. Interfacial tension measurement of a reactive polymer blend by the neumann triangle method. *Macromolecules*, 33(25):9161–9165, 2000.

[127] Kilwon Cho, Hyun Kyoung Jeon, Chan Eon Park, Jungahn Kim, and Kwang Ung Kim. The effect of end-sulfonated polystyrene on the interfacial tension of nylon-6/polystyrene blends. *Polymer*, 37(7):1117–1122, 1996.

[128] M Wagner and BA Wolf. Effect of block copolymers on the interfacial tension between two 'immiscible'homopolymers. *Polymer*, 34(7):1460–1464, 1993.

[129] Yulia Lyatskaya, Dilip Gersappe, Anna C Balazs, et al. Effect of copolymer architecture on the efficiency of compatibilizers. *Macromolecules*, 28(18):6278–6283, 1995.

[130] ML Di Lorenzo and M Frigione. Compatibilization criteria and procedures for binary blends: A review. *Journal of polymer engineering*, 17(6):429–459, 1997.

[131] Brian D Edgecombe, Jason A Stein, Jean MJ Fréchet, Zhihua Xu, and Edward J Kramer. The role of polymer architecture in strengthening polymer- polymer interfaces: A comparison of graft, block, and random copolymers containing hydrogen-bonding moieties. *Macromolecules*, 31(4):1292–1304, 1998.

[132] Costantino Creton, Edward J Kramer, Hugh R Brown, and Chung-Yuen Hui. Adhesion and fracture of interfaces between immiscible polymers: from the molecular to the continuum scal. In *Molecular Simulation Fracture Gel Theory*, pages 53–136. Springer, 2001.

[133] M Volmer. Thermodynamische folgerungen aus der zustandsgleichung fur adsorbierte stoffe. *Z. phys. Chem*, 115:253–261, 1925.

[134] Hideko T Oyama and Takashi Inoue. Kinetics and mechanism of coupling of functionalized chains at the immiscible polymer- polymer interface. *Macromolecules*, 34(10):3331–3338, 2001.

[135] Todd D Jones, Jonathan S Schulze, Christopher W Macosko, and Timothy P Lodge. Effect of thermodynamic interactions on reactions at polymer/polymer interfaces. *Macromolecules*, 36(19):7212–7219, 2003.

[136] Ph Guégan, CW Macosko, Takashi Ishizone, Akira Hirao, Seiichi Nakahama, et al. Kinetics of chain coupling at melt interfaces. *Macromolecules*, 27(18):4993–4997, 1994.

[137] Zhihui Yin, Christian Koulic, Christophe Pagnoulle, and Robert Jérôme. Reactive blending of functional ps and pmma: interfacial behavior of in situ formed graft copolymers. *Macromolecules*, 34(15):5132–5139, 2001.

[138] Xiaobo Yu, Yang Wu, Binyao Li, and Yanchun Han. Studies on interfacial reaction kinetics and properties at a reactive compatibilization interface. *Polymer*, 46(10):3337–3342, 2005.

[139] Hyun K Jeon, Christopher W Macosko, Bongjin Moon, Thomas R Hoye, and Zhihui Yin. Coupling reactions of end-vs mid-functional polymers. *Macromolecules*, 37(7):2563–2571, 2004.

[140] Bumjoon J Kim, Huiman Kang, Kookheon Char, Kirill Katsov, Glenn H Fredrickson, and Edward J Kramer. Interfacial roughening induced by the reaction of end-functionalized polymers at a ps/p2vp interface: quantitative analysis by dsims. *Macromolecules*, 38(14):6106–6114, 2005.

[141] Toshihiro Tanaka, Hiroki Goto, Masashi Nakamoto, Masanori Suzuki, Masahito Hanao, Masafumi Zeze, Hideaki Yamamura, and Takeshi Yoshikawa. Dynamic changes in interfacial tension between liquid fe alloy and molten slag induced by chemical reactions. *ISIJ International*, 56(6):944–952, 2016.

[142] Glenn H Fredrickson. Diffusion-controlled reactions at polymer-polymer interfaces. *Physical review letters*, 76(18):3440, 1996.

[143] Marcus Müller. Reactions at polymer interfaces: a monte carlo simulation. *Macromolecules*, 30(20):6353–6357, 1997.

[144] Ben O'Shaughnessy and Dimitrios Vavylonis. Reactions at polymer interfaces: Transitions from chemical to diffusion-control and mixed order kinetics. *EPL (Europhysics Letters)*, 45(5):638, 1999.

[145] Jonathan S Schulze, Jeffrey J Cernohous, Akira Hirao, Timothy P Lodge, and Christopher W Macosko. Reaction kinetics of end-functionalized chains at a polystyrene/poly (methyl methacrylate) interface. *Macromolecules*, 33(4):1191–1198, 2000.

[146] CA Orr, JJ Cernohous, P Guegan, A Hirao, HK Jeon, and CW Macosko. Homogeneous reactive coupling of terminally functional polymers. *Polymer*, 42(19):8171–8178, 2001.

[147] Anatoly V Berezkin and Yaroslav V Kudryavtsev. End-coupling reactions in incompatible polymer blends: From droplets to complex micelles through interfacial instability. *Macromolecules*, 46(12):5080–5089, 2013.

[148] Chris Scott and Chris Macosko. Model experiments for the interfacial reaction between polymers during reactive polymer blending. *Journal of Polymer Science Part B: Polymer Physics*, 32(2):205–213, 1994.

[149] Edward J Kramer. Grafting kinetics of end-functional polymers at melt interfaces. *Israel journal of chemistry*, 35(1):49–54, 1995.

[150] Hwang Yong Kim, Unyong Jeong, and Jin Kon Kim. Reaction kinetics and morphological changes of reactive polymer- polymer interface. *Macromolecules*, 36(5):1594–1602, 2003.

[151] Jinbao Jiao, Edward J Kramer, Sicco de Vos, Martin Möller, and Cor Koning. Morphological changes of a molten polymer/polymer interface driven by grafting. *Macromolecules*, 32(19):6261–6269, 1999.

[152] Jianbin Zhang, Shengxiang Ji, Jie Song, Timothy P Lodge, and Christopher W Macosko. Flow accelerates interfacial coupling reactions. *Macromolecules*, 43(18):7617–7624, 2010.

[153] Jie Song, Adam M Baker, Christopher W Macosko, and Randy H Ewoldt. Reactive coupling between immiscible polymer chains: Acceleration by compressive flow. *AIChE Journal*, 59(9):3391–3402, 2013.

[154] Ula El-Jaby, Michael Cunningham, and Timothy FL McKenna. Miniemulsions via in situ surfactant generation. *Macromolecular Chemistry and Physics*, 211(12):1377–1386, 2010.

[155] Hyun K Jeon, Jianbin Zhang, and Christopher W Macosko. Premade vs. reactively formed compatibilizers for pmma/ps melt blends. *Polymer*, 46(26):12422–12429, 2005.

[156] GI Taylor. The formation of emulsions in definable fields of flow. *Proceedings of the Royal Society of London. Series A, Containing Papers of a Mathematical and Physical Character*, 146(858):501–523, 1934.

[157] Souheng Wu. Formation of dispersed phase in incompatible polymer blends: Interfacial and rheological effects. *Polymer Engineering & Science*, 27(5):335–343, 1987.

[158] Scott T Milner and Haowen Xi. How copolymers promote mixing of immiscible homopolymers. *Journal of Rheology*, 40(4):663–687, 1996.

[159] Peter Van Puyvelde, Sachin Velankar, and Paula Moldenaers. Rheology and morphology of compatibilized polymer blends. *Current opinion in colloid & interface science*, 6(5):457–463, 2001.

[160] Chris E Scott and Christopher W Macosko. Morphology development during reactive and nonreactive blending of an ethylene-propylene rubber with two thermoplastic matrices. *Polymer*, 35(25):5422–5433, 1994.

[161] Sabu Thomas and Gabriël Groeninckx. Reactive compatibilisation of heterogeneous ethylene propylene rubber (epm)/nylon 6 blends by the addition of compatibiliser precursor epm-g-ma. *Polymer*, 40(21):5799–5819, 1999.

[162] NC Beck Tan, S-K Tai, and RM Briber. Morphology control and interfacial reinforcement in reactive polystyrene/amorphous polyamide blends. *Polymer*, 37(16):3509–3519, 1996.

[163] P Charoensirisomboon, T Chiba, SI Solomko, T Inoue, and M Weber. Reactive blending of polysulfone with polyamide: a difference in interfacial behavior between in situ formed block and graft copolymers. *Polymer*, 40(24):6803–6810, 1999.

[164] K Dedecker and Gabriël Groeninckx. Reactive compatibilisation of a/(b/c) polymer blends. part 1. investigation of the phase morphology development and stabilisation. *Polymer*, 39(21):4985–4992, 1998.

[165] CW Macosko, Philippe Guegan, Ashish K Khandpur, Akinari Nakayama, Philippe Marechal, and Takashi Inoue. Compatibilizers for melt blending: Premade block copolymers. *Macromolecules*, 29(17):5590–5598, 1996.

[166] G Wildes, H Keskkula, and DR Paul. Coalescence in pc/san blends: effect of reactive compatibilization and matrix phase viscosity. *Polymer*, 40(20):5609–5621, 1999.

[167] Nicholas Ballard, Maitane Salsamendi, Paula Carretero, and José M Asua. An investigation into the nature and potential of in-situ surfactants for low energy miniemulsification. *Journal of colloid and interface science*, 458:69–78, 2015.

[168] Warren E Baker, Chris E Scott, Guo-Hua Hu, and MK Akkapeddi. *Reactive polymer blending*, volume 1. Hanser Munich, 2001.

[169] Steven L Regen, Alok Singh, Günther Oehme, and Maninder Singh. Polymerized phosphatidyl choline vesicles. stabilized and controllable time-release carriers. *Biochemical and biophysical research communications*, 101(1):131–136, 1981.

[170] Faruk Nome, Wayne Reed, Mario Politi, Pietro Tundo, and Janos H Fendler. Cleft formation upon polymerization of surfactant vesicles. *J. Am. Chem. Soc*, 106(26):8086–8093, 1984.

[171] Philip E Eaton, Patrick G Jobe, and Kayson Nyi. Polymerized vesicles'. *J. Am. Chem. Soc*, 102(21):6638–6640, 1980.

[172] Mark Summers and Julian Eastoe. Applications of polymerizable surfactants. *Advances in Colloid and Interface Science*, 100:137–152, 2003.

[173] Kenneth R Shull, Andrew J Kellock, Vaughn R Deline, and Scott A MacDonald. Vanishing interfacial tension in an immiscible polymer blend. *The Journal of chemical physics*, 97(3):2095–2104, 1992.

[174] Z Xu, KD Jandt, EJ Kramer, BD Edgecombe, and JMJ Frechet. Direct observation of a diblock copolymer-induced microemulsion at a polymer/polymer interface. *Journal of Polymer Science Part B: Polymer Physics*, 33(17):2351–2357, 1995.

[175] Dong Wang, So Fujinami, Hao Liu, Ken Nakajima, Toshio Nishi, et al. Investigation of reactive polymer- polymer interface using nanomechanical mapping. *Macromolecules*, 43(13):5521, 2010.

[176] Jinbao Jiao, Edward J Kramer, Sicco de Vos, Martin Möller, and Cor Koning. Polymer interface instability caused by a grafting reaction. *Polymer*, 40(12):3585–3588, 1999.

[177] Su-Ping Lyu, Jeff J Cernohous, Frank S Bates, and Christopher W Macosko. Interfacial reaction induced roughening in polymer blends. *Macromolecules*, 32(1):106–110, 1999.

[178] AZ Patashinski, R Orlik, K Paclawski, MA Ratner, and BA Grzybowski. The unstable and expanding interface between reacting liquids: theoretical interpretation of negative surface tension. *Soft Matter*, 8(5):1601–1608, 2012.

[179] Steven D Fields, Edwin L Thomas, and Julio M Ottino. Visualization of interfacial urethane polymerizations by means of a new microstage reactor. *Polymer*, 27(9):1423–1432, 1986.

[180] R Granek, RC Ball, and ME Cates. Dynamics of spontaneous emulsification. *Journal de Physique II*, 3(6):829–849, 1993.

[181] Pascale Angelica Bachmann, Peter Walde, Pier Luigi Luisi, and Jacques Lang. Self-replicating micelles: aqueous micelles and enzymatically driven reactions in reverse micelles. *Journal of the American Chemical Society*, 113(22):8204–8209, 1991.

[182] Eugene G Rochow. *Chemistry of the Silicones*, chapter 1. Wiley-VCH, New York, USA, 1948.

[183] Laurence Lestel, Hervé Cheradame, and Sylvie Boileau. Crosslinking of polyether networks by hydrosilylation and related side reactions. *Polymer*, 31(6):1154–1158, 1990.

[184] Norma A Alcantar, Eray S Aydil, and Jacob N Israelachvili. Polyethylene glycol-coated biocompatible surfaces. *Journal of biomedical materials research*, 51(3):343–351, 2000.

[185] Andrew Pryde. Chemically bonded stationary phases—preparation and application to high speed liquid chromatography, 1974.

[186] Ghislaine Torrès, Pierre-Jean Madec, and Ernest Maréchal. Synthesis of polysulfone-block-polysiloxane copolymers, 5. a model study on the hydrosilylation side-reactions. *Die Makromolekulare Chemie*, 190(11):2789–2803, 1989.

[187] O Lichtenberger and J Woltersdorf. On the atomic mechanisms of water-enhanced silicon wafer direct bonding. *Materials chemistry and physics*, 44(3):222–232, 1996.

[188] Elham Gharibshahi and Elias Saion. Influence of dose on particle size and optical properties of colloidal platinum nanoparticles. *International journal of molecular sciences*, 13(11):14723–14741, 2012.

[189] Tomas Frømyr, Finn Knut Hansen, A Kotzev, and Andre Laschewsky. Adsorption and surface elastic properties of corresponding fluorinated and nonfluorinated cationic polymer films measured by drop shape analysis. *Langmuir*, 17(17):5256–5264, 2001.

[190] Anthony Yeung and Lichun Zhang. Shear effects in interfacial rheology and their implications on oscillating pendant drop experiments. *Langmuir*, 22(2):693–701, 2006.

[191] Rolf Myrvold and Finn Knut Hansen. Surface elasticity and viscosity from oscillating bubbles measured by automatic axisymmetric drop shape analysis. *Journal of colloid and interface science*, 207(1):97–105, 1998.

[192] D Langevin and F Monroy. Marangoni stresses and surface compression rheology of surfactant solutions. achievements and problems. *Advances in colloid and interface science*, 206:141–149, 2014.

[193] Ya-Chi Lee, Kathleen J Stebe, Hwai-Shen Liu, and Shi-Yow Lin. Adsorption and desorption kinetics of c m e 8 on impulsively expanded or compressed air–water interfaces. *Colloids and Surfaces A: Physicochemical and Engineering Aspects*, 220(1):139–150, 2003.

[194] Alex CM Kuo. Poly (dimethylsiloxane).

[195] Leoncio Garrido, James E Mark, Jerome L Ackerman, and Robert A Kinsey. Studies of self-diffusion of poly (dimethylsiloxane) chains in pdms model networks by pulsed field gradient nmr. *Journal of Polymer Science Part B: Polymer Physics*, 26(11):2367–2377, 1988.

[196] Ranting Wu, Angelika Menner, and Alexander Bismarck. Macroporous polymers made from medium internal phase emulsion templates: Effect of emulsion formulation on the pore structure of polymipes. *Polymer*, 54(21):5511–5517, 2013.

[197] Jennifer L Robinson, Robert S Moglia, Melissa C Stuebben, Madison AP McEnery, and Elizabeth Cosgriff-Hernandez. Achieving interconnected pore architecture in injectable polyhipes for bone tissue engineering. *Tissue Engineering Part A*, 20(5-6):1103–1112, 2014.

[198] Denis Weaire and Tomaso Aste. *The pursuit of perfect packing*. CRC Press, 2008.

[199] Thomas C Hales. A proof of the kepler conjecture. *Annals of mathematics*, 162(3):1065–1185, 2005.

[200] Andrea J Liu and Sidney R Nagel. Nonlinear dynamics: Jamming is not just cool any more. *Nature*, 396(6706):21–22, 1998.

[201] Denis L Weaire and Stefan Hutzler. *The physics of foams*. Oxford University Press, 2001.

[202] Isabelle Cantat, Sylvie Cohen-Addad, Florence Elias, François Graner, Reinhard Höhler, Olivier Pitois, Florence Rouyer, and Arnaud Saint-Jalmes. *Foams: structure and dynamics*. OUP Oxford, 2013.

[203] Reinhard Höhler, Yann Yip Cheung Sang, Elise Lorenceau, and Sylvie Cohen-Addad. Osmotic pressure and structures of monodisperse ordered foam. *Langmuir*, 24(2):418–425, 2008.

[204] J-F Métayer, Donald J Suntrup III, Charles Radin, Harry L Swinney, and Matthias Schröter. Shearing of frictional sphere packings. *EPL (Europhysics Letters)*, 93(6):64003, 2011.

[205] Corey S O'hern, Leonardo E Silbert, Andrea J Liu, and Sidney R Nagel. Jamming at zero temperature and zero applied stress: The epitome of disorder. *Physical Review E*, 68(1):011306, 2003.

[206] Eric R Weeks. Soft jammed materials. *Statistical physics of complex fluids, Eds S Maruyama, M Tokuyama, pag*, 2(1):87, 2007.

[207] Rudchenko Illya. Development of a parallel simulation environment of granular materials. `http://masters.donntu.org/2010/fknt/rudchenko/diss/indexe.htm`, 2010. [Online; accessed 09-August-2017].

[208] Fernando Leal-Calderon, Véronique Schmitt, and Jerome Bibette. *Emulsion science: basic principles*. Springer Science & Business Media, 2007.

[209] M Van Hecke. Jamming of soft particles: geometry, mechanics, scaling and isostaticity. *Journal of Physics: Condensed Matter*, 22(3):033101, 2009.

[210] Reinhard Höhler and Sylvie Cohen-Addad. Many-body interactions in soft jammed materials. *Soft matter*, 13(7):1371–1383, 2017.

[211] Fabien Soulie, Fabien Cherblanc, Moulay Saïd El Youssoufi, and C Saix. Influence of liquid bridges on the mechanical behaviour of polydisperse granular materials. *International journal for numerical and analytical methods in geomechanics*, 30(3):213–228, 2006.

[212] Mario Scheel, Ralf Seemann, Martin Brinkmann, M Di Michiel, Adrian Sheppard, and Stephan Herminghaus. Liquid distribution and cohesion in wet granular assemblies beyond the capillary bridge regime. *Journal of Physics: Condensed Matter*, 20(49):494236, 2008.

[213] Vincent Richefeu, Moulay Saıd El Youssoufi, Robert Peyroux, and Farhang Radjai. A model of capillary cohesion for numerical simulations of 3d polydisperse granular media. *International Journal for Numerical and Analytical Methods in Geomechanics*, 32(11):1365–1383, 2008.

[214] L Scholtès, B Chareyre, F Nicot, and F Darve. Micromechanics of granular materials with capillary effects. *International journal of engineering science*, 47(1):64–75, 2009.

[215] Namiko Mitarai and Franco Nori. Wet granular materials. *Advances in Physics*, 55(1-2):1–45, 2006.

[216] Peter Schiffer. Granular physics: a bridge to sandpile stability. *Nature Physics*, 1(1):21, 2005.

[217] Arnaud Hemmerle, Matthias Schröter, and Lucas Goehring. A cohesive granular material with tunable elasticity. *Scientific reports*, 6, 2016.

[218] Maik Hadorn, Eva Boenzli, Kristian T Sørensen, Harold Fellermann, Peter Eggenberger Hotz, and Martin M Hanczyc. Specific and reversible dna-directed self-assembly of oil-in-water emulsion droplets. *Proceedings of the National Academy of Sciences*, 109(50):20320–20325, 2012.

[219] Lang Feng, Lea-Laetitia Pontani, Rémi Dreyfus, Paul Chaikin, and Jasna Brujic. Specificity, flexibility and valence of dna bonds guide emulsion architecture. *Soft Matter*, 9(41):9816–9823, 2013.

[220] Lea-Laetitia Pontani, Ivane Jorjadze, Virgile Viasnoff, and Jasna Brujic. Biomimetic emulsions reveal the effect of mechanical forces on cell–cell adhesion. *Proceedings of the National Academy of Sciences*, 109(25):9839–9844, 2012.

[221] Lea-Laetitia Pontani, Martin F Haase, Izabela Raczkowska, and Jasna Brujic. Immiscible lipids control the morphology of patchy emulsions. *Soft Matter*, 9(29):7150–7157, 2013.

[222] Ivane Jorjadze, Lea-Laetitia Pontani, Katherine A Newhall, and Jasna Brujić. Attractive emulsion droplets probe the phase diagram of jammed granular matter. *Proceedings of the National Academy of Sciences*, 108(11):4286–4291, 2011.

[223] KD Danov, DN Petsev, ND Denkov, and R Borwankar. Pair interaction energy between deformable drops and bubbles. *The Journal of chemical physics*, 99(9):7179–7189, 1993.

[224] Jennifer L Anthony and Chris Marone. Influence of particle characteristics on granular friction. *Journal of Geophysical Research: Solid Earth*, 110(B8), 2005.

[225] L Staron and EJ Hinch. The spreading of a granular mass: role of grain properties and initial conditions. *Granular Matter*, 9(3-4):205, 2007.

[226] E Kolb, T Mazozi, E Clément, and J Duran. Force fluctuations in a vertically pushed granular column. *The European Physical Journal B-Condensed Matter and Complex Systems*, 8(3):483–491, 1999.

[227] Matthias Schröter. A local view on the role of friction and shape. *arXiv preprint arXiv:1703.07151*, 2017.

[228] Daniel L Blair, Nathan W Mueggenburg, Adam H Marshall, Heinrich M Jaeger, and Sidney R Nagel. Force distributions in three-dimensional granular assemblies: Effects of packing order and interparticle friction. *Physical review E*, 63(4):041304, 2001.

[229] GACM Spierings. Wet chemical etching of silicate glasses in hydrofluoric acid based solutions. *Journal of Materials Science*, 28(23):6261–6273, 1993.

[230] Sonia Utermann, Philipp Aurin, Markus Benderoth, Cornelius Fischer, and Matthias Schröter. Tailoring the frictional properties of granular media. *Physical Review E*, 84(3):031306, 2011.

[231] Karl Shellenberger and Bruce E Logan. Effect of molecular scale roughness of glass beads on colloidal and bacterial deposition. *Environmental science & technology*, 36(2):184–189, 2002.

[232] ME Cates, JP Wittmer, J-P Bouchaud, and Ph Claudin. Jamming, force chains, and fragile matter. *Physical review letters*, 81(9):1841, 1998.

[233] Thierry Darnige, Ary Bruand, Eric Clement, et al. Creep and fluidity of a real granular packing near jamming. *Physical review letters*, 107(13):138303, 2011.

[234] Patrick Perrin. Droplet- droplet interactions in both direct and inverse emulsions stabilized by a balanced amphiphilic polyelectrolyte. *Langmuir*, 16(3):881–884, 2000.

[235] Sylvie Cohen-Addad and Reinhard Höhler. Rheology of foams and highly concentrated emulsions. *Current Opinion in Colloid & Interface Science*, 19(6):536–548, 2014.

[236] Jysoo Lee and Hans J Herrmann. Angle of repose and angle of marginal stability: molecular dynamics of granular particles. *Journal of Physics A: Mathematical and General*, 26(2):373, 1993.

[237] YC Zhou, BH Xu, AB Yu, and Paul Zulli. Numerical investigation of the angle of repose of monosized spheres. *Physical Review E*, 64(2):021301, 2001.

[238] YC Zhou, Bao Hua Xu, Ai-Bing Yu, and P Zulli. An experimental and numerical study of the angle of repose of coarse spheres. *Powder technology*, 125(1):45–54, 2002.

[239] M Ghazavi, M Hosseini, and M Mollanouri. A comparison between angle of repose and friction angle of sand. In *The 12th International Conference for International Association for Computer Methods and Advances in Geomechanics (IACMAG)*, pages 1–6, 2008.

[240] Trushant S Majmudar and Robert P Behringer. Contact force measurements and stress-induced anisotropy in granular materials. *Nature*, 435(7045):1079, 2005.

[241] J-P Bouchaud, P Claudin, Dov Levine, and Matthias Otto. Force chain splitting in granular materials: A mechanism for large-scale pseudo-elastic behaviour. *The European Physical Journal E: Soft Matter and Biological Physics*, 4(4):451–457, 2001.

[242] Maya Muthuswamy and Antoinette Tordesillas. How do interparticle contact friction, packing density and degree of polydispersity affect force propagation in particulate assemblies? *Journal of Statistical Mechanics: Theory and Experiment*, 2006(09):P09003, 2006.

[243] Tomaso Aste, T Di Matteo, Mohammad Saadatfar, Tim J Senden, Matthias Schröter, and Harry L Swinney. An invariant distribution in static granular media. *EPL (Europhysics Letters)*, 79(2):24003, 2007.

[244] Gerd E Schröder-Turk, Walter Mickel, Matthias Schröter, Gary W Delaney, Mohammad Saadatfar, Tim J Senden, Klaus Mecke, and Tomaso Aste. Disordered spherical bead packs are anisotropic. *EPL (Europhysics Letters)*, 90(3):34001, 2010.

[245] AJ Meagher, M Mukherjee, D Weaire, S Hutzler, J Banhart, and F Garcia-Moreno. Analysis of the internal structure of monodisperse liquid foams by x-ray tomography. *Soft Matter*, 7(21):9881–9885, 2011.

[246] Ha Seong Kim and Thomas G Mason. Advances and challenges in the rheology of concentrated emulsions and nanoemulsions. *Advances in Colloid and Interface Science*, 2017.

[247] Ivane Jorjadze, Lea-Laetitia Pontani, and Jasna Brujic. Microscopic approach to the nonlinear elasticity of compressed emulsions. *Physical review letters*, 110(4):048302, 2013.

[248] Wiebke Drenckhan and Stefan Hutzler. Structure and energy of liquid foams. *Advances in colloid and interface science*, 224:1–16, 2015.

[249] HP Zhang and HA Makse. Jamming transition in emulsions and granular materials. *Physical Review E*, 72(1):011301, 2005.

[250] DJ Durian. Foam mechanics at the bubble scale. *Physical review letters*, 75(26):4780, 1995.

[251] Gijs Katgert, Brian P Tighe, and Martin van Hecke. The jamming perspective on wet foams. *Soft Matter*, 9(41):9739–9746, 2013.

[252] Leonardo E Silbert, Andrea J Liu, and Sidney R Nagel. Structural signatures of the unjamming transition at zero temperature. *Physical Review E*, 73(4):041304, 2006.

[253] Yann Bertho, Frédérique Giorgiutti-Dauphiné, and Jean-Pierre Hulin. Dynamical janssen effect on granular packing with moving walls. *Physical review letters*, 90(14):144301, 2003.

[254] P Philippe and D Bideau. Compaction dynamics of a granular medium under vertical tapping. *EPL (Europhysics Letters)*, 60(5):677, 2002.

[255] Richard Patrick, Mario Nicodemi, Renaud Delannay, Philippe Ribiere, and Daniel Bideau. Slow relaxation and compaction of granular systems. *Nature materials*, 4(2):121, 2005.

[256] Ph Ribière, Patrick Richard, Pierre Philippe, Daniel Bideau, and Renaud Delannay. On the existence of stationary states during granular compaction. *The European Physical Journal E: Soft Matter and Biological Physics*, 22(3):249–253, 2007.

[257] ER Nowak, JB Knight, ML Povinelli, HM Jaeger, and SR Nagel. Reversibility and irreversibility in the packing of vibrated granular material. *Powder technology*, 94(1):79–83, 1997.

[258] Edmund R Nowak, James B Knight, Eli Ben-Naim, Heinrich M Jaeger, and Sidney R Nagel. Density fluctuations in vibrated granular materials. *Physical Review E*, 57(2):1971, 1998.

[259] GD Scott and DM Kilgour. The density of random close packing of spheres. *Journal of Physics D: Applied Physics*, 2(6):863, 1969.

[260] Hernán A Makse, David L Johnson, and Lawrence M Schwartz. Packing of compressible granular materials. *Physical review letters*, 84(18):4160, 2000.

[261] Chaoming Song, Ping Wang, and Hernán A Makse. A phase diagram for jammed matter. *Nature*, 453(7195):629, 2008.

[262] Melissa Jerkins, Matthias Schröter, Harry L Swinney, Tim J Senden, Mohammad Saadatfar, and Tomaso Aste. Onset of mechanical stability in random packings of frictional spheres. *Physical review letters*, 101(1):018301, 2008.

[263] Fabian M Schaller, Max Neudecker, Mohammad Saadatfar, Gary W Delaney, Gerd E Schröder-Turk, and Matthias Schröter. Local origin of global contact numbers in frictional ellipsoid packings. *Physical review letters*, 114(15):158001, 2015.

[264] TS Majmudar, M Sperl, Stefan Luding, and Robert P Behringer. Jamming transition in granular systems. *Physical review letters*, 98(5):058001, 2007.

[265] Leonardo E Silbert, Deniz Ertaş, Gary S Grest, Thomas C Halsey, and Dov Levine. Geometry of frictionless and frictional sphere packings. *Physical Review E*, 65(3):031304, 2002.

[266] Lea-Laetitia Pontani, Ivane Jorjadze, and Jasna Brujic. Cis and trans cooperativity of e-cadherin mediates adhesion in biomimetic lipid droplets. *Biophysical journal*, 110(2):391–399, 2016.

[267] Ling-Nan Zou, Xiang Cheng, Mark L Rivers, Heinrich M Jaeger, and Sidney R Nagel. The packing of granular polymer chains. *Science*, 326(5951):408–410, 2009.

[268] Maxime Clusel, Eric I Corwin, Alexander ON Siemens, and Jasna Brujic. A'granocentric'model for random packing of jammed emulsions. *Nature*, 460(7255):611, 2009.

[269] PY Liu, RY Yang, and AB Yu. Dynamics of wet particles in rotating drums: effect of liquid surface tension. *Physics of fluids*, 23(1):013304, 2011.

[270] NK Myshkin, MI Petrokovets, and AV Kovalev. Tribology of polymers: adhesion, friction, wear, and mass-transfer. *Tribology International*, 38(11):910–921, 2006.

[271] Simon Weis, Philipp WA Schönhöfer, Fabian M Schaller, Matthias Schröter, and Gerd E Schröder-Turk. Pomelo, a tool for computing generic set voronoi diagrams of aspherical particles of arbitrary shape. *arXiv preprint arXiv:1703.03643*, 2017.

[272] GE Schröder-Turk, Walter Mickel, SC Kapfer, MA Klatt, FM Schaller, MJF Hoffmann, Nicola Kleppmann, Patrick Armstrong, Amer Inayat, Daniel Hug, et al. Minkowski tensor shape analysis of cellular, granular and porous structures. *Advanced Materials*, 23(22-23):2535–2553, 2011.

[273] Costantino Creton and Matteo Ciccotti. Fracture and adhesion of soft materials: a review. *Reports on Progress in Physics*, 79(4):046601, 2016.

[274] Bharat Bhushan. Adhesion and stiction: mechanisms, measurement techniques, and methods for reduction. *Journal of Vacuum Science & Technology B: Microelectronics and Nanometer Structures Processing, Measurement, and Phenomena*, 21(6):2262–2296, 2003.

[275] Liliane Léger and Costantino Creton. Adhesion mechanisms at soft polymer interfaces. *Philosophical Transactions of the Royal Society of London A: Mathematical, Physical and Engineering Sciences*, 366(1869):1425–1442, 2008.

[276] Anand Jagota and Chung-Yuen Hui. Adhesion, friction, and compliance of bio-mimetic and bio-inspired structured interfaces. *Materials Science and Engineering: R: Reports*, 72(12):253–292, 2011.

[277] Cyprien Gay. Stickiness—some fundamentals of adhesion. *Integrative and comparative biology*, 42(6):1123–1126, 2002.

[278] Lev Davidovich Landau, AM Kosevich, Lev Petrovich Pitaevskii, and Evgenii Mikhailovich Lifshitz. Theory of elasticity. 1986.

[279] Paul J Flory. *Principles of polymer chemistry*. Cornell University Press, 1953.

[280] Céline Cohen. *Mécanismes moléculaires de la friction aux interfaces polymères souples*. PhD thesis, Paris 11, 2011.

[281] Pierre-Gilles De Gennes and Thomas A Witten. Scaling concepts in polymer physics, 1980.

[282] Montgomery T Shaw and William J MacKnight. *Introduction to polymer viscoelasticity*. John Wiley & Sons, 2005.

[283] Hubert M James and Eugene Guth. Theory of the increase in rigidity of rubber during cure. *The Journal of Chemical Physics*, 15(9):669–683, 1947.

[284] William W Graessley. Statistical mechanics of random coil networks. *Macromolecules*, 8(2):186–190, 1975.

[285] AE Oberth. Effect and detection of loose chain ends in crosslinked polyurethane elastomers. *Rubber Chemistry and Technology*, 44(1):152–165, 1971.

[286] RE Cohen and NW Tschoegl. Dynamic mechanical properties of block copolymer blends–a study of the effects of terminal chains in elastomeric materials i. torsion pendulum measurements. *International Journal of Polymeric Materials*, 2(1):49–69, 1972.

[287] EH Andrews and AJ Kinloch. Mechanics of adhesive failure. ii. In *Proceedings of the Royal Society of London A: Mathematical, Physical and Engineering Sciences*, volume 332, pages 401–414. The Royal Society, 1973.

[288] DE Packham. Work of adhesion: contact angles and contact mechanics. *International journal of adhesion and adhesives*, 16(2):121–128, 1996.

[289] Nicolas Amouroux. *Etude des mécanismes de modulation de l'adhérence entre un élastomère silicone et un adhésif acrylique*. PhD thesis, Paris VI, 1998.

[290] Daniel Maugis. *Contact, adhesion and rupture of elastic solids*, volume 130. Springer Science & Business Media, 2013.

[291] Luciano F Boesel, Christian Greiner, Eduard Arzt, and Aránzazu Del Campo. Gecko-inspired surfaces: a path to strong and reversible dry adhesives. *Advanced Materials*, 22(19):2125–2137, 2010.

[292] Anand Jagota and Stephen J Bennison. Mechanics of adhesion through a fibrillar microstructure. *Integrative and Comparative Biology*, 42(6):1140–1145, 2002.

[293] NJ Glassmaker, A Jagota, C-Y Hui, and J Kim. Design of biomimetic fibrillar interfaces: 1. making contact. *Journal of The Royal Society Interface*, 1(1):23–33, 2004.

[294] C-Y Hui, NJ Glassmaker, T Tang, and A Jagota. Design of biomimetic fibrillar interfaces: 2. mechanics of enhanced adhesion. *Journal of The Royal Society Interface*, 1(1):35–48, 2004.

[295] Gerrit Huber, Stanislav N Gorb, Naoe Hosoda, Ralph Spolenak, and Eduard Arzt. Influence of surface roughness on gecko adhesion. *Acta Biomaterialia*, 3(4):607–610, 2007.

[296] Christophe Poulard, Frédéric Restagno, Raphaël Weil, and Liliane Léger. Mechanical tuning of adhesion through micro-patterning of elastic surfaces. *Soft matter*, 7(6):2543–2551, 2011.

[297] Marleen Kamperman, Elmar Kroner, Aranzazu del Campo, Robert M McMeeking, and Eduard Arzt. Functional adhesive surfaces with "gecko" effect: The concept of contact splitting. *Advanced Engineering Materials*, 12(5):335–348, 2010.

[298] Michael D Bartlett, Andrew B Croll, Daniel R King, Beth M Paret, Duncan J Irschick, and Alfred J Crosby. Looking beyond fibrillar features to scale gecko-like adhesion. *Advanced materials*, 24(8):1078–1083, 2012.

[299] HR Brown. A molecular interpretation of the toughness of glassy polymers. *Macromolecules*, 24(10):2752–2756, 1991.

[300] Alan A Griffith. The phenomena of rupture and flow in solids. *Philosophical transactions of the royal society of london. Series A, containing papers of a mathematical or physical character*, 221:163–198, 1921.

[301] Heinrich Hertz. Über die berührung fester elastischer körper. *Journal für die reine und angewandte Mathematik*, 92:156–171, 1882.

[302] KL Johnson, K Kendall, and AD Roberts. Surface energy and the contact of elastic solids. In *Proceedings of the Royal Society of London A: Mathematical, Physical and Engineering Sciences*, volume 324, pages 301–313. The Royal Society, 1971.

[303] Joseph Boussinesq. *Application des potentiels à l'étude de l'équilibre et du mouvement des solides élastiques*, volume 4. Gauthier-Villars, 1885.

[304] Philippe Coussot. *Rhéophysique des pâtes et des suspensions*. EDP sciences, 2012.

[305] JM Lederman. The prediction of the tensile properties of flexible foams. *Journal of Applied Polymer Science*, 15(3):693–703, 1971.

[306] S Baxter and TT Jones. Physical properties of foamed plastics and their dependence on structure. *PLASTICS & POLYMERS*, 40(146):69, 1972.

[307] PJ Phillips and NR Waterman. The mechanical properties of high-density rigid polyurethane foams in compression: I. modulus. *Polymer Engineering & Science*, 14(1):67–71, 1974.

[308] DR Moore, KH Couzens, and MJ Iremonger. The deformational behaviour of foamed thermoplastics. *Journal of Cellular Plastics*, 10(3):135–139, 1974.

[309] SK Maiti, LJ Gibson, and MF Ashby. Deformation and energy absorption diagrams for cellular solids. *Acta metallurgica*, 32(11):1963–1975, 1984.

[310] Richard Chan and Masao Nakamura. Mechanical properties of plastic foams: the dependence of yield stress and modulus on the structural variables of closed-cell and open-cell foams. *Journal of Cellular Plastics*, 5(2):112–118, 1969.

[311] CA Brighton and AE Meazey. Expanded polyvinyl chloride. In *Expanded Plastics—Trends in Performance Requirements"—A Micro Symposium organized by QMC Industrial Research Ltd*, 1973.

[312] M Wilsea, KL Johnson, and MF Ashby. Indentation of foamed plastics. *International Journal of Mechanical Sciences*, 17(7):457IN5–460IN6, 1975.

[313] JB Walsh, WF Brace, and AW England. Effect of porosity on compressibility of glass. *Journal of the American Ceramic Society*, 48(12):605–608, 1965.

[314] James G Zwissler and Marc A Adams. Fracture mechanics of cellular glass. *Fracture mechanics of ceramics.*, 6:211–241, 1983.

[315] John D Eshelby. The determination of the elastic field of an ellipsoidal inclusion, and related problems. In *Proceedings of the Royal Society of London A: Mathematical, Physical and Engineering Sciences*, volume 241, pages 376–396. The Royal Society, 1957.

[316] Rodney Hill. Elastic properties of reinforced solids: some theoretical principles. *Journal of the Mechanics and Physics of Solids*, 11(5):357–372, 1963.

[317] Francesco Mancarella, Robert W Style, and John S Wettlaufer. Surface tension and the mori–tanaka theory of non-dilute soft composite solids. In *Proc. R. Soc. A*, volume 472, page 20150853. The Royal Society, 2016.

[318] Francesco Mancarella, Robert W Style, and John S Wettlaufer. Interfacial tension and a three-phase generalized self-consistent theory of non-dilute soft composite solids. *Soft matter*, 12(10):2744–2750, 2016.

[319] Yuhao Wang and David L Henann. Finite-element modeling of soft solids with liquid inclusions. *Extreme Mechanics Letters*, 9:147–157, 2016.

[320] James L Bries and Michael D Hamerski. Removable foam adhesive tape, May 15 2001. US Patent 6,231,962.

[321] Michael S Sylvester. Self-adhesive reinforced foam gasket, April 22 2003. US Patent 6,551,425.

[322] Nicholas J Glassmaker, Anand Jagota, Chung-Yuen Hui, William L Noderer, and Manoj K Chaudhury. Biologically inspired crack trapping for enhanced adhesion. *Proceedings of the National Academy of Sciences*, 104(26):10786–10791, 2007.

[323] Lulin Shen, Nicholas J Glassmaker, Anand Jagota, and Chung-Yuen Hui. Strongly enhanced static friction using a film-terminated fibrillar interface. *Soft Matter*, 4(3):618–625, 2008.

[324] H Yao, G Della Rocca, PR Guduru, and H Gao. Adhesion and sliding response of a biologically inspired fibrillar surface: experimental observations. *Journal of The Royal Society Interface*, 5(24):723–733, 2008.

[325] Abhijit Majumder, Ashutosh Sharma, and Animangsu Ghatak. A bioinspired wet/dry microfluidic adhesive for aqueous environments. *Langmuir*, 26(1):521–525, 2009.

[326] Aarash Sofla, Erkin Seker, James P Landers, and Matthew R Begley. Pdms-glass interface adhesion energy determined via comprehensive solutions for thin film bulge/blister tests. *Journal of Applied Mechanics*, 77(3):031007, 2010.

[327] AN Gent and J Schultz. Effect of wetting liquids on the strength of adhesion of viscoelastic material. *The Journal of Adhesion*, 3(4):281–294, 1972.

[328] D Maugis and M Barquins. Fracture mechanics and adherence of viscoelastic solids. In *Adhesion and adsorption of polymers*, pages 203–277. Springer, 1980.

[329] David Martina, Constantino Creton, Pascal Damman, Mélanie Jeusette, and Anke Lindner. Adhesion of soft viscoelastic adhesives on periodic rough surfaces. *Soft Matter*, 8(19):5350–5357, 2012.

[330] Julia Nase, Osvanny Ramos, Costantino Creton, and Anke Lindner. Debonding energy of pdms. *European Physical Journal E–Soft Matter*, 36(9), 2013.

[331] Joseph D Berry, Michael J Neeson, Raymond R Dagastine, Derek YC Chan, and Rico F Tabor. Measurement of surface and interfacial tension using pendant drop tensiometry. *Journal of colloid and interface science*, 454:226–237, 2015.

[332] JE Mark. Rubber elasticity, 1981.

université PARIS-SACLAY
ÉCOLE DOCTORALE
Physique en île-de-France (EDPIF)

Titre : Lien entre propriétés adhésives et structure de polyHIPEs de silicone stabilisées via des réactions chimiques

Mots clefs : Matériaux cellulaires, réactions aux interfaces, structure, adhésion

Résumé : Les matériaux cellulaires font l'objet de beaucoup de recherches du fait de leurs remarquables propriétés. Celles-ci proviennent de la structure interne du matériau, dans lequel des inclusions cellulaires sont compactées dans une matrice solide. Comprendre et contrôler l'organisation des cellules dans la phase continue est donc primordial pour pouvoir contrôler les propriétés finales du solide poreux.

L'influence des propriétés d'objets sur leur organisation dans un volume a souvent été étudiée pour des systèmes granulaires durs monodisperses, où la friction entre deux grains implique que l'arrangement global sera désorganisé, ou pour des systèmes mous comme les bulles dans les mousses aqueuses, où la très faible friction aux interfaces conduit à un empilement organisé et compact de sphères. Une question importante est de comprendre comment s'empilent des objets déformables présentant de la friction à l'interface. Pour répondre à cela, nous nous intéressons ici à un système modèle de gouttes de PEG (polyéthylèneglycol) dispersées dans une phase continue de PDMS (polydiméthylsiloxane). La coalescence entre les gouttes est empêchée grâce à une réaction à l'interface qui crée un gel de polymère à la surface des gouttes au contact avec le PDMS. Cette peau de polymères induit de la friction et de l'adhésion entre les gouttes. Pour étudier l'influence des propriétés de la peau sur la sédimentation des gouttes, nous caractérisons la fraction volumique finale sous gravité grâce à la tomographie sous rayons X. Nous montrons que la présence de friction et d'adhésion à l'interface induit une organisation non-conventionnelle des gouttes en comparaison avec celle d'émulsions stabilisées par des tensioactifs.

Nous examinons ensuite les propriétés mécaniques et adhésives des émulsions solides, composées de gouttes liquides dans une matrice solide, avec un test de probe-tack. Nous étudions l'impact de la taille ainsi que de la densité de gouttes sur l'augmentation des dissipations d'énergie dans le volume.

Title : Linking adhesive properties and pore organisation of silicone emulsions obtained by reactive blending

Keywords : Cellular materials, interfaces, reactive stabilisation, structure, adhesion

Abstract : Macro-cellular polymers are highly searched-for materials thanks to their rich physical properties. These arise from the internal structuration of the material, in which discrete cells of gas or liquid are tightly packed within a continuous polymeric solid. The size and organisation of these cells have an important influence on the overall material properties.

The influence of the properties of spheres on their final packing morphology has led to numerous studies usually dealing with either hard frictional or soft frictionless grains, which are the two extremes of the spectrum of possible systems. An important question remains as to what happens for systems which are in-between these extremes, i.e. highly deformable grains presenting a frictional surface. To tackle this problem, we work with a model system of ultra-stable emulsions which consist of PEG (polyethyleneglycol) drops which are dispersed in a continuous phase of PDMS (polydimethylsiloxane). Coalescence of the drops is prohibited by a reactive blending approach which creates a solid-like skin around the PEG drops upon contact with the PDMS. This skin creates adhesion and friction between the drops. To study the influence of the skin properties on the sedimentation of the drops, we characterise the final drop packing under gravity using absorption contrast X-Ray. We show that the presence of friction and adhesion at the interface makes the liquid drops pack unconventionally regarding density and organization compared to classic surfactant stabilized emulsions.

We then investigated the adhesive properties of the solid emulsions i.e. elastomers containing liquid drops in their substructure, using a probe-tack test. We studied the impact of the drop size and density on the increase of the bulk's dissipations of energy which enhance the adhesive properties of the material.

Université Paris-Saclay
Espace Technologique / Immeuble Discovery
Route de l'Orme aux Merisiers RD 128 / 91190 Saint-Aubin, France